



Balducci, Giulia (2015) *Lightweight metal hydride – hydroxide systems for solid state hydrogen storage*. PhD thesis.

<http://theses.gla.ac.uk/6534/>

Copyright and moral rights for this thesis are retained by the author

A copy can be downloaded for personal non-commercial research or study

This thesis cannot be reproduced or quoted extensively from without first obtaining permission in writing from the Author

The content must not be changed in any way or sold commercially in any format or medium without the formal permission of the Author

When referring to this work, full bibliographic details including the author, title, awarding institution and date of the thesis must be given

**Lightweight Metal Hydride – Hydroxide**  
**Systems for Solid State Hydrogen Storage**



University  
of Glasgow

Giulia Balducci

Submitted in fulfilment of the requirements for the  
Degree of Doctor of Philosophy

School of Chemistry  
College of Science and Engineering

University of Glasgow  
(March 2015)

## Abstract

This thesis describes the preparation and characterisation of potential ‘modular’ solid state hydrogen storage solutions for on-board applications. The systems investigated throughout this work are based on reactions between light weight hydroxides and hydrides.

In many senses *light metal hydroxides* can be seen as attractive candidates for hydrogen storage: they are low cost, present negligible toxicity and it is not possible to poison the fuel cell with decomposition products, unlike in nitrogen or boron containing systems. However, as the dehydrogenation products are the respective oxides, the major drawback of such systems lays in the fact the thermodynamics of rehydrogenation are not favourable for on-board applications. Hence, the system must be considered as a ‘charged module’, where the regeneration is performed *ex-situ*. Dehydrogenation can be achieved through reaction with light metal hydrides such as LiH or MgH<sub>2</sub>.

A wide range of ‘modular’ release systems can be studied, however the most interesting in terms of theoretical gravimetric capacity, kinetics and thermodynamics within reasonable temperature range (RT - 350°C) use magnesium and lithium hydroxide and their hydrate forms. The present work focuses on the full investigation of three main systems:

- Mg(OH)<sub>2</sub> – MgH<sub>2</sub> system
- Mg(OH)<sub>2</sub> – LiH system
- LiOH(·H<sub>2</sub>O) – MgH<sub>2</sub> system (both anhydrous and monohydrate LiOH were used)

Mixtures of hydroxides and hydrides were prepared by manually grinding stoichiometric amounts of the starting materials. Further, nanostructuring the reactants was investigated as a means to control the dehydrogenation reaction and enhance the kinetics and thermodynamics of the process. Nanostructured Mg(OH)<sub>2</sub> and LiOH(·H<sub>2</sub>O) have been successfully obtained using both novel and conventional synthetic routes. Reduction of the particle size of both hydrides was effectively achieved by mechanically milling the bulk materials. As detailed throughout Chapters 3, 4 and 5, promising results were obtained when employing nanosized reactants. The onset temperatures of hydrogen release were decreased and the overall systems performances enhanced. Particularly interesting results were obtained for the LiOH – MgH<sub>2</sub> system, which exhibit a dramatic decrease of the onset temperature of H<sub>2</sub> release of nearly 100 K when working with milled and nanostructured materials with respect to bulk reagents.

All systems were characterised mainly by Powder X-ray diffraction (PXD) and simultaneous thermogravimetric analysis (TG-DTA) mass spectroscopy (MS). TG-DTA-

MS experiments were performed to obtain information on the onset and peak temperature of hydrogen release, weight loss percentage and nature and amount of the gases evolved during the reaction. *Ex-situ* PXD studies have been performed for each system in order to try and identify any intermediate species forming during the dehydrogenation process and ultimately propose a mechanism of H<sub>2</sub> release. Since two fundamentally different types of reaction pathway could be proposed for the Mg(OH)<sub>2</sub> – LiH system, powder neutron diffraction (PND) was employed for following the reaction *in-situ*. Developing a complete model of the dehydrogenation process in terms of mechanistic steps was found to be pivotal in order to understand and enhance such systems further.

# Table of Contents

Abstract .....	1
Table of Contents .....	3
List of Tables.....	8
List of Figures .....	13
Acknowledgement.....	25
Abbreviations and Definitions .....	26
1 Introduction .....	27
1.1 Hydrogen: a clean and renewable energy carrier .....	27
1.2 Fuel Cells.....	29
1.2.1 Low Temperature Fuel Cells.....	31
1.2.1.1 Polymer Electrolyte Membrane Fuel Cells .....	31
1.2.1.2 Alkaline Fuel Cells .....	32
1.2.1.3 Phosphoric Acid Fuel Cells.....	32
1.2.1.4 Direct Methanol Fuel Cells .....	33
1.2.2 High Temperature Fuel Cells .....	34
1.2.2.1 Solid Oxide Fuel Cell .....	34
1.2.2.2 Molten Carbonate Fuel Cells.....	35
1.2.3 Fuel cells technologies comparison.....	36
1.3 Solid State Hydrogen Storage .....	37
1.3.1 Chemical hydrogen storage .....	37
1.3.1.1 Light metal hydrides.....	38
1.3.1.2 Complex hydrides.....	40
1.3.1.3 Nitrides, imides and amides: N-H-based materials .....	41
1.3.2 Hydride – Hydroxide hydrogen release systems .....	43
1.4 Light metal hydroxides.....	48
1.4.1 Magnesium hydroxide: structure and dehydrogenation properties .....	48
1.4.2 Lithium hydroxide: structure and dehydrogenation properties .....	50

1.5	Scope of this work .....	52
1.6	References .....	53
2	Experimental .....	65
2.1	Air Sensitive Handling Techniques.....	65
2.1.1	Dry Glove Boxes .....	65
2.2	Preparative Methods.....	66
2.2.1	Ball Milling .....	66
2.2.1.1	Ball Milling of Light Metal Hydrides .....	68
2.2.1.2	Ball Milling of Light Metal Hydroxides .....	68
2.2.2	Synthesis of Nanostructured Light Metal Hydroxides.....	69
2.2.2.1	Microwave Synthesis of Nanostructured Magnesium Hydroxide .....	69
2.2.2.2	Selective Synthesis of Nanostructured Lithium Hydroxide .....	74
2.3	Characterisation Techniques .....	76
2.3.1	Powder X-Ray Diffraction (PXD).....	76
2.3.1.1	PXD Instrumentation and Sample Preparation .....	80
2.3.1.2	Data Analysis .....	82
2.3.2	In-Situ Powder Neutron Diffraction (PND).....	82
2.3.2.1	The Polaris instrument at Rutherford Appleton Laboratory (RAL).....	83
2.3.2.2	Sample Preparation and Data Collection on Polaris.....	85
2.3.3	PXD and PND Data Analysis: Rietveld Refinement .....	86
2.3.4	Simultaneous Thermogravimetric Analysis (STA) Mass Spectrometry (MS) 90	
2.3.4.1	Simultaneous Thermogravimetric Analysis (STA).....	90
2.3.4.2	Mass Spectrometry (MS).....	92
2.3.5	Scanning Electron Microscopy (SEM).....	94
2.3.5.1	Preparation of samples .....	96
2.4	References .....	97
3	The magnesium hydride – magnesium hydroxide ‘modular’ release system.....	101
3.1	Introduction .....	101

3.2	Experimental .....	103
3.2.1	Preparation of the systems.....	103
3.2.2	Microwave-Hydrothermal Synthesis of nanostructured Mg(OH) <sub>2</sub> .....	103
3.2.3	Ball milling of Mg(OH) <sub>2</sub> .....	103
3.2.4	Ball milling of MgH <sub>2</sub> .....	104
3.2.5	TG-DTA-MS studies .....	104
3.2.6	Powder X-ray diffraction (PXD) experiments .....	105
3.2.7	Scanning Electron Microscopy (SEM) imaging.....	105
3.2.8	Summary of samples and reactions .....	106
3.3	Results and Discussion.....	108
3.3.1	Preparation of the system components.....	108
3.3.1.1	Nanostructured Mg(OH) <sub>2</sub> .....	108
3.3.1.2	Ball milled Mg(OH) <sub>2</sub> .....	111
3.3.1.3	Ball milled MgH <sub>2</sub> .....	112
3.3.1.4	TG-DTA-MS data .....	114
3.3.2	Ex-situ PXD and Proposed Mechanisms.....	125
3.3.2.1	Bulk System .....	125
3.3.2.2	Milled system .....	127
3.3.2.3	Nanostructured system .....	130
3.4	Conclusions and Future Work.....	133
3.5	References .....	136
4	The lithium hydride – magnesium hydroxide ‘modular’ release system: an <i>in-situ</i> powder neutron diffraction study .....	139
4.1	Introduction .....	139
4.2	Experimental .....	140
4.2.1	Preparation of the Mg(OH) <sub>2</sub> – LiH system .....	140
4.2.2	Preparation of the Mg(OD) <sub>2</sub> – LiD system for PND experiments .....	141
4.2.3	Synthesis of nanostructured Mg(OH) <sub>2</sub> (Mg(OD) <sub>2</sub> ) .....	141
4.2.4	Ball milling of LiH(D) .....	141

4.2.5	TG-DTA-MS studies .....	142
4.2.6	Powder X-ray diffraction (PXD) experiments .....	143
4.2.7	Scanning Electron Microscopy (SEM) imaging.....	143
4.2.8	<i>In-situ</i> powder neutron diffraction (PND) experiments .....	144
4.2.9	Rietveld refinement against PND data .....	145
4.3	Results and Discussion.....	146
4.3.1	The Mg(OH) <sub>2</sub> – LiH system.....	146
4.3.1.1	Preparation of the system components .....	146
4.3.1.2	TG-DTA-MS data .....	148
4.3.1.3	<i>Ex-situ</i> PXD analysis and proposed mechanisms: an intermediate study of the nanostructured system.....	151
4.3.2	Powder neutron diffraction experiments .....	154
4.3.2.1	Preparation and preliminary characterisation of the system.....	154
4.3.3	The Polaris experiment.....	156
4.3.3.1	First mechanistic step: Mg(OD) <sub>2</sub> dehydration and LiD hydrolysis.....	166
4.3.3.2	Second mechanistic step: reaction of the remaining LiD.....	169
4.4	Conclusions .....	171
4.5	References .....	173
5	The magnesium hydride – lithium hydroxide ‘modular’ release system: H <sub>2</sub> desorption properties when working with anhydrous or monohydrate lithium hydroxide.....	176
5.1	Introduction .....	176
5.2	Experimental .....	179
5.2.1	Preparation of the systems.....	179
5.2.2	Selective Synthesis of nanostructured LiOH(·H <sub>2</sub> O) .....	179
5.2.3	Ball milling of LiOH(·H <sub>2</sub> O).....	180
5.2.4	Ball milling of MgH <sub>2</sub> .....	180
5.2.5	TG-DTA-MS studies .....	180
5.2.6	Powder X-ray diffraction (PXD) experiments .....	181
5.2.7	Scanning Electron Microscopy (SEM) imaging.....	182

5.2.8	Summary of samples and reactions .....	182
5.3	Results and Discussion .....	186
5.3.1	Preparation of the system components .....	186
5.3.1.1	Nanostructured LiOH( $\cdot$ H <sub>2</sub> O) .....	186
5.3.1.2	Ball milled LiOH( $\cdot$ H <sub>2</sub> O) .....	192
5.3.1.3	Ball milled MgH <sub>2</sub> .....	193
5.3.2	TG-DTA-MS data .....	194
5.3.2.1	Starting Materials .....	194
5.3.2.2	LiOH – MgH <sub>2</sub> system .....	199
5.3.2.3	LiOH $\cdot$ H <sub>2</sub> O – MgH <sub>2</sub> system .....	205
5.3.3	Ex-situ PXD and Proposed Mechanisms .....	211
5.3.3.1	LiOH – MgH <sub>2</sub> system .....	212
5.3.3.1.1	Bulk system .....	212
5.3.3.1.2	Milled system .....	214
5.3.3.1.3	Nanostructured system .....	217
5.3.3.2	LiOH $\cdot$ H <sub>2</sub> O – MgH <sub>2</sub> system .....	220
5.3.3.2.1	Bulk system .....	220
5.3.3.2.2	Milled system .....	222
5.3.3.2.3	Nanostructured system .....	225
5.4	Conclusions and Future Work .....	228
5.5	References .....	231
6	Conclusions and Future Work .....	235
6.1	Conclusions .....	235
6.2	Future Work .....	239
6.3	References .....	241
7	Appendices .....	243
7.1	Appendix A: Tables and Figures for Chapter 3 .....	243
7.2	Appendix B: Tables and Figures for Chapter 4 .....	253
7.3	Appendix C: Figures for Chapter 5 .....	264

## List of Tables

Table 1-1: Selected DoE technical system targets for on-board hydrogen storage for light-duty hydrogen powdered vehicles. Adapted from Reference 12. ....	28
Table 1-2: Comparison of different fuel cell types. Adapted from Reference 59.....	36
Table 1-3: Molecular weight, theoretical gravimetric and volumetric hydrogen capacities, temperatures of decomposition for selected light metal binary hydrides. Adapted from Reference 70.....	38
Table 1-4: Molecular weight, theoretical gravimetric and volumetric hydrogen capacities, temperatures of H <sub>2</sub> desorption for selected borohydrates and alanates. Adapted from Reference 70.....	40
Table 2-1: Summary of the seven crystal systems and respective symmetry elements.....	78
Table 2-2: Equations for calculating d-spacing in the different crystal systems. ....	79
Table 3-1: Summary of starting materials employed in the Mg(OH) <sub>2</sub> – MgH <sub>2</sub> ‘modular’ release systems.....	106
Table 3-2: Summary of preparations carried out for the bulk ‘modular’ system.....	106
Table 3-3: Summary of preparations carried out for the mechanically milled ‘modular’ system.....	106
Table 3-4: Summary of preparations carried out for the nanostructured ‘modular’ system. ....	107
Table 3-5: Summary of preparations carried out for activation energy calculations.....	107
Table 3-6: Selected data from the PXD Rietveld refinement for Sample 1, synthesised nano Mg(OH) <sub>2</sub> . <sup>5</sup> .....	109
Table 3-7: Onset temperature, peak temperatures, weight losses and identified released gaseous species for Sample 1 (nano Mg(OH) <sub>2</sub> ), Sample 2 (milled Mg(OH) <sub>2</sub> ) and as-received Mg(OH) <sub>2</sub> .....	114
Table 3-8: Onset temperature, peak temperatures, weight losses and identified released gaseous species for Sample 3 (milled MgH <sub>2</sub> ) and for as-received MgH <sub>2</sub> .....	116

Table 3-9: Onset temperature, peak temperatures, weight losses and identified released gaseous species for Samples 5, 11 and 15. If not otherwise specified, the thermal events are endothermic.....	118
Table 3-10: Summary of the integrated peak area calculated from the MS spectra and normalised to the mass weight of each sample. ....	122
Table 3-11: Kissinger plot data for Samples 18, 19 and 20. Literature reported values for activation energy of Mg(OH) <sub>2</sub> and MgH <sub>2</sub> are given at the bottom of the table. ....	124
Table 3-12: Summary of the temperature points and respective phases present for <i>ex-situ</i> PXD analysis for Samples 4, 5, 6, 7, 8 and 9.....	127
Table 3-13: Summary of the temperature points and respective phases present for <i>ex-situ</i> PXD analysis for Samples 10, 11, 12 and 13.....	129
Table 3-14: Summary of the temperature points and respective phases present for <i>ex-situ</i> PXD analysis for Samples 14, 15, 16 and 17.....	132
Table 4-1: Summary of samples and preparations carried out for the development of the Mg(OH) <sub>2</sub> – LiH ‘modular’ system.....	142
Table 4-2: Summary of reactions carried out for activation energy calculations. ....	143
Table 4-3: Summary of samples prepared for <i>in-situ</i> PND experiment at POLARIS. ....	144
Table 4-4: Summary of data collected during the variable temperature <i>in-situ</i> PND experiment for the Mg(OH) <sub>2</sub> – LiH system under flowing Argon.....	145
Table 4-5: Onset temperature, peak temperatures and weight losses for Samples 3 and 4. ....	148
Table 4-6: Kissinger plot data for Samples 6. Literature reported values for activation energy of Mg(OH) <sub>2</sub> , LiH and LiOH are given at the bottom of the table.....	150
Table 4-7: Calculated weight fractions from the PND Rietveld refinement data for the phases present in Samples 11, 12, 20, 24 and 25. ....	157
Table 4-8: Selected data from the PND Rietveld refinement for Sample 11 (298 K). ....	158
Table 4-9: Selected data from the PND Rietveld refinement for Sample 12 (448 K). ....	159
Table 4-10: Selected data from the PND Rietveld refinement of Sample 20 (523 K).....	161
Table 4-11: Selected data from the PND Rietveld refinement for Sample 24 (573 K). ....	162
Table 4-12: Selected data from the PND Rietveld refinement for Sample 25 (673 K). ....	164

Table 4-13: Calculated weight fractions from the PND Rietveld refinement data for the phases present in Samples 12 to 19.....	168
Table 4-14: Calculated wt. % from the PND Rietveld refinement data for the phases present in Samples 21-25. ....	170
Table 5-1: Summary of starting materials employed in the LiOH – MgH <sub>2</sub> hydrogen release systems. ....	182
Table 5-2: Summary of preparations carried out for the bulk LiOH – MgH <sub>2</sub> system. ....	183
Table 5-3: Summary of preparations carried out for the mechanically milled LiOH – MgH <sub>2</sub> system.....	183
Table 5-4: Summary of preparations carried out for the nanostructured LiOH – MgH <sub>2</sub> system.....	183
Table 5-5: Summary of preparations carried out for activation energy calculations for the LiOH – MgH <sub>2</sub> system. ....	184
Table 5-6: Summary of preparations carried out for the bulk LiOH·H <sub>2</sub> O – MgH <sub>2</sub> system. ....	184
Table 5-7: Summary of preparations carried out for the mechanically milled LiOH·H <sub>2</sub> O – MgH <sub>2</sub> system.....	185
Table 5-8: Summary of preparations carried out for the nanostructured LiOH·H <sub>2</sub> O – MgH <sub>2</sub> system.....	185
Table 5-9: Summary of preparations carried out for activation energy calculations for the LiOH·H <sub>2</sub> O – MgH <sub>2</sub> system. ....	186
Table 5-10: Selected data from the PXD Rietveld refinement for Sample 1, synthesised nano LiOH.....	188
Table 5-11: Selected data from the PXD Rietveld refinement for Sample 2, synthesised n-LiOH·H <sub>2</sub> O.....	191
Table 5-12: Onset temperature, peak temperatures, weight losses and identified released gaseous species for Sample 1 (n-LiOH), Sample 3 (m-LiOH) and as-received LiOH (b-LiOH). ....	195
Table 5-13: Onset temperature, peak temperatures, weight losses and identified released gaseous species for Sample 2 (n-LiOH·H <sub>2</sub> O), Sample 4 (m-LiOH·H <sub>2</sub> O) and as-received LiOH·H <sub>2</sub> O (b- LiOH·H <sub>2</sub> O). ....	197

Table 5-14: Onset temperature, peak temperatures, weight losses and identified released gaseous species for Sample 5 (milled MgH <sub>2</sub> ) and for as-received MgH <sub>2</sub> .....	199
Table 5-15: Onset temperature, peak temperatures, weight losses and identified released gaseous species for Samples 7, 12 and 17. ....	199
Table 5-16: Calculated activation energies for Samples 20, 21 and 22. Literature reported values for activation energy for LiOH and MgH <sub>2</sub> are given at the bottom of the table.....	204
Table 5-17: Onset temperature, peak temperatures, weight losses and identified released gaseous species for Samples 24, 30 and 36. If not otherwise specified, the thermal events are endothermic. ....	205
Table 5-18: Calculated activation energies for Samples 40, 41 and 42. Literature reported values for activation energy for LiOH·H <sub>2</sub> O, Mg(OH) <sub>2</sub> , LiOH and MgH <sub>2</sub> are given at the bottom of the table. ....	210
Table 5-19: Summary of the temperature points and respective phases present for <i>ex-situ</i> PXD analysis for Samples 6, 7, 8, 9 and 10.....	214
Table 5-20: Summary of the temperature points and respective phases present for <i>ex-situ</i> PXD analysis for Samples 11, 12, 13, 14 and 15.....	216
Table 5-21: Summary of the temperature points and respective phases present for <i>ex-situ</i> PXD analysis for Samples 16, 17, 18 and 19.....	219
Table 5-22: Summary of the temperature points and respective phases present for <i>ex-situ</i> PXD analysis for Samples 23, 24, 25, 26, 27 and 28.....	222
Table 5-23: Summary of the temperature points and respective phases present for <i>ex-situ</i> PXD analysis for Samples 29, 30, 31, 32, 33 and 34.....	224
Table 5-24: Summary of the temperature points and respective phases present for <i>ex-situ</i> PXD analysis for Samples 35, 36, 37, 38 and 39.....	227
Table 7-1: Selected data from the PXD Rietveld refinement for commercial β-MgH <sub>2</sub> .....	244
Table 7-2: Selected data from the PND Rietveld refinement for Sample 13 (458 K). ....	254
Table 7-3: Selected data from the PND Rietveld refinement for Sample 14 (468 K). ....	255
Table 7-4: Selected data from the PND Rietveld refinement for Sample 15 (478 K). ....	256
Table 7-5: Selected data from the PND Rietveld refinement for Sample 16 (488 K). ....	257
Table 7-6: Selected data from the PND Rietveld refinement for Sample 17 (498 K). ....	258

Table 7-7: Selected data from the PND Rietveld refinement for Sample 18 (508 K). .....	259
Table 7-8: Selected data from the PND Rietveld refinement for Sample 19 (518 K). .....	260
Table 7-9: Selected data from the PND Rietveld refinement for Sample 21 (528 K). .....	261
Table 7-10: Selected data from the PND Rietveld refinement for Sample 22 (538 K). ....	262
Table 7-11: Selected data from the PND Rietveld refinement for Sample 23 (548 K). ....	263

## List of Figures

Figure 1-1: Schematic of a sustainable hydrogen cycle.....	27
Figure 1-2: Schematic of a hydrogen powered fuel cell. ....	30
Figure 1-3: Comparison of theoretical gravimetric and volumetric capacity for solid state hydrogen storage hydrides. ....	38
Figure 1-4: Schematic of the proposed ‘modular’ hydrogen release system; H <sub>2</sub> fuel source is given from the reaction between hydride and hydroxide. ....	43
Figure 1-5: Proposed ‘modular’ solid state hydrogen release system .....	45
Figure 1-6: Crystal structure of Mg(OH) <sub>2</sub> . Olive green spheres indicate magnesium, red spheres oxygen and white spheres hydrogen respectively. ....	49
Figure 1-7: Crystal structure of LiOH. Blue spheres indicate lithium, red spheres oxygen and white spheres hydrogen respectively.....	50
Figure 1-8: Crystal structure of LiOH·H <sub>2</sub> O. Blue spheres indicate lithium, red spheres oxygen and white spheres hydrogen respectively.....	51
Figure 2-1: a) Omega Saffron Scientific glove box and b) LABstar mBraun glove box. Adapted from References 1 and 2.....	66
Figure 2-2: (a) Retsch PM100 planetary ball mill configuration; (b) cross section of the milling jar.....	67
Figure 2-3: The electromagnetic spectrum. ....	70
Figure 2-4: Typical autoclave used for hydrothermal synthesis. Figure (a) shows the full set-up, whilst Figure (b) shows the cross section of the autoclave. Adapted from Reference 24.....	72
Figure 2-5: Microwave autoclave used for the synthesis of n-Mg(OH) <sub>2</sub> . Figure (a) shows the full set-up, while Figure (b) shows the cross section of the autoclave. Adapted from Reference 24.....	73
Figure 2-6: Schematic of a typical Schlenk apparatus. ....	75
Figure 2-7: Schematic of diffraction of a crystal used for deriving Bragg’s law. ....	77
Figure 2-8: definition of axis, unit cell dimensions and angles for a general unit cell.....	78
Figure 2-9: Debye-Scherrer transmission geometry. ....	81

Figure 2-10: Bragg-Brentano reflection geometry.....	81
Figure 2-11: Schematic of Polaris diffractometer. The numbers indicate the different detector banks.....	85
Figure 2-12: Polaris experiment: (a) sample placed at the bottom of the quartz tube for a total height of <i>ca.</i> 40 mm; (b) full experimental setup single glass quartz tube with inner stainless steel pipe for the flow of argon.....	86
Figure 2-13: Schematic of the Netzsch STA 409 PC.....	90
Figure 2-14: Schematic of the sample and reference crucible arrangement on the DTA sample carrier.....	91
Figure 2-15: Quadrupole mass analyser developed by W. Paul. Adapted from Reference <sup>54</sup> .....	93
Figure 2-16: Schematic of possible scattering of electrons from a typical SEM experiment.....	95
Figure 2-17: Schematic of a Scanning Electron Microscope.....	96
Figure 3-1: PXD pattern for Sample 1, synthesised n-Mg(OH) <sub>2</sub> .....	108
Figure 3-2: Collected SEM images for Sample 1: a) 1 μm scale b) 200 nm scale .....	109
Figure 3-3: Observed, calculated and difference (OCD) plot from the PXD Rietveld refinement for Sample 1, synthesised n-Mg(OH) <sub>2</sub> .....	110
Figure 3-4: Proposed growth processes for (a) conventional hydrothermal synthesis of Mg(OH) <sub>2</sub> nanoplates and (b) MW-HT synthesis of Mg(OH) <sub>2</sub> nanoplates performed during this project.....	111
Figure 3-5: PXD pattern for Sample 2, ball milled magnesium hydroxide.....	111
Figure 3-6: Collected SEM images for Sample 2: a) 1 μm scale b) 200 nm scale .....	112
Figure 3-7: PXD pattern for Sample 3, ball milled magnesium hydride (β-MgH <sub>2</sub> ). Triangles and circles indicate γ-MgH <sub>2</sub> and Mg metal respectively. ....	113
Figure 3-8: Collected SEM images: a) commercial MgH <sub>2</sub> (10 μm scale) and b) Sample 3 (2 μm scale) .....	113
Figure 3-9: Higher magnification SEM image for Sample 3 (200 nm scale).....	113
Figure 3-10: (a) TG and (b) DTA data comparison for commercial (red), nanostructured (1; blue) and milled (2, green) magnesium hydroxide. ....	114

Figure 3-11: MS profiles Vs time for commercial (red), nanostructured (1; blue) and milled (2, green) magnesium hydroxide.....	115
Figure 3-12: (a) TG and (b) DTA data comparison for commercial (red) and milled (3, blue) magnesium hydride.....	116
Figure 3-13: MS profiles Vs time for commercial (red) and milled (3, blue) magnesium hydride.....	117
Figure 3-14: (a) TG and (b) DTA data comparison for Sample 5 (bulk; red), Sample 11 (milled; green) and Sample 15 (nano; blue).....	118
Figure 3-15: MS profiles Vs time for Sample 5 (bulk), Sample 11 (milled) and Sample 15 (nano). The black line denotes hydrogen release. In the insert, water release for bulk, milled and nanostructured materials is denoted by red, green and blue lines respectively. ....	120
Figure 3-16: Kissinger plots for Samples 18 (bulk; red triangles), 19 (milled; green dots) and 20 (nano; blue squares): (a) plots calculated for the LT thermal event; (b) plots calculated for the HT thermal event.....	124
Figure 3-17: TG (green line) and DTA (blue line) data obtained for Sample 5. The temperature values are those selected for subsequent TG-DTA and PXD experiments....	125
Figure 3-18: <i>Ex-situ</i> PXD patterns for Samples 4, 5, 6, 7, 8 and 9 collected at 298, 873 638, 673, 723 and 773 K respectively. Triangles denote Mg(OH) <sub>2</sub> , circles β-MgH <sub>2</sub> , squares Mg and crosses MgO respectively.....	126
Figure 3-19: TG (green line) and DTA (blue line) data obtained for Sample 11. ....	128
Figure 3-20: <i>Ex-situ</i> PXD patterns for Samples 10, 11, 12 and 13 collected at 298, 873, 658 and 758 K respectively. Triangles denote Mg(OH) <sub>2</sub> , circles β-MgH <sub>2</sub> , squares Mg and crosses MgO respectively. ....	128
Figure 3-21: TG (green line) and DTA (blue line) data obtained for Sample 15. ....	130
Figure 3-22: <i>Ex-situ</i> PXD patterns for Samples 14, 15, 16 and 17 collected at 298, 873, 673 and 773 K respectively. Triangles denote Mg(OH) <sub>2</sub> , circles β-MgH <sub>2</sub> , crosses MgO and squares Mg respectively. ....	131
Figure 3-23: Collected SEM images for Sample 15: a) 200 nm scale b) 100 nm scale.....	133
Figure 4-1: SEM image of Sample 2, m-LiH.....	146
Figure 4-2: PXD pattern of Sample 1, synthesised n-Mg(OH) <sub>2</sub> . ....	147

Figure 4-3: PXD pattern of Sample 2, m-LiH. The black circles indicate the presence of $\text{Li}_2\text{O}$ .	147
Figure 4-4: (a) TG and (b) DTA data comparison for bulk (3; red) and nanostructured (4; blue) $\text{Mg}(\text{OH})_2 - \text{LiH}$ materials.	149
Figure 4-5: MS profiles Vs time for Sample 3 (bulk mixture, red line) and Sample 4 (nanostructured mixture, blue line).	149
Figure 4-6: a) Kissinger plots for Samples 6: (a) plots calculated for the LT thermal event; (b) plots calculated for the HT thermal event.	150
Figure 4-7: <i>Ex-situ</i> PXD patterns of Samples 4 and 5 compared to the mixture of starting materials at room temperature (PXD patterns of Sample 4 were collected at 298 K, prior to thermal treatment). Crosses denote $\text{Mg}(\text{OH})_2$ , squares LiH, stars $\text{MgO}$ , triangles LiOH and circles $\text{Li}_2\text{O}$ respectively.	152
Figure 4-8: PXD pattern of Sample 7, synthesised nanostructured $\text{Mg}(\text{OD})_2$ .	154
Figure 4-9: PXD analysis showing the experimental pattern of Sample 8, ball milled LiD. The black circles indicate the presence of $\text{Li}_2\text{O}$ .	155
Figure 4-10: TG (green line) and DTA (blue line) data obtained for Sample 9.	156
Figure 4-11: Bank 5 (back scattered) data obtained for the full temperature range showing the phase changes throughout the dehydrogenation process (Samples 11, 12, 20, 24 and 25). Crosses denote $\text{Mg}(\text{OD})_2$ , squares LiD, stars $\text{MgO}$ , triangles LiOD and circles $\text{Li}_2\text{O}$ respectively.	157
Figure 4-12: Observed, calculated and difference (OCD) plot from the PND Rietveld refinement for Sample 11 (298 K) from PND data, Bank 3 (low angle, $2\theta^\circ$ 40-67). The black and red tick marks indicate reflections from $\text{Mg}(\text{OD})_2$ and LiD respectively.	158
Figure 4-13: Observed, calculated and difference (OCD) plot from the PND Rietveld refinement for Sample 12 (448 K) from PND data, Bank 3 (low angle, $2\theta^\circ$ 40-67). The red, black, blue and green tick marks indicate reflections from LiD, $\text{Mg}(\text{OD})_2$ , $\text{MgO}$ and $\text{Li}_2\text{O}$ respectively.	160
Figure 4-14: Observed, calculated and difference (OCD) plot from the PND Rietveld refinement for Sample 20 (523 K) from PND data, Bank 3 (low angle, $2\theta^\circ$ 40-67). The green, blue, red and black tick marks indicate reflections from LiD, $\text{MgO}$ , $\text{Li}_2\text{O}$ and LiOD respectively.	161

Figure 4-15: Observed, calculated and difference (OCD) plot from the PND Rietveld refinement for Sample 24 (573 K) from PND data, Bank 3 (low angle, 20° 40-67). The green, blue, red and black tick marks indicate reflections from LiD, Li <sub>2</sub> O, MgO and LiOD respectively. ....	163
Figure 4-16: Observed, calculated and difference (OCD) plot from the PND Rietveld refinement for Sample 25 (673 K) from PND data, Bank 3 (low angle, 20° 40-67). The blue, red and black tick marks indicate reflections from LiD, Li <sub>2</sub> O and MgO respectively. ....	164
Figure 4-17: Variation of lattice parameters Vs temperature obtained by Rietveld refinement across the complete temperature range.....	165
Figure 4-18: Calculated weight fractions from the PND Rietveld refinement data for all phases present across the complete temperature range.....	166
Figure 4-19: Bank 5 (back scattered) data obtained over a temperature range of 448-518 K (Samples 12 to 19). Crosses denote Mg(OD) <sub>2</sub> , squares LiD, stars MgO, triangles LiOD and circles Li <sub>2</sub> O respectively. ....	167
Figure 4-20: Layered structure for LiH hydrolysis.....	169
Figure 4-21: Bank 5 (back scattered) data obtained at 528-673 K, showing the phase changes throughout the dehydrogenation process (Samples 21, 22, 23 and 25). Squares denote LiD, stars MgO, triangles LiOD and circles Li <sub>2</sub> O respectively. ....	170
Figure 5-1: PXD pattern for Sample 1, synthesised n-LiOH.....	187
Figure 5-2: Collected SEM images: a) commercial LiOH (100 µm scale) and b) Sample 1 (20 µm scale).....	187
Figure 5-3: Collected SEM images for Sample 1: a) 2 µm scale b) 200 nm scale. ....	188
Figure 5-4: Observed (green line), calculated (red dots) and difference (pink line) (OCD) plot from the PXD Rietveld refinement for Sample 1, synthesised n-LiOH. Black tick marks indicate n-LiOH reflections.....	189
Figure 5-5: PXD pattern for Sample 2, synthesised n-LiOH·H <sub>2</sub> O. ....	189
Figure 5-6: Collected SEM images: a) commercial LiOH (100 µm scale) and b) Sample 2 (20 µm scale).....	190
Figure 5-7: Collected SEM images for Sample 2: a) 2 µm scale b) 100 nm scale. ....	190

Figure 5-8: Observed (green line), calculated (red dots) and difference (pink line) (OCD) plot from the PXD Rietveld refinement for Sample 2, synthesised n-LiOH·H <sub>2</sub> O. Black tick marks indicate n-LiOH·H <sub>2</sub> O reflections. ....	191
Figure 5-9: PXD pattern for Sample 3, ball m-LiOH. ....	192
Figure 5-10: PXD pattern for Sample 4, m-LiOH·H <sub>2</sub> O. ....	192
Figure 5-11: Collected SEM images for Sample 3: a) 2 μm scale b) 1 μm scale. ....	193
Figure 5-12: Collected SEM images for Sample 4: a) 2 μm scale b) 1 μm scale. ....	193
Figure 5-13: PXD pattern for Sample 5, ball milled magnesium hydride (β-MgH <sub>2</sub> ). Triangles and circles indicate γ-MgH <sub>2</sub> and Mg metal respectively. ....	194
Figure 5-14: (a) TG and (b) DTA data comparison for commercial (red), nanostructured (1; blue) and milled (2, green) anhydrous lithium hydroxide.....	195
Figure 5-15: MS profiles Vs time for commercial (red), nanostructured (1; blue) and milled (3, green) anhydrous lithium hydroxide.....	196
Figure 5-16: (a) TG and (b) DTA data comparison for commercial (red), nanostructured (3; blue) and milled (4, green) lithium hydroxide monohydrate. ....	197
Figure 5-17: MS profiles Vs time for commercial (red), nanostructured (2; blue) and milled (4, green) lithium hydroxide monohydrate. ....	198
Figure 5-18: (a) TG and (b) DTA data comparison for Sample 7 (bulk; red), Sample 12 (milled; green) and Sample 17 (nano; blue).....	200
Figure 5-19: MS profiles Vs time for Sample 7 (bulk), Sample 12 (milled) and Sample 17 (nano). ....	200
Figure 5-20: Kissinger plots for Samples 20 (bulk; red triangles), 21 (milled; green circles) and 22 (nano; blue squares): (a) plots calculated for the LT thermal event; (b) plots calculated for the HT thermal event.....	203
Figure 5-21: (a) TG and (b) DTA data comparison for Sample 24 (bulk; red), Sample 30 (milled; green) and Sample 36 (nano; blue).....	205
Figure 5-22: MS profiles Vs time for Sample 24 (bulk), Sample 30 (milled) and Sample 36 (nano). Black line denotes hydrogen release. In the inserts, water release for bulk, milled and nanostructured materials is denoted by red, green and blue lines respectively.....	206
Figure 5-23: Kissinger plots for Samples 40 (bulk; red triangles), 41 (milled; green dots) and 42 (nano; blue squares): (a) plots calculated for thermal event 1; (b) plots calculated	

for thermal event 2; (c) plots calculated for thermal event 3; (d) plots calculated for thermal event 4. ....	209
Figure 5-24: TG (green line) and DTA (blue line) data obtained for Sample 7. ....	212
Figure 5-25: <i>Ex-situ</i> PXD patterns for Samples 6, 7, 8, 9 and 10 collected at 298, 873, 673, 758 and 773 K respectively. Squares denote LiOH, circles MgH <sub>2</sub> , stars Mg, triangles Li <sub>2</sub> O and crosses MgO respectively.....	213
Figure 5-26: TG (green line) and DTA (blue line) data obtained for Sample 12. ....	215
Figure 5-27: <i>Ex-situ</i> PXD patterns for Samples 11, 12, 13, 14 and 15 collected at 298, 873, 623, 648 and 773 K respectively. Squares denote LiOH, circles MgH <sub>2</sub> , stars Mg, triangles Li <sub>2</sub> O and crosses MgO respectively. ....	215
Figure 5-28: TG (green line) and DTA (blue line) data obtained for Sample 17. ....	217
Figure 5-29: <i>Ex-situ</i> PXD patterns for Samples 16, 17, 18 and 19 collected at 298, 873, 648 and 773 K respectively. Squares denote LiOH, circles MgH <sub>2</sub> , stars Mg, triangles Li <sub>2</sub> O and crosses MgO respectively. ....	218
Figure 5-30: Collected SEM images for Sample 17: a) 2 μm scale b) 200 nm scale. ....	220
Figure 5-31: TG (green line) and DTA (blue line) data obtained for Sample 24. ....	220
Figure 5-32: <i>Ex-situ</i> PXD patterns for Samples 23, 24, 25, 26, 27 and 28 collected at 298, 873, 408, 673, 758 and 773 K respectively. Asterisks denote LiOH·H <sub>2</sub> O, squares LiOH, circles MgH <sub>2</sub> , stars Mg, triangles Li <sub>2</sub> O and crosses MgO respectively. ....	221
Figure 5-33: TG (green line) and DTA (blue line) data obtained for Sample 30. ....	223
Figure 5-34: <i>Ex-situ</i> PXD patterns for Samples 29, 30, 31, 32, 33 and 34 collected at 298, 873, 408, 573, 673 and 773 K respectively. Asterisks denote LiOH·H <sub>2</sub> O, squares LiOH, circles MgH <sub>2</sub> , rhombuses Mg(OH) <sub>2</sub> , triangles Li <sub>2</sub> O and crosses MgO respectively. ....	223
Figure 5-35: TG (green line) and DTA (blue line) data obtained for Sample 36. ....	225
Figure 5-36: <i>Ex-situ</i> PXD patterns for Samples 35, 36, 37, 38 and 39 collected at 298, 873, 408, 623 and 773 K respectively. Asterisks denote LiOH·H <sub>2</sub> O, squares LiOH, circles MgH <sub>2</sub> , rhombuses Mg(OH) <sub>2</sub> , triangles Li <sub>2</sub> O and crosses MgO respectively.....	226
Figure 5-37: Collected SEM images for Sample 36: a) 1 μm scale b) 200 nm scale. ....	228
Figure 7-1: PXD pattern for commercial β-MgH <sub>2</sub> . Circles indicate Mg metal.....	243

Figure 7-2: Observed, calculated and difference (OCD) plot from the PXD Rietveld refinement for commercial $\beta$ -MgH <sub>2</sub> . The black and red tick marks indicate reflections from MgH <sub>2</sub> and Mg respectively. ....	243
Figure 7-3: DTA profiles used to obtain Kissinger plots for Sample 18 (bulk). Dashed and full lines indicate temperature and DTA profiles respectively. ....	244
Figure 7-4: Kissinger plot for the LT thermal event for Sample 18 (bulk).....	245
Figure 7-5: Kissinger plot for the HT thermal event for Sample 18 (bulk). ....	245
Figure 7-6: DTA profiles used to obtain Kissinger plots for Sample 19 (milled). Dashed and full lines indicate temperature and DTA profiles respectively.....	246
Figure 7-7: Kissinger plot for the LT thermal event for Sample 19 (milled). ....	246
Figure 7-8: Kissinger plot for the HT thermal event for Sample 19 (milled).....	247
Figure 7-9: DTA profiles used to obtain Kissinger plots for Sample 20 (nano). Dashed and full lines indicate temperature and DTA profiles respectively. ....	247
Figure 7-10: Kissinger plot for the LT thermal event for Sample 20 (nano).....	248
Figure 7-11: Kissinger plot for the HT thermal event for Sample 20 (nano). ....	248
Figure 7-12: TG (dashed line) and DTA (full line) data obtained for Sample 6. ....	249
Figure 7-13: TG (dashed line) and DTA (full line) data obtained for Sample 7. ....	249
Figure 7-14: TG (dashed line) and DTA (full line) data obtained for Sample 8. ....	250
Figure 7-15: TG (dashed line) and DTA (full line) data obtained for Sample 9. ....	250
Figure 7-16: TG (dashed line) and DTA (full line) data obtained for Sample 12. ....	251
Figure 7-17: TG (dashed line) and DTA (full line) obtained for Sample 13. ....	251
Figure 7-18: TG (dashed line) and DTA (full line) data obtained for Sample 16. ....	252
Figure 7-19: TG (dashed line) and DTA (full line) data obtained for Sample 17. ....	252
Figure 7-20: DTA profiles used to obtain Kissinger plots for Sample 6 (nano). Dashed and full lines indicate temperature and DTA profiles respectively. ....	253
Figure 7-21: Observed, calculated and difference (OCD) plot from the PND Rietveld refinement for Sample 13 (458 K) from PND data, Bank 3 (low angle, 20° 40-67). The green, blue, red and black tick marks indicate reflections from Li <sub>2</sub> O, MgO, LiD and LiOD respectively. ....	254

Figure 7-22: Observed, calculated and difference (OCD) plot from the PND Rietveld refinement for Sample 14 (468 K) from PND data, Bank 3 (low angle, 2θ° 40-67). The purple, green, blue, red and black tick marks indicate reflections from Mg(OD)<sub>2</sub>, LiOD, LiD, Li<sub>2</sub>O and MgO respectively.....255

Figure 7-23: Observed, calculated and difference (OCD) plot from the PND Rietveld refinement for Sample 15 (478 K), Bank 3 (low angle, 2θ° 40-67). The purple, green, blue, red and black tick marks indicate reflections from Mg(OD)<sub>2</sub>, LiOD, LiD, Li<sub>2</sub>O and MgO respectively. ....256

Figure 7-24: Observed, calculated and difference (OCD) plot from the PND Rietveld refinement for Sample 16 (488 K) from PND data, Bank 3 (low angle, 2θ° 40-67). The purple, green, blue, red and black tick marks indicate reflections from Mg(OD)<sub>2</sub>, LiOD, LiD, Li<sub>2</sub>O and MgO respectively. ....257

Figure 7-25: Observed, calculated and difference (OCD) plot from the PND Rietveld refinement for Sample 17 (498 K) from PND data, Bank 3 (low angle, 2θ° 40-67). The purple, green, blue, red and black tick marks indicate reflections from Mg(OD)<sub>2</sub>, LiOD, LiD, Li<sub>2</sub>O and MgO respectively.....258

Figure 7-26: Observed, calculated and difference (OCD) plot from the PND Rietveld refinement for Sample 18 (508 K) from PND data, Bank 4 (90 degrees, 2θ° 75-113). The green, blue, red and black tick marks indicate reflections from LiOD, LiD, Li<sub>2</sub>O and MgO respectively. The black circle indicates the presence of Mg(OD)<sub>2</sub>.....259

Figure 7-27: Observed, calculated and difference (OCD) plot from the PND Rietveld refinement for Sample 19 (518 K) from PND data, Bank 3 (low angle, 2θ° 40-67). The green, blue, red and black tick marks indicate reflections from LiOD, LiD, Li<sub>2</sub>O and MgO respectively. ....260

Figure 7-28: Observed, calculated and difference (OCD) plot from the PND Rietveld refinement for Sample 21 (528 K) from PND data, Bank 3 (low angle, 2θ° 40-67). The green, blue, red and black tick marks indicate reflections from LiOD, LiD, Li<sub>2</sub>O and MgO respectively. ....261

Figure 7-29: Observed, calculated and difference (OCD) plot from the PND Rietveld refinement for Sample 22 (538 K) from PND data, Bank 3 (low angle, 2θ° 40-67). The green, blue, red and black tick marks indicate reflections from LiOD, LiD, Li<sub>2</sub>O and MgO respectively. ....262

Figure 7-30: Observed, calculated and difference (OCD) plot from the PND Rietveld refinement for Sample 23 (548 K) from PND data, Bank 3 (low angle, 2θ° 40-67). The green, blue, red and black tick marks indicate reflections from LiD, Li <sub>2</sub> O, MgO and LiOD respectively. ....	263
Figure 7-31: DTA profiles used to obtain Kissinger plots for Sample 20 (bulk LiOH – MgH <sub>2</sub> system). Dashed and full lines indicate temperature and DTA profiles respectively. ....	264
Figure 7-32: Kissinger plot for the LT thermal event for Sample 20 (bulk LiOH – MgH <sub>2</sub> system). ....	264
Figure 7-33: Kissinger plot for the HT thermal event for Sample 20 (bulk LiOH – MgH <sub>2</sub> system). ....	265
Figure 7-34: DTA profiles used to obtain Kissinger plots for Sample 21 (milled LiOH – MgH <sub>2</sub> system). Dashed and full lines indicate temperature and DTA profiles respectively. ....	265
Figure 7-35: Kissinger plot for the LT thermal event for Sample 21 (milled LiOH – MgH <sub>2</sub> system). ....	266
Figure 7-36: Kissinger plot for the HT thermal event for Sample 21 (milled LiOH – MgH <sub>2</sub> system). ....	266
Figure 7-37: DTA profiles used to obtain Kissinger plots for Sample 22 (nano LiOH – MgH <sub>2</sub> system). Dashed and full lines indicate temperature and DTA profiles respectively. ....	267
Figure 7-38: Kissinger plot for the LT thermal event for Sample 22 (nano LiOH – MgH <sub>2</sub> system). ....	267
Figure 7-39: Kissinger plot for the HT thermal event for Sample 22 (nano LiOH – MgH <sub>2</sub> system). ....	268
Figure 7-40: DTA profiles used to obtain Kissinger plots for Sample 40 (bulk LiOH·H <sub>2</sub> O – MgH <sub>2</sub> system). Dashed and full lines indicate temperature and DTA profiles respectively. ....	268
Figure 7-41: Kissinger plot for the thermal event 1 for Sample 40 (bulk LiOH·H <sub>2</sub> O – MgH <sub>2</sub> system). ....	269
Figure 7-42: Kissinger plot for the thermal event 2 for Sample 40 (bulk LiOH·H <sub>2</sub> O – MgH <sub>2</sub> system). ....	269

Figure 7-43: Kissinger plot for the thermal event 3 for Sample 40 (bulk $\text{LiOH}\cdot\text{H}_2\text{O} - \text{MgH}_2$ system). .....	270
Figure 7-44: DTA profiles used to obtain Kissinger plots for Sample 41 (milled $\text{LiOH}\cdot\text{H}_2\text{O} - \text{MgH}_2$ system). Dashed and full lines indicate temperature and DTA profiles respectively. ....	270
Figure 7-45: Kissinger plot for the thermal event 1 for Sample 41 (milled $\text{LiOH}\cdot\text{H}_2\text{O} - \text{MgH}_2$ system). .....	271
Figure 7-46: Kissinger plot for the thermal event 2 for Sample 41 (milled $\text{LiOH}\cdot\text{H}_2\text{O} - \text{MgH}_2$ system). .....	271
Figure 7-47: Kissinger plot for the thermal event 3 for Sample 41 (milled $\text{LiOH}\cdot\text{H}_2\text{O} - \text{MgH}_2$ system). .....	272
Figure 7-48: Kissinger plot for the thermal event 4 for Sample 41 (milled $\text{LiOH}\cdot\text{H}_2\text{O} - \text{MgH}_2$ system). .....	272
Figure 7-49: DTA profiles used to obtain Kissinger plots for Sample 42 (nano $\text{LiOH}\cdot\text{H}_2\text{O} - \text{MgH}_2$ system). Dashed and full lines indicate temperature and DTA profiles respectively. ....	273
Figure 7-50: Kissinger plot for the thermal event 1 for Sample 42 (nano $\text{LiOH}\cdot\text{H}_2\text{O} - \text{MgH}_2$ system). .....	273
Figure 7-51: Kissinger plot for the thermal event 2 for Sample 42 (nano $\text{LiOH}\cdot\text{H}_2\text{O} - \text{MgH}_2$ system). .....	274
Figure 7-52: Kissinger plot for the thermal event 3 for Sample 42 (nano $\text{LiOH}\cdot\text{H}_2\text{O} - \text{MgH}_2$ system). .....	274
Figure 7-53: Kissinger plot for the thermal event 4 for Sample 42 (nano $\text{LiOH}\cdot\text{H}_2\text{O} - \text{MgH}_2$ system). .....	275
Figure 7-54: TG (dashed line) and DTA (full line) data obtained for Sample 8. ....	275
Figure 7-55: TG (dashed line) and DTA (full line) data obtained for Sample 9. ....	276
Figure 7-56: TG (dashed line) and DTA (full line) data obtained for Sample 10. ....	276
Figure 7-57: TG (dashed line) and DTA (full line) data obtained for Sample 13. ....	277
Figure 7-58: TG (dashed line) and DTA (full line) data obtained for Sample 14. ....	277
Figure 7-59: TG (dashed line) and DTA (full line) data obtained for Sample 15. ....	278

Figure 7-60: TG (dashed line) and DTA (full line) data obtained for Sample 18. ....	278
Figure 7-61: TG (dashed line) and DTA (full line) data obtained for Sample 19. ....	279
Figure 7-62: TG (dashed line) and DTA (full line) data obtained for Sample 25. ....	279
Figure 7-63: TG (dashed line) and DTA (full line) data obtained for Sample 26. ....	280
Figure 7-64: TG (dashed line) and DTA (full line) data obtained for Sample 27. ....	280
Figure 7-65: TG (dashed line) and DTA (full line) data obtained for Sample 28. ....	281
Figure 7-66: TG (dashed line) and DTA (full line) data obtained for Sample 31. ....	281
Figure 7-67: TG (dashed line) and DTA (full line) data obtained for Sample 32. ....	282
Figure 7-68: TG (dashed line) and DTA (full line) data obtained for Sample 33. ....	282
Figure 7-69: TG (dashed line) and DTA (full line) data obtained for Sample 34. ....	283
Figure 7-70: TG (dashed line) and DTA (full line) data obtained for Sample 37. ....	283
Figure 7-71: TG (dashed line) and DTA (full line) data obtained for Sample 38. ....	284
Figure 7-72: TG (dashed line) and DTA (full line) data obtained for Sample 39. ....	284

## **Acknowledgement**

I would like to thank Professor Duncan H Gregory for giving me the opportunity to undertake this journey and for the guidance and support throughout my PhD. I would also like to thank all the past and present members of C3-13. I would like to acknowledge Dr Nuria Tapia-Ruiz, Dr Sina Saremi-Yarahmadi and Dr James Hanlon for help, the patience and the valuable advice they gave me since day 1. A really really really big thank you goes to the Italo-Spanish delegation and Stanley the Turtle for being so supportive, especially during the writing up. But hey... Guys! Guys! Guys! Thank you all!

A big hug goes to my good old friends. I am going to tell you more, I could not have done this without you. You know who you are and you are basically a second family to me. And also a big hug to the new incredible friends I made during the last few years: thanks for all the dancing, the giggling, the laughing and the fun. You made these Scottish years way better! And Glasgow, you have been so good to me! A bit wet though!

But mostly, a heartfelt thanks goes to my family. Grazie ai miei genitori, Eliana e Gilberto, a mio fratello Cristiano e a Fabrizia per avermi supportata ed essermi stata sempre accanto, pur vivendo dall'altra parte d'Europa. Grazie.

## **Abbreviations and Definitions**

AFC: Alkaline Fuel Cell

DMFC: Direct Methanol Fuel Cell

DMO: Domestic Microwave Oven

DTA: Differential Thermal Analysis

EDX: Energy Dispersive X-ray Spectroscopy

FC: Fuel Cell

HT: Hydrothermal

MCFC: Molten Carbonate Fuel Cell

MS: Mass Spectrometry

MW: Microwaves

PAFC: Phosphoric Acid Fuel Cell

PEMFC: Proton Membrane Exchange Fuel Cell

PND: Powder Neutron Diffraction

PXD: Powder X-ray Diffraction

SEM: Scanning Electron Microscopy

SOFC: Solid Oxide Fuel Cell

STA: Simultaneous Thermogravimetric Analysis

TGA: Thermogravimetric Analysis

US DoE: US Department of Energy

# 1 Introduction

## 1.1 Hydrogen: a clean and renewable energy carrier

One of the major challenges facing modern society is to find a means of sustainable fuel generation, storage and delivery and overcome our reliance on non-renewable fossil fuels such as oil, coal and natural gases. If the negative effects of global warming, degradation of the ozone layer and consequent world's climate change is to be stopped, the development and use of a green and renewable energy vector is mandatory.<sup>1</sup> Further, projections to 2040 predict an increase of 56 % in the global world energy demand.<sup>2,3</sup> *Hydrogen* is undoubtedly one of the key alternatives to replace fossil fuels and petroleum products as a clean energy carrier for both transportation and stationary applications. Hence, over the past decades, great efforts have been made towards the development of non-carbon emitting sustainable vehicular hydrogen storage solutions.<sup>4,5</sup> However, less than 1 % of hydrogen is available as H<sub>2</sub>. Most of hydrogen exists in H<sub>2</sub>O and some of it is bound to C in liquid or gaseous hydrocarbons. The energy density of hydrogen, however, is greater than that of fossil fuels or other non-renewables.<sup>1</sup> The production, storage, consumption and regeneration of H<sub>2</sub> fuel is known as 'hydrogen economy' and the 'sustainable hydrogen cycle' on which it is based is presented in Figure 1-1.

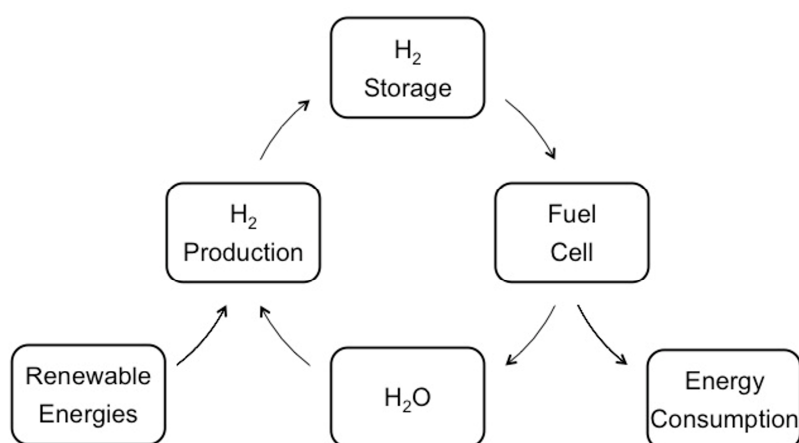


**Figure 1-1: Schematic of a sustainable hydrogen cycle.**

Current research is focused mainly on the production and storage of hydrogen, the two steps of the whole cycle which still represent a bottle neck to the usage of H<sub>2</sub> more widely as energy vector especially for on-board applications.

Today, hydrogen can be produced from renewable sources using different methods with minimum environmental impact, although not very efficiently in many cases: for instance solar, wind, hydro, electrolysis, photolysis, water splitting, biomass gasification and fermentation can be used for hydrogen production.<sup>6,7,8,9</sup>

Before the hydrogen economy can become completely viable, the safe storage and availability of H<sub>2</sub> is an issue that must be overcome. The major challenge in terms of using hydrogen as a fuel is to develop effective methods for its storage that can not only store H<sub>2</sub> safely, but also supply it when and where it is needed. Another key factor worth considering is that the storage systems have to be cost-competitive as well as energy efficient. H<sub>2</sub> can be stored as gas, liquid or in the solid state. At present, in industry hydrogen is normally stored in the form of a compressed gas or liquid. Nevertheless, there are issues related to the safety and volume restrictions for the storage of high pressure hydrogen gas, preventing its application more widely.<sup>1,10,11</sup> Recent research is thus focusing on the development of safer solid state storage solutions. Further, the cost advantages would be dramatic if it could be possible to store H<sub>2</sub> in the solid state using naturally occurring, cheap or waste materials. Potential solid state hydrogen storage materials need to meet certain criteria: the US Department of Energy recently adjusted its targets in 2012 to new ones with an ultimate system gravimetric capacity of 2.5 wt. % H<sub>2</sub>, an ultimate volumetric capacity of 2.3 kWh/L and overall storage system cost to be 8 \$/kWh, which can be also expressed as 266 \$/kg H<sub>2</sub>. Selected technical system targets for solid state on-board H<sub>2</sub> storage are shown in Table 1-1.

**Table 1-1: Selected DoE technical system targets for on-board hydrogen storage for light-duty hydrogen powdered vehicles. Adapted from Reference 12.**

<b>Storage Parameter</b>	<b>2017</b>	<b>Ultimate</b>
<b>System Gravimetric Capacity / kWh kg<sup>-1</sup></b> (kg H <sub>2</sub> kg <sup>-1</sup> system)	1.8 (0.055)	2.5 (0.075)
<b>System Volumetric Capacity / kWh L<sup>-1</sup></b> (L H <sub>2</sub> L <sup>-1</sup> system)	1.3 (0.040)	2.3 (0.070)
<b>Storage System Cost / \$ kWh<sup>-1</sup> net</b> (\$ kg <sup>-1</sup> H <sub>2</sub> )	12 (400)	8 (266)
<b>Charging / discharging Rates</b> <b>(system fill time; 5 kg) / min</b>	3.3	2.5

Beside these criteria, other properties must be taken into account when considering candidate materials. They must exhibit favourable hydrogen uptake and release kinetics and thermodynamics and must exhibit negligible toxicity. Further, the poisoning of the fuel cell due to decomposition or reaction by-products is an issue that must be avoided as it may result in a decreased lifespan of the cell as well as a diminished efficiency.<sup>13,14,15</sup> A wide range of materials is currently under investigation. Research is focusing on improving the hydrogen desorption/absorption processes with particular emphasis on enhancing the kinetics and thermodynamics of dehydrogenation.<sup>16,17,18</sup> Light metal hydrides and complex hydrides are considered the most promising candidates for realising an on-board storage system.<sup>19,20,21,22,23</sup> However, solid state chemists must also face other issues relative to the usage of such materials, as many are sensitive to both moisture and air. Therefore handling represents another challenge, which requires inert techniques at all times. The most recent progress in terms of materials for solid state hydrogen storage will be presented in a brief literature review (Section 1.3) with respect to the materials of interest employed during this work.

If hydrogen can be safely stored, it becomes available to the fuel cell for consumption. The reaction between  $H_2$  and  $O_2$  to form  $H_2O$  and generate power is the basis of fuel cell operation. An overview on the working principles of fuel cells, categorised based on operating temperature and the type of electrolyte employed, will be briefly described in the following section.

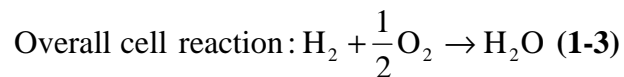
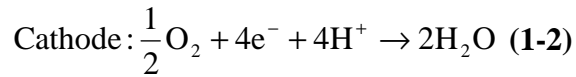
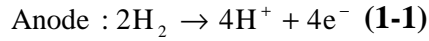
## 1.2 Fuel Cells

Fuel cells (FC) are quickly becoming one of the promising energy sources of the 21<sup>st</sup> century for both stationary and on-board applications. FCs produce electricity via a chemical reaction between a fuel (commonly hydrogen) and oxygen. Although hydrogen is the most used fuel, other ones such as methanol or ethanol can be employed as well.

A typical setup of a hydrogen powered fuel cell consists of three main components: the anode, the cathode and the electrolyte, which is located between the two electrodes. As can be seen from Figure 1-2, oxygen (typically  $O_2$  from the atmosphere) is supplied to the cathode while hydrogen is transferred to the anode. At the anode, hydrogen is stripped of its electrons to yield positive ions and electrons. Only the positive ions are then allowed to pass through the specifically designed electrolyte membrane and flow to the cathode. The electrons flow from anode to cathode through an external electrical circuit creating current.

Once protons and electrons reach the cathode they recombine and react with the oxidant (O<sub>2</sub>) to form water and expel exhausted oxidizing agent.

The reactions taking place respectively at the anode and cathode are presented in Equations 1-1 and 1-2, whilst Equation 1-3 shows the overall reaction occurring.



Electricity production from a FC usually continues as long as fuel and oxidizing agents are supplied and there is no poisoning of the apparatus. FC poisoning may be caused by the presence of impurities in the fuel (*i.e.* CO, CO<sub>2</sub>, H<sub>2</sub>S and NH<sub>3</sub>) or air pollutants such as NO, SO and CO, ultimately resulting in a shortened FC lifetime.

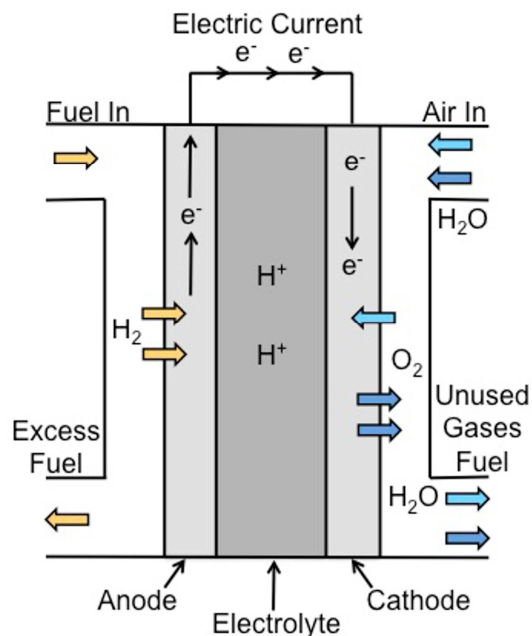


**Figure 1-2: Schematic of a hydrogen powered fuel cell.**

As today, FCs can be divided into two major categories depending on their operational temperature range: it is possible to distinguish between low temperature (50-350 °C), intermediate temperature (350-600 °C) and high temperature FCs (600-1000°C).<sup>24</sup> Further, FCs can also be classified in terms of the type of electrolyte employed.<sup>25</sup> Low temperature fuel cells comprise Proton Membrane Exchange Fuel Cells (PEMFC), Alkaline Fuel Cells

(AFC), Phosphoric Acid Fuel Cells (PAFC) and Direct Methanol Fuel Cells (DMFC). High temperature fuel cells include Solid Oxide Fuel Cells (SOFC), also known as ceramic fuel cells, and Molten Carbonate Fuel Cells (MCFC). An overview of the materials employed for anode, cathode and electrolytes for each FC is given in the following Sections 1.1.1 and 1.1.2.

## 1.2.1 Low Temperature Fuel Cells

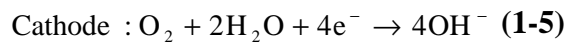
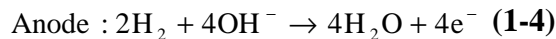
### 1.2.1.1 Polymer Electrolyte Membrane Fuel Cells

The PEM fuel cells operate in the temperature range of 50-100 °C and therefore they are suitable for both stationary and portable applications to replace rechargeable batteries.<sup>26</sup> This type of FC uses a solid polymer as electrolyte, usually Nafion, a Teflon-like membrane which acts as conductor for protons and as insulator for electrons.<sup>27</sup> This is positioned between anode and cathode. The latter is usually made of porous carbon. In PEMFCs, the hydrogen is activated by a catalyst. A wide range of catalysts has been studied,<sup>28</sup> although platinum or platinum alloys such as Pt/C are still used.<sup>29,27</sup> The chemical reactions occurring at the anode and cathode as well as the overall reaction are given in Equations 1-1, 1-2 and 1-3.

A PEM fuel cell presents many advantages. An efficiency in the 50-60 % range and a high power density together with a low operating temperature makes them ideal for transportation, especially considering their short start-up time. Moreover, they use a solid electrolyte, which avoids the handling of liquids and the relative refilling problems.<sup>25</sup> Conversely, their major drawback resides in the fact that the FC can be easily contaminated by impurities present in the hydrogen fuel (CO, CO<sub>2</sub>, H<sub>2</sub>S and NH<sub>3</sub>) and also by air pollutants such as NO, SO and CO or cations produced by the corrosion of the FC components (Fe<sup>3+</sup> and Cu<sup>2+</sup>).<sup>30</sup> This sensitivity problem eventually led to the development of Direct Methanol Fuel Cells (Section 1.1.1.4). Lastly, it is important to remember that they use a platinum catalyst and a solid polymer membrane, both of which are very expensive. Moreover, the Pt catalyst can also be partially deactivated by the presence of CO. In fact, carbon monoxide blocks the active catalyst sites where the hydrogen absorption and dissociation take place, rendering the fuel cell less efficient.<sup>31,32</sup>

### 1.2.1.2 Alkaline Fuel Cells

The AFC, as its name indicates, uses an alkaline water based solution as an electrolyte, usually KOH.<sup>33</sup> The operating temperature range is similar to the PEMFC one (60-100 °C). Alkaline fuel cells were the first FC developed by Francis Thomas Bacon in the 1940s at the Department of Colloid Science, University of Cambridge.<sup>34</sup> Since their invention, AFCs have found their major application in the aerospace field. AFCs are in fact the primary source of electricity on human spaceflights for over 40 years now.<sup>35</sup> The electrochemistry on which these types of FC are based presented in Equations 1-4 and 1-5, with the overall cell reaction given in Equation 1-6.



Besides the low working temperature, which makes AFCs suitable for transport applications as they have a fast start-up, they present several advantages such as a high efficiency (50%), low-weight and low-volume and they do not present corrosion problems. Moreover, they require a little amount of catalyst, which lowers the costs of the whole FC apparatus. The major disadvantage lies in an extreme sensitivity to CO<sub>2</sub> and CO, limiting the types of fuels (both hydrogen and oxidizing agent) that can be employed. The use of liquid electrolytes could be seen as a disadvantage, as it can result in handling problems of the apparatus. They also present a low power density (*ca.* 1 kW m<sup>-3</sup>), limiting their applications for large scale energy applications. Schulze *et al.* published several papers in which they investigated deeply AFCs in terms of focusing on the long term operation of AFC electrodes and their poisoning as an effect of the presence of CO<sub>2</sub> as well as long term investigations on the degradation of different types of anodes and cathodes.<sup>36,37,38,35</sup> An extensive review on the different anion exchange membranes that can be employed for alkaline fuel cells has been recently published by Nijmeijer *et al.*<sup>39</sup> Fuel sources using methanol and ethanol instead of pure hydrogen have been investigated as well.<sup>40</sup>

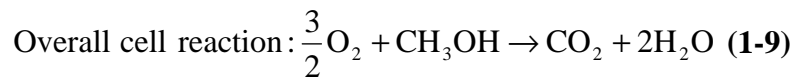
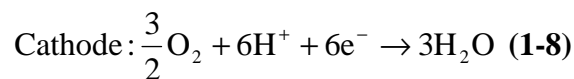
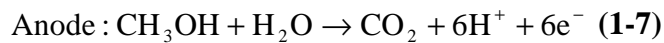
### 1.2.1.3 Phosphoric Acid Fuel Cells

Phosphoric acid fuel cells (PAFCs) use phosphoric acid (H<sub>3</sub>PO<sub>4</sub>) as an electrolyte and high surface area graphite electrodes with Pt or Pt alloys as catalysts.<sup>24</sup> They follow the same working principles as PEMFCs, although their operating temperature is in the 150-200 °C

range, due to the poor ionic conductivity of phosphoric acid at low temperatures. Although PAFCs are well-developed and commercially available, the use of very expensive catalysts is needed and their market has not progressed because of their high cost. Another disadvantage can be identified in the corrosive nature of the liquid electrolyte employed. Currently, PAFC plants with size of 100, 200 and 500 kW are available for stationary and heat applications.<sup>25</sup> Phosphoric acid FCs present several advantages however. Since CO<sub>2</sub> does not affect the electrolyte or cell performances, PAFCs do not require pure oxygen as fuel and atmospheric air can be used as the oxidizing agent. Moreover, the electrolyte the use is stable and presents low volatility even at the operating temperature of the FC. Further, this FC technology is able to use the waste heat produced when working at medium temperatures for cogeneration of electricity and useful heat.<sup>34</sup>

#### 1.2.1.4 Direct Methanol Fuel Cells

DMFCs are based on the same working principles of PEMFCs, although the fuel is methanol instead of pure hydrogen. At the anode CH<sub>3</sub>OH is oxidised to carbon dioxide, while the cathode is fed with atmospheric oxygen from air. The electrochemical reactions occurring at anode and cathode respectively are shown in Equations 1-7 and 1-8, with the overall cell reaction given in Equation 1-9.<sup>41,42</sup>



The main advantage in employing DMFCs is the use of methanol as liquid fuel resulting in faster refilling times. They are reasonably efficient (30-40 %) at operating temperatures in the 60-200 °C range. Further, they demonstrate long lifetime and do not need to be subjected to any recharging process. On the other hand, their efficiency is lower compared to PEMFCs. Moreover, to be operational at temperatures as low as 60 °C, a high amount of catalyst is needed for the electro-oxidation of methanol fuel, which reflects in increased production costs. Ethanol has also been proposed as fuel for FCs based on the same setup.<sup>43,44,45</sup>

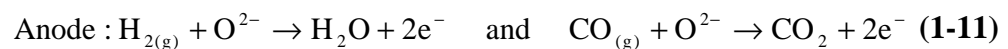
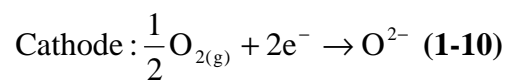
## 1.2.2 High Temperature Fuel Cells

### 1.2.2.1 Solid Oxide Fuel Cell

Solid oxide fuel cells work at high temperatures, in the 300-1000 °C region.<sup>46</sup>

SOFCs use a solid ceramic electrolyte, positioned in between porous anode and cathode. Many electrolyte materials have been investigated and include perovskites and related structures, apatites, LAMOX and fluorite-base systems such as zirconia or ceria, although recently YSZ (yttrium stabilized zirconia) has been extensively employed. Perovskites are typically used for the cathode, whereas Ni and Ni/YSZ composites are commonly used for the anode. A number of reviews on the state of art of SOFCs and materials employed are available. Further, recent efforts have been focusing on exploring suitable materials for lowering the effective operating temperature of the cell to the 300-600 °C range.<sup>46,47,48,49,50</sup>

The main difference between SOFCs and other FCs lays in the fact that the charge carriers are oxide ions  $O^{2-}$  and not protons;  $O_2$  is stripped of two electrons at the cathode, yielding  $O^{2-}$ . Oxygen ions then migrate to the anode, where they react with the fuel. The majority of SOFCs use hydrocarbons as fuel at the anode. When hydrocarbons are employed (usually  $CH_4$ ),  $O^{2-}$  will react with hydrogen and CO to form  $H_2O$  and  $CO_2$ . However, if the source is pure hydrogen, the only product of the electrochemical reaction will be water. The reactions occurring at the cathode and the anode and the overall reaction occurring in a typical SOFC are shown below.



SOFCs have a very high efficiency that can be as high as 60% when pure hydrogen is used as fuel.<sup>26</sup> Solid oxide fuel cells generate electricity when operating at temperatures as high as 1000 °C. There is no need for an expensive noble metal catalyst and the presence of solid electrolytes avoids handling problems related to the presence of liquid inside the stacks. Further, it is not possible to poison the fuel cell with CO from fossil fuels, as the FC is able to convert it to  $CO_2$ . The start-up of SOFCs is still slow and they show sensitivity to sulphur.<sup>51</sup> The study of solid state electrolytes with a good conductivity at low SOFC

operating temperatures that are compatible with the other FC components is still an open research field.

#### **1.2.2.2 Molten Carbonate Fuel Cells**

MCFCs are fuel cells operating at high temperatures in the 600-700 °C range, which are mainly used in stationary applications such as power plants and other industrial applications.<sup>52</sup> The electrolyte is usually a mixture of lithium carbonate and potassium carbonate, impregnated inside an  $\text{LiAlO}_2$  matrix.<sup>53</sup> Unlike most fuel cells, in MCFCs  $\text{CO}_3^{2-}$  ions migrate from the cathode to the anode. At the anode, the carbonate ions will react with the hydrocarbon fuel gas (typically methane,  $\text{CH}_4$ ) and  $\text{H}_2$  react to yield water,  $\text{CO}_2$  and  $2e^-$  via a series of reductions and oxidations. The electrons will travel to the cathode to generate electricity. The anode is commonly Ni and Ni-alloys,<sup>54,55</sup> whilst the cathode materials typically used include nickel oxide, NiO composites and  $\text{LiFeO}_2$ .<sup>56,57,58</sup> Due to the high working temperatures, noble metals are not required as catalysts and Ni is usually employed and presents good activity as well as low price. Other than this, MCFC are characterised by high efficiency (50-60 %). Moreover, the high temperatures allow the regeneration of the system inside the cell stacks, improving the overall efficiency of the FC. However, one of the drawbacks are the long times needed to reach the operating temperature, which translate to a slow start up and generation of power. Other drawbacks include intolerance to sulphur, particularly for the anode, corrosive nature of the electrolyte and partial dissolution of the cathode's NiO in the electrolyte. All these factors tend to result in a shorter lifespan for MCFCs compared to SOFCs.<sup>53</sup>

### 1.2.3 Fuel cells technologies comparison

Table 1-2: Comparison of different fuel cell types. Adapted from Reference 59.

Parameters	Fuel Cell Type					
	PEMFC	AFC	PAFC	DMFC	SOFC	MCFC
<b>Electrolyte</b>	Solid polymer membrane (Nafion)	KOH aqueous solution	Phosphoric acid (H <sub>3</sub> PO <sub>4</sub> )	Solid polymer membrane	Stabilised solid oxide electrolyte	Li <sub>2</sub> CO <sub>3</sub> and K <sub>2</sub> CO <sub>3</sub> in LiAlO <sub>2</sub> matrix
<b>Operating Temperature /°C</b>	50-100	50-200	Ca. 200	60-200	300-1000	Ca. 650
<b>Charge Carrier</b>	H <sup>+</sup>	OH <sup>-</sup>	H <sup>+</sup>	H <sup>+</sup>	O <sup>2-</sup>	CO <sub>3</sub> <sup>2-</sup>
<b>Fuel</b>	Pure H <sub>2</sub>	Pure H <sub>2</sub>	Pure H <sub>2</sub>	CH <sub>3</sub> OH	H <sub>2</sub> , CO, CH <sub>4</sub>	H <sub>2</sub> , CO, CH <sub>4</sub>
<b>Oxidant</b>	O <sub>2</sub> from atmosphere	O <sub>2</sub> from atmosphere	O <sub>2</sub> from atmosphere	O <sub>2</sub> from atmosphere	O <sub>2</sub> from atmosphere	O <sub>2</sub> from atmosphere
<b>Efficiency</b>	40-50 %	Ca. 50 %	40 %	40 %	> 50 %	> 50 %
<b>Power</b>	3.8-6.5	Ca. 1	0.8-1.9	Ca. 0.6	0.1-1.5	1.5-2.6
<b>Density /kWm<sup>-3</sup></b>						
<b>Cogeneration</b>	–	–	Yes	No	Yes	Yes
<b>Applications</b>	Residential, industry, transports, backup or portable power, vehicles	Transport, space shuttles, portable power	Transports, commercial cogeneration, portable power	Replace batteries in mobile phones, laptops and devices	Residential, commercial cogeneration, utility power plants, auxiliary power	Transports, industries, utility power plants

## 1.3 Solid State Hydrogen Storage

Solid state hydrogen storage materials have been widely investigated and the state of the art on such topic is reported in various literature reviews.<sup>16,60,17,61</sup> The storage of hydrogen in the solid state can be divided into two main categories: *physical storage* and *chemical storage*. The former requires H<sub>2</sub> to be bound or included in a host by relatively weak interactions commonly referred to as physisorption or physical absorption. Most studied materials employed for physically storing H<sub>2</sub> include MOFs (metal-organic frameworks), COFs (covalent-organic frameworks), polymers, porous carbon and zeolites.<sup>62,22,63,64,65,66</sup> The study of these materials goes beyond the scope of the present work, hence it will not be further covered. In the latter storage category, the hydrogen is chemically bound in a compound and the uptake/release process involves chemical reactions. In this scenario hydrogen is relatively strongly bound and recent efforts focus on enhancing the thermodynamics and kinetics of the dehydrogenation process for the materials employed for storing hydrogen. The work carried out during this project focuses on chemical hydrogen storage with particular emphasis on hydride – hydroxide systems, and therefore recent developments on chemical storage of hydrogen in the solid state are summarised in the following section.

### 1.3.1 Chemical hydrogen storage

Metal hydrides have been extensively studied as a hydrogen store medium because of their light weight and high theoretical gravimetric as well as volumetric hydrogen capacity.<sup>19,67,68</sup> A comparison overview of some hydrogen storage hydrides is given in Figure 1-3.

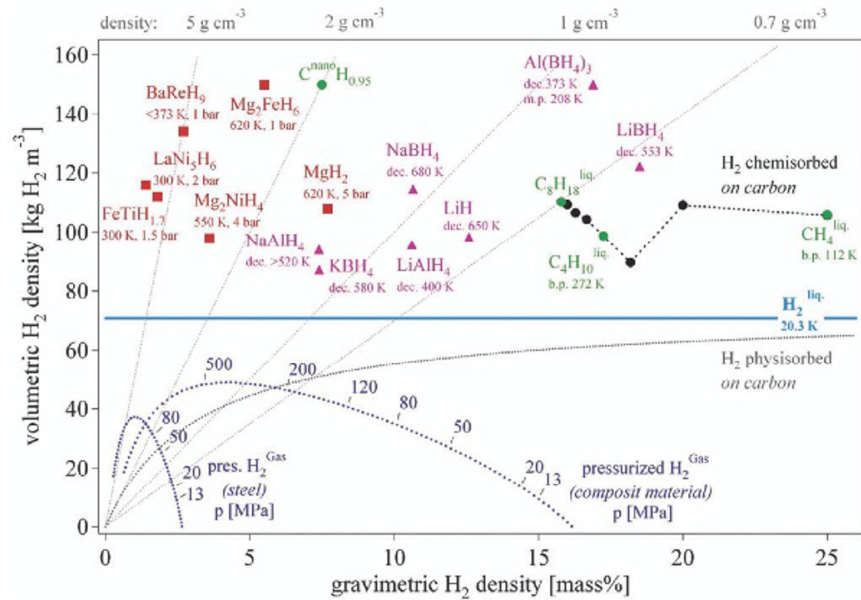


**Figure 1-3: Comparison of theoretical gravimetric and volumetric capacity for solid state hydrogen storage hydrides.<sup>69</sup>**

Accordingly, studies have focused on alkali and alkaline earth metal hydrides. Most efforts have been pointing towards the development of cost- and energy-efficient solid state hydrogen storage solutions.

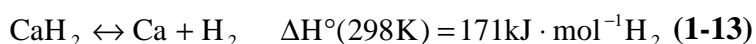
### 1.3.1.1 Light metal hydrides

In terms of light metal hydrides, LiH, NaH, CaH<sub>2</sub> and MgH<sub>2</sub> attracted the most interest in terms of solid state hydrogen storage. In Table 1-3 are reported the molecular weight, gravimetric and volumetric hydrogen capacities and decomposition temperatures for the aforementioned hydrides.

**Table 1-3: Molecular weight, theoretical gravimetric and volumetric hydrogen capacities, temperatures of decomposition for selected light metal binary hydrides. Adapted from Reference 70.**

Hydride	MW / g·mol <sup>-1</sup>	Theoretical wt. % H <sub>2</sub>	Theoretical volume H <sub>2</sub> / kg·m <sup>-3</sup>	T <sub>dec</sub> / °C
LiH	7.95	12.59	98.60	720
NaH	23.99	4.17	57.73	425
MgH <sub>2</sub>	26.31	7.60	110.03	327
CaH <sub>2</sub>	42.09	4.75	92.37	600

Lithium hydride can store up to 12.59 wt. % H<sub>2</sub>, whilst the percentage decreases to 4.17 wt. % H<sub>2</sub> for sodium hydride. Both LiH and NaH are extremely air sensitive and therefore their manipulation and storage is more difficult when compared to magnesium or calcium hydride. In addition, LiH is characterised by very high decomposition temperatures of nearly 720 °C (and a melting point of 680 °C)<sup>71</sup>, rendering the use of LiH on its own unsuitable for storing H<sub>2</sub> in the solid state. However, the use of LiH has been widely investigated as a component of Li-N-H systems for direct and indirect H<sub>2</sub> storage as well as a component for hydride – hydroxide ‘modular’ hydrogen release systems. The employment of lithium hydride in such systems will be discussed in Sections 1.3.1.3 and 1.3.2 respectively. Similarly to NaH, CaH<sub>2</sub> is able to store 4.75 wt. % of hydrogen and like LiH is characterised by high decomposition temperatures. Like MgH<sub>2</sub>, CaH<sub>2</sub> the dehydrogenation process is reversible (Equation 1-13) and calcium hydride is typically synthesised by reaction of calcium metal with high pressure hydrogen at high temperature.<sup>72,73</sup>



As per LiH, due to its high T<sub>dec</sub>, CaH<sub>2</sub> is usually employed as a component in composite systems. Its behaviour in the presence of borohydrides, amides and ammonia borane has been investigated over the recent years.<sup>74,75,21,76,77</sup>

The most promising light metal hydride to be employed for solid state H<sub>2</sub> storage solutions is MgH<sub>2</sub>, with a theoretical gravimetric capacity of 7.60 wt. % H<sub>2</sub>. Further, magnesium is cheap and abundant and hence plays a pivotal role in the development of solid state hydrogen storage solutions. However, due to its thermal stability, MgH<sub>2</sub> decomposition occurs at temperatures as high as 327 °C via a single endothermic event associated with hydrogen release (Equation 1-14).<sup>69</sup>



Two main strategies have been investigated in order to enhance the thermodynamic performances by reducing the enthalpy of decomposition of MgH<sub>2</sub>: nanostructuring the material and the use of additives. Many catalysts/additives have been tested. These include calcium hydride, lithium hydride and sodium hydride to yield ternary hydrides and composites<sup>78,79</sup>, graphite and/or silicon carbide<sup>80</sup> as well as transition metals such as multi-valence vanadium- and titanium-based materials, Ni, Nb and Pd.<sup>81,82,83,84,85,86</sup> Only

recently, alkali metal hydroxides have been proposed as additives for MgH<sub>2</sub>, with the aim of improving the hydrogen desorption properties of nanosized MgH<sub>2</sub>.<sup>87</sup>

Tailoring hydrogen storage materials is currently one of the major fields in solid state H<sub>2</sub> storage research; in particular, nanostructuring materials is seen as a means to have a better control over the dehydrogenation process and enhance the performances of H<sub>2</sub> release/uptake.<sup>88,89</sup> The reduction of the particle size to the nanoscale is usually achieved by mechanical milling, as chemical methods for yielding nanomaterials like hydrothermal/solvothermal syntheses, templating or sol-gel syntheses often cannot be employed due to the air-sensitive nature of the hydrides. Nanostructured magnesium hydride has been successfully obtained by ball-milling the bulk material.<sup>78,90,91</sup>

### 1.3.1.2 Complex hydrides

The interest in the use of complex hydrides has increased recently. Boron and aluminium, like magnesium, are cheap and light-weight and ternary hydrides containing alkaline and alkaline-earth metals are able to store an increased amount of hydrogen compared to the respective binary hydrides. For these reasons, borohydrides and alanates have been widely investigated as cheap and abundant H<sub>2</sub> storage mediums.<sup>21,92</sup> Table 1-4 gives an overview of the molecular weight, gravimetric and volumetric hydrogen capacities and decomposition temperatures for the most promising complex hydrides.

**Table 1-4: Molecular weight, theoretical gravimetric and volumetric hydrogen capacities, temperatures of H<sub>2</sub> desorption for selected borohydrides and alanates. Adapted from Reference 70.**

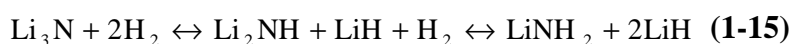
<b>Hydride</b>	<b>MW / g·mol<sup>-1</sup></b>	<b>Theoretical wt. % H<sub>2</sub></b>	<b>Theoretical volume H<sub>2</sub> / kg·m<sup>-3</sup></b>	<b>T<sub>des</sub> / °C</b>
<b>LiBH<sub>4</sub></b>	21.75	18.39	124.02	380
<b>NaBH<sub>4</sub></b>	37.81	10.58	118.02	400
<b>Mg(BH<sub>4</sub>)<sub>2</sub></b>	53.93	14.84	117.23	280
<b>Ca(BH<sub>4</sub>)<sub>2</sub></b>	69.70	11.48	124.07	347 - 497
<b>LiAlH<sub>4</sub></b>	37.95	10.55	74.02	115
<b>NaAlH<sub>4</sub></b>	53.97	7.41	97.41	220
<b>Mg(AlH<sub>4</sub>)<sub>2</sub></b>	86.3	9.27	98.15	110 - 200
<b>Ca(AlH<sub>4</sub>)<sub>2</sub></b>	102.04	7.84	96.97	200 - 250

As can be observed from Table 1-4, lithium borohydride and sodium borohydride are the most promising complex hydride in terms of H<sub>2</sub> gravimetric capacity (18.39 wt. % H<sub>2</sub> and 10.58 wt. % H<sub>2</sub> for LiBH<sub>4</sub> and NaBH<sub>4</sub> respectively). However, they are characterised by poor reversibility in addition to not particularly favourable dehydrogenation kinetics and thermodynamics. Hence, over the past years efforts have been focused on improving their hydrogen release/uptake performance. Many approaches have been employed for enhancing the dehydrogenation properties of these complex hydrides. Nanostructuring the materials has been investigated as a means to lower the onset temperatures of hydrogen release for the hydrides. Ball milling the bulk materials with one or multiple additives has proved to be a viable approach for promoting hydrogen release by destabilising the hydride. In this sense, promising results have been obtained for both LiBH<sub>4</sub> and NaBH<sub>4</sub>.<sup>93,94</sup> Nanoconfinement is one of the main focuses of current research. Incorporating the borohydrides inside a porous scaffold host such as carbon has showed promising results in terms of lowering the dehydrogenation temperature when compared to the respective bulk materials. In fact, enhanced dehydrogenation performances were observed when nanoconfining both LiBH<sub>4</sub> and NaBH<sub>4</sub>.<sup>95,96</sup> Further, through this nano-engineering approach it was possible to increase the reversibility of the H<sub>2</sub> release-uptake process with either lithium borohydrides or sodium borohydride.<sup>97,98</sup>

The role of borohydrides and other complex hydrides will not be covered in any more detail in this thesis, hence reviews on the latest progress in terms of LiBH<sub>4</sub> and NaBH<sub>4</sub> for hydrogen storage can be consulted to obtain additional information on the subject.<sup>99,100</sup>

### 1.3.1.3 Nitrides, imides and amides: N-H-based materials

Nitrides and their hydrogenated compounds imides and amides gained attention in 2002, when Chen *et al.* discovered Li<sub>3</sub>N to be an extremely promising medium for storing hydrogen in the solid state.<sup>101</sup> In fact, Li<sub>3</sub>N can theoretically store 10.4 wt. % H<sub>2</sub> when subjected to the hydrogenation process presented in Equation 1-15:



However, experimentally the system was found to release only 9.3-10 wt. % of hydrogen.<sup>101</sup> Further, the system suffers from poor kinetics and the thermodynamics of the dehydrogenation step from imide to nitride occurs at temperatures as high as 320 °C and pressures as low as 10<sup>-5</sup> mbar. Hence, only the imide-amide conversion (second step of the overall mechanism) is reversible at practical working temperatures. Nonetheless, the

second step alone can yield 6.5 wt. % H<sub>2</sub>, which is a value realistically near to the targets set by the US DoE.

Following Chen's discovery, a large variety of Metal-N-H systems have been investigated, employing light-weight materials containing aluminium, magnesium, boron and sodium.<sup>102,103</sup> Most attention was focused on the ternary Li-N-H system although also the quaternary Li-Mg-N-H system has been thoroughly investigated. Nanostructuring such materials using different approaches was one of the main aims in the nitride-imide-amide research area with the ultimate goal of enhancing the performances of such systems. Reduction of the particle size of the reactants via ball milling as well as the use of catalysts and nano-catalysts and additives have been studied in this respect. The behaviour of complex amides and nanocomposites has been investigated as well. Further, great effort has been devoted to reaching a complete understanding of the decomposition pathways of such materials.<sup>76,88,89,104,105,106</sup>

A crucial objective related to the work in this thesis is to clarify the reaction pathways of hydrogenation with particular focus on the second step of the process, when the conversion from imide to amide occurs. In fact, the first step is a hydrogenation process where one H replaces one Li inside the nitride structure to give Li<sub>2</sub>NH and LiH; in the second step an interaction between hydride and imide takes place resulting in the formation of LiNH<sub>2</sub> and LiH. In this situation, the hydrogen bonded to N is positively charged (H<sup>+</sup>) because of the electronegativity relative to nitrogen, whilst the H in hydrides is negatively charged (H<sup>-</sup>). The combination between H<sup>+</sup> and H<sup>-</sup>, together with the electrostatic attraction between the cation in the hydride and the 'N anion' in the amide, leads to the reaction between amide and hydride, which ultimately results in the evolution of H<sub>2</sub>.

On this evidence, a whole new category of systems based on the reaction between negatively charged ionic hydrides and compounds containing protons can be identified and hence investigated. In fact, the present work will focus on the reaction between light metal hydroxides and light metal hydrides as a basis for the so-called 'modular' hydrogen release systems. The concept of 'modular' systems as well a review of the latest progress in terms of such systems is given in the following section.

### 1.3.2 Hydride – Hydroxide hydrogen release systems

As previously stated, no single material or system has been able to meet the targets set by the DoE yet.<sup>12</sup> In many senses, *light metal hydroxides* could be seen as attractive candidates for storing hydrogen in the solid state; they are low cost, they do not present toxicity and moreover it is not possible to poison the fuel cell with undesired by-products, unlike in systems containing nitrogen or boron. However, as the end products of the dehydrogenation process are their corresponding oxides, the rehydrogenation thermodynamics are unfavourable for on-board applications. The system must therefore be considered as a ‘charged module’, where its regeneration can be performed inexpensively *ex-situ*. These ‘charged modules’ are regenerated/recycled offline and plugged into the desired appliance/vehicle by the user (Figure 1-4). In this sense, refuelling time may be decreased, although the whole process of dehydrogenation-rehydrogenation needs to be cost- and energy-efficient.

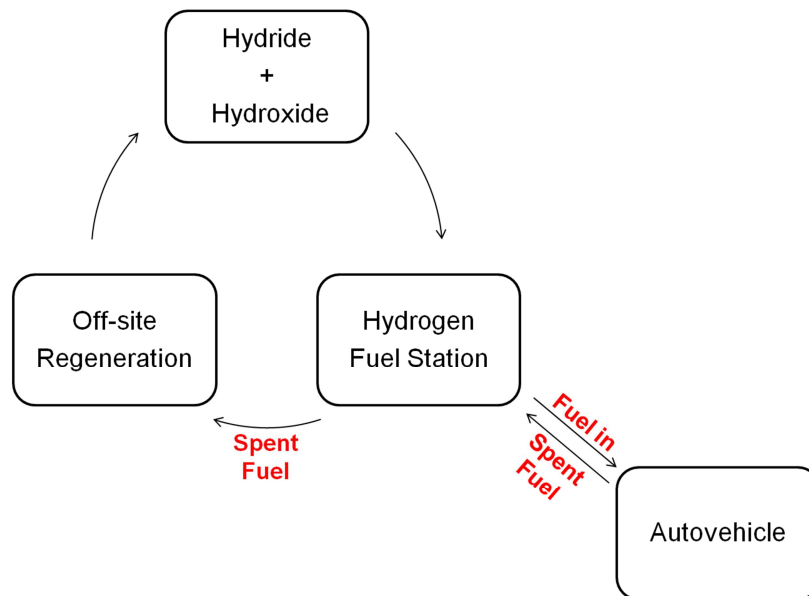


**Figure 1-4: Schematic of the proposed ‘modular’ hydrogen release system; H<sub>2</sub> fuel source is given from the reaction between hydride and hydroxide.**

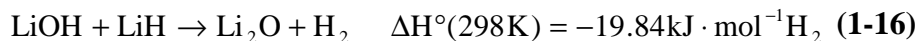
A wide range of ‘modular’ hydrogen release systems can be studied, however the most interesting ones in terms of both theoretical gravimetric capacity and kinetics within reasonable temperature range (RT – 623 K) use magnesium, lithium and sodium hydroxide and their hydrate forms. Dehydrogenation can be achieved by reaction with light metal hydrides, such as LiH, MgH<sub>2</sub>, LiBH<sub>4</sub> or NaBH<sub>4</sub>. In fact, the H<sup>+</sup> - H<sup>-</sup> interaction mechanism proposed by Chen for the lithium amide – lithium hydride<sup>107</sup> would suggest that light metal hydroxide should effectively destabilise the hydride, promoting the dehydrogenation process due to the H<sup>+</sup> - H<sup>-</sup> coupling between the proton of the hydroxide’s OH<sup>-</sup> and the

anion of the hydride. Other evidence of this coupling reaction is reported for systems employing nitrogen-containing compounds and hydrides, where the hydrogen release is driven by the  $H^+ - H^-$  interaction force.<sup>101,108,109,110</sup> Ultimately, light metal hydroxide – hydride systems could meet the criteria set by the DoE since they are cheap, could be tailored to yield high hydrogen capacities at low hydrogen release temperature and could be sustainably regenerated by reacting the dehydrogenated oxides either with water or with high pressure hydrogen gas.

In 2004, Vajo *et al.* were the first ones to propose the study of the solid state reactions between light metal hydrides and alkali hydroxides to yield the respective oxides together with the evolution of hydrogen when heated to 673 K.<sup>111</sup> In particular the LiH – LiOH, 2LiH – NaOH, LiBH<sub>4</sub> – LiOH and LiBH<sub>4</sub> – LiOH·H<sub>2</sub>O systems were preliminarily investigated, working under a pressure of  $1.3 \cdot 10^{-6}$  Pa. Further, ball milling was found to be a promising technique for the preparation of hydroxide – hydride mixtures as no major reactions occurs during the milling procedure. The best results in terms of hydrogen desorption were obtained when working with lithium borohydride. In particular the thermal treatment of LiBH<sub>4</sub> – LiOH was found to generate 6.6 wt. % of hydrogen, whereas the reaction between LiBH<sub>4</sub> and LiOH·H<sub>2</sub>O was found to evolve *ca.* 10 wt. % H<sub>2</sub> below 543 K, with the dehydrogenation process starting at temperatures as low as 313 – 323 K. For both borohydride – hydroxide composites the end products were found to be Li<sub>2</sub>O, Li<sub>3</sub>BO<sub>3</sub> and Li<sub>4</sub>B<sub>2</sub>O<sub>5</sub>. The reaction between lithium hydride and lithium hydroxide instead was found to evolve *ca.* 5.5 wt. % of hydrogen and yield Li<sub>2</sub>O, when heating the mixture to 523 K: the dehydrogenation performances for the system were found to improve when a catalytic amount of 2-10 mol % of TiCl<sub>3</sub> was added. It was proposed that the added TiCl<sub>3</sub> may have acted either as a catalyst, facilitating diffusion and desorption of hydrogen, or as a dispersant, resulting in a finer mixing of the LiOH and LiH phases. The less promising results were obtained for the 2 LiH – NaOH system, where only 3.2 wt. % H<sub>2</sub> was generated, with the final products being Li<sub>2</sub>O and NaH. The absence of Na<sub>2</sub>O as final product was proposed to be due to its instability in a hydrogen environment below 673 K.

More recently, the use of LiOH and its hydrate for hydrogen generation with facile regeneration of the monohydrated hydroxide by reaction with water was further investigated by Lu *et al.*<sup>112</sup>. Dehydrogenation is achieved by reaction with lithium hydride at temperatures below 623 K. Moreover, high capacities are possible. The theoretical gravimetric capacity of hydrogen is 6.3 wt. % H<sub>2</sub> for the anhydrous lithium hydroxide –

lithium hydride system, whilst it can be as high as 8.8 wt. % H<sub>2</sub> when lithium hydroxide monohydrate is employed (Equations 1-16 and 1-17).



In addition, both hydride and hydroxide can be easily regenerated from the dehydrogenated oxide. With this hybrid approach for hydrogen storage, the release and uptake of hydrogen is reversible via a series of simple reaction based on the reaction between LiOH or its hydrates and LiH with good kinetics within a practically reasonable temperature range. Further, the recharge of hydrogen is accomplished by reaction with water, rather than high pressure H<sub>2</sub> gas, resulting in an overall energetically favourable reversible cycle despite the high temperature magnesothermic reduction step. A schematic of the reaction cycle is presented in Figure 1-5.

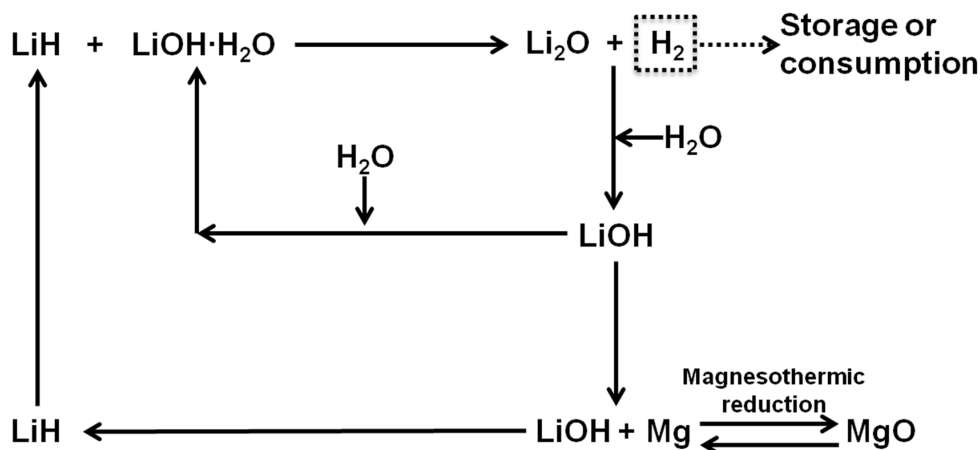


Figure 1-5: Proposed 'modular' solid state hydrogen release system<sup>112</sup>

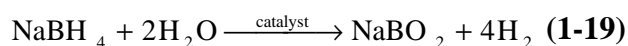
In 2009, Leardini *et al.* investigated the Mg(OH)<sub>2</sub>-MgH<sub>2</sub> hydrogen release system, which can theoretically release 4.7 wt. % H<sub>2</sub> (Equation 1-18).<sup>113</sup>



In this work, hydride-hydroxide composites were obtained by exposing MgH<sub>2</sub> to ambient atmosphere for a certain amount of time. Rietveld refinement against X-ray diffraction data was used to exactly calculate the weight fractions of the two components. Together with

water and hydrogen releases due to magnesium hydroxide and magnesium hydride decomposition reactions respectively, two other hydrogen desorption events were identified, which were believed to be related to solid state reactions between Mg(OH)<sub>2</sub> and MgH<sub>2</sub>. The three dehydrogenation events were found to take place at 423, 623 and 723 K.

The use of lithium borohydride and sodium borohydride as the hydride in the hydride – hydroxide ‘modular’ hydrogen release systems has gained momentum over recent years. Sodium borohydride was first proposed as suitable starting material to be employed in the so-called *Millennium Cell*,<sup>114</sup> based on the reaction of NaBH<sub>4</sub> with H<sub>2</sub>O (Equation 1-19):

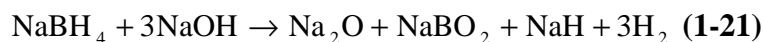


The systems presents a theoretical gravimetric capacity of 10.8 wt. % H<sub>2</sub>. The reaction products were found to be only hydrogen and NaBO<sub>2</sub>, which would then be regenerated offsite to re-obtain the borohydride. The hydrogen would be evolved from the borohydride aqueous solution with the help of a catalyst at a working temperature in the 333 – 353 K range. However, this setup involves the use of water and it is not suitable for developing solid state hydrogen storage on-board solutions. Nonetheless the use of NaBH<sub>4</sub> as well as LiBH<sub>4</sub> has been further investigated, also in the light of the aforementioned results reported in 2005 by Vajo *et al.*<sup>111</sup>. In 2007, Drozd *et al.* investigated the NaBH<sub>4</sub> – Mg(OH)<sub>2</sub> system, which can theoretically release 5.2 wt. % H<sub>2</sub> (Equation 1-20).<sup>115</sup>



Hydrogen evolution was found to start at approximately at 563 K, with the mechanistic steps believed to be a simultaneous brucite dehydration and hydride hydrolysis. Moreover, ball milling was employed to reduce the particle size of the reactants: a smaller particle size resulted in an increased reaction rate. The activation energy for the whole process was calculated and found to be 155.9 kJ mol<sup>-1</sup>. Differences in the dehydrogenation properties were found when different preparative methods were employed. Hand mixing with mortar and pestle resulted in a 54 wt. % release of hydrogen with respect to the theoretical figure, whereas mechanically milling the starting materials for 30 minutes lead to an improved 93 wt. % mass change with respect to the theoretical 5.2 wt. % H<sub>2</sub>. Further, cobalt oxide and SiO<sub>2</sub> were tested as catalysts for the system: the former was found to have little or no effect on the dehydrogenation performances of the composite, whilst the latter was found to have improvements on the hydrogen generation. In 1969, Mikheeva *et al.*<sup>116</sup> studied the thermal

behaviour of the NaBH<sub>4</sub> – NaOH system, which was found to follow the stoichiometry presented in Equation 1-21.



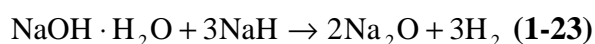
The sodium borohydride – magnesium hydroxide system was further investigated in 2012 by Varin and Parviz, who additionally studied the lithium borohydride – magnesium hydroxide composite system.<sup>117</sup> They also investigated the addition of nanometric nickel as an additive in order to improve dehydrogenation kinetics and thermodynamics for both systems. Both NaBH<sub>4</sub> – Mg(OH)<sub>2</sub> and LiBH<sub>4</sub> – Mg(OH)<sub>2</sub> composites were prepared by high energy ball milling. The sodium-based system was found to undergo one single dehydrogenation as an exothermic reaction with H<sub>2</sub> release starting at *ca.* 513 K, whereas the lithium-based counterpart was found to undergo two distinct events, one exothermic and one endothermic although no reaction mechanism was proposed for the latter dehydrogenation process. The hydrogen evolution for the LiBH<sub>4</sub>-based system was found to begin at approximately 473 K, showing a lower onset temperature of hydrogen release with respect to the sodium-based counterpart. In addition, the presence of nanometric nickel in the mixture does not seem to affect the dehydrogenation behaviour for both Na- and Li-based composites. Also, in the case of the lithium borohydride – magnesium hydroxide system, the presence of nickel additives results in a decrease of evolved hydrogen and specifically a 10% decrease for each dehydrogenation step with respect to the un-doped composite.

In 2014, Pan *et al.* systematically studied the dehydrogenation properties of non-stoichiometric mixtures of the LiBH<sub>4</sub> – x Mg(OH)<sub>2</sub> system.<sup>118</sup> The study concluded that the optimal performances were found for the LiBH<sub>4</sub> – 0.3 Mg(OH)<sub>2</sub> composite, which was found to release *ca.* 9.6 wt. % H<sub>2</sub>, with an onset temperature of hydrogen release of 373 K. The mechanistic steps of dehydrogenation were investigated as well. The reaction was believed to proceed via a series of endothermic and exothermic reactions with the intermediate species being LiMgBO<sub>3</sub>, LiH, B<sub>2</sub>O<sub>3</sub>, Li<sub>2</sub>B<sub>12</sub>H<sub>12</sub> and B. Reversibility studies on the materials showed that the dehydrogenated systems was able to uptake *ca.* 4.7 wt. % of hydrogen at 723 K and 100 bar H<sub>2</sub>.

At the same time, Zhu *et al.* investigated the dehydrogenation behaviour of lithium borohydride when mechanically mixed with alkali hydroxides.<sup>119</sup> LiOH, KOH and NaOH were used and a destabilization due to the interaction between H<sup>+</sup> in [OH]<sup>-</sup> and H<sup>-</sup> in [BH<sub>4</sub>]<sup>-</sup> was hypothesised. This destabilisation was found to be greatest when employing LiOH,

reduced when using NaOH with the minimum found for KOH. The most promising composite was found to be the  $\text{LiBH}_4 - x \text{LiOH}$  system and it was further investigated using different stoichiometric ratios (1:1, 1:1.36 and 1:4). Different dehydrogenation pathways were proposed based on the stoichiometry examined. The fastest dehydrogenation kinetics were observed for the  $\text{LiBH}_4 - 4 \text{LiOH}$  composite. Also, increasing the ratio resulted in a higher amount of hydrogen evolved: the weight change associated with  $\text{H}_2$  release was found to increase from 4.1 wt. % to 6.5 wt. % when employing the 1:4 ratio, although also the onset temperature of hydrogen release was found to increase from 480 to 523 K.

A very interesting reversible ternary system studied by Xu *et al.* is the NaOH-NaH- $\text{Na}_2\text{O}$ - $\text{H}_2$  system.<sup>120,121,122</sup> It is possible to study the dehydrogenation behaviour of sodium hydride in presence of sodium hydroxide both anhydrous and monohydrate (Equation 1-22 and Equation 1-23).



Although the theoretical gravimetric capacity for the systems is not very high (4.2 wt. %  $\text{H}_2$  when working with NaOH and 4.6 wt. %  $\text{H}_2$  when using  $\text{NaOH} \cdot \text{H}_2\text{O}$ ), it has been widely proved that the release/uptake of hydrogen is a reversible process, with the full system being able to desorb and absorb hydrogen.

## 1.4 Light metal hydroxides

As explained in the previous section, the role of light metal hydroxide is becoming more and more important in the development of novel solid state hydrogen storage solutions. The prominent hydroxides used were found to be  $\text{Mg}(\text{OH})_2$  and  $\text{LiOH}$  and therefore their structure, decomposition and dehydrogenation properties must be understood.

### 1.4.1 Magnesium hydroxide: structure and dehydrogenation properties

A wide variety of methods for yielding nanostructured  $\text{Mg}(\text{OH})_2$  from  $\text{MgO}$  and  $\text{H}_2\text{O}$  have been reported. Conventional heating syntheses have been studied as well as microwave preparations to give nanosized magnesium hydroxide. The use of additives and templating

agents was explored as well, resulting in crystals with different morphologies: hexagonal nanoplates, nanotubes, nanorods, nanosheets and a mixture of nanosheets and nanoparticles were obtained.<sup>123,124,125,126,127,128,129,130</sup>

Magnesium hydroxide crystallises in the tetragonal  $P-3m1$  space group, with lattice parameters of  $a = 3.15(1) \text{ \AA}$  and  $c = 4.80(2) \text{ \AA}$  (Figure 1-6).<sup>131,132</sup>

For  $\text{Mg}(\text{OH})_2$ , every magnesium atom can coordinate 6 hydroxyl groups, resulting in an octahedral layered structure, with the octahedra linked together by O-O hydrogen bonds.

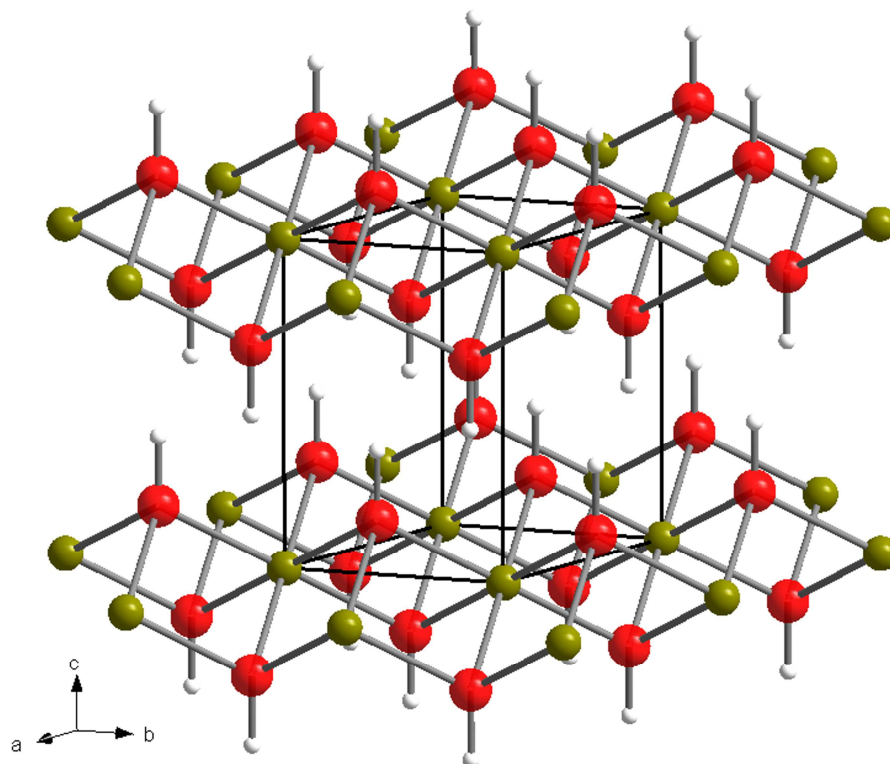
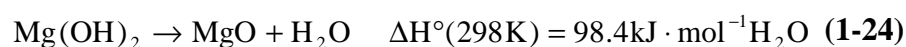


**Figure 1-6: Crystal structure of  $\text{Mg}(\text{OH})_2$ . Olive green spheres indicate magnesium, red spheres oxygen and white spheres hydrogen respectively.**

When heated to temperatures above 623 K,  $\text{Mg}(\text{OH})_2$  decomposes undergoing a dehydration process which results in the formation of  $\text{MgO}$  (cubic,  $Fm-3m$ )<sup>133</sup> and evolution of water (Equation 1-24).<sup>134,135</sup> Magnesium hydroxide can theoretically evolve 30.8 wt. %  $\text{H}_2\text{O}$ . However hydrogen cannot normally be extracted,  $\text{Mg}(\text{OH})_2$  can indirectly store 3.4 wt. % of hydrogen.



Due to its light weight, low cost, low toxicity and facile synthesis,  $\text{Mg}(\text{OH})_2$  can be seen as an ideal candidate to be employed in ‘modular’ hydrogen release systems.

## 1.4.2 Lithium hydroxide: structure and dehydrogenation properties

Anhydrous lithium hydroxide crystallises in the tetragonal  $P4/nmm$  space group,<sup>136</sup> whereas lithium hydroxide monohydrate crystallises in the monoclinic  $C2/m$  space group.<sup>137,138</sup> Crystal structures for LiOH and LiOH·H<sub>2</sub>O are presented in Figure 1-7 and Figure 1-8 respectively.

LiOH structure comprises of alternate layers of lithium atoms coordinating 4 oxygen and hydroxyls, in which hydrogen bonding is not present. In the LiOH·H<sub>2</sub>O structure every Li atom coordinates 4 oxygen atoms to form a tetrahedron. Of the 4 oxygens, 2 come from the hydroxyl groups and 2 come from the water molecules. The chains are linked together by hydrogen bonds O-H-O.

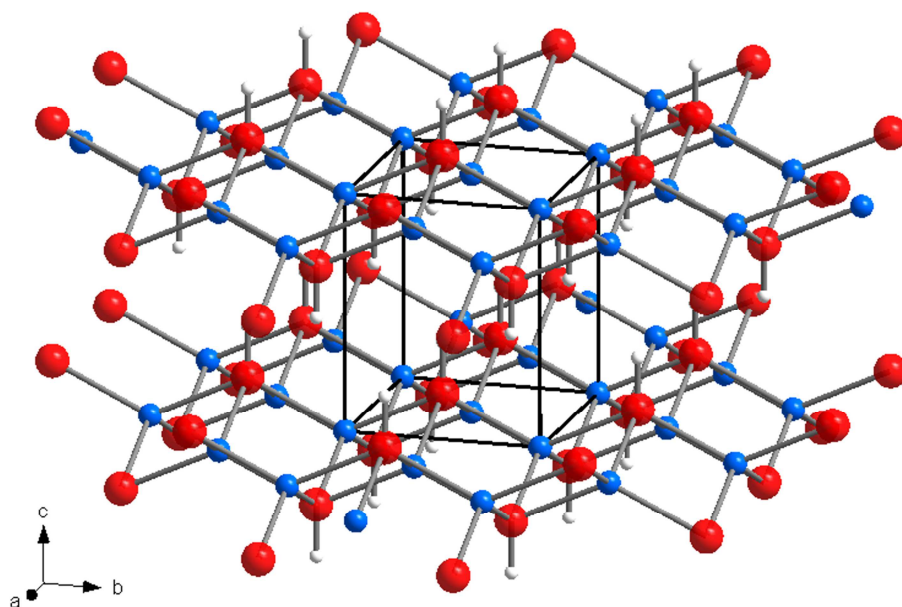
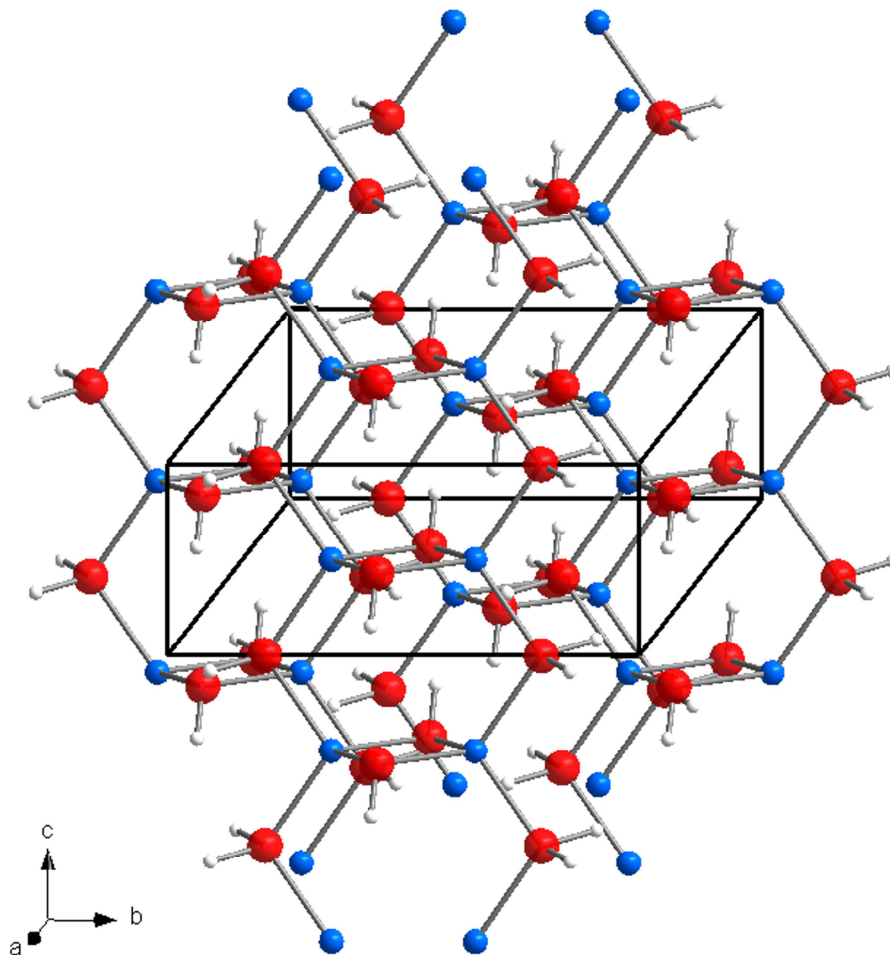
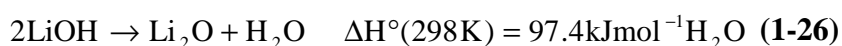


Figure 1-7: Crystal structure of LiOH. Blue spheres indicate lithium, red spheres oxygen and white spheres hydrogen respectively.



**Figure 1-8: Crystal structure of LiOH·H<sub>2</sub>O. Blue spheres indicate lithium, red spheres oxygen and white spheres hydrogen respectively.**

As per Mg(OH)<sub>2</sub>, the decomposition of LiOH(·H<sub>2</sub>O) involves a dehydration processes to yield Li<sub>2</sub>O (cubic, *Fm-3m*)<sup>139</sup> and evolution of water. Both LiOH and LiOH·H<sub>2</sub>O dehydration reactions have been widely investigated and they are given in Equations 1-25 and 1-26.<sup>140,141,142</sup> LiOH can theoretically release 37.6 wt. % of water and indirectly store 4.2 wt. % of H<sub>2</sub>, whilst LiOH·H<sub>2</sub>O can evolve 64.4 wt. % of H<sub>2</sub>O and indirectly store 7.2 wt. % of hydrogen.



Moreover, it is common knowledge that both anhydrous lithium hydroxide and its monohydrate are characterised by an air sensitive nature. Both LiOH and LiOH·H<sub>2</sub>O react with CO<sub>2</sub> under ambient atmosphere in a carbonisation reaction which leads to the formation of lithium carbonate and evolves water (Equations 1-27 and 1-28).



However this reaction can easily be overcome by working under a controlled inert atmosphere, perhaps this may be the reason why, as today, no successful synthesis of nanostructured LiOH(·H<sub>2</sub>O) has been reported in the literature.

## 1.5 Scope of this work

The work presented in this thesis is focused on the study of ‘modular’ hydrogen release systems, based on the reaction between light metal hydroxides and light metal hydrides. Three different systems were fully investigated:

- Magnesium hydroxide – magnesium hydride system
- Magnesium hydroxide – lithium hydride system
- Lithium hydroxide – magnesium hydride system, employing both anhydrous LiOH and its monohydrate

The aim of this thesis was to investigate the hydrogen release behaviour of all systems when subjected to thermal treatment, focusing the attention on the onset and peak temperature of hydrogen release events in each case. The experimental weight change was compared with the theoretical gravimetric H<sub>2</sub> storage capacity. The performances of each system were studied as a function of particle size and morphology of the starting materials; nanostructuring the reactants was seen as a means to improve the dehydrogenation kinetics and have a better control over the overall hydrogen release process. In this sense, both novel and conventional synthetic routes have been employed for the preparation of nanosized light metal hydroxides. Mechanical milling was identified as another route for achieving reduction of the particle size distribution of all hydroxides and hydrides used throughout the whole project. Data obtained for nanostructured, milled and bulk materials were compared, with the final goal being the identification of the most promising H<sub>2</sub>

release systems. *Ex-situ* powder X-ray diffraction was used to try and isolate any intermediate species forming during the dehydrogenation reaction and to propose a mechanism of hydrogen release for each studied system. Further, the Mg(OH)<sub>2</sub> – LiH system was studied using *in-situ* powder neutron diffraction in order to elucidate the mechanism of hydrogen release. Ultimately, understanding the dehydrogenation process in terms of mechanistic steps is pivotal to have a better insight on the reaction occurring and therefore further improve kinetics and thermodynamics for each system.

## 1.6 References

1. Schlapbach, L.; Züttel, A., Hydrogen-storage materials for mobile applications. *Nature* **2001**, *414* (6861), 353-358.
2. International Energy Outlook 2013 With Projections to 2040. [www.eia.gov/ieo/](http://www.eia.gov/ieo/) (accessed 6<sup>th</sup> February 2015).
3. International Energy Outlook 2014 With Projections to 2040. [www.eia.gov/forecasts/aeo](http://www.eia.gov/forecasts/aeo) (accessed 6<sup>th</sup> February 2015).
4. Dresselhaus, M. S.; Thomas, I. L., Alternative energy technologies. *Nature* **2001**, *414* (6861), 332-337.
5. Van den Berg, A. W. C.; Arean, C. O., Materials for hydrogen storage: current research trends and perspectives. *Chemical communications* **2008**, (6), 668-681.
6. Dincer, I.; Acar, C. Review and evaluation of hydrogen production methods for better sustainability. <http://www.sciencedirect.com/science/article/pii/S0360319914034119> (accessed 23<sup>rd</sup> February 2015).
7. Alves, H. J.; Bley Junior, C.; Niklevicz, R. R.; Frigo, E. P.; Frigo, M. S.; Coimbra-Araújo, C. H., Overview of hydrogen production technologies from biogas and the applications in fuel cells. *International Journal of Hydrogen Energy* **2013**, *38* (13), 5215-5225.
8. Granovskii, M.; Dincer, I.; Rosen, M. A., Exergetic life cycle assessment of hydrogen production from renewables. *Journal of Power Sources* **2007**, *167* (2), 461-471.
9. Holladay, J. D.; Hu, J.; King, D. L.; Wang, Y., An overview of hydrogen production technologies. *Catalysis Today* **2009**, *139* (4), 244-260.
10. U.S. Department of Energy - Gaseous and liquid hydrogen storage. <http://energy.gov/eere/fuelcells/gaseous-and-liquid-hydrogen-storage> (accessed 3<sup>rd</sup> February 2015).

11. Sørensen, B., *Hydrogen and Fuel Cells: emerging technologies and applications*. Elsevier Ltd: Roskilde University - Institute of Environmental, Social and Spatial Change, 2012.
12. U.S. Department of Energy - On-Board Hydrogen Storage System Targets. [http://energy.gov/sites/prod/files/2015/01/f19/fcto\\_myrrdd\\_table\\_onboard\\_h2\\_storage\\_systems\\_doe\\_targets\\_ldv.pdf](http://energy.gov/sites/prod/files/2015/01/f19/fcto_myrrdd_table_onboard_h2_storage_systems_doe_targets_ldv.pdf) (accessed 4<sup>th</sup> February 2015).
13. Satyapal, S.; Petrovic, J.; Read, C.; Thomas, G.; Ordaz, G., The U.S. Department of Energy's National Hydrogen Storage Project: Progress towards meeting hydrogen-powered vehicle requirements. *Catalysis Today* **2007**, *120* (3–4), 246-256.
14. Guo, Z. X.; Shang, C.; Aguey-Zinsou, K. F., Materials challenges for hydrogen storage. *Journal of the European Ceramic Society* **2008**, *28* (7), 1467-1473.
15. Pasini, J. M.; Corgnale, C.; van Hassel, B. A.; Motyka, T.; Kumar, S.; Simmons, K. L., Metal hydride material requirements for automotive hydrogen storage systems. *International Journal of Hydrogen Energy* **2013**, *38* (23), 9755-9765.
16. Mandal, T. K.; Gregory, D. H., Hydrogen storage materials: present scenarios and future directions. *Annual Reports Section "A" (Inorganic Chemistry)* **2009**, *105*, 21.
17. Gregory, D. H.; Mandal, T. K., Hydrogen: a future energy vector for sustainable development. *Proceedings of the Institution of Mechanical Engineers, Part C: Journal of Mechanical Engineering Science* **2010**, *224* (3), 539-558.
18. Churchard, A. J.; Banach, E.; Borgschulte, A.; Caputo, R.; Chen, J. C.; Clary, D.; Fijalkowski, K. J.; Geerlings, H.; Genova, R. V.; Grochala, W.; Jaron, T.; Juanes-Marcos, J. C.; Kasemo, B.; Kroes, G. J.; Ljubic, I.; Naujoks, N.; Norskov, J. K.; Olsen, R. A.; Pendolino, F.; Remhof, A.; Romaszki, L.; Tekin, A.; Vegge, T.; Zach, M.; Züttel, A., A multifaceted approach to hydrogen storage. *Physical chemistry chemical physics : PCCP* **2011**, *13* (38), 16955-72.
19. Sakintuna, B.; Lamari-Darkrim, F.; Hirscher, M., Metal hydride materials for solid hydrogen storage: A review. *International Journal of Hydrogen Energy* **2007**, *32* (9), 1121-1140.
20. Orimo, S. I.; Nakamori, Y.; Eliseo, J. R.; Züttel, A.; Jensen, C. M., Complex hydrides for hydrogen storage. *Chem. Rev.* **2007**, *107* (10), 4111-4132.
21. Li, H. W.; Yan, Y. G.; Orimo, S.; Züttel, A.; Jensen, C. M., Recent Progress in Metal Borohydrides for Hydrogen Storage. *Energies* **2011**, *4* (1), 185-214.
22. Lozano-Castelló, D.; Suárez-García, F.; Linares-Solano, Á.; Cazorla-Amorós, D., Chapter 12 - Advances in Hydrogen Storage in Carbon Materials. In *Renewable Hydrogen Technologies*, Diéguez, L. M. G. A. M., Ed. Elsevier: Amsterdam, 2013; pp 269-291.

23. Lim, K. L.; Kazemian, H.; Yaakob, Z.; Daud, W. R. W., Solid-state Materials and Methods for Hydrogen Storage: A Critical Review. *Chem. Eng. Technol.* **2010**, *33* (2), 213-226.
24. Williams, M. C., Chapter 2 - Fuel Cells. In *Fuel Cells*, Shekhawat, D.; Berry, J. J. S. A., Eds. Elsevier: Amsterdam, 2011; pp 11-27.
25. Mekhilef, S.; Saidur, R.; Safari, A., Comparative study of different fuel cell technologies. *Renewable and Sustainable Energy Reviews* **2012**, *16* (1), 981-989.
26. Basu, S., *Recent Trends in Fuel Cell Science and Technology*. Springer: 2007.
27. T. E. Springer, T. A. Z. a. S. G., Polymer Electrolyte Fuel Cell Model. *Journal of Electrochemical Society* **1991**, *138* (8), 2334-2342.
28. Shao, Y.; Liu, J.; Wang, Y.; Lin, Y., Novel catalyst support materials for PEM fuel cells: current status and future prospects. *Journal of Materials Chemistry* **2009**, *19* (1), 46.
29. Gasteiger, H. A.; Kocha, S. S.; Sompalli, B.; Wagner, F. T., Activity benchmarks and requirements for Pt, Pt-alloy, and non-Pt oxygen reduction catalysts for PEMFCs. *Applied Catalysis B: Environmental* **2005**, *56* (1-2), 9-35.
30. Cheng, X.; Shi, Z.; Glass, N.; Zhang, L.; Zhang, J.; Song, D.; Liu, Z.-S.; Wang, H.; Shen, J., A review of PEM hydrogen fuel cell contamination: Impacts, mechanisms, and mitigation. *Journal of Power Sources* **2007**, *165* (2), 739-756.
31. Chung, D. Y.; Kim, H.-i.; Chung, Y.-H.; Lee, M. J.; Yoo, S. J.; Bokare, A. D.; Choi, W.; Sung, Y.-E., Inhibition of CO poisoning on Pt catalyst coupled with the reduction of toxic hexavalent chromium in a dual-functional fuel cell. *Sci. Rep.* **2014**, *4*.
32. Rodrigues, A.; Amphlett, J. C.; Mann, R. F.; Peppley, B. A.; Roberge, P. R. In *Carbon monoxide poisoning of proton-exchange membrane fuel cells*, Energy Conversion Engineering Conference, 1997. IECEC-97., Proceedings of the 32nd Intersociety, 27 Jul-1 Aug 1997; 1997; pp 768-773 vol.2.
33. Mohammed Alhassan, M. U. G., Design of an Alkaline Fuel Cell. *Leonardo Electronic Journal of Practices and Technologies* **2006**, (9), 99-106.
34. Andújar, J. M.; Segura, F., Fuel cells: History and updating. A walk along two centuries. *Renewable and Sustainable Energy Reviews* **2009**, *13* (9), 2309-2322.
35. Wagner, N.; Schulze, M.; Gülzow, E., Long term investigations of silver cathodes for alkaline fuel cells. *Journal of Power Sources* **2004**, *127* (1-2), 264-272.
36. Gülzow, E. a. S., M., Long-term operation of AFC electrodes with CO<sub>2</sub> containing gases. *Journal of Power Sources* **2004**, *127* (1-2), 243-251.

37. Gülzow, E.; Schulze, M.; Steinhilber, G., Investigation of the degradation of different nickel anode types for alkaline fuel cells (AFCs). *Journal of Power Sources* **2002**, *106* (1–2), 126-135.
38. Schulze, M.; Gülzow, E., Degradation of nickel anodes in alkaline fuel cells. *Journal of Power Sources* **2004**, *127* (1–2), 252-263.
39. Merle, G.; Wessling, M.; Nijmeijer, K., Anion exchange membranes for alkaline fuel cells: A review. *Journal of Membrane Science* **2011**, *377* (1-2), 1-35.
40. Antolini, E.; Gonzalez, E. R., Alkaline direct alcohol fuel cells. *Journal of Power Sources* **2010**, *195* (11), 3431-3450.
41. Arico, A. S.; Srinivasan, S.; Antonucci, V., DMFCs: From Fundamental Aspects to Technology Development. *Fuel Cells* **2001**, *1* (2), 133-161.
42. Krewer, U.; Vidakovic-Koch, T.; Rihko-Struckmann, L., Electrochemical Oxidation of Carbon-Containing Fuels and Their Dynamics in Low-Temperature Fuel Cells. *ChemPhysChem* **2011**, *12* (14), 2518-2544.
43. Lamy, C.; Rousseau, S.; Belgsir, E. M.; Coutanceau, C.; Léger, J. M., Recent progress in the direct ethanol fuel cell: development of new platinum–tin electrocatalysts. *Electrochimica Acta* **2004**, *49* (22–23), 3901-3908.
44. Antolini, E., Catalysts for direct ethanol fuel cells. *Journal of Power Sources* **2007**, *170* (1), 1-12.
45. Rousseau, S.; Coutanceau, C.; Lamy, C.; Léger, J. M., Direct ethanol fuel cell (DEFC): Electrical performances and reaction products distribution under operating conditions with different platinum-based anodes. *Journal of Power Sources* **2006**, *158* (1), 18-24.
46. Ormerod, R. M., Solid oxide fuel cells. *Chemical Society reviews* **2003**, *32* (1), 17-28.
47. Jacobson, A. J., Materials for Solid Oxide Fuel Cells. *Chemistry of Materials* **2010**, *22* (3), 660-674.
48. Patakangas, J.; Ma, Y.; Jing, Y. F.; Lund, P., Review and analysis of characterization methods and ionic conductivities for low-temperature solid oxide fuel cells (LT-SOFC). *Journal of Power Sources* **2014**, *263*, 315-331.
49. Ignatiev, A.; Chen, X.; Wu, N.; Lu, Z.; Smith, L., Nanostructured thin solid oxide fuel cells with high power density. *Dalton transactions* **2008**, (40), 5501-6.
50. Brett, D. J.; Atkinson, A.; Brandon, N. P.; Skinner, S. J., Intermediate temperature solid oxide fuel cells. *Chemical Society reviews* **2008**, *37* (8), 1568-78.

51. Matsuzaki, Y.; Yasuda, I., The poisoning effect of sulfur-containing impurity gas on a SOFC anode: Part I. Dependence on temperature, time, and impurity concentration. *Solid State Ionics* **2000**, *132* (3–4), 261-269.
52. Wee, J.-H., Molten carbonate fuel cell and gas turbine hybrid systems as distributed energy resources. *Applied Energy* **2011**, *88* (12), 4252-4263.
53. Dicks, A. L., Molten carbonate fuel cells. *Current Opinion in Solid State and Materials Science* **2004**, *8* (5), 379-383.
54. Nguyen, H. V. P.; Othman, M. R.; Seo, D.; Yoon, S. P.; Ham, H. C.; Nam, S. W.; Han, J.; Kim, J., Nano Ni layered anode for enhanced MCFC performance at reduced operating temperature. *International Journal of Hydrogen Energy* **2014**, *39* (23), 12285-12290.
55. Jang, S.-C.; Lee, B. Y.; Nam, S. W.; Ham, H. C.; Han, J.; Yoon, S. P.; Oh, S.-G., New method for low temperature fabrication of Ni–Al alloy powder for molten carbonate fuel cell applications. *International Journal of Hydrogen Energy* **2014**, *39* (23), 12259-12265.
56. Fukui, T.; Ohara, S.; Okawa, H.; Naito, M.; Nogi, K., Synthesis of metal and ceramic composite particles for fuel cell electrodes. *Journal of the European Ceramic Society* **2003**, *23* (15), 2835-2840.
57. Escudero, M. J.; Rodrigo, T.; Soler, J.; Daza, L., Electrochemical behaviour of lithium–nickel oxides in molten carbonate. *Journal of Power Sources* **2003**, *118* (1–2), 23-34.
58. Wijayasinghe, A.; Bergman, B.; Lagergren, C., LiFeO<sub>2</sub>-LiCoO<sub>2</sub>-NiO cathodes for molten carbonate fuel cells. *Journal of the Electrochemical Society* **2003**, *150* (5), A558-A564.
59. Kirubakaran, A.; Jain, S.; Nema, R. K., A review on fuel cell technologies and power electronic interface. *Renewable and Sustainable Energy Reviews* **2009**, *13* (9), 2430-2440.
60. Eberle, U.; Felderhoff, M.; Schüth, F., Chemical and Physical Solutions for Hydrogen Storage. *Angewandte Chemie International Edition* **2009**, *48* (36), 6608-6630.
61. Bhattacharyya, R.; Mohan, S., Solid state storage of hydrogen and its isotopes: An engineering overview. *Renew. Sust. Energ. Rev.* **2015**, *41*, 872-883.
62. Ren, Y.; Chia, G. H.; Gao, Z., Metal–organic frameworks in fuel cell technologies. *Nano Today* **2013**, *8* (6), 577-597.
63. Kustov, L. M.; Tarasov, A. L.; Sung, J.; Godovsky, D. Y., Hydrogen storage materials. *Mendeleev Communications* **2014**, *24* (1), 1-8.

64. Yeung, K. L.; Han, W., Zeolites and mesoporous materials in fuel cell applications. *Catalysis Today* **2014**, *236*, 182-205.
65. Furukawa, H.; Yaghi, O. M., Storage of Hydrogen, Methane, and Carbon Dioxide in Highly Porous Covalent Organic Frameworks for Clean Energy Applications. *Journal of the American Chemical Society* **2009**, *131* (25), 8875-8883.
66. Feng, X.; Ding, X. S.; Jiang, D. L., Covalent organic frameworks. *Chemical Society reviews* **2012**, *41* (18), 6010-6022.
67. Klebanoff, L. E.; Keller, J. O., 5 Years of hydrogen storage research in the U.S. DOE Metal Hydride Center of Excellence (MHCoE). *International Journal of Hydrogen Energy* **2013**, *38* (11), 4533-4576.
68. Grochala, W.; Edwards, P. P., Thermal Decomposition of the Non-Interstitial Hydrides for the Storage and Production of Hydrogen. *Chem. Rev.* **2004**, *104* (3), 1283-1316.
69. Züttel, A., Materials for hydrogen storage. *Materials Today* **2003**, *6* (9), 24-33.
70. George, L.; Saxena, S. K., Structural stability of metal hydrides, alanates and borohydrides of alkali and alkali- earth elements: A review. *International Journal of Hydrogen Energy* **2010**, *35* (11), 5454-5470.
71. *CRC Handbook of Chemistry and Physics*. 95th Edition ed.; CRC Press: Boca Raton, Florida 33431, 1980-1981.
72. Bulanov, A. D.; Troshin, O. Y.; Balabanov, V. V., Synthesis of High-Purity Calcium Hydride. *Russian Journal of Applied Chemistry* **2004**, *77* (6), 875-877.
73. Wolverton, C.; Ozolins, V., Hydrogen storage in calcium alanate: First-principles thermodynamics and crystal structures. *Phys. Rev. B* **2007**, *75* (6), 15.
74. Yang, J.; Sudik, A.; Wolverton, C., Destabilizing LiBH<sub>4</sub> with a Metal (M = Mg, Al, Ti, V, Cr, or Sc) or Metal Hydride (MH<sub>2</sub> = MgH<sub>2</sub>, TiH<sub>2</sub>, or CaH<sub>2</sub>). *The Journal of Physical Chemistry C* **2007**, *111* (51), 19134-19140.
75. Ozolins, V.; Majzoub, E. H.; Wolverton, C., First-Principles Prediction of Thermodynamically Reversible Hydrogen Storage Reactions in the Li-Mg-Ca-B-H System. *Journal of the American Chemical Society* **2009**, *131* (1), 230-237.
76. Cao, H.; Zhang, Y.; Wang, J.; Xiong, Z.; Wu, G.; Chen, P., Materials design and modification on amide-based composites for hydrogen storage. *Progress in Natural Science: Materials International* **2012**, *22* (6), 550-560.
77. Nakagawa, Y.; Isobe, S.; Ikarashi, Y.; Ohnuki, S., AB-MH (Ammonia Borane-Metal Hydride) composites: systematic understanding of dehydrogenation properties. *Journal of Materials Chemistry A* **2014**, *2* (11), 3926-3931.

78. Huot, J.; Liang, G.; Boily, S.; Van Neste, A.; Schulz, R., Structural study and hydrogen sorption kinetics of ball-milled magnesium hydride. *Journal of Alloys and Compounds* **1999**, 293–295 (0), 495-500.
79. Tessier, J. P.; Palau, P.; Huot, J.; Schulz, R.; Guay, D., Hydrogen production and crystal structure of ball-milled  $\text{MgH}_2\text{-Ca}$  and  $\text{MgH}_2\text{-CaH}_2$  mixtures. *Journal of Alloys and Compounds* **2004**, 376 (1–2), 180-185.
80. Reardon, H. Synthesis, structure and characterisation of novel lightweight energy materials based on group I & II metal compounds. PhD Thesis, University of Glasgow, 2014.
81. Bazzanella, N.; Checchetto, R.; Miotello, A., Atoms and Nanoparticles of Transition Metals as Catalysts for Hydrogen Desorption from Magnesium Hydride. *Journal of Nanomaterials* **2011**, 2011, 1-11.
82. Ren, C.; Fang, Z. Z.; Zhou, C. S.; Lu, J.; Ren, Y.; Zhang, X. Y., Hydrogen Storage Properties of Magnesium Hydride with V-Based Additives. *J. Phys. Chem. C* **2014**, 118 (38), 21778-21784.
83. Cui, J.; Wang, H.; Liu, J.; Ouyang, L.; Zhang, Q.; Sun, D.; Yao, X.; Zhu, M., Remarkable enhancement in dehydrogenation of  $\text{MgH}_2$  by a nano-coating of multi-valence Ti-based catalysts. *Journal of Materials Chemistry A* **2013**, 1 (18), 5603-5611.
84. Shahi, R. R.; Bhatnagar, A.; Pandey, S. K.; Dixit, V.; Srivastava, O. N., Effects of Ti-based catalysts and synergistic effect of SWCNTs-TiF<sub>3</sub> on hydrogen uptake and release from  $\text{MgH}_2$ . *International Journal of Hydrogen Energy* **2014**, 39 (26), 14255-14261.
85. Varin, R. A.; Zbroniec, L.; Polanski, M.; Bystrzycki, J., A Review of Recent Advances on the Effects of Microstructural Refinement and Nano-Catalytic Additives on the Hydrogen Storage Properties of Metal and Complex Hydrides. *Energies* **2011**, 4 (1), 1-25.
86. Bazzanella, N.; Checchetto, R.; Miotello, A., Atoms and Nanoparticles of Transition Metals as Catalysts for Hydrogen Desorption from Magnesium Hydride. *Journal of Nanomaterials* **2011**, 11.
87. Wang, H.; Zhang, J.; Liu, J. W.; Ouyang, L. Z.; Zhu, M., Improving hydrogen storage properties of  $\text{MgH}_2$  by addition of alkali hydroxides. *International Journal of Hydrogen Energy* **2013**, 38 (25), 10932-10938.
88. Reardon, H.; Hanlon, J. M.; Hughes, R. W.; Godula-Jopek, A.; Mandal, T. K.; Gregory, D. H., Emerging concepts in solid-state hydrogen storage: the role of nanomaterials design. *Energy & Environmental Science* **2012**, 5 (3), 5951-5979.

89. Hanlon, J. M.; Reardon, H.; Tapia-Ruiz, N.; Gregory, D. H., The Challenge of Storage in the Hydrogen Energy Cycle: Nanostructured Hydrides as a Potential Solution. *Aust. J. Chem.* **2012**, *65* (6), 656-671.
90. Hanada, N.; Ichikawa, T.; Orimo, S. I.; Fujii, H., Correlation between hydrogen storage properties and structural characteristics in mechanically milled magnesium hydride MgH<sub>2</sub>. *Journal of Alloys and Compounds* **2004**, *366* (1-2), 269-273.
91. Schimmel, H. G.; Johnson, M. R.; Kearley, G. J.; Ramirez-Cuesta, A. J.; Huot, J.; Mulder, F. M., Structural information on ball milled magnesium hydride from vibrational spectroscopy and ab-initio calculations. *Journal of Alloys and Compounds* **2005**, *393* (1-2), 1-4.
92. Schuth, F.; Bogdanovic, B.; Felderhoff, M., Light metal hydrides and complex hydrides for hydrogen storage. *Chemical communications* **2004**, (20), 2249-2258.
93. Zhang, B. J.; Liu, B. H.; Li, Z. P., Destabilization of LiBH<sub>4</sub> by (Ce, La)(Cl, F)<sub>3</sub> for hydrogen storage. *Journal of Alloys and Compounds* **2011**, *509* (3), 751-757.
94. Varin, R. A.; Zbroniec, L., The effects of ball milling and nanometric nickel additive on the hydrogen desorption from lithium borohydride and manganese chloride (3LiBH<sub>4</sub>:MnCl<sub>2</sub>) mixture. *International Journal of Hydrogen Energy* **2010**, *35* (8), 3588-3597.
95. Nielsen, T. K.; Bösenberg, U.; Gosalawit, R.; Dornheim, M.; Cerenius, Y.; Besenbacher, F.; Jensen, T. R., A Reversible Nanoconfined Chemical Reaction. *ACS Nano* **2010**, *4* (7), 3903-3908.
96. Ampoumogli, A.; Steriotis, T.; Trikalitis, P.; Giasafaki, D.; Bardaji, E. G.; Fichtner, M.; Charalambopoulou, G., Nanostructured composites of mesoporous carbons and boranates as hydrogen storage materials. *Journal of Alloys and Compounds* **2011**, *509*, Supplement 2 (0), S705-S708.
97. Liu, X.; Peaslee, D.; Jost, C. Z.; Majzoub, E. H., Controlling the Decomposition Pathway of LiBH<sub>4</sub> via Confinement in Highly Ordered Nanoporous Carbon. *The Journal of Physical Chemistry C* **2010**, *114* (33), 14036-14041.
98. Ngene, P.; van den Berg, R.; Verkuijlen, M. H. W.; de Jong, K. P.; de Jongh, P. E., Reversibility of the hydrogen desorption from NaBH<sub>4</sub> by confinement in nanoporous carbon. *Energy & Environmental Science* **2011**, *4* (10), 4108-4115.
99. Li, C.; Peng, P.; Zhou, D. W.; Wan, L., Research progress in LiBH<sub>4</sub> for hydrogen storage: A review. *International Journal of Hydrogen Energy* **2011**, *36* (22), 14512-14526.
100. Mao, J. F.; Gregory, D. H., Recent Advances in the Use of Sodium Borohydride as a Solid State Hydrogen Store. *Energies* **2015**, *8* (1), 430-453.

101. Chen, P.; Xiong, Z.; Luo, J.; Lin, J.; Tan, K. L., Interaction of hydrogen with metal nitrides and imides. *Nature* **2002**, *420* (6913), 302-304.
102. Gregory, D. H., Lithium nitrides, imides and amides as lightweight, reversible hydrogen stores. *Journal of Materials Chemistry* **2008**, *18* (20), 2321-2330.
103. Chen, P.; Zhu, M., Recent progress in hydrogen storage. *Materials Today* **2008**, *11* (12), 36-43.
104. Liang, C.; Liu, Y. F.; Fu, H. L.; Ding, Y. F.; Gao, M. X.; Pan, H. G., Li-Mg-N-H-based combination systems for hydrogen storage. *Journal of Alloys and Compounds* **2011**, *509* (30), 7844-7853.
105. Hu, Y. H.; Ruckenstein, E., Ultrafast Reaction between  $\text{Li}_3\text{N}$  and  $\text{LiNH}_2$  To Prepare the Effective Hydrogen Storage Material  $\text{Li}_2\text{NH}$ . *Industrial & Engineering Chemistry Research* **2006**, *45* (14), 4993-4998.
106. Sorbie, N. Synthesis and Structure of Group I and II Nitrides as Potential Hydrogen Stores. PhD Thesis, University of Glasgow, 2011.
107. Chen, P.; Xiong, Z.; Luo, J.; Lin, J.; Tan, K. L., Interaction between Lithium Amide and Lithium Hydride. *The Journal of Physical Chemistry B* **2003**, *107* (39), 10967-10970.
108. Zheng, X.; Wu, G.; Li, W.; Xiong, Z.; He, T.; Guo, J.; Chen, H.; Chen, P., Releasing 17.8 wt%  $\text{H}_2$  from lithium borohydride ammoniate. *Energy & Environmental Science* **2011**, *4* (9), 3593-3600.
109. Guo, Y.; Xia, G.; Zhu, Y.; Gao, L.; Yu, X., Hydrogen release from amminelithium borohydride,  $\text{LiBH}_4\cdot\text{NH}_3$ . *Chemical communications* **2010**, *46* (15), 2599-2601.
110. Luo, J.; Wu, H.; Zhou, W.; Kang, X.; Fang, Z.; Wang, P.,  $\text{LiBH}_4\cdot\text{NH}_3\text{BH}_3$ : A new lithium borohydride ammonia borane compound with a novel structure and favorable hydrogen storage properties. *International Journal of Hydrogen Energy* **2012**, *37* (14), 10750-10757.
111. Vajo, J. J.; Skeith, S. L.; Mertens, F.; Jorgensen, S. W., Hydrogen-generating solid-state hydride/hydroxide reactions. *Journal of Alloys and Compounds* **2005**, *390* (1-2), 55-61.
112. Lu, J.; Fang, Z. Z.; Sohn, H. Y., A hybrid method for hydrogen storage and generation from water. *Journal of Power Sources* **2007**, *172* (2), 853-858.
113. Leardini, F.; Ares, J. R.; Bodega, J.; Fernandez, J. F.; Ferrer, I. J.; Sanchez, C., Reaction pathways for hydrogen desorption from magnesium hydride/hydroxide composites: bulk and interface effects. *Phys. Chem. Chem. Phys.* **2010**, *12* (3), 572-577.

114. Basic Research Needs for the Hydrogen Economy. [http://www.hydrogen.energy.gov/pdfs/nhe\\_rpt.pdf](http://www.hydrogen.energy.gov/pdfs/nhe_rpt.pdf) (accessed 12<sup>th</sup> February 2015).
115. Drozd, V.; Saxena, S.; Garimella, S. V.; Durygin, A., Hydrogen release from a mixture of NaBH<sub>4</sub> and Mg(OH)<sub>2</sub>. *International Journal of Hydrogen Energy* **2007**, 32 (15), 3370-3375.
116. Mikheeva, V. I.; Breitsis, V. B.; Kuznetsova, V.; Kryukova, O. N., Reaction between sodium hydridoborate and sodium hydroxide. *Doklady Akademii Nauk Sssr* **1969**, 187 (1), 103.
117. Varin, R. A.; Parviz, R., Hydrogen generation from the ball milled composites of sodium and lithium borohydride (NaBH<sub>4</sub>/LiBH<sub>4</sub>) and magnesium hydroxide (Mg(OH)<sub>2</sub>) without and with the nanometric nickel (Ni) additive. *International Journal of Hydrogen Energy* **2012**, 37 (2), 1584-1593.
118. Liu, Y.; Zhang, Y.; Zhou, H.; Zhang, Y.; Gao, M.; Pan, H., Reversible hydrogen storage behavior of LiBH<sub>4</sub>-Mg(OH)<sub>2</sub> composites. *International Journal of Hydrogen Energy* **2014**, 39 (15), 7868-7875.
119. Cai, W.; Wang, H.; Sun, D.; Zhang, Q.; Yao, X.; Zhu, M., Destabilization of LiBH<sub>4</sub> dehydrogenation through H<sup>+</sup>-H<sup>-</sup> interactions by cooperating with alkali metal hydroxides. *RSC Advances* **2014**, 4 (6), 3082.
120. Xu, Q.; Wang, R.; Kiyobayashi, T.; Kuriyama, N.; Kobayashi, T., Reaction of hydrogen with sodium oxide: A reversible hydrogenation/dehydrogenation system. *Journal of Power Sources* **2006**, 155 (2), 167-171.
121. Myles, K. M.; Cafasso, F. A., The reciprocal ternary system Na-NaOH-Na<sub>2</sub>O-NaH. *Journal of Nuclear Materials* **1977**, 67 (3), 249-253.
122. Veleckis, E.; Leibowitz, L., Phase relations for reactions of hydrogen with sodium oxide between 500 and 900°C. *Journal of Nuclear Materials* **1987**, 144 (3), 235-243.
123. Al-Hazmi, F.; Umar, A.; Dar, G. N.; Al-Ghamdi, A. A.; Al-Sayari, S. A.; Al-Hajry, A.; Kim, S. H.; Al-Tuwirqi, R. M.; Alnowaiserb, F.; El-Tantawy, F., Microwave assisted rapid growth of Mg(OH)<sub>2</sub> nanosheet networks for ethanol chemical sensor application. *Journal of Alloys and Compounds* **2012**, 519, 4-8.
124. Fan, W.; Sun, S.; Song, X.; Zhang, W.; Yu, H.; Tan, X.; Cao, G., Controlled synthesis of single-crystalline Mg(OH)<sub>2</sub> nanotubes and nanorods via a solvothermal process. *Journal of Solid State Chemistry* **2004**, 177 (7), 2329-2338.
125. Jiang, W.; Hua, X.; Han, Q.; Yang, X.; Lu, L.; Wang, X., Preparation of lamellar magnesium hydroxide nanoparticles via precipitation method. *Powder Technology* **2009**, 191 (3), 227-230.

126. Lv, J.; Qiu, L.; Qu, B., Controlled growth of three morphological structures of magnesium hydroxide nanoparticles by wet precipitation method. *Journal of Crystal Growth* **2004**, *267* (3-4), 676-684.
127. Yan, H.; Zhang, X.-h.; Wu, J.-m.; Wei, L.-q.; Liu, X.-g.; Xu, B.-s., The use of CTAB to improve the crystallinity and dispersibility of ultrafine magnesium hydroxide by hydrothermal route. *Powder Technology* **2008**, *188* (2), 128-132.
128. Al-Gaashani, R.; Radiman, S.; Al-Douri, Y.; Tabet, N.; Daud, A. R., Investigation of the optical properties of Mg(OH)<sub>2</sub> and MgO nanostructures obtained by microwave-assisted methods. *Journal of Alloys and Compounds* **2012**, *521*, 71-76.
129. Zhuo, L.; Ge, J.; Cao, L.; Tang, B., Solvothermal Synthesis of CoO, Co<sub>3</sub>O<sub>4</sub>, Ni(OH)<sub>2</sub> and Mg(OH)<sub>2</sub> Nanotubes. *Crystal Growth & Design* **2008**, *9* (1), 1-6.
130. Jin, D.; Gu, X.; Yu, X.; Ding, G.; Zhu, H.; Yao, K., Hydrothermal synthesis and characterization of hexagonal Mg(OH)<sub>2</sub> nano-flake as a flame retardant. *Materials Chemistry and Physics* **2008**, *112* (3), 962-965.
131. Desgranges, L.; Calvarin, G.; Chevrier, G., Interlayer interactions in M(OH)<sub>2</sub>: a neutron diffraction study of Mg(OH)<sub>2</sub>. *Acta Crystallographica Section B* **1996**, *52* (1), 82-86.
132. Kazimirov, V. Y.; Smirnov, M. B.; Bourgeois, L.; Guerlou-Demourgues, L.; Servant, L.; Balagurov, A. M.; Natkaniec, I.; Khasanova, N. R.; Antipov, E. V., Atomic structure and lattice dynamics of Ni and Mg hydroxides. *Solid State Ionics* **2010**, *181* (39-40), 1764-1770.
133. Tsirelson, V.; Avilov, A.; Abramov, Y. A.; Belokoneva, E.; Kitaneh, R.; Feil, D., X-ray and electron diffraction study of MgO. *Acta crystallographica Section B: Structural science* **1998**, *54* (1), 8-17.
134. James M. Hanlon; Laura Bravo Diaz; Giulia Balducci; Blane A. Stobbs; Marek Bielewski; Chung, P.; Gregory, a. D. H., Rapid surfactant-free synthesis of Mg(OH)<sub>2</sub> nanoplates and pseudomorphic dehydration to MgO. *CrystEngComm* **2015**.
135. Turner, R. C.; Hoffman, I.; Chen, D., Thermogravimetry of the dehydration of Mg(OH)<sub>2</sub>. *Canadian Journal of Chemistry* **1963**, *41* (2), 243-251.
136. Ernst, T., Description and crystal structure of lithium hydroxide. *Z. Phys. Chem. B-Chem. Elem. Aufbau. Mater.* **1933**, *20* (1/2), 65-88.
137. Ojamae, L.; Hermansson, K.; Pisani, C.; Causa, M.; Roetti, C., Structural, vibrational and electronic-properties of a crystalline hydrate form from ab-initio periodic Hartree-Fock calculations. *Acta Crystallogr. Sect. B-Struct. Commun.* **1994**, *50*, 268-279.

138. Pepinsky, R., Crystal structure of lithium hydroxide monohydrate. *Z. Kristall.* **1939**, *102* (2), 119-131.
139. Farley, T. W. D.; Hayes, W.; Hull, S.; Hutchings, M. T.; Vrtis, M., Investigation of thermally induced Li<sup>+</sup> ion disorder in Li<sub>2</sub>O using neutron diffraction. *Journal of Physics-Condensed Matter* **1991**, *3* (26), 4761-4781.
140. Monnin, C.; Dubois, M., Thermodynamics of the LiOH + H<sub>2</sub>O System. *Journal of Chemical & Engineering Data* **2005**, *50* (4), 1109-1113.
141. Dinh, L. N.; McLean li, W.; Schildbach, M. A.; LeMay, J. D.; Siekhaus, W. J.; Balooch, M., The nature and effects of the thermal stability of lithium hydroxide. *Journal of Nuclear Materials* **2003**, *317* (2-3), 175-188.
142. Popescu, C.; Jianu, V.; Alexandrescu, R.; Mihăilescu, I. N.; Morjan, I.; Pascu, M. L., Dehydration of some inorganic compounds by CW CO<sub>2</sub> laser irradiation and thermal heating: A comparative study. *Thermochimica Acta* **1988**, *129* (2), 269-276.

## 2 Experimental

In this work, different synthetic techniques including microwave and conventional synthetic methods have been used in order to prepare nanostructured hydrogen storage materials to be used in 'modular' hydrogen release systems.

A wide range of techniques has been used to investigate the structure and the properties of such materials and systems fully. Powder X-ray diffraction has been used as the main method of characterisation. However, a variety of complementary techniques have been employed, such as *in-situ* powder neutron diffraction, simultaneous thermogravimetric analysis, mass spectroscopy and scanning electron microscopy.

The aim of this chapter is to give an overview of both the synthetic and characterisation techniques used throughout the whole project.

### 2.1 Air Sensitive Handling Techniques

#### 2.1.1 Dry Glove Boxes

Most materials used in this project are air and moisture sensitive, and therefore they must be handled inside a recirculating glove box under an inert atmosphere. During this project two types of recirculating glove boxes have been used. These were manufactured by Saffron Scientific<sup>1</sup> and mBraun<sup>2</sup> (Figure 2-1) and they were set to work respectively under argon and nitrogen atmosphere.

The atmosphere inside the glove box is kept clean by the continuous flow of inert gas through a system of molecular sieves and a catalyst. For the mBraun glove box, the typical O<sub>2</sub> and H<sub>2</sub>O levels are below 0.5 ppm, whereas for the Saffron Scientific glove box, the typical O<sub>2</sub> levels are in the 0-5 ppm range and H<sub>2</sub>O levels are in the 0-30 ppm range. In order to keep the atmosphere inside the glove box within the aforementioned levels, regeneration processes were conducted every two months or less, depending on the usage of the box.

The regeneration of the Saffron glove box is conducted *off-box*: the molecular sieve, which removes the moisture, is regenerated by heating under vacuum for 12 hours. The

commercial catalysts, which remove the oxygen, are regenerated by heating under a flow of 5% H<sub>2</sub> in N<sub>2</sub> and subsequently heated under vacuum for 12 hours in order to remove the water formed as by-product of the first regeneration reaction. The regeneration of the mBraun glove box is conducted *in-situ* by flowing 5% H<sub>2</sub> in Ar for 16 hours. At any time the levels in both of the glove boxes are monitored by oxygen and moisture sensors.

Samples and preparative equipment are transferred into and out of the glove box through an antechamber, which is vacuumed and filled with inert gas for three times, in order to preserve the atmosphere inside the box. The antechamber is kept under vacuum when not in use.

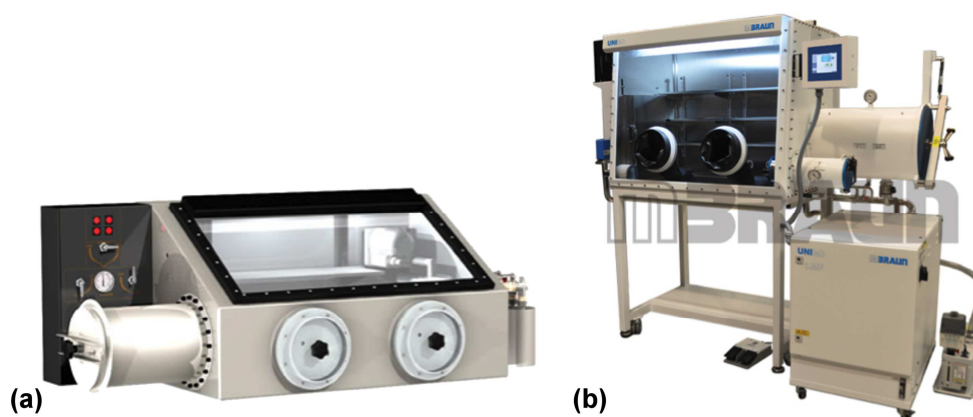


Figure 2-1: a) Omega Saffron Scientific glove box and b) LABstar mBraun glove box. Adapted from References 1 and 2.

## 2.2 Preparative Methods

### 2.2.1 Ball Milling

A mechano-chemical reaction is defined by IUPAC as a “*chemical reaction that is induced by the direct absorption of mechanical energy*”.<sup>3</sup>

Mechanochemistry has recently become a widely used technique, also because of its effectiveness in promoting reaction between solids. Today the term ‘mechanochemistry’ usually refers to solvent-free solid state reactions, whose driving force is the mechanical energy produced during the grinding process taking place in ball mills. One of the most well-established areas of mechanochemical synthesis involves the use of inorganic materials<sup>4</sup>, however a wide range of materials can be studied. In addition, ball milling

techniques are one of the most used processing methods for the developments of novel materials as well as novel composites for hydrogen storage and release.<sup>5</sup>

Ball milling can be seen also as a top-down approach for yielding nanomaterials. In fact, during the mechanochemical procedures there is a reduction of the particle size of the crystallites: the products are often nanoparticles or amorphous phases,<sup>6</sup> which usually exhibit a higher surface area leading to an increased reactivity.

The milling processes have been carried out using a Retsch PM100 planetary ball mill. This involves the rotation of a milling jar containing a grinding medium and the sample to be milled. The jar is placed on a sun wheel and clamped with a counterweight for balancing purposes, in order to prevent any oscillations and vibrations disturbing the instrument. The sun wheel acts as a counter rotating plate during the mechanical milling, with the jar and sun wheel moving in opposite directions with a 2:1 ratio. The grinding balls within the jar are subjected to Coriolis forces, which are superimposed rotational movements dependent on the velocity of the moving object together with their centrifugal force. The difference in speeds between the balls and grinding jars produces an interaction between frictional and impact forces, resulting in the generation of the high dynamic energy required for the milling operations and effectively reduces the particle size of the sample (Figure 2-2).<sup>7</sup>

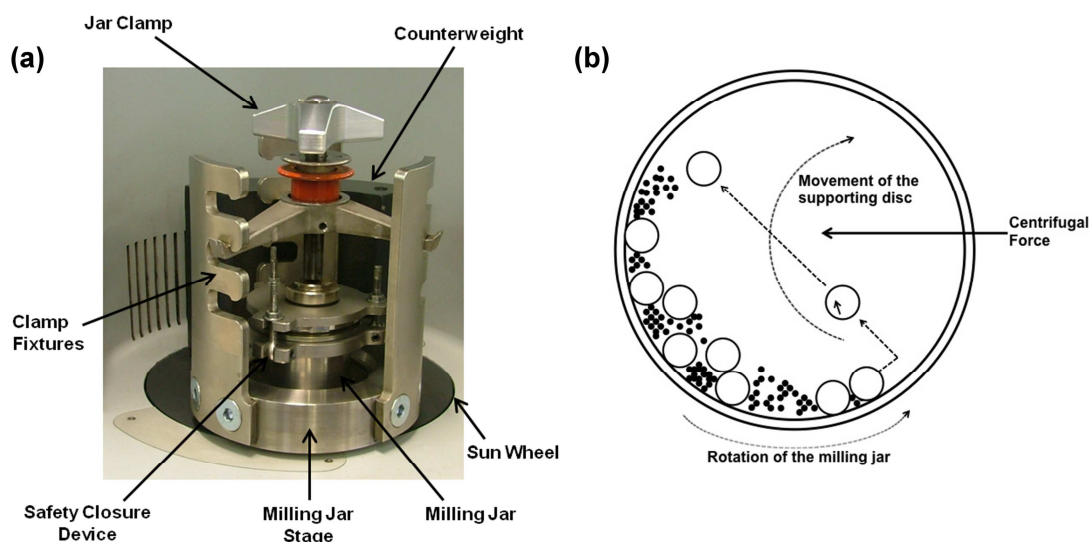


Figure 2-2: (a) Retsch PM100 planetary ball mill configuration; (b) cross section of the milling jar.

Moreover, various reaction parameters can be controlled, such as the milling speed and time, the rotation direction (clockwise and anticlockwise) and rotation direction reversal, the type of milling tools (*i.e.* stainless steel or agate jar), the type, number and size of the grinding medium as well as the mass of the material or materials used. All these variables contribute to the formation of the desired final product.

The ball milling operations conducted during this project involve the reduction of the particle size of both light metal hydrides ( $\text{MgH}_2$  and  $\text{LiH}$ ) and light metal hydroxides ( $\text{Mg}(\text{OH})_2$ ,  $\text{LiOH}$  and  $\text{LiOH}\cdot\text{H}_2\text{O}$ ). Generally, 1 gram of sample was loaded into a 50 ml stainless steel jar together with 10 stainless steel balls used as grinding medium (10 mm diameter, 4 g/ball), resulting in a ball-to-powder ratio of 40:1. All preparations have been carried out under inert atmosphere inside an argon-filled or nitrogen-filled recirculating glove box. The jar was then sealed with a rubber O-ring and an air sensitive clamp before being transferred out of the glove box and exposed to air.

#### **2.2.1.1 Ball Milling of Light Metal Hydrides**

Slightly different milling conditions have been employed for the milling of magnesium hydride and lithium hydride. Nevertheless the same 40:1 ball-to-powder ratio was used.

Typically, 1 gram of  $\text{MgH}_2$  (Aldrich, hydrogen-storage grade,  $\geq 96.5\%$ ) was mechanically milled for 5 hours at 450 rpm, using 10 stainless steel balls. A 5 minute interval for every 5 minutes of milling was used.<sup>8</sup> By contrast, 1 gram of  $\text{LiH}$  (Sigma, 95%) was typically ball milled at 450 rpm for 4 hours using 10 stainless steel grinding balls: a rest time of 1 minute per every 15 minutes of ball milling was used.<sup>9</sup>

Henceforth, the ball milled hydrides will be referred to as m- $\text{MgH}_2$  and m- $\text{LiH}$ , whereas the bulk materials will be named as b- $\text{MgH}_2$  and b- $\text{LiH}$ .

#### **2.2.1.2 Ball Milling of Light Metal Hydroxides**

All light metal hydroxides were mechanically milled using the same conditions, based on those reported by Zhu *et al.*<sup>10</sup> However, a 40:1 ball-to-powder ratio was used with respect to the 120:1 used by Zhu.

The as-received light metal hydroxides used were:

- $\text{Mg}(\text{OH})_2$ , Sigma-Aldrich, 95%
- $\text{LiOH}$ , Sigma-Aldrich, 98%
- $\text{LiOH}\cdot\text{H}_2\text{O}$ , Sigma-Aldrich,  $\geq 98\%$

Typically, 1 gram of light metal hydroxide was ball milled for 5 hours at 500 rpm, using 10 stainless steel balls. A 5 minute interval for every 5 minutes of milling was employed.

From this point forward, the mechanically milled hydroxides will be referred to as m- $\text{Mg}(\text{OH})_2$ , m- $\text{LiOH}$  and m- $\text{LiOH}\cdot\text{H}_2\text{O}$ . The bulk materials will be referred to as b- $\text{Mg}(\text{OH})_2$ , b- $\text{LiOH}$  and b- $\text{LiOH}\cdot\text{H}_2\text{O}$ .

## 2.2.2 Synthesis of Nanostructured Light Metal Hydroxides

Different synthetic routes have been employed for yielding nanostructure magnesium hydroxide and lithium hydroxide, both anhydrous and monohydrate. The novel procedures for obtaining these nanostructured light metal hydroxides are discussed below and in subsequent chapters.

$\text{Mg}(\text{OH})_2$  has been synthesised exploiting the synergistic effect of microwave irradiation and hydrothermal treatment, whereas  $\text{LiOH}$  and  $\text{LiOH}\cdot\text{H}_2\text{O}$  have been prepared reacting lithium metal with ionised water inside a Schlenk line apparatus working under dynamic vacuum.

Henceforth, the synthesised nanostructured hydroxides will be referred to as n- $\text{Mg}(\text{OH})_2$ , n- $\text{LiOH}$  and n- $\text{LiOH}\cdot\text{H}_2\text{O}$ .

### 2.2.2.1 Microwave Synthesis of Nanostructured Magnesium Hydroxide

It is widely known that nanostructured  $\text{Mg}(\text{OH})_2$  can be easily synthesised via hydrothermal, solvothermal treatment or wet precipitation methods.<sup>11,12,13</sup> These syntheses require relatively long times of 12 hours or more and the use of surfactants as templating agents.

Nevertheless, the use of microwaves (MW) has gained considerable attention in solid state as well as solvent-based chemistry.<sup>14,15</sup> In fact, using MW heating allows reaction times to

be dramatically decreased from days to even a matter of minutes when compared to conventional heating approaches.

Microwaves belong to the part of the electromagnetic spectrum between radiowave and infrared frequencies (0.3-300 GHz), corresponding to a wavelength range of 1mm – 1m (Figure 2-3).

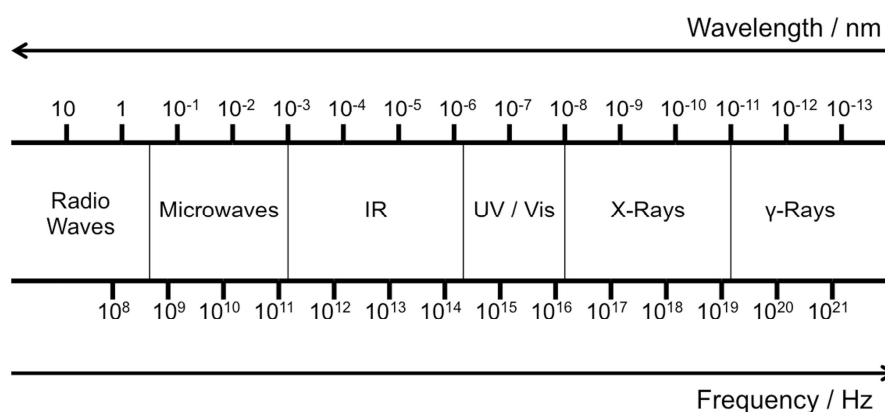


**Figure 2-3: The electromagnetic spectrum.**

A large part of this spectrum is employed for radar technologies as well as telecommunication applications, and only the 900-2450 MHz range is used for heating purposes. Common domestic microwave ovens (DMOs) work at a frequency of 2.45 GHz to avoid interferences with any wireless networks, cellular phones or telecommunication devices. Since not all materials interact with microwaves at that frequency, a susceptor such as silicon carbide or graphite may be used to aid coupling.

Microwaves usually interact with materials in three main ways: reflection, transmission or absorption.<sup>16</sup> Insulating materials transmit microwaves and therefore no heat will be generated and they are usually employed as reaction vessels (i.e. quartz, Teflon, ceramics). If the irradiated sample is a conducting, semi-conducting, ionically conducting or dielectric material, it will couple with microwaves, which will be absorbed and heat will be generated. There are two microwave absorption mechanisms: ionic conduction and dielectric heating (dipole polarisation in liquids).<sup>17</sup>

In liquids, in terms of ionic conduction, heating is produced through resistance to an electric current generated by an oscillating electromagnetic field: the molecules oscillate under the influence of the field colliding with the neighbouring particles creating heat.

In the phenomenon of dipole polarization in liquids, molecules with electrical dipole moments are irradiated with microwaves, they continuously rotate in the attempt to realign themselves with the electromagnetic oscillating applied field. The molecules will change their directions as the field alternates, resulting in collisions with other molecules leading to the generation of kinetic and thermal energy.<sup>17</sup> It is important to remember that the frequency of the oscillating field has to be carefully chosen to allow coupling to the microwave frequency: a frequency of 2.45 GHz is suitable for inorganic synthetic chemistry.<sup>15</sup>

In solid state MW heating, dielectric heating results from the difference in electronegativity values of individual atoms, ultimately resulting in a permanent electric dipole within the molecule, formed by charge separation. The dielectric heating leads to the dissipation of thermal energy which is the driving force of the solid state reaction. The dielectric constant describes the dielectric properties of a material and comprises two terms  $\epsilon'$  and  $\epsilon''$  (Equation 2-1).<sup>18</sup>

$$\epsilon^* = \epsilon' + j\epsilon'' \quad (2-1)$$

Where  $\epsilon'$  is the dielectric constant, which describes the capability of the material to be polarized by the electric field, whereas  $\epsilon''$  is the dielectric loss (Equation 2-2), that indicates the efficiency with which the electromagnetic radiation is converted into heat.  $\epsilon''$  must be taken into account as it directly relates to the electrical conductivity ( $\sigma$ ) of the material (Equation 2-2).

$$\epsilon'' = \frac{\sigma}{\epsilon_0 f} \quad (2-2)$$

Further, Equation 2-3 gives the ability of a solid material to convert electromagnetic radiation to heat at a given frequency.

$$\text{Tan}\delta = \epsilon''/\epsilon' \quad (2-3)$$

Therefore,  $\text{tan}\delta$  is the loss factor describing the ability of the material to absorb MW and dissipate them as energy at a given frequency and temperature.<sup>19</sup> Ultimately, the coupling of materials with microwaves depends on the dielectric constant and thermal properties of the materials, which are related to the chemical and physical composition as well as their conductivity.

In terms of MW preparation of nanostructured  $\text{Mg}(\text{OH})_2$ , great progress has been made over the past few years. According to the paper published in 2012 by Al-Hazmi *et al.*, the rapid growth of  $\text{Mg}(\text{OH})_2$  nanosheet has been proved feasible in 30 minutes starting from  $\text{MgCl}_2$ , urea and NaOH using a multimode cavity microwave reactor.<sup>20</sup> However, Al-Gaashani *et al* reported the first MW-assisted additive-free synthesis of a mixture of nanosheets and nanoparticles of  $\text{Mg}(\text{OH})_2$  starting from Mg metal during the same year.<sup>21</sup>

The novel synthetic route for obtaining nanostructured  $\text{Mg}(\text{OH})_2$  used in the present study is based on a facile route exploiting MW heating coupled with hydrothermal treatment.

Hydrothermal (HT) techniques are commonly used for the synthesis of new crystalline materials and they are based on the reaction of bulk reagents inside a sealed aqueous environment at appropriate temperature and pressure. The pressure range is 1-100 atm whilst the temperature range is usually 373-1273 K, however a subcritical temperature range of 373-513 K is typically used in common industrial and laboratory operations<sup>22</sup>. Typically these reactions usually occur at lower temperature with respect to traditional solid state reactions and they are conducted inside high-pressure sealed autoclaves.<sup>23,24</sup> The reagents are usually a powder and water, which are placed inside a Teflon-lined vessel inside a stainless steel autoclave and heated to a temperature above their boiling point. A typical HT autoclave and its cross section is presented in Figure 2-4.<sup>25</sup>

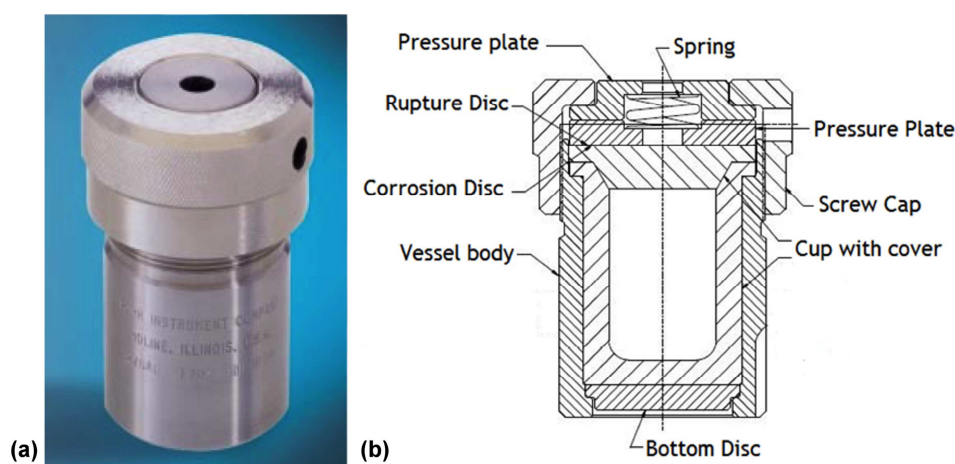


**Figure 2-4: Typical autoclave used for hydrothermal synthesis. Figure (a) shows the full set-up, whilst Figure (b) shows the cross section of the autoclave. Adapted from Reference 24.**

Nevertheless, for safety reasons, there are limitations in the amount of solvent that can be used as well as the temperature to be reached. In fact, it is very important not to over-fill the autoclave as it could result in both an expansion of the volume of the solution and an

escalation of pressure, which increases exponentially. Usually, the volume of solvent must not exceed 2/3 of the total volume of the Teflon-lined vessel. It is also important to consider the temperature limits that the vessel can reach: these are usually 523 K for the most common vessels and 548 K for high-strength ones. Moreover, the materials used during the experiments must be carefully selected. The equipment may be damaged or ruptured if the reaction is highly exothermic or if the products or by-products are corrosive or unstable.

As already mentioned, a new MW-HT synthetic procedure has been used for the preparation of nanostructured  $\text{Mg}(\text{OH})_2$ . As shown in Figure 2-5, the reaction setup comprises of a Teflon-lined vessel sealed with a cap and a Teflon O-ring.<sup>25,26</sup> The autoclave body and screw cap are made from a high strength, insulator polymer to prevent overheating. A safety pressure release valve operates in the event of an overpressure inside the vessel.<sup>27</sup> These autoclaves can be heated to a temperature of 523 K and can reach a pressure limit of 1200 psi.

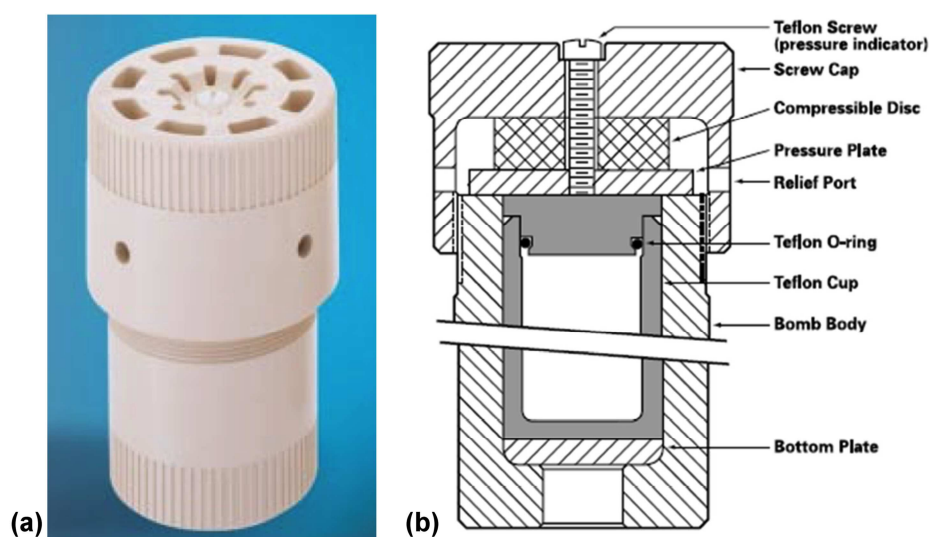


**Figure 2-5: Microwave autoclave used for the synthesis of  $n\text{-Mg}(\text{OH})_2$ . Figure (a) shows the full set-up, while Figure (b) shows the cross section of the autoclave. Adapted from Reference 24.**

Typical reaction conditions for the synthesis of  $\text{Mg}(\text{OH})_2$  nanoplates are described below and will be further specified in Chapter 3.

A certain amount of magnesium oxide was placed inside a Teflon-lined autoclave for microwave synthesis, together with deionised water. The MW autoclave is heated for a total of 4 minutes inside a domestic microwave oven. It is important to allow the autoclave to cool and to ensure that it is not over-filled: rapid pressure rises during heating can lead

to damage of the instrumentation. The rupture of the vessel and the melting of the o-ring and the vessel itself may occur. The product was washed and centrifuged with H<sub>2</sub>O three times. The white precipitate was collected and dried in air overnight.<sup>28</sup> The reaction yields single phase hydroxide. The preparation of nanostructured Mg(OD)<sub>2</sub> employed in the *in-situ* powder neutron experiments (Chapter 4) was successfully carried out following the same synthetic route. The morphology is retained when working with deuterated reagents.

#### **2.2.2.2 Selective Synthesis of Nanostructured Lithium Hydroxide**

The selective synthesis of nanostructured lithium hydroxide was performed using Schlenk apparatus working under dynamic vacuum. This reaction setup, outlined in Figure 2-6, is commonly used to manipulate air and moisture sensitive as well as pyrophoric materials.<sup>29,30</sup> The core of the Schlenk line consists of a two-cross braced manifold with multiple outlets (typically 4 or 6): one end is connected to a source of inert gas (in the present study argon was used) and the other end is connected to a vacuum pump. A two-way valve between gas and vacuum lines is present to allow choosing between vacuum and inert gas flow during the experiment. The excess of argon delivered in the line is vented through a mineral oil bubbler, which also acts as a barrier between the external atmosphere and the internal inert atmosphere inside the line. Also, volatile reaction products and solvent vapours are prevented entry to the vacuum pump through a system of two consecutive liquid nitrogen cooled traps, condensing the gases. Moreover, great attention must be paid to the condensed liquids inside the trap. In fact, if a reasonable amount of air enters the line, liquid oxygen can condense and an explosion may occur as a result of the reaction between oxygen and any compound already present in the trap. Schlenk glassware is similar to common glassware, with the addition of an extra side arm with a tap which is connected to the Schlenk line via PVC connections securely tightened with o-rings. To prevent air and oxygen contaminations and ensure air-tight seals, all joints and taps have to be properly greased: a thin layer of high vacuum grease must be applied on the male joint and then inserted into the neck of the female joint and gently rotated so that the grease is evenly distributed.

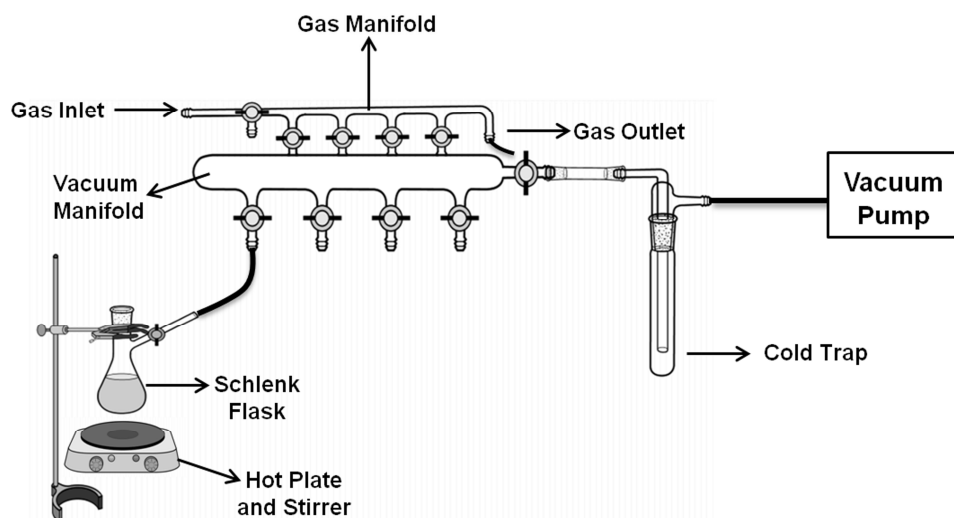


**Figure 2-6: Schematic of a typical Schlenk apparatus.**

For the synthetic procedure to prepare nanostructured LiOH, lithium metal ribbon was carefully cut into small chips inside an argon filled recirculating glove box and put inside a glass vial, which was sealed with parafilm prior to transfer from the glove box. The metal was then quickly transferred inside a Schlenk flask and dissolved in deionised water, minimising the exposure of the lithium metal chips to moisture and air. Once the metal was completely dissolved, the flask was connected to the Schlenk apparatus and the evaporation process started. By carefully tuning the reaction conditions it was possible to synthesise anhydrous LiOH and the monohydrate selectively, exploiting the well-known vacuum evaporation and thermal vacuum evaporation processes.<sup>31,32</sup>

Working in a high vacuum environment at room temperature allows evaporation of only the solvent water, yielding lithium hydroxide monohydrate. Conducting the evaporation process at higher temperature allows to fully dehydrate the LiOH forming in solution during the first step of the reaction, leading to the formation of the anhydrous hydroxide. Specifically, to obtain LiOH, the process was conducted by immersing the flask in an oil bath heated to 343 K. For the synthesis of LiOH·H<sub>2</sub>O, vacuum evaporation was conducted at room temperature. Typical reaction conditions for the synthesis of LiOH and LiOH·H<sub>2</sub>O will be further specified in Chapter 5.

## 2.3 Characterisation Techniques

### 2.3.1 Powder X-Ray Diffraction (PXD)

Powder X-ray diffraction (PXD) is a fundamental technique for both qualitative and quantitative analysis of crystalline solid materials.<sup>33</sup> For this reason PXD was used as the main method of characterisation during this project as it can give information about the phase(s) present in a mixture as well as information about its quantitative phase composition.

The diffraction phenomenon is based on the fact that the wavelength of X-rays (1 Å) is of the same order of magnitude as the interatomic distances (*ca.* 0.5-2.5 Å). Therefore, a crystal behaves as a 3-D grating to an incident beam of X-rays and the resulting diffraction pattern can be used to determine the crystal structure of a material together with its composition.

Diffraction is usually explained using Bragg's Law (Equation 2-4).<sup>34,35</sup>

$$n\lambda = 2d\sin\theta \quad (2-4)$$

Where  $\lambda$  is the wavelength of the incident beam,  $d$  is the perpendicular distance between lattice planes and  $\theta$ , known as Bragg angle, is the angle of incidence. The  $n$  parameter is an integer number that represents the order of the reflection: when  $n = 1$  the reflections are called first order, when  $n = 2$  they are called second order and so on.

As shown in Figure 2-7, two parallel X-rays beam *A* and *B* with a certain wavelength  $\lambda$  and an incidence angle  $\theta$  are 'reflected' by adjacent crystal planes.

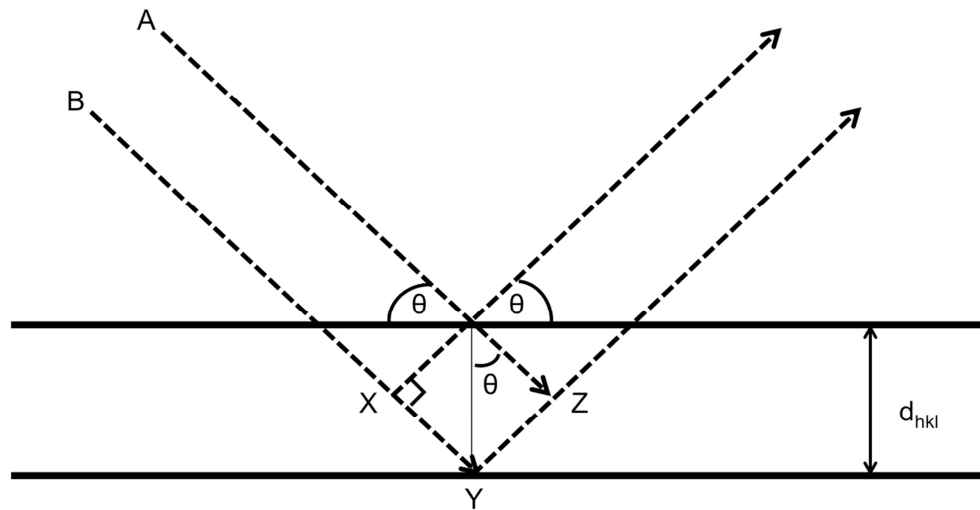


**Figure 2-7: Schematic of diffraction of a crystal used for deriving Bragg's law.**

In order for constructive interference to occur and X-rays beams to be in phase,  $n$  must be an integer number corresponding to an integer number of wavelengths. Beam  $B$  must travel an extra distance  $XYZ$  with respect to beam  $A$ : this is related to the interplanar spacing  $d_{hkl}$  by the relation expressed in Equation 2-5.

$$XYZ = 2d \sin \theta \quad (2-5)$$

However, as previously stated, the additional distance  $XYZ$  covered by beam  $B$  must be an integer number of wavelength for the beam to be in phase (Equation 2-6).

$$XYZ = n\lambda \quad (2-6)$$

The combination of Equations 2-5 and 2-6 yields Bragg's law.

In the case of powdered materials, the sample can be considered as a large number of small randomly oriented crystallites. However, if irregularities in the powder diffraction pattern are noted, these may be due to the preferred orientation of the crystallites, which can result in the increase of the intensities of some peaks attributed to a particular direction.

In a crystal, the unit cell represents the simplest repeating unit of the crystal structure: it has the full symmetry of the crystal and it continuously repeats in all directions. The common way to describe it is by defining symmetry, shape and size, where  $a$ ,  $b$  and  $c$  are the lengths and  $\alpha$ ,  $\beta$  and  $\gamma$  are the angles of the unit cell (Figure 2-8).

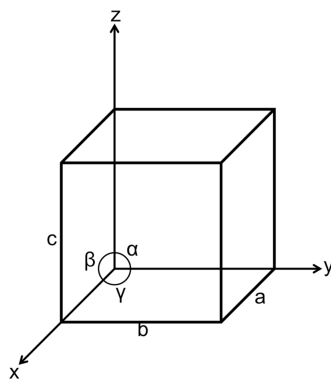


Figure 2-8: definition of axis, unit cell dimensions and angles for a general unit cell<sup>36</sup>.

A summary of all the possible unit cell geometries (crystal systems) and respective symmetry elements is given in Table 2-1.

Table 2-1: Summary of the seven crystal systems and respective symmetry elements<sup>36</sup>.

Crystal system	Unit Cell Parameters	Bravais Lattices	Point Groups
Triclinic	$\alpha \neq \beta \neq \gamma \neq 90^\circ$ $a \neq b \neq c$	<i>P</i>	1, -1
Monoclinic	$\alpha = \gamma = 90^\circ ; \beta \neq 90^\circ$ $a \neq b \neq c$	<i>P, C</i>	2, <i>m</i> , 2/ <i>m</i>
Orthorombic	$\alpha = \beta = \gamma = 90^\circ$ $a \neq b \neq c$	<i>P, C, I, F</i>	222, <i>mm</i> 2, <i>mmm</i>
Tetragonal	$\alpha = \beta = \gamma = 90^\circ$ $a = b \neq c$	<i>P, I</i>	4, -4, 4/ <i>m</i> , 422, 4 <i>mm</i> , -42 <i>m</i> , 4/ <i>mmm</i>
Trigonal	$\alpha = \beta = \gamma \neq 90^\circ$ $a = b = c$	<i>R</i>	3, -3, 32, 3 <i>m</i> , -3 <i>m</i>
Hexagonal	$\alpha = \beta = 90^\circ ; \gamma = 120^\circ$ $a = b \neq c$	<i>P</i>	6, -6, 6/ <i>m</i> , 622, 6 <i>mm</i> , -6 <i>m</i> 2, 6/ <i>mmm</i>
Cubic	$\alpha = \beta = \gamma = 90^\circ$ $a = b = c$	<i>P, I, F</i>	23, 3 <i>m</i> , 432, -43 <i>m</i> , <i>m</i> 3 <i>m</i>

The orientation of the crystal planes can be defined by the Miller indices (*hkl*) which indicate the reciprocal values of the positions where the plane intersects the *a*, *b* and *c* axes respectively. The Miller index values (*hkl*) can be positive, negative or null. The value of  $d_{hkl}$  can be determined for each of the seven crystal systems and the equations used are presented in Table 2-2. The equations for calculating the interplanar distances can be combined with Bragg's law to determine the unit cell dimensions as part of the indexing process.

**Table 2-2: Equations for calculating d-spacing in the different crystal systems.**

Crystal system	Expression for $d_{hkl}$
Triclinic	$\frac{1}{d_{hkl}^2} = \frac{1}{V^2} [h^2 b^2 c^2 \sin^2 \alpha + k^2 a^2 c^2 \sin^2 \beta + l^2 a^2 b^2 \sin^2 \gamma + 2hkabc^2 (\cos \alpha \cos \beta - \cos \gamma) + 2kla^2 bc (\cos \beta \cos \gamma - \cos \alpha) + 2hlab^2 c (\cos \alpha \cos \gamma - \cos \beta)]$ <p>where</p> $V = abc(1 - \cos^2 \alpha - \cos^2 \beta - \cos^2 \gamma + 2 \cos \alpha \cos \beta \cos \gamma)^{1/2}$
Monoclinic	$\frac{1}{d_{hkl}^2} = \frac{1}{\sin^2 \beta} \left( \frac{h^2}{a^2} + \frac{k^2 \sin^2 \beta}{b^2} + \frac{l^2}{c^2} - \frac{2hl \cos \beta}{ac} \right)$
Orthorhombic	$\frac{1}{d_{hkl}^2} = \frac{h^2}{a^2} + \frac{k^2}{b^2} + \frac{l^2}{c^2}$
Tetragonal	$\frac{1}{d_{hkl}^2} = \frac{h^2 + k^2}{a^2} + \frac{l^2}{c^2}$
Hexagonal	$\frac{1}{d_{hkl}^2} = \frac{4}{3} \left( \frac{h^2 + hk + k^2}{a^2} \right) + \frac{l^2}{c^2}$
Cubic	$\frac{1}{d_{hkl}^2} = \frac{h^2 + k^2 + l^2}{a^2}$

Finally, it is important to note that X-rays are scattered by electrons rather than by atomic nuclei and the active scattering centres are given by the electron density distributed in the crystal lattice. Therefore, how well an atom or a material diffracts depends upon the number of electrons present. Atoms with a greater number of electrons (with higher atomic number, heavier atoms) will scatter X-rays more effectively, resulting in a greater intensity of the observed diffraction peaks. On the other hand, materials containing lighter elements such as hydrogen or lithium (the atomic numbers are 1 and 3 respectively) will not scatter strongly when in presence of heavier atoms.

### 2.3.1.1 PXD Instrumentation and Sample Preparation

For data collection a Bruker d8 Advance diffractometer working with a VÅNTEC detector and a PANalytical X'Pert PRO MPD diffractometer equipped with an X'Celerator solid state detector were used. In particular, air sensitive samples were analysed using the d8 instrument, whilst measurements on non-air sensitive materials were performed with the X'Pert diffractometer. All samples were ground to obtain a homogeneous powder as well as to ensure random distribution and avoid preferred orientation of the crystallites. Both instruments use Cu  $K_{\alpha 1}$  radiation ( $\lambda = 1.54056 \text{ \AA}$ ) and an X-ray tube operating at a power of 40 kV and 40 mA. It is important to note that the preparation method of a sample could also affect the diffraction pattern characteristics.

The preparation of air sensitive samples was performed inside an Ar- or N<sub>2</sub>-filled recirculating glove box. The ground samples were loaded into either 0.5 or 0.7 mm diameter glass capillaries to approximately half the height of the capillary (*ca.* 2.5-3 cm). The capillary is sealed with vacuum grease prior to transfer from the glove box and subsequently, flame sealed in order to prevent exposure to air and moisture. The sealed capillaries were placed on the goniometer with wax and aligned rotationally and translationally on an aluminium capillary holder with the help of an optical microscope. This allows the capillary to be perfectly centred with the X-ray beam. Typically, diffraction patterns were collected over a  $2\theta$  range of 5-85° with a step size of 0.0167  $2\theta^\circ$  for one hour for phase identification and overnight for structural refinement purposes.

The d8 diffractometer works in a transmission configuration with Debye-Scherrer geometry (Figure 2-9), where the sample diffracts the X-ray beam in accordance to Bragg's law and produces cones of diffracted beam which reach the detector. To achieve better beam collimation as well as minimise background scattering, a monochromator and divergence slit of 2 mm are employed.

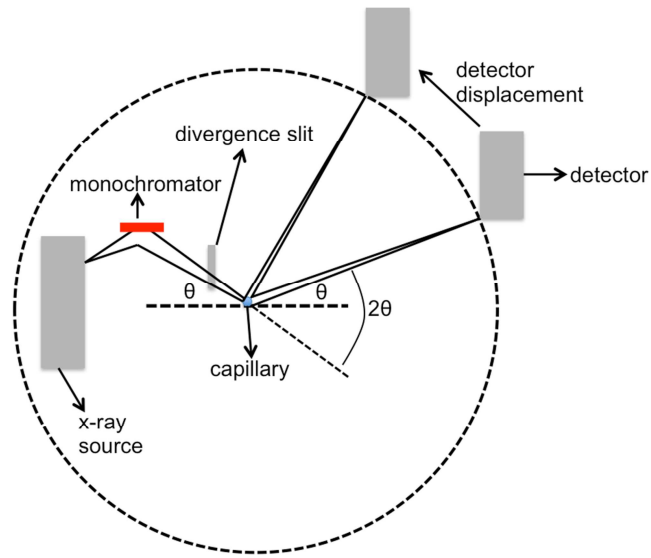


**Figure 2-9: Debye-Scherrer transmission geometry.**

The X'Pert diffractometer works in a reflection configuration in Bragg-Brentano geometry (Figure 2-10). In this type of configuration the X-ray beam is produced by a stationary source and collected by a moving detector. The beam penetrates to a certain depth in the sample and is then diffracted. In particular the sample holder is tilted on an axis by an angle  $\theta$  while the detector is rotated by an angle of  $2\theta$ . The beam is collimated using a 10 mm mask, Soller slits, a  $\frac{1}{2}^\circ$  divergence slit and a  $\frac{1}{2}^\circ$  anti-scatter slit.

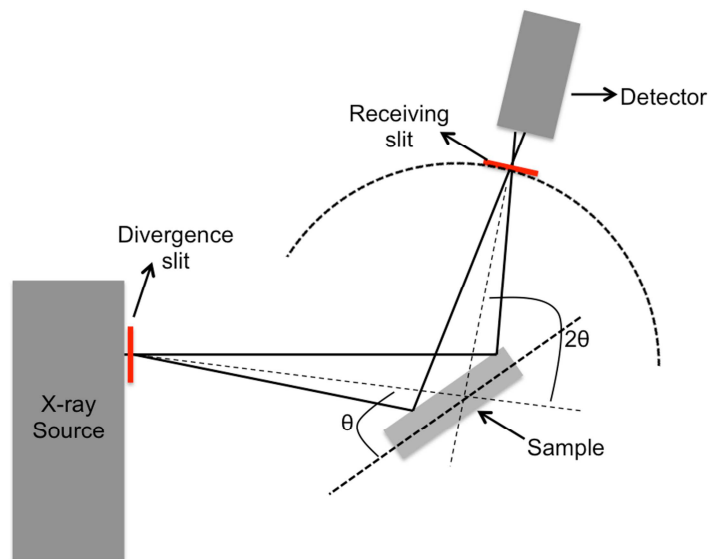


**Figure 2-10: Bragg-Brentano reflection geometry.**

Different sample stages could be used, however in this work only the bracket stage has been employed specifically for the analysis of non-sensitive materials. In this type of stage the sample holder is constituted by a glass slide with an indent. The samples were positioned on a glass slide and gentle pressure applied with the help of a glass slide, resulting in a homogeneously flat powder surface. The holder is then positioned on the goniometer where the collimated beam will irradiate the sample. Standard runs were conducted over a  $2\theta$  range of  $5-85^\circ$  with a step size of  $0.0167^\circ$  and data were collected approximately for 30 minutes for phase identification and three hours when structural refinements were performed.

### **2.3.1.2 Data Analysis**

The Bruker d8 and X'Pert PRO diffractometers produce different data output files; the d8 produces raw data files (.raw) while the X'Pert produces diffraction patterns with the characteristic PANalytical format (.xrdml). The latter can be easily converted into a raw file using the PowDLL convertor software.<sup>37</sup>

PowderCell software was used to visualise the collected raw experimental data.<sup>38</sup> The collected powder patterns were subsequently compared with the appropriate reference ones generated from the ICSD database.<sup>39</sup> Reference patterns present in the ICDD database<sup>40</sup> were consulted when working with the PANalytical HighScore Plus software.

Rietveld refinement against the PXD data were performed using the General Structure Analysis System (GSAS)<sup>41</sup> with the EXPGUI interface<sup>42</sup> as explained in Section 2.3.3.

### **2.3.2 In-Situ Powder Neutron Diffraction (PND)**

Powder Neutron Diffraction (PND) is a powerful tool, although experimentally more expensive when compared to powder X-ray diffraction. Yet, the information obtained using PND is complimentary to that obtained using PXD. As previously mentioned, X-rays interact with the electron cloud of the atoms, making this technique unsuitable for the study of light elements. On the contrary, neutrons interact with the nuclei of the elements. In this sense, powder neutron diffraction becomes a very useful probe for the study of compounds containing light elements, such as hydrogen and hydrogen storage materials. As widely known, hydrogen can exist as three isotopes: protium ( $^1\text{H}$ ), deuterium ( $^2\text{H}$ ) and tritium ( $^3\text{H}$ ). Both hydrogen and deuterium scatter neutrons well. The scattering power is

not strongly affected by an atom mass (atomic number  $z$ ) or the scattering angle  $\theta$ . Although PND is mostly used for crystallographic purposes (solving the structure of crystalline solids or monitoring phase transitions), this technique can also be used for studying reactions *in-situ*.

During this project, PND has been used as an *in-situ* technique to investigate the mechanism of hydrogen release of ‘modular’ hydrogen release systems. *In-situ* experiments were conducted at the ISIS facility, Rutherford Appleton Laboratory in Oxfordshire, using the Polaris instrument. The results obtained are presented and discussed in detail in Chapter 4.

### **2.3.2.1 The Polaris instrument at Rutherford Appleton Laboratory (RAL)**

The neutron source at the ISIS facility of the Rutherford Appleton Laboratory in Oxfordshire was used for PND data collection. This is a spallation (pulsed) neutron source. At such sources neutrons are produced by bombarding a heavy metal target (tungsten at the ISIS facility) with highly energetic particles. The accelerator consists of an injector and a synchrotron. Firstly, hydrogen gas together with hot caesium vapour is fed around a ring and ionised to  $H^-$ . Discrete bunches of  $H^-$  ions are then focussed and accelerated by a Radio Frequency Quadrupole (RFQ) accelerator working at 665 keV and 202.5 MHz. Subsequently, ions are extracted from the ion source in long 200  $\mu s$  pulses and their acceleration continues in the synchrotron, a ring of powerful magnets that bend and focus the beam into a circle. The  $H^-$  ions are stripped of any electrons by a thin alumina foil resulting in a beam of only protons. Once a sufficient amount of protons have been collected, radio frequency electric fields accelerate them. The protons are then separated into two different bunches: each bunch is extracted from the synchrotron by a ‘kicker’ magnet and collides with the tungsten target. The bombardment of the heavy metal target leads to the emission of neutrons from the nuclei of the target atoms. Typically, each proton colliding with the target produces *ca.* 15 neutrons. This process is called spallation and gives a highly intense neutron pulse with modest heat production from the target. Neutrons are then slowed by hydrogenous moderators around the target and redirected to different stations for performing neutron diffraction experiments.<sup>43,44</sup>

In Time-of-Flight (ToF) neutron diffraction, the sample is irradiated with a pulsed beam of neutrons of different wavelengths. Neutrons travel into the material and they are detected as they emerge. In this kind of experiments, scattered neutrons are recorded in banks of

detectors with a fixed  $2\theta$  detection angle together with the time at which they arrive at the detector. The d-spacing and the wavelength of the neutrons are the variables. To calculate the wavelengths (Equation 2-7), the linear relationship between ToF and d-spacing is employed and it is derived from the De Broglie relationship (Equation 2-8) and Bragg's Law (Equation 2-4).

$$\lambda = \frac{h}{m_n v_n} \quad (2-7)$$

$$\lambda = \frac{h}{m_n v_n} = 2d \sin \theta \quad (2-8)$$

Where  $h$  is the Plank constant,  $m_n$  is the neutron mass and  $v_n$  is the neutron velocity.

Neutrons travel a known distance (primary flight path,  $L_1$ ) from the source to the sample and subsequently from the sample to the fixed detectors ( $L_2$ ) at an angle of  $2\theta$  for a total distance  $L$  ( $L_1 + L_2$ ). These correspond to times of flight  $t_1$  and  $t_2$ , with a total time of flight  $t$  given by the sum of  $t_1$  and  $t_2$ . Hence, Equation 2-6 can be rewritten with  $L_1$ ,  $L_2$ ,  $t_1$  and  $t_2$  to give Equation 2-10 through Equation 2-9.

$$\frac{h}{m_n} \frac{(t_1 + t_2)}{(L_1 + L_2)} = 2d \sin \theta = \lambda \quad (2-9)$$

And so

$$t = 2dL \frac{m_n}{h} \sin \theta \quad (2-10)$$

Hence, time of flight is directly proportional to wavelength and the values of  $\lambda$  and  $\theta$  can be used to obtain the d-spacing values using Bragg's law.<sup>45</sup>

The Polaris instrument at ISIS is a high intensity, medium resolution powder diffractometer which was recently rebuilt after a major upgrade and became operational again in May 2012.<sup>45,44</sup> A schematic of the upgraded instrument is presented in Figure 2-1. The upgraded Polaris has a primary flight path of 14 m and features a large vacuum vessel (*ca.* 20.000 l) inside which the detector banks are mounted. The instrument consists of 6 detector banks: bank 1 (very low angle,  $2\theta$  6-14), bank 2 (low angle,  $2\theta$  19-34), bank 3 (low angle,  $2\theta$  40-67), bank 4 (90 degrees,  $2\theta$  75-113), bank 5 (back scattering,  $2\theta$  135-143) and bank 6 (back scattering,  $2\theta$  146-168). The instrument allows data to be collected in rapid time with short counting rates and with small amounts of sample. This is a very

important feature especially when phase transitions or chemical reactions are to be monitored and diffractions patterns collected under non-ambient conditions (*i.e.* while the sample is heated inside a furnace or cooled inside a cryostat).

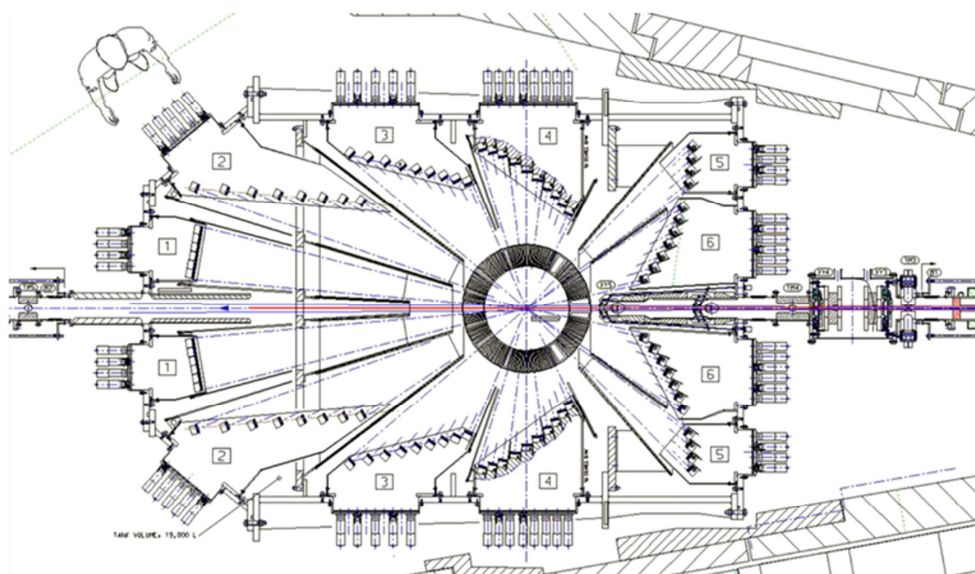


**Figure 2-11: Schematic of Polaris diffractometer.<sup>44</sup> The numbers indicate the different detector banks.**

### 2.3.2.2 Sample Preparation and Data Collection on Polaris

The preparation of the sample for PND analysis was performed inside a recirculating argon-filled glove box at the ISIS facility. Stoichiometric mixtures of  $\text{Mg}(\text{OD})_2$  and  $\text{LiD}$  were ground together using agate mortar and pestle. The mixture was then loaded into a single glass quartz tube with an outer diameter of *ca.* 10 mm, a wall thickness of 1 mm and a total length of approximately 300 mm (Figure 2-12). A stainless steel pipe (1.5 mm inner diameter) running down the quartz tube to about 1 cm above the top of the incident neutron beam ensured a flow of argon throughout the whole duration of the experiment. The gas circulated over the top of the sample and flowed up between the steel and quartz tube to the top of the sample stick where can it be redirected to either a mass spectrometer or an exhaust trap together with any evolved gaseous species. This is done through the presence of Swagelok fittings that can also be vacuum tightened to allow the transfer of the sample stick inside and outside of the glove box. Two external thermocouples to be connected to the Polaris furnace are present and they are placed on opposite sides of the quartz tube just above the incident neutron beam to provide homogeneous heating. The height of the beam at Polaris is 40 mm, which is the same height at which the sample is placed at the bottom of the closed tube. The total length of the apparatus is approximately 450 mm. The stick is

then inserted into the furnace in the sample area, the thermocouples connected to the furnace and data collected. The temperature programme and the experimental conditions used during the PND experiments are detailed in Section 4.2.8. All measurements were performed with the help of Dr Ron Smith.



**Figure 2-12: Polaris experiment: (a) sample placed at the bottom of the quartz tube for a total height of ca. 40 mm; (b) full experimental setup single glass quartz tube with inner stainless steel pipe for the flow of argon.**

### 2.3.3 PXD and PND Data Analysis: Rietveld Refinement

The Rietveld method is a very powerful technique for the refinement of structural data in powder diffraction, which was first developed by H. M. Rietveld for constant wavelength neutron diffraction.<sup>46,47</sup> However, it can be utilised using time of flight neutron data and powder X-ray diffraction data. The Rietveld method is a full profile refinement that fits the observed diffraction data to the structural model of the powdered sample:<sup>48</sup> Rietveld realised that even though many individual Bragg reflections overlapped and could not be modelled as single entities, they could be fitted using simple peak shape parameters to calculate the total intensity of a cluster of diffraction peaks. Rietveld refinements can yield detailed crystal structure information together with an accurate quantitative determination of the weight fractions for multi-phase mixtures.

The process of structure refinement begins with a starting model, usually obtained from a similar or isotopic crystal structure. Having a good starting model is essential; the method is one of refinement rather than of structure solution. The next step involves introducing background parameters. They can be either manually set or calculated using a polynomial expression. An accurate determination of Bragg reflection positions is accomplished by varying the lattice parameters and the zero-point error correction (and/or sample

displacement). Subsequently the refinement of the peak shape parameters is performed followed by the variation of atom positions to fit peak intensities. Thermal displacement parameters are subsequently refined, intensity irregularities may be observed and they may be caused by thermal motion of the atoms within the sample. In some cases it may be possible to vary temperature factors anisotropically. A final refinement of peak shape is then performed (together with further background coefficients if needed) to define asymmetry or peak broadening effects. The software can cope with multi-phase samples, preferred orientation, and peak asymmetry to give full structural data as well as to determine weight fractions. Instrumental parameters can be varied depending on the experiment performed. Refinement is a least squares best fit method which minimises the quantity of the function M (Equation 2-11).

$$M = \sum_i w_i (y_i^{obs} - y_i^{calc})^2 \quad (2-11)$$

Where  $w_i$  is a weighting factor given by  $1/y_i^{obs}$ ,  $y_i^{obs}$  is the observed intensity at each step/point  $i$  ( $2\theta$  for PXD) and  $y_i^{calc}$  is the calculated intensity at each step.

For PXD data,  $y_i^{calc}$  values are determined from the  $|F_k|^2$  values calculated from the structural model by summing the calculated contributions from neighbouring Bragg reflections ( $k$ ) plus a background  $b_i$ .

$$y_i^{calc} = s \sum_k L_k |F_k|^2 \Phi(2\theta_i - 2\theta_k) P_k A + y_{bi} \quad (2-12)$$

Where  $s$  is the scale factor,  $L_k$  comprises Lorentz polarisation and multiplicity factors,  $\Phi$  is a reflection profile function,  $F_k$  is the structure factor for the  $k^{\text{th}}$  Bragg reflection,  $P_k$  is the preferred orientation function,  $A$  is the absorption factor and  $y_{bi}$  is the background intensity for the  $i^{\text{th}}$  step. The Lorentz factors depend upon both instrumental (geometry, detector, beam size) and sample factors (sample volume and geometry).

The background intensities can be obtained by three methods: an operator-supplied table of background intensities, a specified background function or an interpolation between operator selected background points. In GSAS the background can be fitted either manually or using one of the available background function. During this thesis either Function 1 (Chebyshev polynomial) or Function 8 (reciprocal interpolation function) have been used. Function 1 is a polynomial of the first type, whilst the reciprocal interpolation Function 8 divides the pattern into equal  $1/T$  segments where  $T$  is the location. The

intervals are concentrated into small d-spacing regions where changes are more likely to arise.

During a refinement, a comparison between intensities of experimental and calculated data is performed at every point. Therefore it is also vital for the construction of the profile to describe the peak shape of the reflections accurately. Usually the peak shape is governed by the instrument and modelled using the pseudo-Voigt function (*pV*, Equation 2-13), which is a combination of Lorentzian and Gaussian functions.

$$pV = \eta L + (1 - \eta)G \quad (2-13)$$

Where *L* and *G* are the Lorentzian and Gaussian contributions to the peak shape respectively and  $\eta$  is the mixing parameter that can be refined as a linear function of  $2\theta$ .

$$\eta = N_A + N_B (2\theta) \quad (2-14)$$

Where  $N_A$  and  $N_B$  are refinable parameters.

The Gaussian and Lorentzian contributions are represented by Equations 2-15 and 2-16 respectively.

$$G_{i,k} = \frac{2\sqrt{\ln 2}}{H_k \sqrt{\pi}} \exp\left(\frac{-4 \ln 2}{H_k^2} (2\theta_i - 2\theta_k)^2\right) \quad (2-15)$$

$$L_{i,k} = \frac{2}{\pi H_k} \left(1 + \frac{4}{H_k^2} (2\theta_i - 2\theta_k)^2\right) \quad (2-16)$$

Where  $2\theta_k$  is the calculated position for the  $k^{\text{th}}$  Bragg reflection corrected for the counter zero-point and  $H_k$  is the Full-Width-at-Half-Maximum (FWHM) of the  $k^{\text{th}}$  Bragg reflection. The full width half maximum (FWHM) factor  $H_k$  is modelled as shown in Equation 2-17 and it is depending on the scattering angle  $2\theta_k$ .

$$H_k^2 = U \tan^2 \theta + V \tan \theta + W \quad (2-17)$$

Where *U*, *V* and *W* are refinable factors and are both sample and instrument dependent. The FWHM value takes into account peak broadening effects related to the size of the crystallites: in fact broadening of Bragg's peaks can be the result of a particle size reduction or the presence of lattice imperfections.<sup>49</sup>

In order to determine whether the ‘best fit’ for a refinement has been achieved and understand whether the proposed model is correct; the agreement between the observed and calculated profiles must be calculated. For this purpose refinement reliability factors are employed principally:  $R_{profile}$  ( $R_p$ ),  $R_{expected}$  ( $R_{exp}$ ) and  $R_{weighted\ profile}$  ( $R_{wp}$ ). These are described as follows.

$$R_{profile} = R_p = \left[ \frac{\sum_i |y_i^{obs} - y_i^{calc}|}{\sum_i y_i^{obs}} \right] \quad (2-18)$$

$$R_{expected} = R_{exp} = \left[ \frac{(N - P + C)}{\sum_i \omega_i (y_i^{obs})^2} \right]^{1/2} \quad (2-19)$$

Where  $R_{exp}$  is defined from statistics of the refinements,  $N$  is the number of observations,  $P$  is the number of varied parameters and  $C$  is the number of constrains.

From a mathematical point of view, the  $R_{weighted\ profile}$  ( $R_{wp}$ ) is the most meaningful and important of the R-factors because the numerator is the residual being minimised in the refinement process (Equation 2-20). This makes  $R_{wp}$  the most appropriate parameter to reflect the quality of the refinement.

$$R_{wp} = 100 \left[ \frac{\sum_i \omega_i [y_i^{obs} - y_i^{calc}]^2}{\sum_i \omega_i [y_i^{obs}]^2} \right]^{1/2} \quad (2-20)$$

The final goodness of the whole fit, minimised during the refinement, is measured with the chi-squared factor ( $\chi^2$ , Equation 2-21).

$$\chi^2 = \left[ \frac{R_{wp}}{R_{exp}} \right]^2 \quad (2-21)$$

In conclusion, for a good fit the  $R_{wp}$  should statistically approach the  $R_{exp}$  factor. The quality of the fit can also be measured using graphical criteria. The observed and calculated patterns can give an immediate idea of the goodness of the fit and at the same time clues on the source of possible problems present while refining. The difference between the calculated and observed profiles is plotted as well and in a good fit this should be as flat as possible.

All Rietveld refinements presented in this work were performed using the Generalised Structure Analysis System (GSAS)<sup>41</sup> with the EXPGUI interface.<sup>42</sup>

### 2.3.4 Simultaneous Thermogravimetric Analysis (STA) Mass Spectrometry (MS)

Thermal analyses study the changes of chemical or physical properties as a function of the temperature. Thermogravimetric analysis (TGA) and differential thermal analysis (DTA) measurements were performed simultaneously in this project. Simultaneous Thermogravimetric Analysis (STA: TG-DTA) was employed to obtain onset temperatures and peak temperatures of hydrogen release of analysed materials. The activation energy of specific events occurring during heating could also be determined with appropriate experimental procedures and data analysis. Mass Spectrometry (MS) was employed in conjunction with thermal analysis in order to identify the gases evolved during thermal treatment.

#### 2.3.4.1 Simultaneous Thermogravimetric Analysis (STA)

STA-MS experiments were performed using a Netzsch STA 409 PC instrument under flowing argon. A schematic of the STA instrumentation is presented in Figure 2-13.

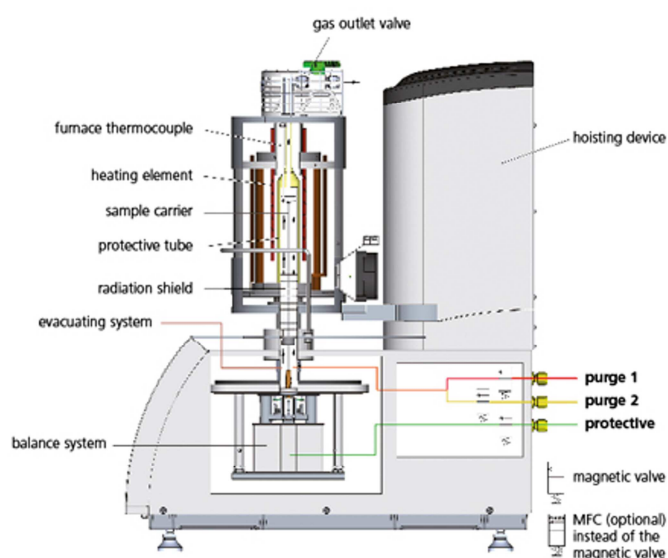
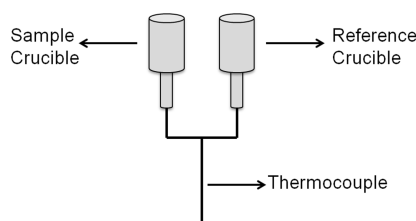


Figure 2-13: Schematic of the Netzsch STA 409 PC.<sup>50</sup>

In a TGA measurement, the mass of a sample is recorded as a function of time and temperature. The output, based on the weight changes observed, can give information on the chemical processes the studied material is subject to.

In DTA the sample is heated against an inert reference material (*i.e.* alumina). The measured parameter is the temperature difference ( $\Delta T$ ) between the sample and the inert reference, with both undergoing the same thermal treatment, as a function of temperature. Figure 2-14 shows the arrangements of both sample and reference crucibles on the sample carrier. As the thermal treatment proceeds, the temperature of both crucibles should be identical unless a thermal event such as decomposition, dehydration, crystallization or a structural phase change occurs in the sample. Through the DTA profile, it is also possible to differentiate between exothermic or an endothermic event, giving important information about the thermal behaviour of the studied material.



**Figure 2-14: Schematic of the sample and reference crucible arrangement on the DTA sample carrier.**

It is more useful to record both DTA and TGA signals simultaneously. This allows categorisation of thermal events and whether they occur with or without an associated weight change.

First, correction files need to be created by heating an empty alumina pan to the target temperature at the desired heating rate. When appropriate, the temperature could be held (*i.e.* for one hour). In a typical experiment, approximately 20-25 mg of sample was loaded into the sample pan inside the apparatus chamber. Initial experiments involved heating from room temperature to 873 K at 5 K min<sup>-1</sup> and holding at that temperature for 1 hour before allow the sample to cool naturally. The relevant data were determined using the Proteus Analysis Software present in the Netzsch TA4\_5 suite. Data could also be exported to be plotted with different software.

TG-DTA experiments were performed to obtain information on the onset and peak temperature of the thermal event occurring during heating and weight loss percentage.

Beyond, data analysis allowed the calculation of activation energy of specific thermal events through the Kissinger method.<sup>51,52</sup> Samples were heated to 773 K using different heating rates ( $\beta$ ) of 2, 5, 10 and 20 K min<sup>-1</sup> respectively and Kissinger plots were obtained applying the mathematic expression given in Equation 2-22:

$$\ln\left(\frac{\beta}{T_m^2}\right) = -\frac{E_a}{RT} \quad (2-22)$$

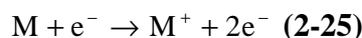
Where  $R$  is the gas constant (8.314 J K<sup>-1</sup> mol<sup>-1</sup>). By plotting the left hand side of Equation 2-22 on the y-axis against  $1/T_m$  on the x-axis and performing a linear fitting on the obtained dataset, it was possible to calculate the activation energy for the desired event. The equation of the linear regression (Equation 2-23) was used to derive the  $E_a$  value from the gradient  $m$  of the calculated equation (Equation 2-24).

$$y = c + m \times x \quad (2-23)$$

$$m = -\frac{E_a}{R} \quad (2-24)$$

#### 2.3.4.2 Mass Spectrometry (MS)

The use of mass spectrometry has been employed in this work to determine the gaseous species evolved during STA experiments. A typical MS analysis consists of four stages. The first process is the ionisation of the sample by an electron source. This causes the sample to lose one or more electrons forming a positive ion (Equation 2-25), where  $M$  is the neutral species present in the sampled gas).



These positive ions are then separated based on their mass-to-charge ratio ( $m/z$ ). The separation is obtained by subjecting them to acceleration as a result of an applied potential. The third stage involves the deflection of the ions by a magnetic field: the lighter the ion the more it is deflected accordingly to Newton's second law of motion (Equation 2-26), which states that the acceleration of a particle is inversely proportional to its mass.

$$f = m \times a \quad (2-26)$$

Where  $f$  is the force,  $m$  is the mass and  $a$  is the acceleration.

In addition, the more positively charged an ion is, the more it will be deflected. At last, the ions are focussed and electrically detected as a function of their  $m/z$  ratio. The signal is amplified, converted and displayed as a mass spectrum.

In this work a Hiden Analytical HPR 20 mass spectrometer was used.<sup>53</sup> This is a quadrupole mass analyser designed for fast transient gas analysis. The quadrupole mass analyser was first developed by Wolfgang Paul (Figure 2-15).<sup>54</sup> It presents four parallel metal rods arranged to form a square. The pairs of rods are connected opposite each other and a radio frequency (RF) voltage is applied. A direct current (DC) potential is then superimposed on the RF voltage. This results in the two opposite rods having an applied potential of  $(U+V\cos(\omega t))$  whilst the other two rods having an equal and opposite applied potential of  $-(U+V\cos(\omega t))$ , where  $U$  is the DC voltage and  $V\cos(\omega t)$  is the RF voltage. The positive ions produced travel along the middle of the rods and the applied voltages affect their trajectory: only ions with the desired mass-to-charge value are stabilised and allowed to the detector whereas other ions will collide with the rods.

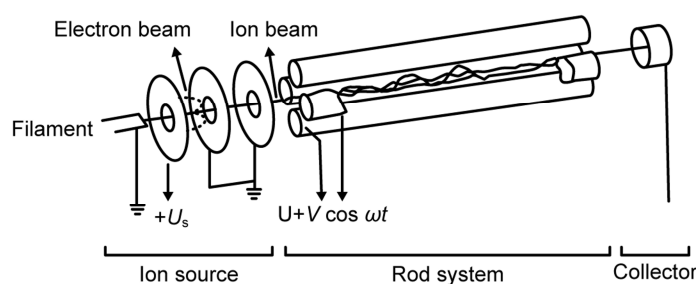


**Figure 2-15: Quadrupole mass analyser developed by W. Paul. Adapted from Reference <sup>54</sup>**

Programmes were set up using the MASsoft Pro software and the detection of specific gases evolved was enabled. Typically, the amount of  $H_2$ ,  $H_2O$ ,  $N_2$  and Ar were monitored. Before every MS experiment, a pre-run of approximately 20-30 minutes was performed to verify the absence of air and moisture and prevent the contact between sample and any non-inert environment.

### **2.3.5 Scanning Electron Microscopy (SEM)**

Scanning electron microscopy (SEM) is a powerful tool for determining the morphology as well as the particle size of both bulk and nanostructured materials. It can be coupled with energy dispersive X-ray spectroscopy (EDX) to obtain additional information about the elemental composition of samples. During this project, SEM was used only for imaging. Since the samples being investigated during this work consisted of lighter elements, the usefulness of EDX would have been minimal and therefore no EDX analysis was performed.

In electron microscopy the visible light source used in optical microscopy is replaced with a high energy incident electron beam.<sup>55,56</sup> The generated electrons can interact with the sample either elastically or inelastically. The former interaction occurs when scattered electrons have the same energy as the incident ones, whilst the latter occurs when the energy of the scattered electrons is different. An elastic collision results in the emission of high energy electrons, known as backscattered electrons. They escape the surface of the sample retaining ca. 60-80 % of their initial energy, reaching the detector with an energy greater than 50 eV.<sup>56</sup> They are used for imaging purposes and diffraction, providing both compositional and topographic information.

However, when the electrons from the incident beam strike the sample; inelastic scattering can yield different types of signals including the emission of secondary electrons, X-rays and Auger electrons (Figure 2-16). In particular, emitted secondary electrons have low energies (on average 3-5 eV). For this reason they can be used for obtaining topographic information with good resolution as they escape within a few nanometres of the sample surface and can be used to mark the position of the beam accurately.

Moreover, when the material is scanned, an inner shell of electrons is ejected by the primary beam, leaving the sample in an excited state. When it relaxes back to the ground state, the sample will emit both Auger electron and X-rays as a result of an electron from an outer shell dropping down to a core level. The Auger electrons and X-rays will be characteristic of the atom they are emitted from and can be employed for the study of the elemental composition of the material by either Auger Electron Spectroscopy (AES) or energy dispersive X-Ray Spectroscopy (EDX).

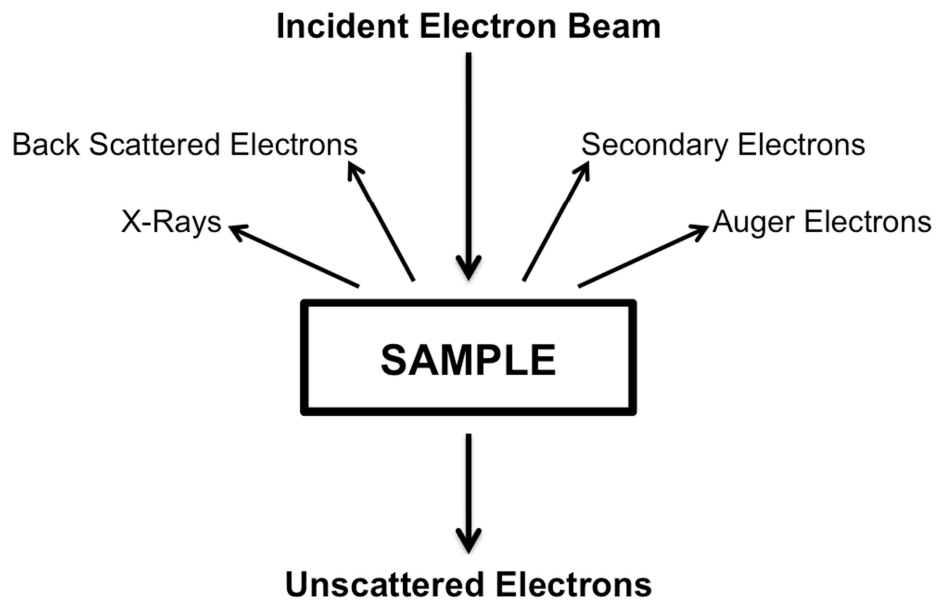


**Figure 2-16: Schematic of possible scattering of electrons from a typical SEM experiment.**

In a common scanning electron microscope, a beam of high energy electrons is emitted by an electron gun. The beam is focused by a condenser lens and travels through a system of magnetic lenses before interacting with the sample. Through the use of scanning coils the focused beam is moved across the surface of the sample, scanning it. The detector then collects the backscattered and secondary electrons, the emitted signals responsible for imaging. The microscope is usually interfaced to a PC, facilitating the viewing and manipulation of the collected images.

The equipment works under high vacuum, in order to avoid oxidation and preserve the filament responsible for the generation of the beam. A high vacuum results also in lower background noise and better image quality.

A schematic of a scanning electron microscope is presented in Figure 2-17.

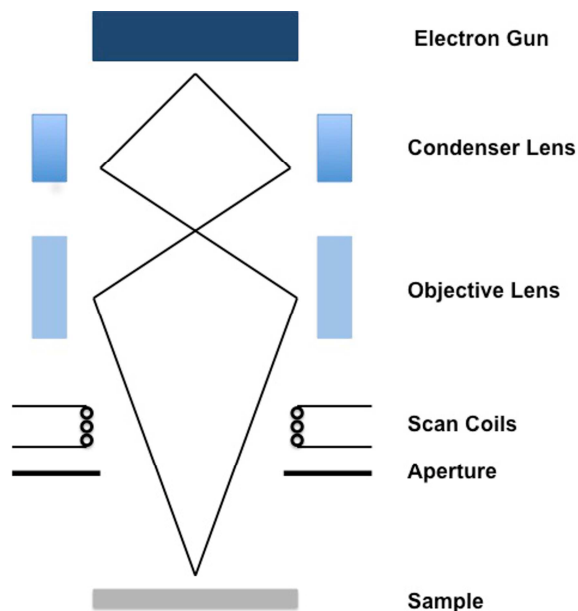


**Figure 2-17: Schematic of a Scanning Electron Microscope.**

### 2.3.5.1 Preparation of samples

In order to collect SEM images, the sample to be analysed is placed onto adhesive carbon tabs fixed to an aluminium stub. Since in this work the analysed materials were often found to charge under the beam, the samples were typically sputter-coated with a 10 nm layer of gold/palladium alloy to achieve better conductivity and increase the quality of the collected images. All manipulations were carried out inside a recirculating glove box under either an argon or nitrogen atmosphere. The samples were put into glass vials and sealed before being transferred out of the glove box to minimise the exposure to air and moisture. The samples were then placed inside the vacuum column of the microscope, which was shut using an air-tight door and evacuated. The measurements were performed using two different scanning electron microscopes.

The images presented in Chapters 3 and 5 were acquired at the Imaging Spectroscopy and Analysis Centre (ISAAC), in the School of Geographical and Earth Sciences (GES) at the University of Glasgow, with the help of Dr Peter Chung. The instrument used was a Carl Zeiss Sigma Variable Pressure Analytical SEM with Oxford Microanalysis using a Schottky thermal field emitter electron source. An accelerating voltage of 15-25 kV and a working distance of typically 5-6 mm were used.

The images presented in Chapter 4 were collected using a Philips XL30 ESEM microscope, operated in high vacuum mode with an applied accelerating voltage of 25 kV and a working distance of 5 mm, suitable for imaging.

## 2.4 References

1. Saffron Scientific Equipment Ltd. <http://www.saffron-uk.com/Products/Omega.aspx> (accessed 6<sup>th</sup> October 2014).
2. mBraun <http://www.mbraun.com/products/glovebox-workstations/labstar-glovebox/> (accessed 6<sup>th</sup> October 2014).
3. IUPAC, *Compendium of Chemical Terminology*. 2nd ed. (the "Gold Book"). Compiled by A. D. McNaught and A. Wilkinson. XML on-line corrected version: <http://goldbook.iupac.org> (2006-) created by M. Nic, J. Jirat, B. Kosata; updates compiled by A. Jenkins. Blackwell Scientific Publications: Oxford, 1997.
4. James, S. L.; Adams, C. J.; Bolm, C.; Braga, D.; Collier, P.; Friscic, T.; Grepioni, F.; Harris, K. D. M.; Hyett, G.; Jones, W.; Krebs, A.; Mack, J.; Maini, L.; Orpen, A. G.; Parkin, I. P.; Shearouse, W. C.; Steed, J. W.; Waddell, D. C., Mechanochemistry: opportunities for new and cleaner synthesis. *Chemical Society reviews* **2012**, *41* (1), 413-447.
5. Huot, J.; Ravnsbæk, D. B.; Zhang, J.; Cuevas, F.; Latroche, M.; Jensen, T. R., Mechanochemical synthesis of hydrogen storage materials. *Progress in Materials Science* **2013**, *58* (1), 30-75.
6. Solsona, P.; Doppiu, S.; Spassov, T.; Suriñach, S.; Baró, M. D., Evolution of amorphous and nanocrystalline phases in mechanically alloyed Mg<sub>1.9</sub>M<sub>0.1</sub>Ni (M=Ti,Zr,V). *Journal of Alloys and Compounds* **2004**, *381* (1–2), 66-71.
7. Retsch <http://www.retsch.com/products/milling/ball-mills/planetary-ball-mill-pm-100/function-features/> (accessed 3<sup>rd</sup> November 2014).
8. Reardon, H. Synthesis, structure and characterisation of novel lightweight energy materials based on group I & II metal compounds. PhD Thesis, University of Glasgow, 2014.
9. J. M. Hanlon, G. B., L. Bravo-Diaz, N. Tapia-Ruiz, B. A. Stobbs, L. MacDonald and D.H. Gregory,, Nanostructured Mg(OH)<sub>2</sub> – LiH as a Hydrogen Release System. 2015.
10. Cai, W.; Wang, H.; Sun, D.; Zhang, Q.; Yao, X.; Zhu, M., Destabilization of LiBH<sub>4</sub> dehydrogenation through H<sup>+</sup>–H<sup>–</sup> interactions by cooperating with alkali metal hydroxides. *RSC Advances* **2014**, *4* (6), 3082.
11. Wang, Q.; Li, C.; Guo, M.; Sun, L.; Hu, C., Hydrothermal synthesis of hexagonal magnesium hydroxide nanoflakes. *Materials Research Bulletin* **2014**, *51* (0), 35-39.
12. Jiang, W.; Hua, X.; Han, Q.; Yang, X.; Lu, L.; Wang, X., Preparation of lamellar magnesium hydroxide nanoparticles via precipitation method. *Powder Technology* **2009**, *191* (3), 227-230.

13. Lv, J.; Qiu, L.; Qu, B., Controlled growth of three morphological structures of magnesium hydroxide nanoparticles by wet precipitation method. *Journal of Crystal Growth* **2004**, *267* (3-4), 676-684.
14. Kitchen, H. J.; Vallance, S. K.; Kennedy, J. L.; Tapia-Ruiz, N.; Carassiti, L.; Harrison, A.; Whittaker, A. G.; Drysdale, T. D.; Kingman, S. W.; Gregory, D. H., Modern Microwave Methods in Solid-State Inorganic Materials Chemistry: From Fundamentals to Manufacturing. *Chem. Rev.* **2014**, *114* (2), 1170-1206.
15. Bilecka, I.; Niederberger, M., Microwave chemistry for inorganic nanomaterials synthesis. *Nanoscale* **2010**, *2* (8), 1358.
16. Rao, K. J.; Vaidhyanathan, B.; Ganguli, M.; Ramakrishnan, P. A., Synthesis of Inorganic Solids Using Microwaves. *Chemistry of Materials* **1999**, *11* (4), 882-895.
17. Zhao, J.; Yan, W., Chapter 8 - Microwave-assisted Inorganic Syntheses. In *Modern Inorganic Synthetic Chemistry*, Xu, R.; Pang, W.; Huo, Q., Eds. Elsevier: Amsterdam, 2011; pp 173-195.
18. Gabriel, C.; Gabriel, S.; H. Grant, E.; H. Grant, E.; S. J. Halstead, B.; Michael P. Mingos, D., Dielectric parameters relevant to microwave dielectric heating. *Chemical Society reviews* **1998**, *27* (3), 213-224.
19. Caddick, S., Microwave assisted organic reactions. *Tetrahedron* **1995**, *51* (38), 10403-10432.
20. Al-Hazmi, F.; Umar, A.; Dar, G. N.; Al-Ghamdi, A. A.; Al-Sayari, S. A.; Al-Hajry, A.; Kim, S. H.; Al-Tuwirqi, R. M.; Alnowaiserb, F.; El-Tantawy, F., Microwave assisted rapid growth of Mg(OH)<sub>2</sub> nanosheet networks for ethanol chemical sensor application. *Journal of Alloys and Compounds* **2012**, *519*, 4-8.
21. Al-Gaashani, R.; Radiman, S.; Al-Douri, Y.; Tabet, N.; Daud, A. R., Investigation of the optical properties of Mg(OH)<sub>2</sub> and MgO nanostructures obtained by microwave-assisted methods. *Journal of Alloys and Compounds* **2012**, *521*, 71-76.
22. Feng, S.; Guanghaiua, L., Chapter 4 - Hydrothermal and Solvothermal Syntheses. In *Modern Inorganic Synthetic Chemistry*, Xu, R.; Pang, W.; Huo, Q., Eds. Elsevier: Amsterdam, 2011; pp 63-95.
23. S. Somiya, R. R., Hydrothermal synthesis of fine oxide powders. *Bull. Mater. Sci.* **2000**, *23* (6), 453-460.
24. Kumada, N., Preparation and crystal structure of new inorganic compounds by hydrothermal reaction. *J. Ceram. Soc. Jpn.* **2013**, *121* (1410), 135-141.
25. Parr, Acid Digestion Vessels Operating Instruction Manual.
26. Parr US Patent No. 4882128.

27. Parr Sample Preparation Bombs Manual. [http://www.parrinst.com/wp-content/uploads/downloads/2011/06/4700MB Parr Sample-Preparation-Vessels-Literature.pdf](http://www.parrinst.com/wp-content/uploads/downloads/2011/06/4700MB_Parr_Sample-Preparation-Vessels-Literature.pdf) (accessed 5<sup>th</sup> December 2014).
28. James M. Hanlon, Laura Bravo Diaz, Giulia Balducci, Blane A. Stobbs, Marek Bielewski, Pietro Moretto, Peter Chung and Duncan H. Gregory, Rapid surfactant-free synthesis of Mg(OH)<sub>2</sub> nanoplates and pseudomorphic dehydration to MgO. *Green Chemistry* **2014**.
29. Chandra, T.; Zebrowski, J. P., Reactivity control using a Schlenk line. *Journal of Chemical Health and Safety* **2014**, *21* (3), 22-28.
30. D. F. Shriver, M. A. D., *The manipulation of air sensitive compound*. 2<sup>nd</sup> ed.; Wiley: New York, 1986.
31. Mattox, D. M., 5 - Vacuum Evaporation and Vacuum Deposition. In *Handbook of Physical Vapor Deposition (PVD) Processing*, Mattox, D. M., Ed. William Andrew Publishing: Westwood, NJ, 1998; pp 288-342.
32. Sadtler, P. B., Vacuum evaporation. *J. Ind. Eng. Chem.* **1909**, *1*, 644-653.
33. Zavalij, V. K. P. a. P. Y. *Fundamentals of Powder Diffraction and Structural Characterization of Materials*, Springer Science and Business Media: New York, 2009.
34. Bragg, W. L., The structure of some crystals as indicated by their diffraction of X-rays. *Proc. R. soc. Lond. Ser. A-Contain. Pap. Math. Phys. Character* **1913**, *89* (610), 248-277.
35. Bragg, W. H., The reflection of x-rays by crystals. (II.). *Proc. R. soc. Lond. Ser. A-Contain. Pap. Math. Phys. Character* **1913**, *89* (610), 246-248.
36. Yoshio Waseda, E. M. a. K. S., *X-Ray Diffraction Crystallography*. Springer Science and Business Media: New York, 2011.
37. Kourkoumelis, N., PowDLL: a reusable .NET component for interconverting powder diffraction data. *International Union of Crystallography - Commission on Powder Diffraction* **2005**, *Newsletter* *30*.
38. Belsky, A.; Hellenbrandt, M.; Karen, V. L.; Luksch, P., New developments in the Inorganic Crystal Structure Database (ICSD): accessibility in support of materials research and design. *Acta Crystallographica Section B* **2002**, *58* (3 Part 1), 364-369.
39. Liu, G.; Wang, Y.; Jiao, L.; Yuan, H., Solid-state synthesis of amorphous TiB<sub>2</sub> nanoparticles on graphene nanosheets with enhanced catalytic dehydrogenation of MgH<sub>2</sub>. *International Journal of Hydrogen Energy* **2014**, *39* (8), 3822-3829.

40. Bazzanella, N.; Checchetto, R.; Miotello, A., Atoms and Nanoparticles of Transition Metals as Catalysts for Hydrogen Desorption from Magnesium Hydride. *Journal of Nanomaterials* **2011**, *2011*, 1-11.
41. A. C. Larson, R. B. v. D. *General Structure Analysis System (GSAS)*; Los Alamos Laboratory: Los Alamos, NM, USA, 1995, 1995; pp 86-748.
42. Toby, B. H., EXPGUI, a graphical user interface for GSAS. *J. Appl. Crystallogr.* **2001**, *34*, 210-213.
43. Smith, R. I., ISIS Course - Neutron Training Manual.
44. S.T. Norberg, I. A., R.I. Smith, S.G. Eriksson, L.C. Chapon and S. Hull, The Polaris Diffractometer at ISIS: Planned Upgrade and New Facilities.
45. Hull, R. I. S. a. S., User Guide for the Polaris Powder Diffractometer at ISIS.
46. Rietveld, H. M., Line profiles of neutron powder-diffraction peaks for structure refinement. *Acta Crystallographica* **1967**, *22*, 151-&.
47. Rietveld, H. M., A profile refinement method for nuclear and magnetic structures. *J. Appl. Crystallogr.* **1969**, *2*, 65.
48. Young, R. A., *The Rietveld Method*. Oxford University Press: 1995.
49. Harold P. Klug; Alexander, L. E., *X-Ray Diffraction Procedures for Polycrystalline and Amorphous Materials*. Sixth Edition ed.; John Wiley & Sons, Inc.: 1970.
50. Netzsch Thermal Analysis. <http://www.netzsch-thermal-analysis.com/en/home.html> (accessed 11<sup>th</sup> December 2014).
51. Kissinger, H. E., Reaction Kinetics in Differential Thermal Analysis. *Analytical Chemistry* **1957**, *29* (11), 1702-1706.
52. Kissinger, H. E., Variation on Peak Temperature With Heating Rate in Differential Thermal Analysis. *Journal of Research of The National Bureau of Standards* **1956**, *57* (4), 5.
53. Hiden Analytical. <http://www.hidenanalytical.com> (accessed 11<sup>th</sup> December 2014).
54. Paul, W., Electromagnetic Traps for Charged and Neutral Particles (Nobel Lecture). *Angewandte Chemie International Edition in English* **1990**, *29* (7), 739-748.
55. J. Goldenstein, D. N., D. Joy, C. Lyman, P. Echlin, E. Lifshin, L. Sawyer, J. Michael, *Scanning Electron Microscopy and X-ray Microanalysis*. 3rd ed.; Springer Science and Business Media Inc.: 2003.
56. Weilie Zhou, Z. L. W., *Scanning Microscopy for Nanotechnology*. Springer Science and Business Media Inc.: 2007.

## 3 The magnesium hydride – magnesium hydroxide ‘modular’ release system

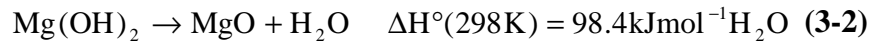
### 3.1 Introduction

The magnesium hydroxide – magnesium hydride system was one of the first ‘modular’ hydrogen release system to be proposed by Leardini *et al.* in 2009.<sup>1</sup> More recently, Wang *et al.* studied the improved hydrogen storage and release properties of mechanically milled magnesium hydride when mixed with catalytic amounts of alkali hydroxides in 2013.<sup>2</sup> Furthermore, the use of magnesium hydroxide in these kind of systems has also recently been proposed in combination with lithium borohydride and sodium borohydride.<sup>3,4</sup>

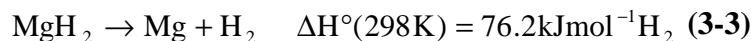
The  $\text{Mg(OH)}_2$  –  $\text{MgH}_2$  dehydrogenation system, presented in Equation 3-1, is thermodynamically favourable. It can theoretically release up to 4.7 wt. % of hydrogen and involves the reaction between magnesium hydroxide and magnesium hydride to yield magnesium oxide together with and the evolution of hydrogen.



The decomposition of both magnesium hydroxide and magnesium hydride as individual components have been widely studied. In the case of  $\text{Mg(OH)}_2$ , the decomposition is a dehydration process (Equation 3-2), which theoretically leads to the release of 30.8 wt. %  $\text{H}_2\text{O}$ .<sup>5,6</sup>



Magnesium hydride can theoretically release up to 7.6 wt. %  $\text{H}_2$ , although the kinetics and thermodynamics of the dehydrogenation process are (Equation 3-3) characterised by slow  $\text{H}_2$  desorption at high temperatures.<sup>7</sup>



In this work  $\text{Mg(OH)}_2$  and  $\text{MgH}_2$  have been employed together as a single system: a stoichiometric amount of the two reagents have been mixed together as shown in Equation 3-1. Bulk, mechanically-milled and chemically nanostructured materials were used. First,

mixtures of as-received  $\text{Mg}(\text{OH})_2$  and  $\text{MgH}_2$  were ground together manually and their dehydrogenation investigated. Following the study of the bulk system, mechanically milled materials were employed: both bulk  $\text{Mg}(\text{OH})_2$  and  $\text{MgH}_2$  were ball milled to reduce particle size and subsequently manually mixed and used as a 'modular' system.

Furthermore, nanostructured  $\text{Mg}(\text{OH})_2$  with an hexagonal platelet morphology has been successfully synthesised. The hydroxide was mixed with milled  $\text{MgH}_2$  and the behaviour of the whole system investigated. As mentioned in Section 1.3.2, the reduction of the particle size of the materials in these kinds of systems can lead to an enhancement of the thermodynamics and kinetics of hydrogen release and can potentially yield better control of the whole dehydrogenation process.

All starting materials and systems were characterised using simultaneous thermogravimetric analysis (TG-DTA) mass spectroscopy (MS), powder X-ray diffraction and scanning electron microscopy. TG-DTA-MS studies were conducted to obtain information on the onset and peak temperature of any thermal event occurring, weight loss percentage and nature and amount of the gas evolved during the reaction. *Ex-situ* PXD has been used to monitor the various dehydrogenation steps occurring during the thermal treatment and ultimately to propose a mechanism of hydrogen release for each studied system. Scanning electron microscopy was employed for imaging: the morphology of both milled and nanostructured materials have been studied before and after the heating process in order to verify any retention of the morphology, especially for nanostructured magnesium hydroxide.

The aim of this chapter is to give an overview on the  $\text{Mg}(\text{OH})_2 - \text{MgH}_2$  system with particular focus on the comparison among chemically nanostructured, mechanically milled materials and bulk reagents dehydrogenation properties. TG-DTA-MS studies were performed on each system in order to obtain onset and peak temperature of any thermal event occurring, associated weight loss percentages and nature and amount of the gas evolved during heating. *Ex-situ* PXD experiments were conducted to try and isolate any intermediate phases forming during dehydrogenation and propose a mechanism of hydrogen release for bulk, milled and nano systems. Scanning Electron Microscopy was employed for morphology studies of both milled and nanostructured materials before and after heating.

## 3.2 Experimental

### 3.2.1 Preparation of the systems

All ‘modular’ systems were prepared by manually mixing materials with a mortar and pestle stoichiometric amounts of the starting for 5 minutes. All mixtures were prepared by mixing 222 mg of magnesium hydroxide and 100 mg of magnesium hydride. All preparations were carried out under an inert atmosphere inside either an argon- or nitrogen-filled recirculating glove box.

Three different kinds of systems were prepared:

- Bulk ‘modular’ system: as-received  $\text{Mg}(\text{OH})_2$  (Sigma-Aldrich, 95%) and  $\text{MgH}_2$  (Aldrich, hydrogen-storage grade,  $\geq 96.5\%$ ) were mixed (denoted b- $\text{Mg}(\text{OH})_2$  and b- $\text{MgH}_2$  respectively).
- Mechanically milled ‘modular’ system: mixtures of mechanically milled magnesium hydroxide (denoted m- $\text{Mg}(\text{OH})_2$ ) and mechanically milled magnesium hydride (m- $\text{MgH}_2$ ) were prepared.
- Nanostructured ‘modular’ system: nanostructured  $\text{Mg}(\text{OH})_2$  (denoted n- $\text{Mg}(\text{OH})_2$ ) was mixed together with mechanically milled  $\text{MgH}_2$ .

### 3.2.2 Microwave-Hydrothermal Synthesis of nanostructured $\text{Mg}(\text{OH})_2$

To obtain *ca.* 2 grams of n- $\text{Mg}(\text{OH})_2$ , approximately 1.6 grams of magnesium oxide (Sigma Aldrich, 98%) were placed inside a Teflon-lined autoclave for microwave synthesis together with 30 ml of deionised water. The MW autoclave was heated for a total of 4 minutes (1 minute followed by 30 minutes of cooling each time) inside single mode cavity, adapted domestic microwave oven. Products were washed and centrifuged with  $\text{H}_2\text{O}$  three times and the white precipitate collected and dried in air overnight.<sup>5,8</sup>

### 3.2.3 Ball milling of $\text{Mg}(\text{OH})_2$

Magnesium hydroxide was mechanically milled using the same conditions reported by Zhu *et al.*<sup>9</sup> However, a 40:1 ball-to-powder ratio was used as opposed to the 120:1 employed by Zhu.

During a typical milling experiment, 1 gram of  $\text{Mg}(\text{OH})_2$  (Sigma-Aldrich, 95%) was ball milled for 5 hours at 500 rpm, using 10 stainless steel balls. A 5 minute interval followed every 5 minutes of milling.

### **3.2.4 Ball milling of $\text{MgH}_2$**

Nanostructured  $\text{MgH}_2$  was produced by mechanically milling the as-received hydride (Aldrich, hydrogen-storage grade,  $\geq 96.5\%$ ). Typically, 1 gram of  $\text{MgH}_2$  was loaded into a 50 ml stainless steel jar using 10 stainless steel balls as grinding medium. The milling process was performed for 5 hours at 450 rpm. A 5 minute interval was applied after every 5 minutes of milling.<sup>10</sup>

### **3.2.5 TG-DTA-MS studies**

The hydroxide – hydride system was characterised by thermogravimetric-differential thermal analysis coupled with mass spectroscopy. These experiments were performed to obtain information on the onset and peak temperature of the thermal event occurring during heating, weight loss percentage and nature and amount of the gas evolved during the reaction. TG-DTA experiments were carried out using a Netzsch STA 409 PC coupled to a Hiden HPR20 mass spectrometer as detailed in Section 2.3.4. All measurements were performed under a flow of argon and all manipulations were conducted inside inert atmosphere glove boxes.

First correction files were created and then the materials analysed (Section 2.3.4.1). Initial experiments involved heating from room temperature to 873 K at  $5 \text{ K min}^{-1}$  and holding that temperature for 1 hour before undergoing natural cooling. Subsequent experiments were planned based on the initial TG-DTA results obtained and intermediate temperature points were studied to isolate any intermediate species forming to facilitate the proposal of a mechanism of hydrogen release. For each experiment, approximately 20-25 mg of sample were subjected to thermal treatment.

As mentioned in Section 2.3.4.1, TG-DTA analyses was performed in order to calculate the activation energy for the system using the Kissinger method.<sup>11,12</sup> Samples were heated to 773 K using heating rates of 2, 5, 10 and  $20 \text{ K min}^{-1}$  respectively (Table 3-5) and Kissinger plots were obtained.

### **3.2.6 Powder X-ray diffraction (PXD) experiments**

All starting materials and ‘modular’ hydrogen release systems were analysed by PXD as described in paragraph 2.3.1.1. Capillaries were prepared for the characterisation of air sensitive materials and these were analysed with a d8 Bruker diffractometer. Data were typically collected from  $2\theta$  5-85 for one hour for phase identification. Non-air sensitive materials were characterised using a PANalytical X’Pert powder diffractometer, employing the bracket stage. Data were usually collected from  $2\theta$  5-85 for 30 minutes for phase identification and for 3 hours for Rietveld refinements studies.

The data obtained were compared with the appropriate reference powder diffraction patterns using the ICSD database<sup>13</sup> on PowderCell<sup>14</sup> or using the ICDD PDF database<sup>15</sup> with the PANalytical HighScore Plus software.

As already discussed in Section 2.3.3, Rietveld refinements against the PXD data were performed using the General Structure Analysis System (GSAS)<sup>16</sup> with the EXPGUI interface<sup>17</sup>. The background was successfully modelled using Function 1 (Chebyshev function, polynomial of the first type). This was followed by the refinement of the cell parameters, atomic positions, profile parameters and temperature factors. The peak shape was modelled using Function 2, which is a multi-term Simpson’s integration of the Pseudo-Voigt function.

### **3.2.7 Scanning Electron Microscopy (SEM) imaging**

Samples for SEM imaging were prepared accordingly to Section 2.5.2.1. In each case a small amount of sample was placed onto an adhesive carbon tab fixed on an aluminium stub. Since the analysed materials were observed to charge under the electron beam, samples were sputter-coated with a 10 nm layer of gold/palladium alloy in order to achieve better conductivity and increase the quality of the collected images. All manipulations were carried out inside a recirculating glove box under inert atmosphere. The samples were put into glass vials and sealed before being transferred out of the glove box. The samples were then placed inside the vacuum column of the microscope, which was shut and evacuated.

Images were acquired using a Carl Zeiss Sigma Variable Pressure Analytical SEM with Oxford Microanalysis employing a Schottky thermal field emitter electron source. SEM imaging was performed with an accelerating voltage of 15-25 kV and a working distance

of typically 5-6 mm. The instrument is situated at the Imaging Spectroscopy and Analysis Centre (ISAAC), School of Geographical and Earth Sciences (GES) at the University of Glasgow. All images were collected with the help of Dr Peter Chung.

### 3.2.8 Summary of samples and reactions

**Table 3-1: Summary of starting materials employed in the  $\text{Mg}(\text{OH})_2 - \text{MgH}_2$  ‘modular’ release systems.**

Sample	Material	Preparation Conditions	Heating program / K
1	n- $\text{Mg}(\text{OH})_2$	4 min MW synthesis	873 / 5 K $\text{min}^{-1}$ + 1 h dwell
2	m- $\text{Mg}(\text{OH})_2$	5 h milling @ 500 rpm (5/5)	873 / 5 K $\text{min}^{-1}$ + 1 h dwell
3	m- $\text{MgH}_2$	5 h milling @ 450 rpm (5/5)	873 / 5 K $\text{min}^{-1}$ + 1 h dwell

**Table 3-2: Summary of preparations carried out for the bulk ‘modular’ system.**

Sample	Material	Preparation Conditions	Heating program / K
4	b- $\text{Mg}(\text{OH})_2 - \text{b-MgH}_2$	5 min manual mixing	–
5	b- $\text{Mg}(\text{OH})_2 - \text{b-MgH}_2$	5 min manual mixing	873 / 5 K $\text{min}^{-1}$ + 1 h dwell
6	b- $\text{Mg}(\text{OH})_2 - \text{b-MgH}_2$	5 min manual mixing	638 / 5 K $\text{min}^{-1}$
7	b- $\text{Mg}(\text{OH})_2 - \text{b-MgH}_2$	5 min manual mixing	673 / 5 K $\text{min}^{-1}$
8	b- $\text{Mg}(\text{OH})_2 - \text{b-MgH}_2$	5 min manual mixing	723 / 5 K $\text{min}^{-1}$
9	b- $\text{Mg}(\text{OH})_2 - \text{b-MgH}_2$	5 min manual mixing	773 / 5 K $\text{min}^{-1}$

**Table 3-3: Summary of preparations carried out for the mechanically milled ‘modular’ system.**

Sample	Material	Preparation Conditions	Heating program / K
10	m- $\text{Mg}(\text{OH})_2 - \text{m-MgH}_2$	5 min manual mixing	–
11	m- $\text{Mg}(\text{OH})_2 - \text{m-MgH}_2$	5 min manual mixing	873 / 5 K $\text{min}^{-1}$ + 1 h dwell
12	m- $\text{Mg}(\text{OH})_2 - \text{m-MgH}_2$	5 min manual mixing	658 / 5 K $\text{min}^{-1}$
13	m- $\text{Mg}(\text{OH})_2 - \text{m-MgH}_2$	5 min manual mixing	758 / 5 K $\text{min}^{-1}$

**Table 3-4: Summary of preparations carried out for the nanostructured ‘modular’ system.**

<b>Sample</b>	<b>Material</b>	<b>Preparation Conditions</b>	<b>Heating program / K</b>
<b>14</b>	n-Mg(OH) <sub>2</sub> – m-MgH <sub>2</sub>	5 min manual mixing	–
<b>15</b>	n-Mg(OH) <sub>2</sub> – m-MgH <sub>2</sub>	5 min manual mixing	873 / 5 K min <sup>-1</sup> + 1 h dwell
<b>16</b>	n-Mg(OH) <sub>2</sub> – m-MgH <sub>2</sub>	5 min manual mixing	673 / 5 K min <sup>-1</sup>
<b>17</b>	n-Mg(OH) <sub>2</sub> – m-MgH <sub>2</sub>	5 min manual mixing	773 / 5 K min <sup>-1</sup>

**Table 3-5: Summary of preparations carried out for activation energy calculations.**

<b>Sample</b>		<b>Preparation Conditions</b>	<b>Heating program / K</b>
<b>18a</b>	b-Mg(OH) <sub>2</sub> – b-MgH <sub>2</sub>	5 min manual mixing	773 (2 K min <sup>-1</sup> )
<b>18b</b>			773 (5 K min <sup>-1</sup> )
<b>18c</b>			773 (10 K min <sup>-1</sup> )
<b>18d</b>			773 (20 K min <sup>-1</sup> )
<b>19a</b>	m-Mg(OH) <sub>2</sub> – m-MgH <sub>2</sub>	5 min manual mixing	773 (2 K min <sup>-1</sup> )
<b>19b</b>			773 (5 K min <sup>-1</sup> )
<b>19c</b>			773 (10 K min <sup>-1</sup> )
<b>19d</b>			773 (20 K min <sup>-1</sup> )
<b>20a</b>	n-Mg(OH) <sub>2</sub> – m-MgH <sub>2</sub>	5 min manual mixing	773 (2 K min <sup>-1</sup> )
<b>20b</b>			773 (5 K min <sup>-1</sup> )
<b>20c</b>			773 (10 K min <sup>-1</sup> )
<b>20d</b>			773 (20 K min <sup>-1</sup> )

## 3.3 Results and Discussion

### 3.3.1 Preparation of the system components

#### 3.3.1.1 Nanostructured $\text{Mg}(\text{OH})_2$

Nanostructured  $\text{Mg}(\text{OH})_2$  (Sample 1) was successfully obtained using the synthetic route described in Section 3.2.1.<sup>5</sup>

The synthesised nanostructured magnesium hydroxide was characterised by PXD and SEM. As shown in the PXD pattern (Figure 3-1) pure-phase  $\text{Mg}(\text{OH})_2$  nanoplates are synthesised with no trace of  $\text{MgO}$  starting material present. Crystallites were of hexagonal platelet morphology with a typical thickness of 10 – 60 nm, a diameter and diagonals varying in the 100 nm – 300 nm and 200 – 600 nm range respectively (Figure 3-2).

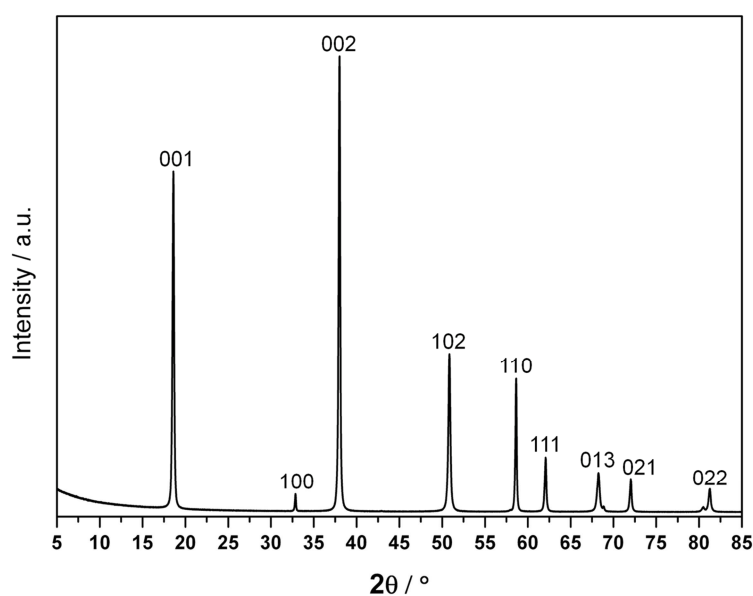
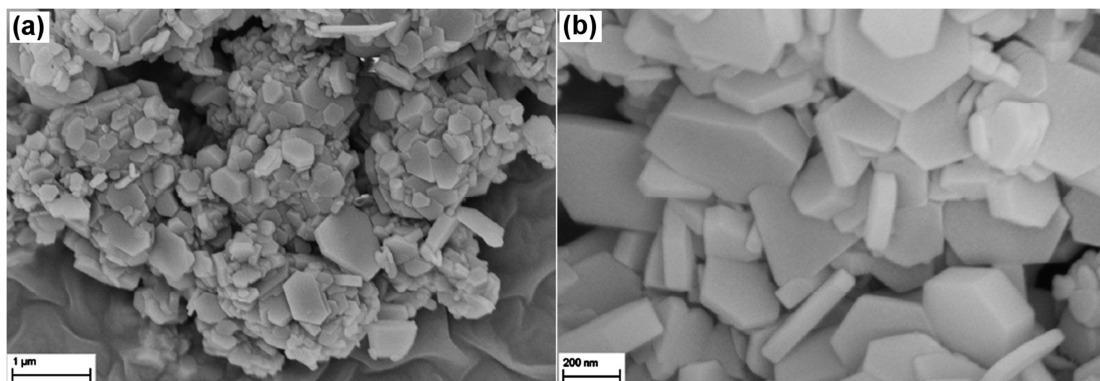


Figure 3-1: PXD pattern for Sample 1, synthesised  $\text{n-Mg}(\text{OH})_2$ .



**Figure 3-2: Collected SEM images for Sample 1: a) 1  $\mu\text{m}$  scale b) 200 nm scale**

Due to the non-uniform size distribution of the sample, the Scherrer method has not been used to give an estimation of the particle size of the synthesised  $\text{Mg}(\text{OH})_2$ . Rietveld refinement was performed against PXD data with GSAS<sup>16</sup> using the EXPGUI<sup>17</sup> interface. Crystallographic data are presented in Table 3-6 and the cell parameters are in good agreement with the literature values.<sup>18</sup> The observed, calculated and difference (OCD) plot from the PXD Rietveld refinement for Sample 1 is presented in Figure 3-3.

**Table 3-6: Selected data from the PXD Rietveld refinement for Sample 1, synthesised nano  $\text{Mg}(\text{OH})_2$ .**<sup>5</sup>

<b>Empirical Formula</b>	<b><math>\text{Mg}(\text{OH})_2</math></b>
<b>Crystal System</b>	Trigonal
<b>Space Group</b>	$P-3m1$
<b>Lattice Parameters</b>	
$a / \text{\AA}$	3.150(4)
$c / \text{\AA}$	4.774(9)
$V / \text{\AA}^3$	41.0(1)
<b>Z</b>	1
<b>Unit Cell Formula</b>	
<b>Weight / <math>M_w</math></b>	58.319
<b>Density / <math>\text{g cm}^{-3}</math></b>	2.360
<b>No. of Variables</b>	31
<b>No. of Observations</b>	9573
<b>Rwp %</b>	9.31
<b>Rp %</b>	3.61
$\chi^2$	4.43

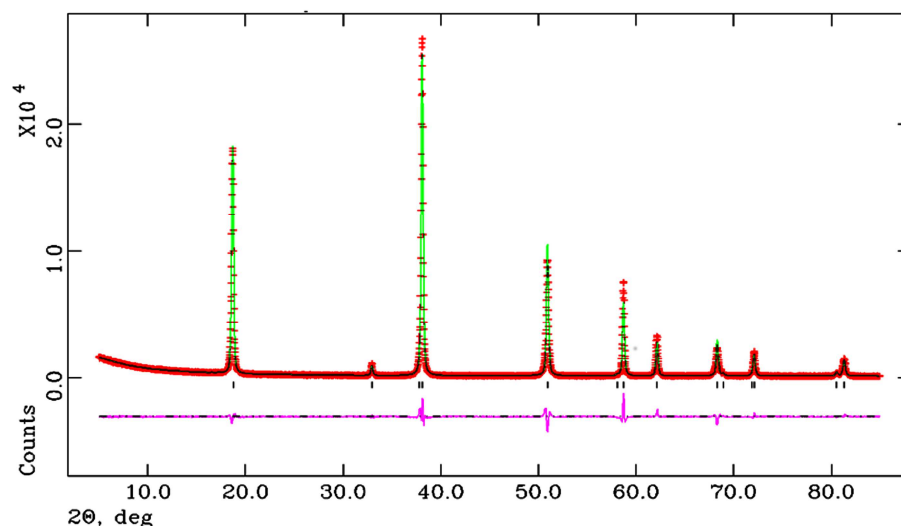
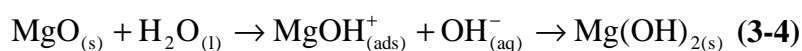


**Figure 3-3: Observed, calculated and difference (OCD) plot from the PXD Rietveld refinement for Sample 1, synthesised n-Mg(OH)<sub>2</sub>.**

A possible mechanism of nanoplates growth was proposed in 2003 by Yu *et al.*, who studied the conventional HT synthesis of Mg(OH)<sub>2</sub> hexagonal nanoplates from only MgO and H<sub>2</sub>O.<sup>19</sup> This process starts with the dissolution of bulk MgO in water, forming primary particles, and then proceeds with the aggregation of those particles to yield mesoporous nanoplates.

The mechanism herein proposed for the MW-HT synthesis is different to the one reported above and it consists of a dissolution-precipitation process (Equation 3-4). The use of MW results in a much higher rate of both heating and cooling and this could lead to an extremely fast initial MgO dissolution step. Even though the solubility of MgO and Mg(OH)<sub>2</sub> is poor under ambient conditions, these increase with increasing temperature.<sup>20,21</sup> The mechanism then involves the formation of magnesium hydroxide on the oxide surface via intermediate Mg(OH)<sup>+</sup> species. This is then followed by the removal of Mg(OH)<sub>2</sub> from MgO surface.<sup>22,23</sup>



The oxide is believed to rapidly react with H<sub>2</sub>O, with the formation of Mg(OH)<sub>2</sub> particles being faster than their removal from the surface of the oxide.

The final step of the process is the cooling which is when the agglomeration of the particles is believed to occur. In this sense, this suggests that the mechanism is different to the one proposed by Yu *et al.*<sup>19</sup> Both mechanisms are presented in Figure 3-4.

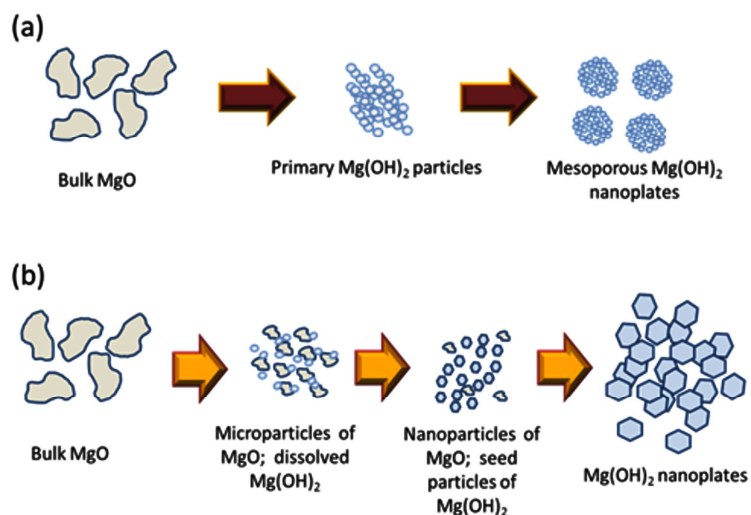


Figure 3-4: Proposed growth processes for (a) conventional hydrothermal synthesis of Mg(OH)<sub>2</sub> nanoplates<sup>19</sup> and (b) MW-HT synthesis of Mg(OH)<sub>2</sub> nanoplates performed during this project.<sup>5</sup>

### 3.3.1.2 Ball milled Mg(OH)<sub>2</sub>

Magnesium hydroxide (Sample 2) was ball milled for 5 h at 500 rpm; as shown in Figure 3-5, the post-milling product is still single phase Mg(OH)<sub>2</sub>. SEM images were collected (Figure 3-6) and show particles with a typical particle size of 70-200 nm in diameter. However, it is also possible to notice that the milled Mg(OH)<sub>2</sub> particles tend to agglomerate in bigger clusters with a diameter of typically a few μm.

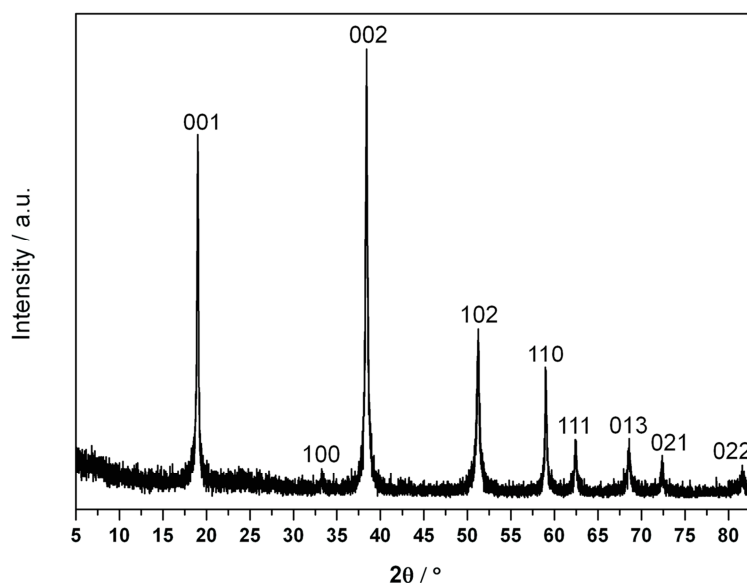
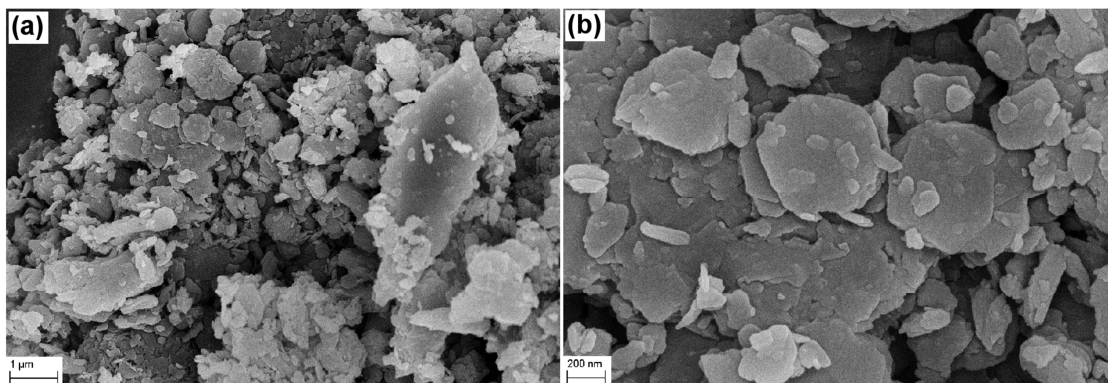


Figure 3-5: PXD pattern for Sample 2, ball milled magnesium hydroxide.



**Figure 3-6: Collected SEM images for Sample 2: a) 1  $\mu\text{m}$  scale b) 200 nm scale**

### **3.3.1.3 Ball milled $\text{MgH}_2$**

Magnesium hydride (Sample 3) was ball milled for 5 h at 450 rpm. As shown in the PXD pattern (Figure 3-7), no major reaction occurs during the milling time, although it is possible to identify peaks assignable to different  $\text{MgH}_2$  polymorphs:  $\beta\text{-MgH}_2$  and  $\gamma\text{-MgH}_2$ . Nonetheless, the  $\gamma\text{-MgH}_2$  reflections are very low in intensity and  $\beta\text{-MgH}_2$  is still the main phase present. Magnesium metal is also present as impurity. Its presence was identified in the as-received hydride, before the milling process was performed. Rietveld refinement was performed against the collected PXD data and the calculated weight fractions were found to be  $96 \pm 1\%$   $\text{MgH}_2$  and  $4 \pm 1\%$  Mg. The PXD pattern of the as-received  $\text{MgH}_2$  together with selected crystallographic data and the observed, calculated and difference (OCD) plot from the PXD Rietveld Refinement can be found in Appendix A.

SEM images were collected prior and after the ball milling (Figures 3-8 and 3-9). The images show a dramatic reduction of the particle size with respect to the as-received hydride. The milling process results in a typical particle size of 70-150 nm in diameter. The collected SEM images show nonetheless that the particles tend to agglomerate in clusters with a diameter of typically 1-2  $\mu\text{m}$ , as was previously observed for milled  $\text{Mg}(\text{OH})_2$ .

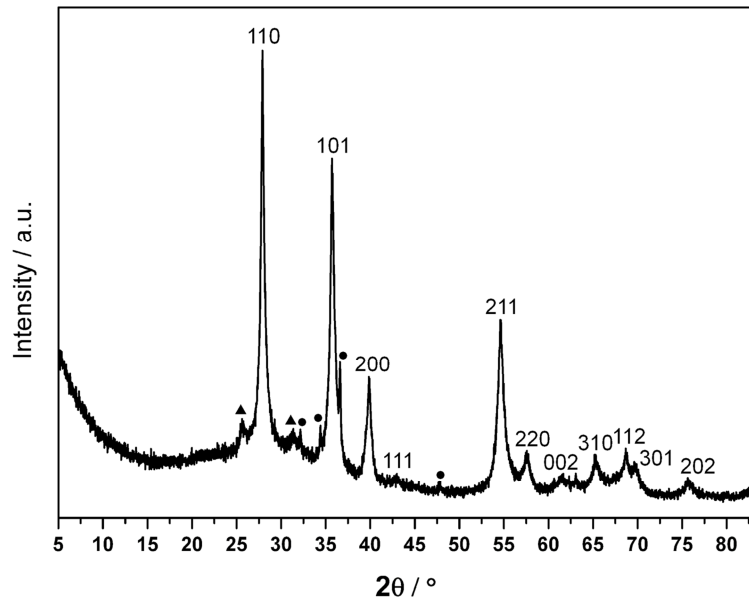


Figure 3-7: PXD pattern for Sample 3, ball milled magnesium hydride ( $\beta$ - $\text{MgH}_2$ ). Triangles and circles indicate  $\gamma$ - $\text{MgH}_2$  and Mg metal respectively.

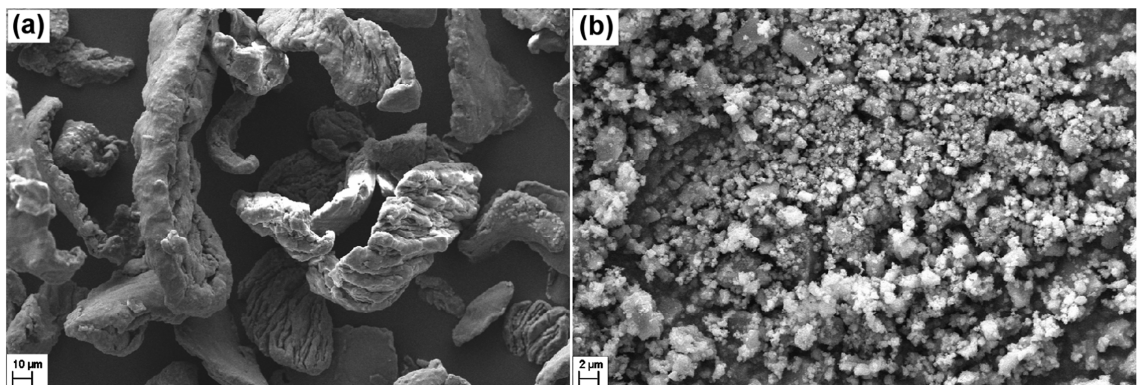


Figure 3-8: Collected SEM images: a) commercial  $\text{MgH}_2$  (10  $\mu\text{m}$  scale) and b) Sample 3 (2  $\mu\text{m}$  scale)

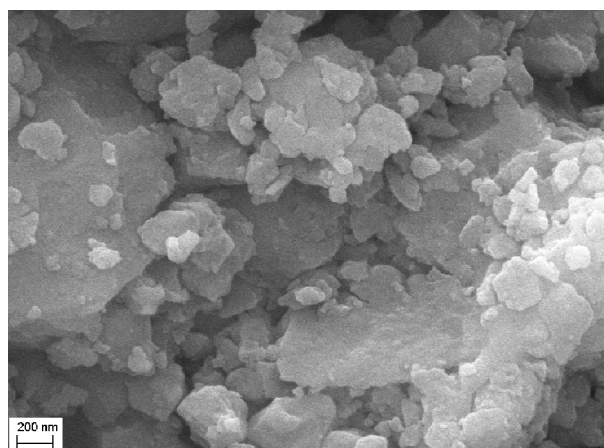


Figure 3-9: Higher magnification SEM image for Sample 3 (200 nm scale)

### 3.3.1.4 TG-DTA-MS data

Prior to the study of the ‘modular’ release system, TG-DTA-MS studies were carried out on each of the starting materials. Samples 1, 2 and 3 and the commercial magnesium hydroxide and magnesium hydride were analysed individually in order to compare onset and peak temperatures of dehydration and dehydrogenation for  $\text{Mg}(\text{OH})_2$  and  $\text{MgH}_2$  respectively, as well as weight losses and the evolution of gaseous species occurring during heating.

A summary of the results obtained for magnesium hydroxide is reported in Table 3-7.

**Table 3-7: Onset temperature, peak temperatures, weight losses and identified released gaseous species for Sample 1 (nano  $\text{Mg}(\text{OH})_2$ ), Sample 2 (milled  $\text{Mg}(\text{OH})_2$ ) and as-received  $\text{Mg}(\text{OH})_2$ .**

Sample	Onset T / K	Peak T / K	Weight Loss / %	Evolved Gases
<b>1</b> n- $\text{Mg}(\text{OH})_2$	560	663	29.7	$\text{H}_2\text{O}$
<b>2</b> m- $\text{Mg}(\text{OH})_2$	528	615 653	30.4	$\text{H}_2\text{O}$
<b>Commercial</b> <b><math>\text{Mg}(\text{OH})_2</math></b>	553	603 631	30.6	$\text{H}_2\text{O}$

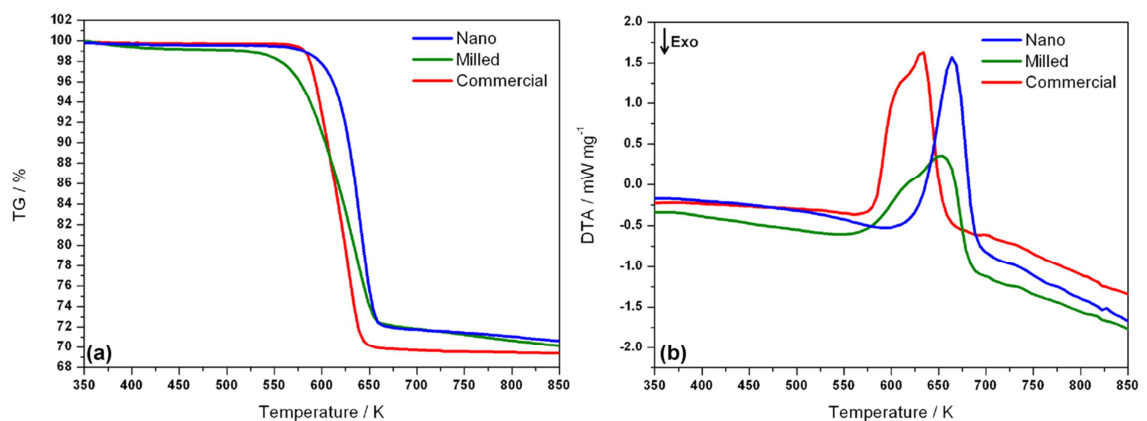


**Figure 3-10: (a) TG and (b) DTA data comparison for commercial (red), nanostructured (1; blue) and milled (2, green) magnesium hydroxide.**

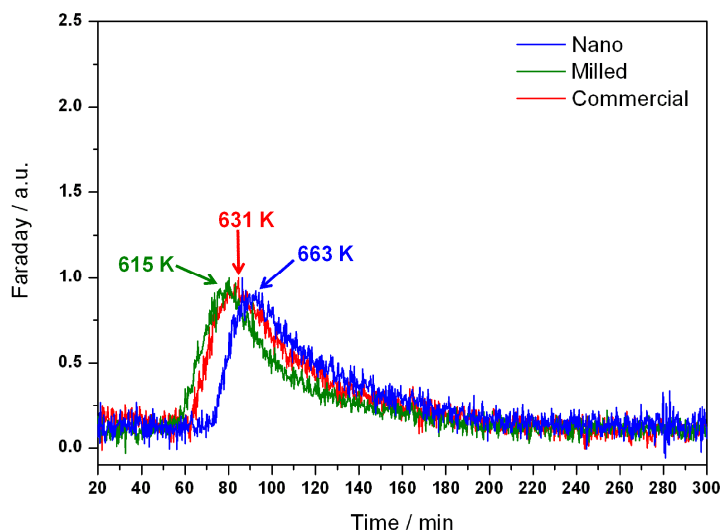


**Figure 3-11: MS profiles Vs time for commercial (red), nanostructured (1; blue) and milled (2, green) magnesium hydroxide.**

Figure 3-10 presents the TG-DTA data collected for Sample **1** (nano  $\text{Mg}(\text{OH})_2$ ), **2** (milled  $\text{Mg}(\text{OH})_2$ ) and commercial  $\text{Mg}(\text{OH})_2$ . All weight losses appear to be consistent: the lowest can be observed for the nanostructured hydroxide (Sample **1**), where a mass loss of 29.7 wt. % is observed, corresponding to 96.4 % of the theoretical 30.8 wt. %. The thermal treatment of Sample **2** leads to a mass loss of 30.4 wt. % (98.8 % of the theoretical one), whereas the as-received  $\text{Mg}(\text{OH})_2$  dehydration process results a weight loss of 30.6 %, which is 99.4 % of the theoretical figure. The DTA profiles show differences amongst the materials: the onset temperature of dehydration are found to be 560 K, 528 K and 553 K for nano, milled and commercial  $\text{Mg}(\text{OH})_2$  respectively. The profile for Sample **1** suggests that the dehydration process takes place in a single step, with a peak temperature of 663 K. DTA profiles for commercial magnesium hydroxide and Sample **2** suggest the dehydration to be a two-step process instead, as previously reported: Turner *et al.* suggest that this may be due to differences in surface energy and the presence of crystal lattice defects.<sup>6</sup> Two different peaks may be identified with peak temperatures of 603 and 631 K for as-received  $\text{Mg}(\text{OH})_2$  and 615 and 653 K for milled  $\text{Mg}(\text{OH})_2$  (Sample **2**). However, this is not completely in agreement with the MS spectra collected (Figure 3-11): the only gaseous specie detected is water as expected, although for all samples the release of water appears to happen in a single event, with the maxima being 615, 631 and 663 K for milled, commercial and nanostructured magnesium hydroxide respectively.

Based on the data presented, Sample **2** (milled magnesium hydroxide) appears to be most promising of the hydroxides to be employed together with  $\text{MgH}_2$  in this type of ‘modular’

system in order to achieve the best hydrogen release performances, as its onset and peak dehydration temperatures are lowered when compared to the bulk material, suggesting an improved reactivity.

A summary of the data collected for magnesium hydride are presented in Table 3-8.

**Table 3-8: Onset temperature, peak temperatures, weight losses and identified released gaseous species for Sample 3 (milled MgH<sub>2</sub>) and for as-received MgH<sub>2</sub>.**

Sample	Onset T / K	Peak T / K	Weight Loss / %	Evolved Gases
<b>3</b> <b>m-MgH<sub>2</sub></b>	580	625	6.4	H <sub>2</sub>
<b>Commercial</b> <b>MgH<sub>2</sub></b>	667	696	6.9	H <sub>2</sub>

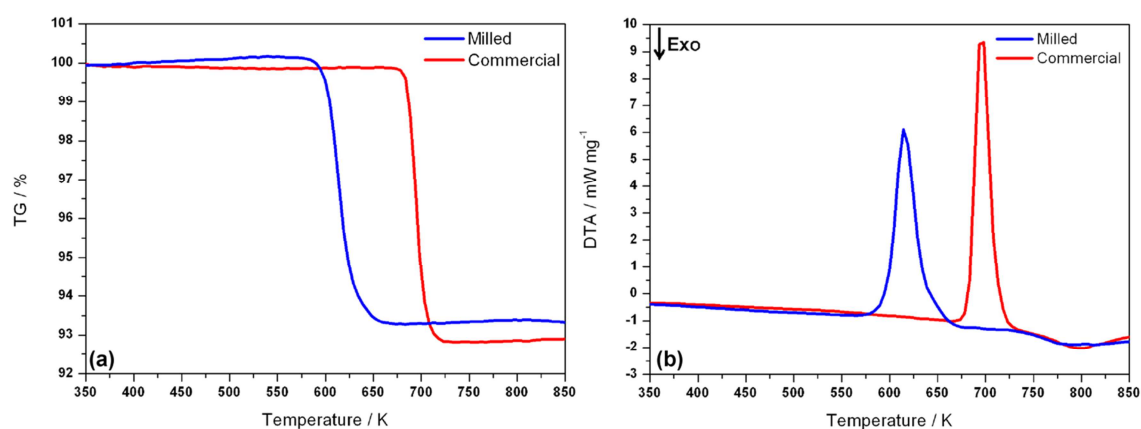


**Figure 3-12: (a) TG and (b) DTA data comparison for commercial (red) and milled (3, blue) magnesium hydride.**

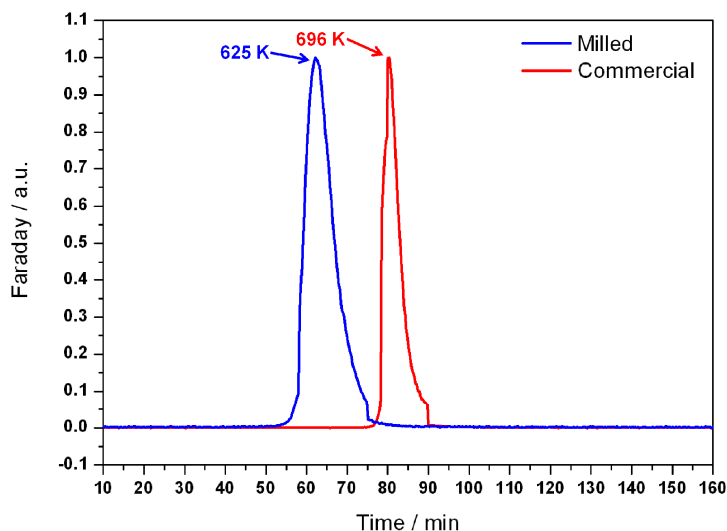


**Figure 3-13: MS profiles Vs time for commercial (red) and milled (3, blue) magnesium hydride.**

As can be observed in Figure 3-12, the TG-DTA profile shows great improvement in the dehydrogenation properties magnesium hydride as a result of ball milling. In fact, the milling procedure results in a decrease of the onset temperature of hydrogen release by almost 100 K with respect to the as-received  $\text{MgH}_2$ . The kinetics of  $\text{H}_2$  release appear to be slightly slower when compared to the bulk materials as a broadening of the DTA peak relative to  $\text{H}_2$  desorption can be observed for Sample **3**. However, this could be an effect of the size distribution of particles in the sample. The MS profiles (Figure 3-13) show that the only gaseous species evolved during the thermal treatment is hydrogen. From the data collected, it is also clear that the dehydrogenation process for milled material occurs *ca.* 30 minutes before the bulk one (lowered by *ca.* 90 K), although it seems to require more time to go to completion (roughly 25 minutes for milled  $\text{MgH}_2$  against the 15 minutes of non-milled  $\text{MgH}_2$ ). On the other hand, for the as-received hydride a weight loss of 6.9 wt. % (nearer to the theoretical 7.6 wt. %  $\text{H}_2$ ) can be observed. The thermal treatment of Sample **3** leads to a mass loss of 6.4 wt. %, which is 84.2 % of the expected 7.6 %. (91 % of the theoretical value for the bulk). The lower weight losses can be attributed to the presence of magnesium metal as an impurity in the pre-milled hydride as well as  $\gamma\text{-MgH}_2$  as previously explained in Section 3.3.1.3.

Initial TG-DTA-MS experiments were performed on Samples **5**, **11** and **15** to determine the onset temperature as well as the peak temperature of hydrogen release and the weight loss for bulk, milled and nanostructured systems (Figures 3-14 and 3-15). The results obtained are summarised in Table 3-9. The mixtures were heated to 873 K and that temperature was held for one hour (Samples **5**, **11** and **15**).

**Table 3-9: Onset temperature, peak temperatures, weight losses and identified released gaseous species for Samples 5, 11 and 15. If not otherwise specified, the thermal events are endothermic**

Sample	Onset T / K	Peak T / K	Weight Loss / %	Evolved Gases
<b>5</b> <b>b-Mg(OH)<sub>2</sub> – b-MgH<sub>2</sub></b>	567	611	21.5	H <sub>2</sub> ; H <sub>2</sub> O
		645		
	688	716		
		737		
<b>11</b> <b>m-Mg(OH)<sub>2</sub> – m-MgH<sub>2</sub></b>	527	642 (exo)	12.6	H <sub>2</sub> ; H <sub>2</sub> O
	718	743		
		779		
<b>15</b> <b>n-Mg(OH)<sub>2</sub> – m-MgH<sub>2</sub></b>	530	615 (exo)	7.9	H <sub>2</sub>
	713	753		
		776		

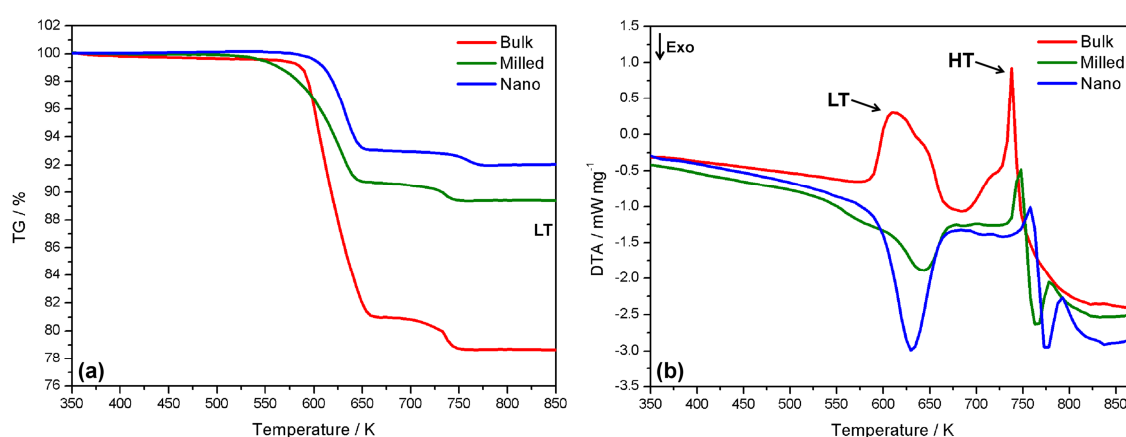


**Figure 3-14: (a) TG and (b) DTA data comparison for Sample 5 (bulk; red), Sample 11 (milled; green) and Sample 15 (nano; blue).**

As can be clearly seen from Figure 3-14, interesting differences can be appreciated among the three studied systems in terms of both weight loss and differential thermal analysis. Although the onset temperature of H<sub>2</sub> release is not dramatically decreased when reducing the particle size of the starting materials (567, 527 and 530 K for Sample **5**, bulk, **11**, milled, and **15**, nano respectively), great differences can be observed in the DTA profiles. The most important distinction between samples is related to the thermodynamic nature of the events occurring. Sample **5** shows the presence of four main endothermic events: the first one starting at 567 K (with a peak temperature of 611 K) and the second starting immediately afterwards with a peak temperature of 645 K. The third endothermic shows an onset temperature of 688 K and a peak temperature of 716 K and the last endothermic event occurs immediately after with a peak temperature of 737 K. The DTA profile for Samples **11** and **15** show that the presence of three events only. Further, the first event appears now to be exothermic for both samples whilst the other events remain endothermic. In particular, for Sample **11** the first event starts at 527 K and shows a peak temperature of 642 K. The second event starts at 718 K (with a peak temperature of 743 K) and it is immediately followed by the third and last endothermic event which presents a peak temperature of 779 K. A similar profile can be observed for Sample **15**, with slight shifts in temperatures with respect to **11**. The first event presents an onset temperature of 530 K and a peak temperature of 615 K, whereas the second event starts at 713 K (753 K peak temperature) with the third endothermic event starting immediately after with a peak temperature of 776 K.

TGA profiles show that the weight losses are much higher than expected for the evolution of hydrogen. In fact the theoretical figure for this system is 4.7 wt. % H<sub>2</sub>. The observed mass losses were found to be 21.5, 12.6 and 7.9 wt. % for Samples **5** (bulk), **11** (milled) and **15** (nano) respectively. This could be explained by taking into account the DTA profiles as well as the MS spectra showing the gaseous species evolved during the thermal treatment of each sample (Figure 3-15).

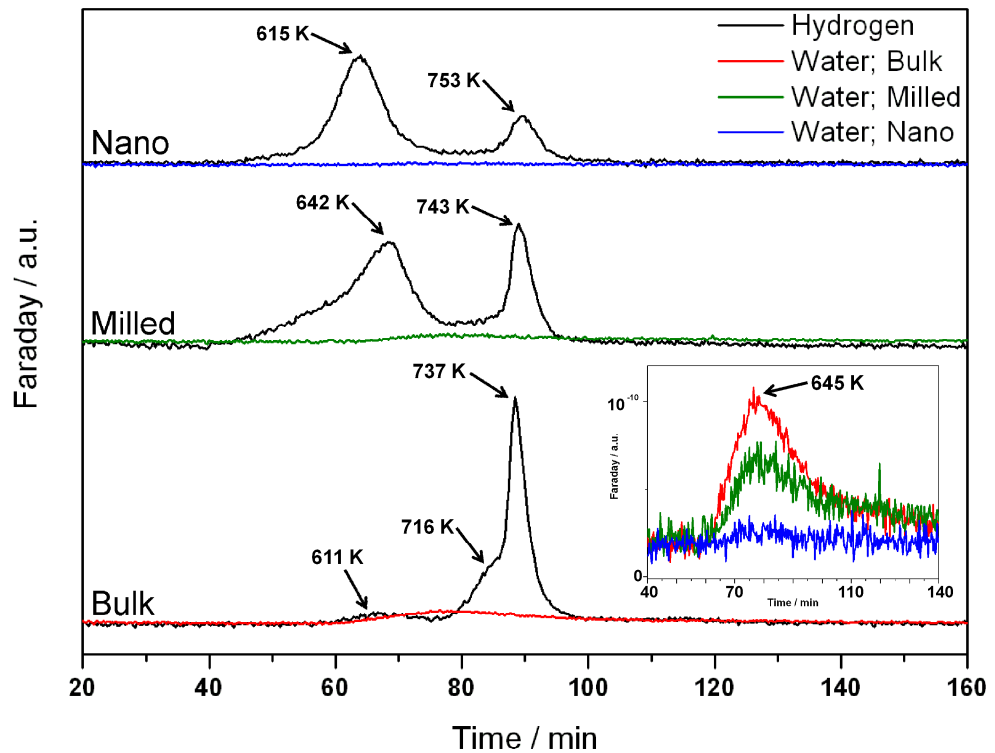


**Figure 3-15: MS profiles Vs time for Sample 5 (bulk), Sample 11 (milled) and Sample 15 (nano). The black line denotes hydrogen release. In the insert, water release for bulk, milled and nanostructured materials is denoted by red, green and blue lines respectively.**

As previously stated, the gravimetric capacity of the system is 4.7 wt. % of hydrogen according to Equation 3-1 presented in Section 3.1.

However, if the decomposition of the two starting materials is considered as being two independent thermal events; *i.e.* the dehydration of  $\text{Mg}(\text{OH})_2$  and the dehydrogenation of  $\text{MgH}_2$  (Equations 3-2 and 3-3 previously given in Section 3.1), then the system would theoretically release 21.3 wt. %  $\text{H}_2\text{O}$  from  $\text{Mg}(\text{OH})_2$  and 2.4 wt. %  $\text{H}_2$  from  $\text{MgH}_2$ , resulting in a total weight loss of 23.5 wt. %.

This is in broad agreement with both the DTA profile (only endothermic events can be identified) and the mass loss observed for Sample 5, which was found to be 21.5 % (91.5 % of the expected  $\text{H}_2\text{O}/\text{H}_2$  weight loss of 23.5 %). The MS spectrum of sample 5 shows in fact the release of both hydrogen and water during TG-DTA analysis. The lower mass loss may be imputed to the Mg metal impurity present in the hydride as well as a slight reaction of  $\text{MgH}_2$  with the  $\text{H}_2\text{O}$  released from the hydroxide during the first step of the reaction, associated with the evolution of a small amount of hydrogen.

Both Samples **11** and **15** show a lower mass loss with respect to the bulk materials as well as different DTA profiles as previously discussed. A weight loss of 12.6 % is observed for the milled system (**11**) and again both water and hydrogen are evolved during the thermal treatment according to the mass spectrum. Nevertheless, H<sub>2</sub> is released in two different steps, which coincide with the first LT exothermic event and the second HT endothermic event. This suggests that dehydration of hydroxide still occurs, but the water evolved is immediately hydrolysing part of the hydride leading to H<sub>2</sub> release together with H<sub>2</sub>O. Then the remaining hydride decomposes according to Equation 3-3 and hydrogen is evolved. The last endothermic event could be related to the melting of Mg resulting from MgH<sub>2</sub> dehydrogenation. Although the melting point of magnesium metal is higher (mp = 922 K)<sup>24</sup>, it may be possible to observe melting of Mg metal at lower temperatures due to a depression of the melting point caused by the reduced particle size of MgH<sub>2</sub>. This is supported also by the fact that no weight change is associated with such thermal event. However, a closer look at the DT profile could also suggest the last two events to be a combination of an endothermic event immediately followed by an exothermic one. In this case the last exothermic event (peak temperature of 758 K) could be related to the formation of MgO from the reaction between Mg resulting from MgH<sub>2</sub> dehydrogenation and the water evolved from Mg(OH)<sub>2</sub> dehydration.

A similar reaction pathway can be proposed for nanostructured materials, however the weight loss for Sample **15** was found to be only 7.9 %. This figure indicates that both H<sub>2</sub> and H<sub>2</sub>O are evolved from the nanostructured mixture. However, only hydrogen is detected in the mass spectrum in a two-step process when heating nanostructured materials. An almost negligible signal for water was observed. The first mechanistic step is hypothesized to be once again the simultaneous dehydration of Mg(OH)<sub>2</sub> and hydrolysis of most of the MgH<sub>2</sub> and this is supported both by the evidence of the LT exothermic event in the DTA profile and the hydrogen peak in the mass spectrum. The subsequent endothermic step of the reaction appears to be the dehydrogenation of the remaining hydride, which is believed to be followed by the melting of the newly formed Mg. However, the weak water signal observed would suggest that the evolved water could partly react with the newly formed Mg metal to yield MgO and release H<sub>2</sub>. In fact, as previously observed for Sample **11** (milled), it is possible the last event to be a combination of endothermic and exothermic events, relative to MgH<sub>2</sub> dehydrogenation and reaction of Mg to yield MgO respectively. As observed for the milled system, the exothermic event presents a peak temperature of 758 K. However, also in this case it is not possible to observe a weight gain associated to

such event. Moreover, the MS profile for **15** suggests that most hydrogen is released during the first exothermic event rather than during the second one.

Further, it is possible to note from DTA profiles as well as MS spectra show that the temperature of the thermal event associated with MgH<sub>2</sub> dehydrogenation is shifted towards higher temperatures when working with nanosized materials. This is believed to be caused by reactions occurring at the hydroxide-hydride interface. In fact, it has been reported by Bobet *et al.* that during the hydrolysis reaction of MgH<sub>2</sub> a passive layer of hydroxide is formed on the surface of the material.<sup>25</sup> In this case, due to the high temperature, that layer is believed to be MgO, associated with H<sub>2</sub>O evolution from Mg(OH)<sub>2</sub>, which leads to a core-shell-like structure with an inner core of MgH<sub>2</sub> and an outer shell of MgO. Moreover, reducing the particle size of the hydride results in an increased surface area and reactivity and thus an increased surface area of the outer MgO layer. This results in a lowered reactivity of the remaining MgH<sub>2</sub> leading to a higher onset and peak temperature of hydrogen release for milled and nanostructured systems. This is also in good agreement with the data previously reported by Leardini *et al.*.<sup>1</sup>

It is important to note that although the water signal is very weak as to that compared to that from hydrogen, the value of the integrated peak areas are comparable. A summary of the integrated peak area calculated from the MS spectra is given in Table 3-10.

**Table 3-10: Summary of the integrated peak area calculated from the MS spectra and normalised to the mass weight of each sample.**

Sample	Mass / mg	H <sub>2</sub> O peak area / Torr·mg <sup>-1</sup>	H <sub>2</sub> peak area (LT event) / Torr·mg <sup>-1</sup>	H <sub>2</sub> peak area (HT event) / Torr·mg <sup>-1</sup>
<b>1</b>	27.11	1.54E-10	–	–
<b>2</b>	27.88	5.77E-10	–	–
<b>Commercial Mg(OH)<sub>2</sub></b>	27.73	2.17E-10	–	–
<b>3</b>	24.49	–	–	8.01E-09
<b>Commercial MgH<sub>2</sub></b>	24.57	–	–	6.02E-09
<b>5</b>	23.66	1.17E-10	4.43E-10	3.63E-10
<b>11</b>	24.51	8.53E-11	4.81E-10	2.26E-10
<b>15</b>	24.50	–	3.61E-10	1.25E-10

The Kissinger method was employed for calculating the activation energies of the two main thermal events.<sup>12,11</sup> The first one a low temperature (LT) is believed to relate to the decomposition of Mg(OH)<sub>2</sub> (and simultaneous MgH<sub>2</sub> hydrolysis for milled and nano mixtures) and the one at high temperature (HT) is believed to correspond to the decomposition of the remaining MgH<sub>2</sub>. Data for obtaining Kissinger plots were collected for bulk, milled and nanostructured mixtures (Samples **18**, **19** and **20**) prepared using the exact same procedure to **4**, **10** and **14** and analysed as previously stated in Section 3.2.5. Kissinger plots for both thermal events are shown in Figure 3-16 (error bars omitted for clarity). A summary of the activation energies and linear regression equations are given in Table 3-11. Single Kissinger plots with relative error bars and DTA profiles are reported in Appendix A.

The activation energy for the LT thermal event was found to be 94±9, 155±6 and 202±8 kJ mol<sup>-1</sup> for Sample **18** (bulk), **19** (milled) and **20** (nano) respectively. The activation energy of 94±9 kJ mol<sup>-1</sup> found for the bulk system is consistent with the values reported in the literature for the dehydration of magnesium hydroxide (98±6 and 86 kJ mol<sup>-1</sup> respectively)<sup>1,26</sup>. However, the values calculated for milled and nanostructured mixtures were found to be higher. This could be explained by the fact that a simultaneous dehydration of Mg(OH)<sub>2</sub> and hydrolysis of MgH<sub>2</sub> is occurring, leading to an overall increased activation energy for the whole mechanistic step.

The activation energy for the HT thermal event corresponding to the decomposition of MgH<sub>2</sub> was found to be 144±9, 159±3 and 175±2 kJ mol<sup>-1</sup> for Sample **18**, **19** and **20** respectively. These values are in agreement with the literature; the activation energy of magnesium hydride in fact does not appear to be very affected from the particle size of the materials. Reported Ea values for bulk MgH<sub>2</sub> are 142, 166±4, 156 kJ mol<sup>-1</sup>, whilst Ea values for milled MgH<sub>2</sub> is 120 kJ mol<sup>-1</sup>.<sup>27,28,29</sup> Nonetheless, a trend can be observed in the samples as the activation energies tend to steadily increase of *ca.* 15 kJ mol<sup>-1</sup> from bulk (**18**) to nanostructured (**20**) mixtures, with the intermediate point found in the milled sample (**19**). This is in good agreement also with the TG-DTA-MS data previously collected for Samples **5** (bulk), **11** (milled) and **15** (nano): as a shifting of the MgH<sub>2</sub> decomposition peak towards higher temperatures was observed with the decreasing of the particle size from bulk to nano together with the aforementioned core-shell effect.

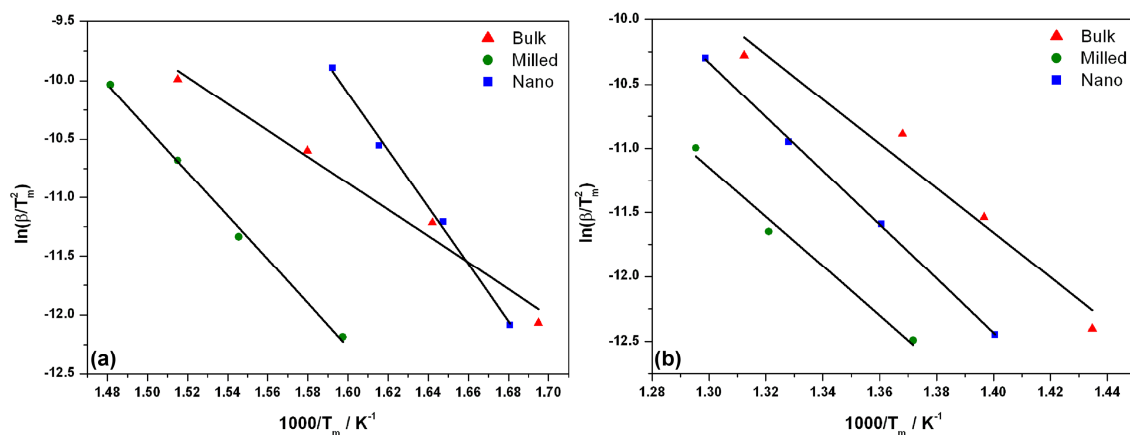


**Figure 3-16: Kissinger plots for Samples 18 (bulk; red triangles), 19 (milled; green dots) and 20 (nano; blue squares): (a) plots calculated for the LT thermal event; (b) plots calculated for the HT thermal event.**

**Table 3-11: Kissinger plot data for Samples 18, 19 and 20. Literature reported values for activation energy of  $Mg(OH)_2$  and  $MgH_2$  are given at the bottom of the table.**

Sample	Thermal Event	$E_a / KJ mol^{-1}$
18	LT	$94 \pm 9$
	HT	$144 \pm 9$
19	LT	$155 \pm 6$
	HT	$159 \pm 3$
20	LT	$202 \pm 8$
	HT	$175 \pm 2$


---

$E_{aMg(OH)_2} = 98 \pm 6 kJ mol^{-1}$  Ref. 1

$E_{aMg(OH)_2} = 86 kJ mol^{-1}$  Ref. 26

$E_{a \text{ bulk } MgH_2} = 142 kJ mol^{-1}$  Ref. 27

$E_{a \text{ bulk } MgH_2} = 166 \pm 4 kJ mol^{-1}$  Ref. 28

$E_{a \text{ bulk } MgH_2} = 156 kJ mol^{-1}$  Ref. 29

$E_{a \text{ milled } MgH_2} = 120 kJ mol^{-1}$  Ref. 29

---

### 3.3.2 Ex-situ PXD and Proposed Mechanisms

*Ex-situ* PXD studies were performed for each studied system in order to propose a mechanism of hydrogen release and to identify any differences in terms of the reaction steps of dehydrogenation when using differently processed starting materials.

Based on the STA results discussed in the previous section, the bulk, milled and nanostructured systems were each studied fully. The results obtained for each system are discussed below.

#### 3.3.2.1 Bulk System

*Ex-situ* PXD experiments were carefully planned based on the data discussed in Section 3.3.1.4. Figure 3-17 illustrates the DT-TGA profile for Sample 5 and the intermediate temperature points selected for *ex-situ* PXD experiments. TG-DTA-MS analysis was performed in order to try and isolate the intermediate phases formed. The intermediate temperature points of the individual thermal analyses are reported in Table 3-2. Six different temperatures points were studied: 298, 638, 673, 723, 773 and 873 K and X-ray diffraction patterns are presented in Figure 3-18. TG-DTA plots of the intermediate temperature point are presented in Appendix A.

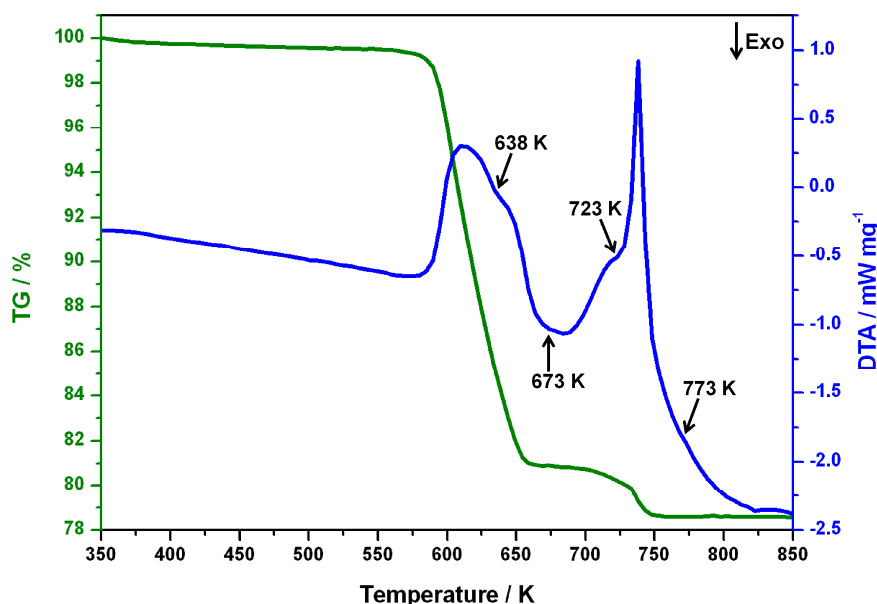


Figure 3-17: TG (green line) and DTA (blue line) data obtained for Sample 5. The temperature values are those selected for subsequent TG-DTA and PXD experiments.

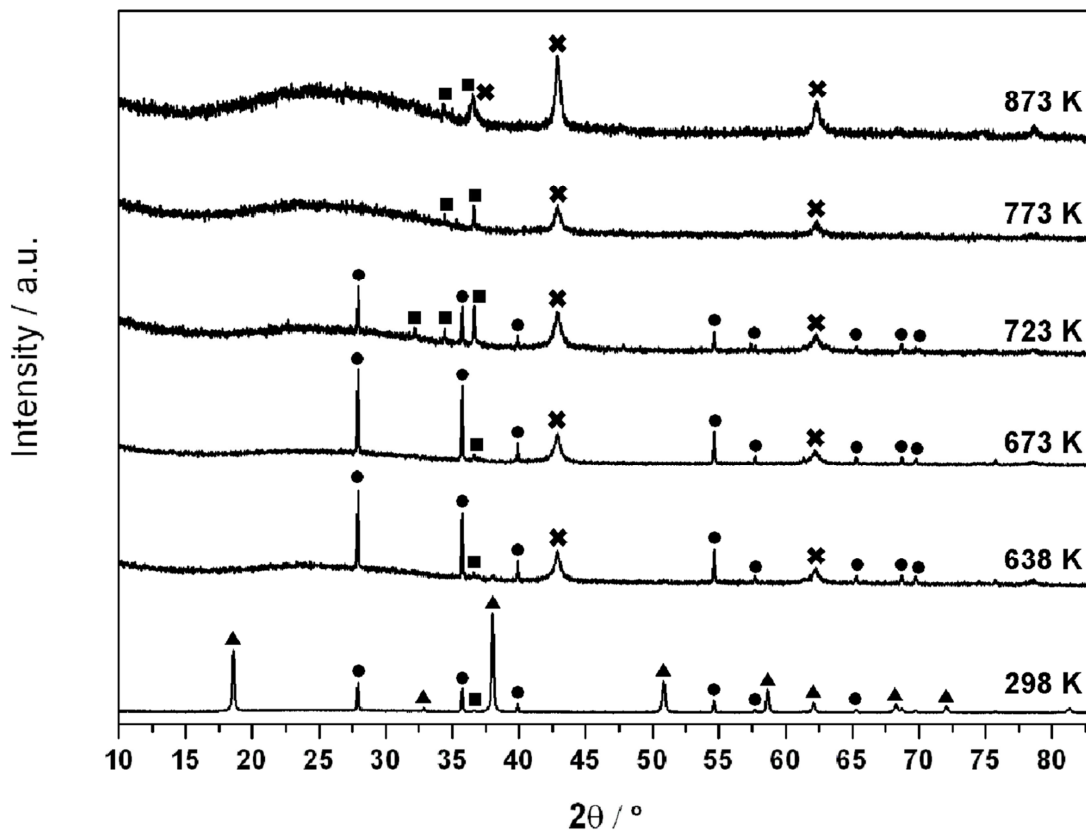


Figure 3-18: *Ex-situ* PXD patterns for Samples 4, 5, 6, 7, 8 and 9 collected at 298, 873 638, 673, 723 and 773 K respectively. Triangles denote  $\text{Mg}(\text{OH})_2$ , circles  $\beta\text{-MgH}_2$ , squares Mg and crosses MgO respectively.

During manual mixing, no reaction occurs between hydroxide and hydride prior to thermal treatment and  $\text{MgH}_2$  and  $\text{Mg}(\text{OH})_2$  were found to be the only phases observed in the diffraction pattern together with Mg impurity. At 873 K the reaction has gone to completion and the main phase present is MgO. Reflections assignable to magnesium metal can be identified as well. PXD patterns collected at 638 and 673 K both reveal the presence of MgO,  $\beta\text{-MgH}_2$  and Mg, suggesting that the complete dehydration of  $\text{Mg}(\text{OH})_2$  is achieved. This is in agreement with the TG-DTA profiles obtained for b- $\text{Mg}(\text{OH})_2$  starting material (Figure 3-10). At 723 K the intensities of reflections relative to MgO and Mg are increased, while the peaks relative to  $\text{MgH}_2$  are decreased in intensity, suggesting that the decomposition of  $\text{MgH}_2$  started. This is also in agreement with the TG-DTA-MS data obtained for  $\text{MgH}_2$  (Figure 3-13). At 773 K the only phases present are magnesium oxide and magnesium. A summary of the phases present at each temperature point is given in Table 3-12.

**Table 3-12: Summary of the temperature points and respective phases present for *ex-situ* PXD analysis for Samples 4, 5, 6, 7, 8 and 9.**

Sample	Temperature / K	Present Phases
4	298	Mg(OH) <sub>2</sub> ; MgH <sub>2</sub> ; Mg
6	638	MgH <sub>2</sub> ; Mg; MgO
7	673	MgH <sub>2</sub> ; Mg; MgO
8	723	MgH <sub>2</sub> ; Mg; MgO
9	773	MgO; Mg
5	873	MgO; Mg

Based on the results shown in Sections 3.3.1.4 and 3.3.2.1, the following mechanism of hydrogen release can be proposed Equation 3-5:



In the proposed mechanism, the first thermal event is the endothermic decomposition of magnesium hydroxide ( $\Delta H = 84.2 \text{ KJ mol}^{-1} \text{ H}_2\text{O}$ ) leading to the formation of magnesium oxide and the evolution of water. This is followed by the dehydrogenation of magnesium hydride ( $\Delta H = 76.2 \text{ KJ mol}^{-1} \text{ H}_2$ ) yielding magnesium metal and hydrogen.

### 3.3.2.2 Milled system

*Ex-situ* PXD experiments for Sample **11** were performed based on the results reported in Section 3.3.1.4. Diffraction data were collected at intermediate temperature points to try and isolate phases formed during the thermal treatment of the sample. In order to do this, TG-DTA-MS experiments were performed and the intermediate temperatures point for which PXD data were collected are summarised in Table 3-3. Four temperatures points were studied: 298, 658, 758, and 873 K: Figure 3-17 shows the full DT-TGA profile for Sample **11**, indicating the intermediate temperature points at which TG-DTA and diffraction data were subsequently obtained. TG-DTA plots from room temperature to each of the intermediate temperature point are presented in Appendix A. The respective *ex-situ* PXD patterns are presented in Figure 3-20.

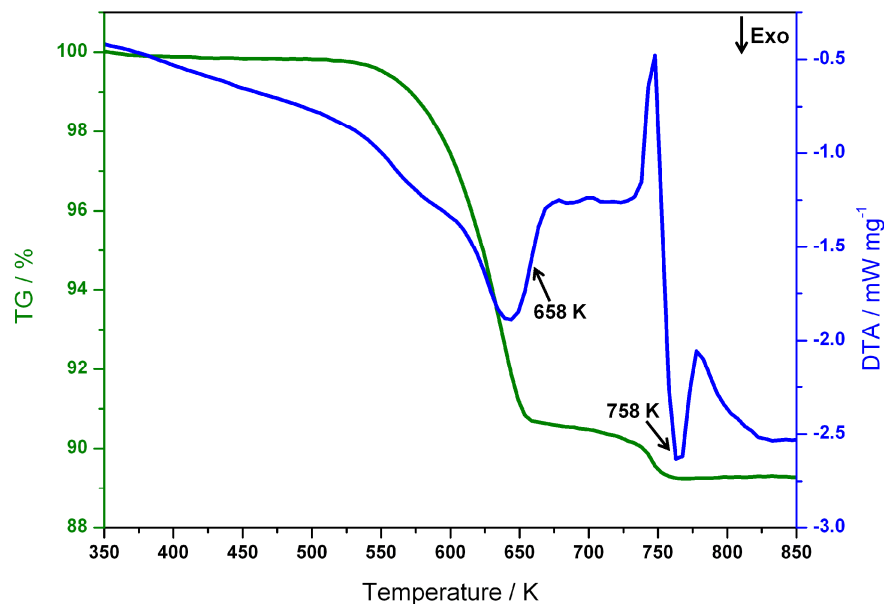


Figure 3-19: TG (green line) and DTA (blue line) data obtained for Sample 11.

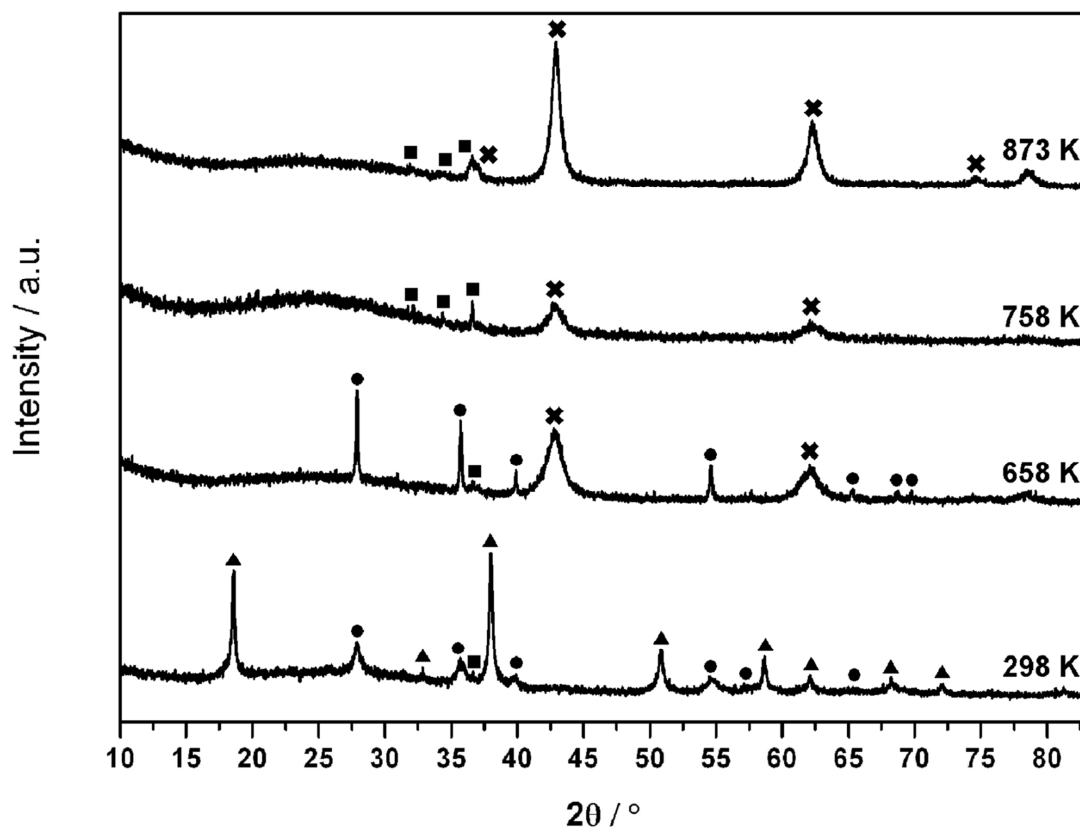


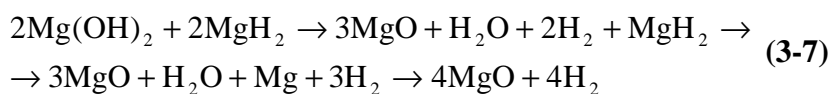
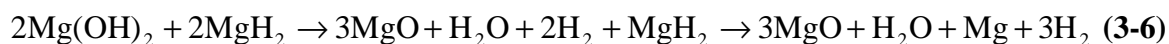
Figure 3-20: *Ex-situ* PXD patterns for Samples 10, 11, 12 and 13 collected at 298, 873, 658 and 758 K respectively. Triangles denote  $\text{Mg}(\text{OH})_2$ , circles  $\beta\text{-MgH}_2$ , squares Mg and crosses MgO respectively.

No reaction apparently occurs between hydroxide and hydride during the manual mixing before the heating treatment as only reflections assignable to MgH<sub>2</sub> and Mg(OH)<sub>2</sub> are present in the powder pattern together with Mg as an impurity. As for the bulk materials, at 873 K the reaction has gone to completion with the major phase present being MgO. However, peaks assignable to Mg metal can be additionally identified. At 658 K it is not possible to assign any peaks to magnesium hydroxide and the only phases present are magnesium oxide, magnesium hydride and magnesium metal. Reaching the 758 K temperature point results in the absence of MgH<sub>2</sub> peaks with the only phases present being MgO and Mg. From 758 to 873 K it is possible to note a decrease in the width of MgO reflections together with increased peak intensity. This would suggest that MgO is forming as the temperature increases, while the melting of magnesium metal is hypothesised to occur. However, based on the TG-DTA data discussed in Section 3.3.1.4, this change in intensity of Mg and MgO reflections could also be attributable to the reaction between Mg and H<sub>2</sub>O to yield MgO and evolve hydrogen. A summary of the phases identified at each temperature point throughout the heating process is given in Table 3-12.

**Table 3-13: Summary of the temperature points and respective phases present for *ex-situ* PXD analysis for Samples 10, 11, 12 and 13.**

Sample	Temperature / K	Phases Present
10	298	Mg(OH) <sub>2</sub> ; MgH <sub>2</sub> ; Mg
12	658	MgH <sub>2</sub> , Mg; MgO
13	758	MgO; Mg
11	873	MgO; Mg

Equations 3-6 and 3-7 illustrate the two proposed dehydrogenation mechanisms for the milled system, based on the results discussed in Sections 3.3.1.4 and 3.3.2.2:



When using milled materials, the first dehydrogenation step is the simultaneous decomposition of Mg(OH)<sub>2</sub> ( $\Delta H = 84.2 \text{ KJ mol}^{-1}\text{H}_2\text{O}$ ) and MgH<sub>2</sub> hydrolysis ( $\Delta H = -138.5 \text{ KJ mol}^{-1}\text{H}_2$ ) leading to the formation of magnesium oxide and the evolution of hydrogen.

Nevertheless, traces of water can still be detected from the MS analysis. This is followed by the decomposition of the remaining hydride ( $\Delta H = 76.2 \text{ KJ mol}^{-1}\text{H}_2$ ) yielding magnesium metal and hydrogen. The final step of the process is yet to be completely understood and two possible pathways are proposed: the mechanism proposed in Equation 3-6 involves the melting of magnesium metal, whilst the dehydrogenation reaction proposed in Equation 3-7 involves the reaction of the newly formed Mg with water to form MgO and release  $\text{H}_2$ .

### 3.3.2.3 Nanostructured system

Once again, based on the STA data discussed in Section 3.3.1.4, *ex-situ* PXD experiments were carefully planned to try and isolate the intermediate species: TG-DTA-MS analysis were performed and diffraction data obtained at intermediate temperature points collected as reported in Table 3-4. The DT-TGA profile for Sample 15 is shown in Figure 3-2. As for the milled system, four temperatures points were studied: 298, 673, 773 and 873 K. *Ex-situ* PXD patterns have been collected at each temperature point and the phases present identified (Figure 3-22). TG-DTA plots of the intermediate temperature point are presented in Appendix A.

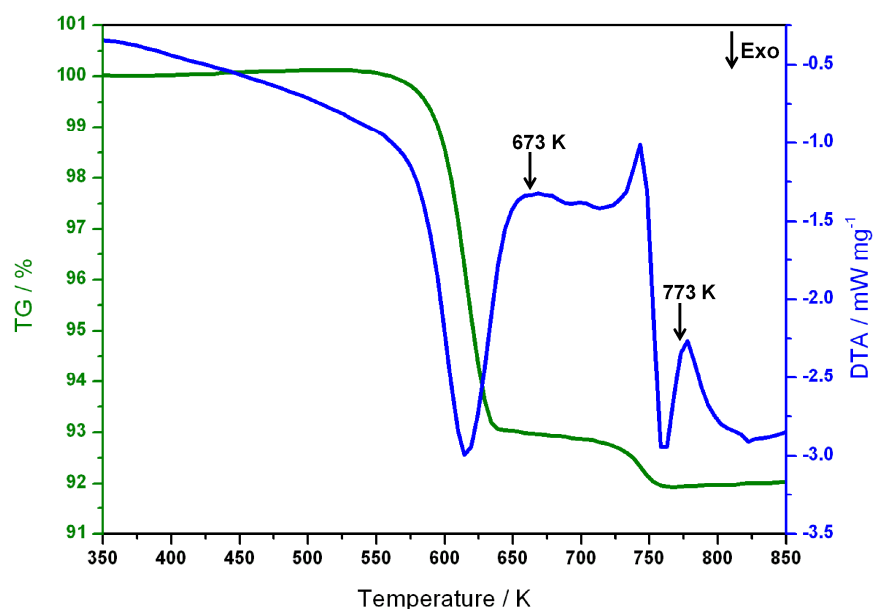


Figure 3-21: TG (green line) and DTA (blue line) data obtained for Sample 15.

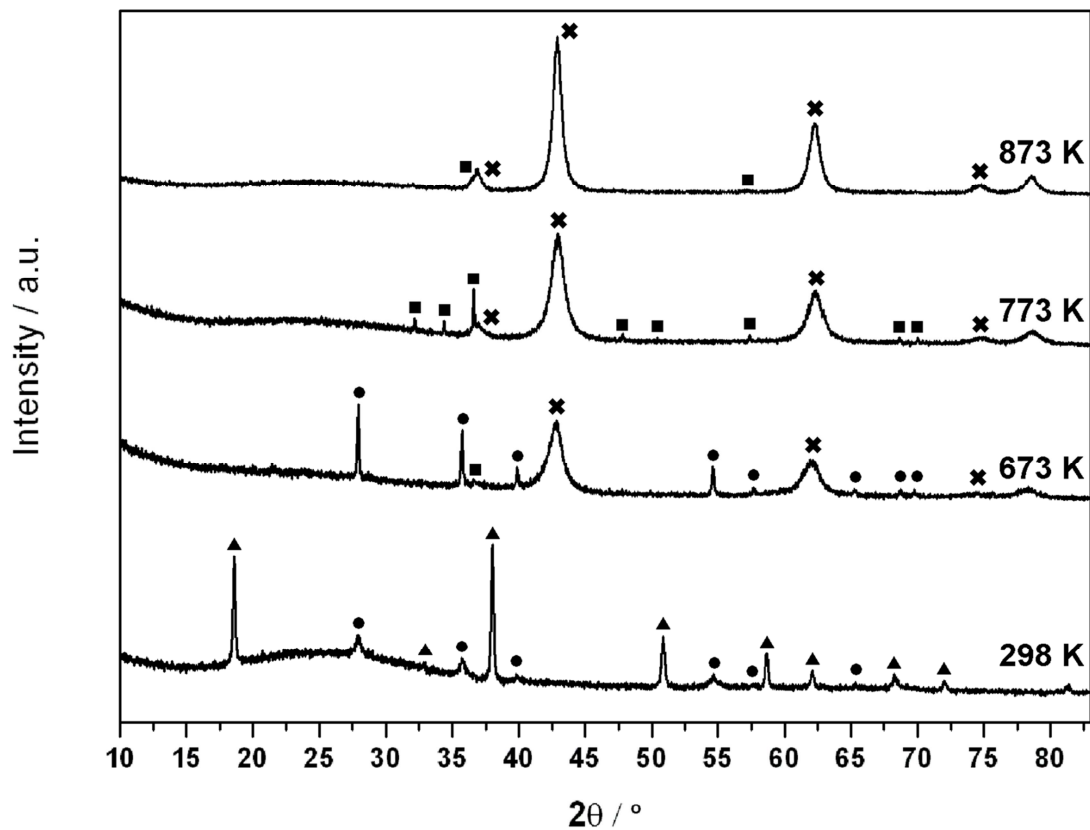


Figure 3-22: *Ex-situ* PXD patterns for Samples 14, 15, 16 and 17 collected at 298, 873, 673 and 773 K respectively. Triangles denote  $\text{Mg}(\text{OH})_2$ , circles  $\beta\text{-MgH}_2$ , crosses  $\text{MgO}$  and squares  $\text{Mg}$  respectively.

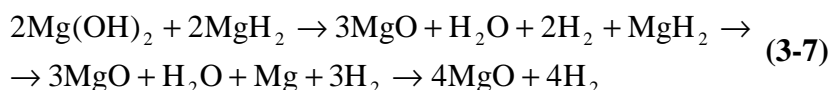
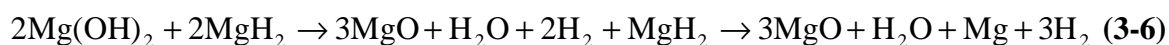
Similarly to the bulk and milled system, no reaction occurs during the manual mixing and the PXD pattern collected at 298 K prior to thermal treatment confirms that the only phases present in the mixture are  $\text{Mg}(\text{OH})_2$  and  $\text{MgH}_2$  together with  $\text{Mg}$  present as impurity from the as-received hydride. Again, the pattern collected after heating to 873 K shows that the only phases present are magnesium oxide and magnesium metal, confirming that the reaction has gone to completion. Reaching 673 K results in the complete absence of  $\text{Mg}(\text{OH})_2$  reflections together with the presence of new peaks attributable to magnesium oxide. At 773 K the reflections of  $\text{MgH}_2$  are completely absent, while  $\text{MgO}$  and  $\text{Mg}$  reflections both show an increased intensity. The 773-873 K range sees a decrease in the intensity of  $\text{Mg}$  reflections, together with an increase of the intensity of  $\text{MgO}$  peaks, suggesting that either  $\text{MgO}$  is forming as the temperature increase while magnesium is melting or  $\text{Mg}$  is reacting with water to form  $\text{MgO}$ .

A summary of the phases present at each intermediate temperature point is presented in Table 3-13.

**Table 3-14: Summary of the temperature points and respective phases present for *ex-situ* PXD analysis for Samples 14, 15, 16 and 17.**

Sample	Temperature / K	Present Phases
14	298	Mg(OH) <sub>2</sub> ; MgH <sub>2</sub> ; Mg
16	673	MgH <sub>2</sub> , Mg; MgO
17	773	MgO; Mg
15	873	MgO; Mg

The proposed mechanisms of hydrogen release when working with nanostructured materials was found to be similar to the dehydrogenation process proposed for the mechanically milled system (Equations 3-6 and 3-7). In fact, the reactions steps are essentially the same; however the two processes differentiate by the slight changes in temperature at which they occur.



As for the milled mixture, the dehydrogenation starts once again with the decomposition of Mg(OH)<sub>2</sub> ( $\Delta H = 84.2 \text{ KJ mol}^{-1}\text{H}_2\text{O}$ ) which takes place simultaneously with the hydrolysis of most of the MgH<sub>2</sub> ( $\Delta H = -138.5 \text{ KJ mol}^{-1}\text{H}_2$ ). This step yields MgO and H<sub>2</sub>. This is then followed by the decomposition of the remaining hydride ( $\Delta H = 76.2 \text{ KJ mol}^{-1}\text{H}_2$ ) leading to the formation magnesium metal and hydrogen. Again, the last step of the process is not completely clarified yet: the first proposed reaction pathway involves the melting of Mg metal (Equation 3-6), while the second one involves the reaction between magnesium and the evolved water to give MgO and H<sub>2</sub> (Equation 3-7). However, when working with nanostructured materials, a very weak signal related to water was detected during the TG-DTA-MS experiments, unlike in the system employing milled materials. This evidence favours the mechanism involving the reaction between Mg and H<sub>2</sub>O to form MgO (Equation 3-7). Data collected so far are although not conclusive.

SEM images were collected after thermal treatment in order to verify if the hexagonal platelet morphology of Mg(OH)<sub>2</sub> was retained. As it can be seen in Figure 3-23, it is possible to still identify hexagonal nanoplates, believed to be MgO relative to the dehydration product of Mg(OH)<sub>2</sub>. However they seem to have agglomerated with what it is

believed to be the melting products of Mg yielded from the decomposition of  $\text{MgH}_2$ . This results in the presence of clusters of Mg and MgO where a partial hexagonal morphology can still be observed.

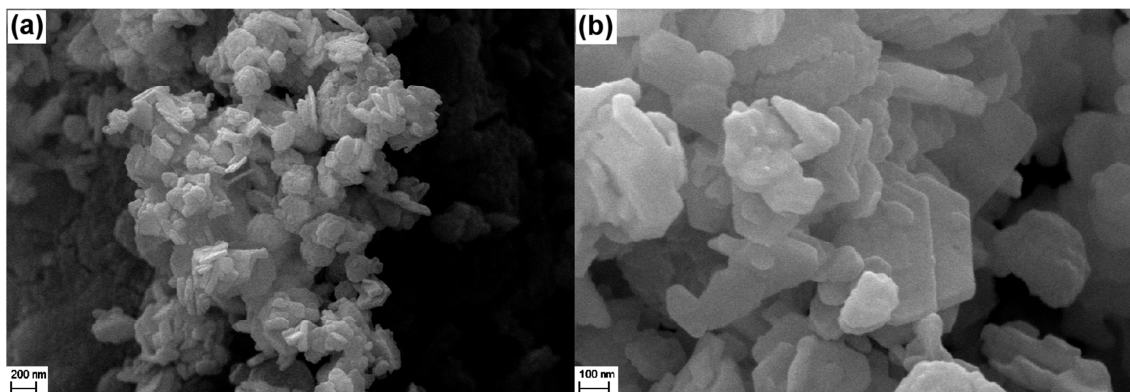


Figure 3-23: Collected SEM images for Sample 15: a) 200 nm scale b) 100 nm scale.

### 3.4 Conclusions and Future Work

Single-phase nanostructured magnesium hydroxide has been successfully synthesised using a facile synthetic route which combines microwave heating and hydrothermal treatment that employs only MgO and  $\text{H}_2\text{O}$  as starting materials.<sup>5,8</sup> The synthesis results in the production of nanostructured hydroxide with an hexagonal platelet morphology of a typical thickness 10-60 nm and a diameter and diagonals varying in the 100-300 nm and 200-600 nm range respectively. Rietveld refinement was performed on the synthesised hydroxide and lattice parameters have been calculated: these were found to be in good agreement with the literature values.<sup>18</sup> A dissolution-precipitation process has been proposed as mechanism of crystal growth (Equation 3-4) in which the formation of  $\text{Mg}(\text{OH})_2$  takes place on the MgO surface with  $\text{Mg}(\text{OH})^+$  forming as intermediate species. This is then followed by the removal of  $\text{Mg}(\text{OH})_2$  from MgO surface.<sup>22,23</sup> The oxide is believed to react with  $\text{H}_2\text{O}$  rapidly, with the formation of  $\text{Mg}(\text{OH})_2$  particles being faster than their removal from the surface of the oxide and the final step of the process being the cooling and agglomeration of the particles.

Reduction of the particle size of as-received magnesium hydroxide has been successfully obtained by mechanically milling the commercial reactant: the typical particle size of the milled hydroxide was found to be 70-200 nm in diameter.

Nanostructured  $\text{MgH}_2$  has been successfully obtained by mechanical milling the commercial reactant. Milling  $\text{MgH}_2$  results in better kinetics of dehydrogenation with an

onset temperature of hydrogen release lowered to 580 K (with a peak temperature of 625 K) with respect to the 667 K (with a peak temperature of 696 K) of the bulk material. This value is in agreement with the data obtained by Zhu *et al.* for milled MgH<sub>2</sub> in the absence of any additives or catalysts.<sup>2</sup> SEM imaging confirmed a decrease in the particle size with respect to the bulk material, with the typical particle size being in the 70-200 nm range.

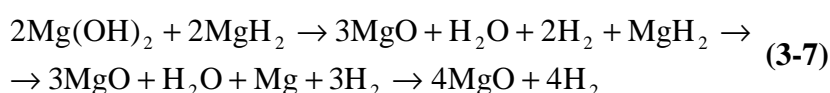
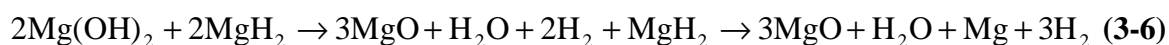
The Mg(OH)<sub>2</sub> – MgH<sub>2</sub> system was studied in detail comparing bulk, milled and nanostructured materials. All samples were prepared by manually mixing stoichiometric amounts of the starting material for 5 minutes under inert atmosphere inside a recirculating Ar- or N<sub>2</sub>-filled glove box. The onset temperature of hydrogen release is not dramatically lowered when comparing milled to nanostructured materials, important differences were observed in the DTA profiles and MS spectra when reducing the particle size to the nanometric scale. In particular, when working with bulk materials only endothermic peaks can be observed. The system releases both water and hydrogen, which are evolved from the decomposition of Mg(OH)<sub>2</sub> and MgH<sub>2</sub> respectively. Using milled materials or nanomaterials results in an exothermic reaction followed by an endothermic event. These are believed to be associated with simultaneous decomposition of both Mg(OH)<sub>2</sub> and MgH<sub>2</sub> followed by the dehydrogenation of the remaining hydride. Water and hydrogen are released from both the milled and nano systems, although the water signal was found to be very weak when employing nanostructured Mg(OH)<sub>2</sub>.

The Mg(OH)<sub>2</sub> – MgH<sub>2</sub> system can theoretically release up to 4.7 wt. % H<sub>2</sub>. However, after thermal treatment to 873 K the weight losses were found to be 21.5, 12.6 and 7.9 wt. % for bulk, milled and nano materials respectively. Activation energies were calculated for the two main thermal events for each system. These were found to be 94±9, 155±6 and 202±8 kJ mol<sup>-1</sup> for the low temperature event for the bulk, milled and nano system respectively. The activation energy values for the second HT event were found to be 144±19, 159±3 and 175±2 kJ mol<sup>-1</sup> for bulk, milled and nano materials respectively.

Two different mechanisms of hydrogen release have been proposed: one for the bulk materials and one for the milled and nanostructured systems, which seem to follow the same dehydrogenation process. In particular, in the bulk system the starting materials were found to behave independently with the first event being the dehydration of Mg(OH)<sub>2</sub> to yield MgO and H<sub>2</sub>O, followed by the dehydrogenation of MgH<sub>2</sub> to give Mg and H<sub>2</sub> (Equation 3-5).



Milled and nano materials were found to follow the same mechanistic steps in terms of H<sub>2</sub> release: the first event was found to be the simultaneous dehydration of Mg(OH)<sub>2</sub> and hydrolysis of MgH<sub>2</sub> to give MgO and evolve both H<sub>2</sub> and H<sub>2</sub>O. This step is then followed by the decomposition of the remaining hydride resulting in the formation of Mg and evolution of H<sub>2</sub> (Equation 3-6). It is not completely clear whether this is then followed by either the reaction between the newly formed Mg and the evolved water to yield MgO and release hydrogen or just the melting of magnesium metal.



Overall, the use of nanostructured materials has led to the best performance in terms of kinetics and thus it was identified to be the most promising one. Therefore all efforts should be focused on the improvement of the nanostructured system. The use of additives or catalysts could lead to improved kinetics of hydrogen release. In fact, finding a suitable candidate able to disrupt the proposed core-shell structure forming during the hydrolysis of MgH<sub>2</sub> should result in an exfoliation of the MgO passivation layer which can lead to faster hydrogen evolution. Several additives and catalysts have been tested in order to enhance the dehydrogenation properties of magnesium hydride by itself, although none of them has been tested in the presence of both Mg(OH)<sub>2</sub> and MgH<sub>2</sub>. These include calcium-, lithium- and sodium hydride to yield ternary hydrides and composites<sup>29,30</sup>, graphite and/or silicon carbide<sup>10</sup>, mixed-valence vanadium- and titanium-based materials and chloride compounds<sup>31,32,33,34,35</sup>. They all could be seen as suitable candidates to be tested on the Mg(OH)<sub>2</sub> – MgH<sub>2</sub> system. Attention should also be focused on developing the system in order to have one single hydrogen release event, while avoiding the release of water. *In-situ* PXD and PND experiments should also be performed in order to fully understand the proposed mechanism of hydrogen release for bulk, milled and nanostructured systems. Elucidating the exact reaction pathway is indeed pivotal in order to understand and improve the system further, especially for the milled and nanostructured systems, for which two different reaction mechanisms were proposed. Further, future studies should be focused also on the recyclability of such system, as the only end product is MgO. However, magnesium Mg metal is present as impurity of the end product: its weight fraction with respect to magnesium oxide should be exactly calculated (*i.e.* via Rietveld refinement). As detailed in Section 3.2.2, to yield nano-Mg(OH)<sub>2</sub>, MgO starting material is

reacted with water and any Mg present would react with water as well resulting in the formation of magnesium hydroxide and evolution of hydrogen. Moreover, the morphology of the synthesised nano  $\text{Mg}(\text{OH})_2$  does depend on the morphology of the starting material employed. In this sense, magnesium oxide should be fully investigated as potentially recyclable starting material for the synthesis of new nanostructured  $\text{Mg}(\text{OH})_2$ .

### 3.5 References

1. Leardini, F.; Ares, J. R.; Bodega, J.; Fernandez, J. F.; Ferrer, I. J.; Sanchez, C., Reaction pathways for hydrogen desorption from magnesium hydride/hydroxide composites: bulk and interface effects. *Phys. Chem. Chem. Phys.* **2010**, *12* (3), 572-577.
2. Wang, H.; Zhang, J.; Liu, J. W.; Ouyang, L. Z.; Zhu, M., Improving hydrogen storage properties of  $\text{MgH}_2$  by addition of alkali hydroxides. *International Journal of Hydrogen Energy* **2013**, *38* (25), 10932-10938.
3. Varin, R. A.; Parviz, R., Hydrogen generation from the ball milled composites of sodium and lithium borohydride ( $\text{NaBH}_4/\text{LiBH}_4$ ) and magnesium hydroxide ( $\text{Mg}(\text{OH})_2$ ) without and with the nanometric nickel (Ni) additive. *International Journal of Hydrogen Energy* **2012**, *37* (2), 1584-1593.
4. Drozd, V.; Saxena, S.; Garimella, S. V.; Durygin, A., Hydrogen release from a mixture of  $\text{NaBH}_4$  and  $\text{Mg}(\text{OH})_2$ . *International Journal of Hydrogen Energy* **2007**, *32* (15), 3370-3375.
5. James M. Hanlon; Laura Bravo Diaz; Giulia Balducci; Blane A. Stobbs; Marek Bielewski; Chung, P.; Gregory, a. D. H., Rapid surfactant-free synthesis of  $\text{Mg}(\text{OH})_2$  nanoplates and pseudomorphic dehydration to MgO. *CrystEngComm* **2015**.
6. Turner, R. C.; Hoffman, I.; Chen, D., Thermogravimetry of the dehydration of  $\text{Mg}(\text{OH})_2$ . *Canadian Journal of Chemistry* **1963**, *41* (2), 243-251.
7. Züttel, A., Materials for hydrogen storage. *Materials Today* **2003**, *6* (9), 24-33.
8. Hanlon, J. M. Synthesis and characterisation of direct and indirect hydrogen storage materials. University of Glasgow, 2013.
9. Cai, W.; Wang, H.; Sun, D.; Zhang, Q.; Yao, X.; Zhu, M., Destabilization of  $\text{LiBH}_4$  dehydrogenation through  $\text{H}^+ - \text{H}^-$  interactions by cooperating with alkali metal hydroxides. *RSC Advances* **2014**, *4* (6), 3082.
10. Reardon, H. Synthesis, structure and characterisation of novel lightweight energy materials based on group I & II metal compounds. PhD Thesis, University of Glasgow, 2014.

11. Kissinger, H. E., Reaction Kinetics in Differential Thermal Analysis. *Analytical Chemistry* **1957**, 29 (11), 1702-1706.
12. Kissinger, H. E., Variation on Peak Temperature With Heating Rate in Differential Thermal Analysis. *Journal of Research of The National Bureau of Standards* **1956**, 57 (4), 5.
13. Inorganic Crystallographic Structure Database (ICSD). <http://cds.rsc.org/> (accessed 22<sup>nd</sup> May 2014).
14. Belsky, A.; Hellenbrandt, M.; Karen, V. L.; Luksch, P., New developments in the Inorganic Crystal Structure Database (ICSD): accessibility in support of materials research and design. *Acta Crystallographica Section B* **2002**, 58 (3 Part 1), 364-369.
15. The International Centre for Diffraction Data (ICDD). <http://www.icdd.com/> (accessed 22<sup>nd</sup> May 2014).
16. A. C. Larson, R. B. v. D. *General Structure Analysis System (GSAS)*; Los Alamos Laboratory: Los Alamos, NM, USA, 1995, 1995; pp 86-748.
17. Toby, B. H., EXPGUI, a graphical user interface for GSAS. *J. Appl. Crystallogr.* **2001**, 34, 210-213.
18. Kazimirov, V. Y.; Smirnov, M. B.; Bourgeois, L.; Guerlou-Demourgues, L.; Servant, L.; Balagurov, A. M.; Natkaniec, I.; Khasanova, N. R.; Antipov, E. V., Atomic structure and lattice dynamics of Ni and Mg hydroxides. *Solid State Ionics* **2010**, 181 (39–40), 1764-1770.
19. Yu, J. C.; Xu, A.; Zhang, L.; Song, R.; Wu, L., Synthesis and Characterization of Porous Magnesium Hydroxide and Oxide Nanoplates. *The Journal of Physical Chemistry B* **2003**, 108 (1), 64-70.
20. Kuhlmann, H. R. a. A., *Z. Analyt. Chem.* **1924**, 65.
21. Gjaldbaek, J. K., *Z. Anorg. Allg. Chem.* **1925**, 144.
22. Bakhshi, G. L. S. a. N. N., The Kinetics and Mechanism of the Hydration of Magnesium Oxide in a Batch Reactor *Canadian Journal of Chemistry* **1969**, 47, 508-513.
23. Rocha, S. D.; Mansur, M. B.; Ciminelli, V. S., Kinetics and mechanistic analysis of caustic magnesia hydration. *Journal of Chemical Technology and Biotechnology* **2004**, 79 (8), 816-821.
24. *CRC Handbook of Chemistry and Physics*. 95<sup>th</sup> Edition ed.; CRC Press: Boca Raton, Florida 33431, 1980-1981.
25. Tayeh, T.; Awad, A. S.; Nakhil, M.; Zakhour, M.; Silvain, J. F.; Bobet, J. L., Production of hydrogen from magnesium hydrides hydrolysis. *International Journal of Hydrogen Energy* **2014**, 39 (7), 3109-3117.

26. Halikia, I.; Neou-Syngouna, P.; Kolitsa, D., Isothermal kinetic analysis of the thermal decomposition of magnesium hydroxide using thermogravimetric data. *Thermochimica Acta* **1998**, *320* (1–2), 75-88.
27. Han, J. S.; Pezat, M.; Lee, J.-Y., Thermal desorption of hydrogen from magnesium hydride. *Scripta Metallurgica* **1986**, *20* (7), 951-956.
28. Fernández, J. F.; Sánchez, C. R., Simultaneous TDS–DSC measurements in magnesium hydride. *Journal of Alloys and Compounds* **2003**, *356–357* (0), 348-352.
29. Huot, J.; Liang, G.; Boily, S.; Van Neste, A.; Schulz, R., Structural study and hydrogen sorption kinetics of ball-milled magnesium hydride. *Journal of Alloys and Compounds* **1999**, *293–295* (0), 495-500.
30. Tessier, J. P.; Palau, P.; Huot, J.; Schulz, R.; Guay, D., Hydrogen production and crystal structure of ball-milled  $\text{MgH}_2\text{–Ca}$  and  $\text{MgH}_2\text{–CaH}_2$  mixtures. *Journal of Alloys and Compounds* **2004**, *376* (1–2), 180-185.
31. Bazzanella, N.; Checchetto, R.; Miotello, A., Atoms and Nanoparticles of Transition Metals as Catalysts for Hydrogen Desorption from Magnesium Hydride. *Journal of Nanomaterials* **2011**, *2011*, 1-11.
32. Ren, C.; Fang, Z. Z.; Zhou, C. S.; Lu, J.; Ren, Y.; Zhang, X. Y., Hydrogen Storage Properties of Magnesium Hydride with V-Based Additives. *J. Phys. Chem. C* **2014**, *118* (38), 21778-21784.
33. Cui, J.; Wang, H.; Liu, J.; Ouyang, L.; Zhang, Q.; Sun, D.; Yao, X.; Zhu, M., Remarkable enhancement in dehydrogenation of  $\text{MgH}_2$  by a nano-coating of multi-valence Ti-based catalysts. *Journal of Materials Chemistry A* **2013**, *1* (18), 5603-5611.
34. Shahi, R. R.; Bhatnagar, A.; Pandey, S. K.; Dixit, V.; Srivastava, O. N., Effects of Ti-based catalysts and synergistic effect of SWCNTs-TiF<sub>3</sub> on hydrogen uptake and release from  $\text{MgH}_2$ . *International Journal of Hydrogen Energy* **2014**, *39* (26), 14255-14261.
35. da Conceicao, M. O. T.; dos Santos, D. S., Catalytic effect of chlorides compounds on hydrogen sorption properties of magnesium hydride. *Journal of Alloys and Compounds* **2014**, *615*, S715-S718.

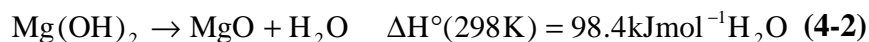
## 4 The lithium hydride – magnesium hydroxide ‘modular’ release system: an *in-situ* powder neutron diffraction study

### 4.1 Introduction

The magnesium hydroxide – lithium hydride system has been extensively studied.<sup>1,2</sup> The system can release up to 5.44 wt. % of hydrogen (Equation 3-1) and involves the reaction between magnesium hydroxide and lithium hydride to yield the respective oxides and the evolution of hydrogen.



The decomposition of both magnesium hydroxide and lithium hydride as individual components have been widely studied. In particular,  $\text{Mg(OH)}_2$  decomposes following a dehydration process to yield  $\text{MgO}$  and  $\text{H}_2\text{O}$  (Equation 4-2). The process can theoretically lead to the release of 30.8 wt. %  $\text{H}_2\text{O}$ .<sup>3,4</sup>



Lithium hydride can theoretically store to 12.59 wt. %  $\text{H}_2$ . However, an extremely air sensitive nature and a very high decomposition temperatures of nearly 720 °C (with a melting point of 680 °C)<sup>5</sup> render the use of  $\text{LiH}$  on its own unsuitable for solid state hydrogen storing solutions. Nonetheless, the use of  $\text{LiH}$  has been widely investigated as a component of Li-N-H systems for direct and indirect  $\text{H}_2$  storage as well as a component for hydride – hydroxide ‘modular’ hydrogen release systems. In terms of ‘modular’ systems, Vajo *et al.* were the first to propose the use of  $\text{LiH}$  in combination with  $\text{LiOH}$  (both as anhydrous and as the monohydrate) working under medium vacuum.<sup>6</sup> Following Vajo’s studies, in 2007 Lu *et al.* published a much more detailed study of the lithium hydride – lithium hydroxide system employing either  $\text{LiOH}$  or  $\text{LiOH}\cdot\text{H}_2\text{O}$ .<sup>7</sup>

During this work, such system has been fully studied using both bulk and nanostructured materials. The use of nanomaterials can be seen as a means to have a better control over the dehydrogenation process, leading to an enhancement of the reaction kinetics. The

system has been characterised using simultaneous thermogravimetric differential thermal analysis (TG-DTA) coupled to mass spectrometry (MS), powder X-ray diffraction and scanning electron microscopy. The results obtained are herein summarised and two mechanisms of hydrogen release are proposed. However, the data previously collected have not been conclusive in order to prefer one mechanism over another.

The aim of this chapter is to give an overview of the  $\text{Mg}(\text{OH})_2 - \text{LiH}$  system and to clarify the mechanism of hydrogen release. To fully understand the mechanism of hydrogen release, *in-situ* powder neutron diffraction (PND) experiments have been carried out. The use of deuterated starting materials has allowed us to identify all the components during the various stages of the reaction, particularly those containing the lightest elements Li and H. The ability to map the transformation/depletion of  $\text{LiH}(\text{D})$  especially has found to be crucial to elucidate the reaction pathway. *In-situ* PND data will be presented and discussed in detail and a conclusive dehydrogenation model will be proposed.

## 4.2 Experimental

### 4.2.1 Preparation of the $\text{Mg}(\text{OH})_2 - \text{LiH}$ system

Stoichiometric amounts of the starting materials were mixed manually using pestle and mortar for 5 minutes. All preparations were carried out under an inert atmosphere inside a recirculating glove box.

Typically, 375 mg of  $\text{Mg}(\text{OH})_2$  was mixed with 110 mg of LiH. Bulk mixtures were prepared using as-received  $\text{Mg}(\text{OH})_2$  (Sigma, 95%; denoted b- $\text{Mg}(\text{OH})_2$ ) and LiH (Sigma, 95%; denoted b-LiH), whereas nanostructured mixtures were prepared mixing synthesised nanostructured  $\text{Mg}(\text{OH})_2$  (denoted n- $\text{Mg}(\text{OH})_2$ ) and milled lithium hydride (denoted m-LiH).

#### 4.2.2 Preparation of the Mg(OD)<sub>2</sub> – LiD system for PND experiments

Stoichiometric amounts of Mg(OD)<sub>2</sub> and LiD were mixed manually using pestle and mortar for 5 minutes inside an Argon-filled glove box.

In order to provide a sufficient amount of sample for the Polaris experiment, 1 g of LiD and 3 g of Mg(OD)<sub>2</sub> were manually mixed for 5 minutes inside a recirculating Argon filled glove box at the RAL facilities.

#### 4.2.3 Synthesis of nanostructured Mg(OH)<sub>2</sub> (Mg(OD)<sub>2</sub>)

Approximately 1.6 g of magnesium oxide (Sigma Aldrich, 98%) were placed inside a 45 ml Teflon-lined autoclave for microwave synthesis, together with 30 ml of deionised water. H<sub>2</sub>O has been used when synthesising Mg(OH)<sub>2</sub>, whereas heavy water D<sub>2</sub>O has been used for the synthesis of Mg(OD)<sub>2</sub>. The MW autoclave was then heated up for a total of 4 minutes (1 minute of heating followed by 30 minutes of cooling each time) inside a domestic microwave oven. The product was then washed and centrifuged with either H<sub>2</sub>O or D<sub>2</sub>O three times. The white precipitate was collected and dried in air overnight. The reaction yields *ca.* 2 grams of pure nanostructured hydroxide as previously discussed in Section 3.2.1. The morphology of hexagonal nanoplates is retained when working with deuterated reagents.<sup>3</sup>

#### 4.2.4 Ball milling of LiH(D)

Nanostructured LiH was produced by mechanically milling the as-received hydride or deuteride (LiH: Sigma, 95%; LiD: Sigma, 98%). Approximately 1 g of hydride was loaded into a 50 ml stainless steel jar using 10 stainless steel balls as a grinding medium, under an Argon atmosphere inside a glove box. The jar was sealed with a rubber O-ring and an air sensitive clamp before being transferred out of the glove box and exposed to air. The milling process has been carried out using a Retsch PM100 planetary ball mill and LiH was milled at 450 rpm for 4 hours (ball-to-powder ratio of 40:1): a rest time of 1 minute per every 15 minutes of ball milling was used.<sup>2</sup>

#### 4.2.5 TG-DTA-MS studies

The hydroxide – hydride system was characterised by thermogravimetric analysis coupled with mass spectroscopy in order to obtain information on the onset and peak temperature of hydrogen release, weight loss percentage with respect to the hydrogen content of the system and the nature and amount of the gas evolved during the reaction.

TG-DTA experiments were performed using a Netzsch STA 409 PC, which was coupled with a Hiden HPR20 mass spectrometer for the identification and analysis of the evolved gas. Correction measurements were carried out using an empty alumina crucible and were created by setting the target temperature and appropriate heating rate until the desired temperature was reached. Where appropriate, the target temperature was typically held for 1 h. Initial experiments involved heating from room temperature to 873 K at 5 K min<sup>-1</sup> and holding for 1 h before cooling naturally to ambient temperature. Subsequent experiments were planned based on the results obtained and intermediate temperature points were studied to isolate any intermediate phases forming and ultimately to propose a mechanism of hydrogen release. All measurements were conducted under a flow of argon. For each experiment, approximately 20-25 mg of sample was loaded into the alumina sample pan inside the sample chamber (Section 2.4.1).

Furthermore, thermogravimetric analysis was performed in order to calculate the activation energy for the system using the Kissinger method.<sup>8,9</sup> Samples were heated to 773 K using heating rates of 2, 5, 10 and 20 K min<sup>-1</sup> respectively (Table 4-3) and Kissinger plots were obtained. A summary of samples and reactions carried out for the magnesium hydroxide – lithium hydride system are herein reported (Tables 4-1 and 4-2).

**Table 4-1: Summary of samples and preparations carried out for the development of the Mg(OH)<sub>2</sub> – LiH ‘modular’ system.**

Sample	Material	Preparation Conditions	Heating program / K
1	n-Mg(OH) <sub>2</sub>	4 min MW synthesis	–
2	m-LiH	4 h ball milling (15/1)	–
3	b-Mg(OH) <sub>2</sub> – b-LiH	5 min manual mixing	873 / 5 K min <sup>-1</sup> + 1 h dwell
4	n-Mg(OH) <sub>2</sub> – m-LiH	5 min manual mixing	873 / 5 K min <sup>-1</sup> + 1 h dwell
5	n-Mg(OH) <sub>2</sub> – m-LiH	5 min manual mixing	513 / 5 K min <sup>-1</sup>

**Table 4-2: Summary of reactions carried out for activation energy calculations.**

Sample	Material	Preparation Conditions	Heating program / K
6a	n-Mg(OH) <sub>2</sub> – m-LiH	5 min manual mixing	773 (2 K min <sup>-1</sup> )
6b			773 (5 K min <sup>-1</sup> )
6c			773 (10 K min <sup>-1</sup> )
6d			773 (20 K min <sup>-1</sup> )

#### 4.2.6 Powder X-ray diffraction (PXRD) experiments

All starting materials and synthesised compounds were analysed by PXD as described in Section 2.3.1.1. Capillaries were prepared for the characterisation of air sensitive materials: these were analysed with a d8 Bruker diffractometer. Data were typically collected between  $5 \leq 2\theta^\circ \leq 85$  for 1 h.

Non-air sensitive materials were characterised using a PANalytical X'Pert powder diffractometer, working in Bragg-Brentano geometry with the bracket stage. Data were usually collected between  $5 \leq 2\theta^\circ \leq 85$  for 30 minutes.

The data obtained were compared with the appropriate reference powder diffraction patterns calculated from data in the ICSD database<sup>10</sup> using the PowderCell package<sup>11</sup> or directly using the ICDD database<sup>12</sup> with the PANalytical HighScore Plus software.

#### 4.2.7 Scanning Electron Microscopy (SEM) imaging

Samples for SEM imaging were prepared as discussed in Section 2.3.5.1. A small amount of sample was deposited onto aluminium stubs using adhesive carbon tabs. The preparation of the samples was carried out inside a recirculating glove box under inert atmosphere. The samples were put into glass vials and sealed before being transferred out of the glove box, to minimise the exposure to air and moisture. Since charging was encountered, the samples were sputter-coated with a 10 nm layer of gold/palladium alloy in order to achieve better conductivity and increase the quality of the images.

The samples were then placed inside the vacuum column of the microscope, which was shut using an air-tight door and evacuated. The measurements were performed using a Philips XL30 ESEM, working in high vacuum mode with an applied accelerating voltage of 25 kV and a working distance of 5 mm, suitable for imaging.

#### 4.2.8 *In-situ* powder neutron diffraction (PND) experiments

In-situ powder neutron diffraction studies were carried out on the Polaris instrument at the ISIS facility at the Rutherford Appleton Laboratory in Didcot. Polaris is a high intensity, medium resolution powder diffractometer which is fully described in Section 2.3.2.1.

A fresh hydroxide – hydride mixture using deuterated reagents was prepared on site inside an Argon filled recirculating glove box and then loaded into a single wall quartz glass tube. The setup, already discussed in detail in Section 2.3.2.2, utilises Swagelok fittings enabling the entire assembly to be made vacuum tight to allow sample transfer into and out of the glove box. Approximately 4 g of mixture were prepared.

The *in-situ* PND experiment in Polaris was carefully planned based on the results obtained by thermogravimetric analysis (Section 4.3.1.1).

The experiment comprised a complete temperature range scan. Data were collected at room temperature before heating the samples to a maximum temperature of 673 K under flowing Argon. Attention was focused on the crucial temperatures of dehydrogenation in order to follow the reaction steps individually: the mixture was heated with short temperature steps and PND patterns collected every 10 K over the 448-548 K range.

Data were collected for approximately 1 h at each temperature point using detector banks 1 (very low angle,  $2\theta^\circ$  6-14), 2 (low angle,  $2\theta^\circ$  19-34), 3 (low angle,  $2\theta^\circ$  40-67), 4 (90 degrees,  $2\theta^\circ$  75-113) and 5 (back scattering,  $2\theta^\circ$  135-143). A summary of samples can be found in Tables 4-3 and 4-4.

Moreover, runs of the empty quartz tube at different temperature points were performed starting from room temperature up to 673 K. This allowed us to re-process all data sets using a Mantid<sup>13</sup> script using the empty quartz tube runs as background.

**Table 4-3: Summary of samples prepared for *in-situ* PND experiment at POLARIS.**

<b>Sample</b>	<b>Material</b>	<b>Preparations Conditions</b>	<b>Heating program / K</b>
<b>7</b>	n-Mg(OD) <sub>2</sub>	4 min MW synthesis	–
<b>8</b>	n-LiD	4 h ball milling (15/1)	–
<b>9</b>	n-Mg(OD) <sub>2</sub> – m-LiD	5 min manual mixing	873 / 5 K min <sup>-1</sup> + 1 h dwell
<b>10</b>	n-Mg(OD) <sub>2</sub> – m-LiD	5 min manual mixing	Table 4-4

**Table 4-4: Summary of data collected during the variable temperature *in-situ* PND experiment for the Mg(OD)<sub>2</sub> – LiD system under flowing Argon.**

<b>Sample</b>	<b>Temperature / K</b>	<b>Duration / min</b>
<b>11</b>	298	60
<b>12</b>	448	60
<b>13</b>	458	60
<b>14</b>	468	60
<b>15</b>	478	60
<b>16</b>	488	60
<b>17</b>	498	60
<b>18</b>	508	60
<b>19</b>	518	60
<b>20</b>	523	60
<b>21</b>	528	60
<b>22</b>	538	60
<b>23</b>	548	60
<b>24</b>	573	60
<b>25</b>	673	60

#### **4.2.9 Rietveld refinement against PND data**

Rietveld refinements against the collected PND ToF data were performed using the General Structure Analysis System (GSAS)<sup>14</sup> with the EXPGUI interface.<sup>15</sup> Prior to Rietveld refinement, all data sets were re-processed using a Mantid<sup>13</sup> script using the empty quartz tube runs as background.

Data from detector banks 3, 4 and 5 were consecutively refined. A total of 25 data sets were collected at various temperatures. First data from bank 5 (back scattering) were refined, followed by the addition of banks 4 (90 degrees) and 3 (low angle) respectively. The background was successfully modelled using Function 8 (reciprocal interpolation function). This was followed by the refinement of the cell parameters, atomic positions, isotropic temperature factors and profile parameters. Modelling of the peak shapes was carried out using Function 3 (an extension of Function 1, developed by Von Dreele, Jorgensen and Windsor)<sup>16</sup>, which is a convolution of a Pseudo-Voigt function with two back-to-back exponentials. This function models strain broadening due to sample effects such as particle size as well as the effects of instrumental design on the width of

reflections. Other phases were then added and refined as appropriate. At last, the phase fractions of the species present were refined in order to obtain an accurate overview of the weight fractions.

## 4.3 Results and Discussion

### 4.3.1 The $\text{Mg}(\text{OH})_2$ – LiH system

#### 4.3.1.1 Preparation of the system components

Nanostructured  $\text{Mg}(\text{OH})_2$  (Sample 1) has been successfully synthesised using the synthetic route described in Section 4.2.1. A detailed discussion of the material obtained can be found in Section 3.3.1.1.

Lithium hydride (Sample 2) was ball milled for 4 h at 450 rpm and this resulted in uniform particles size distribution of 1-3  $\mu\text{m}$  in diameter (Figure 4-1).

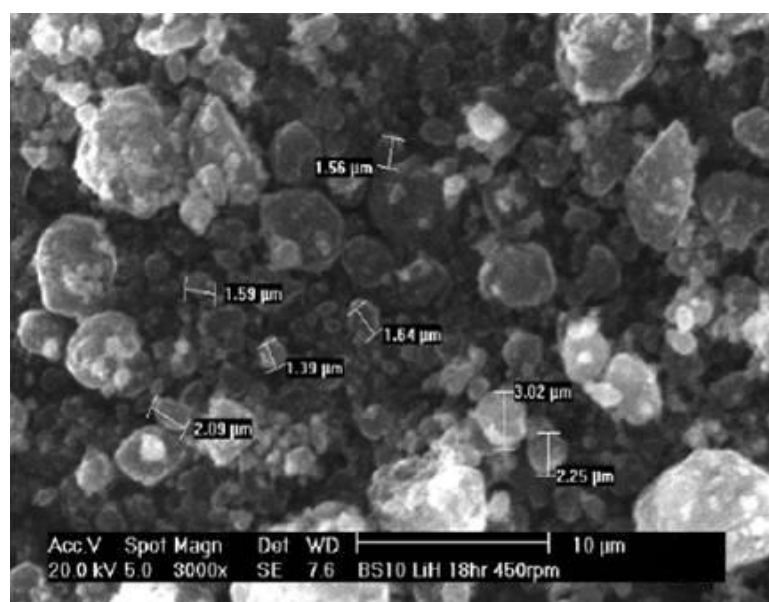


Figure 4-1: SEM image of Sample 2, m-LiH.

Powder X-ray diffraction patterns for both of the starting materials are presented in Figures 4-2 and 4-3. The former shows that the nanostructured magnesium hydroxide starting material is single phase. The latter shows no significant reaction occurs during the milling of LiH. Lithium oxide can be identified as impurity, however its presence was observed in the pre-milled as supplied material and it is not due to the milling process.

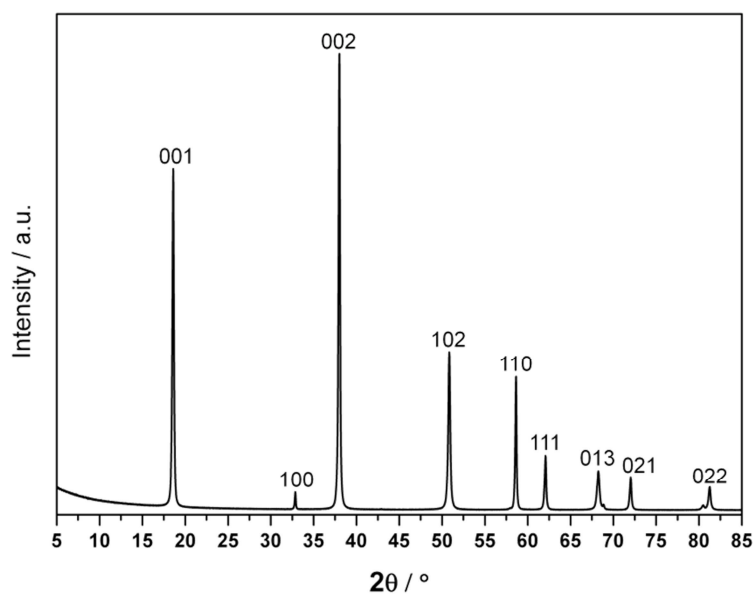


Figure 4-2: PXD pattern of Sample 1, synthesised n-Mg(OH)<sub>2</sub>.

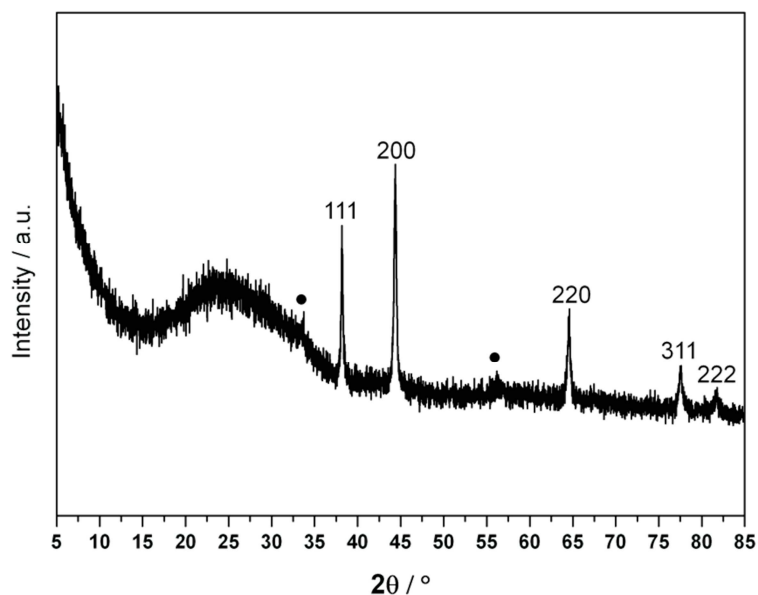


Figure 4-3: PXD pattern of Sample 2, m-LiH. The black circles indicate the presence of Li<sub>2</sub>O.

#### 4.3.1.2 TG-DTA-MS data

TG-DTA-MS experiments were performed on Samples **3** and **4** to determine the onset temperature as well as the peak temperature of hydrogen release and the weight loss for the two systems (Figures 4-4 and 4-5). The results obtained are summarised in Table 4-5.

**Table 4-5: Onset temperature, peak temperatures and weight losses for Samples 3 and 4.**

Sample	Onset T / K	Peak T / K	Weight Loss / %	Evolved Gases
<b>3</b>	478	525	5.1	H <sub>2</sub>
<b>b-Mg(OH)<sub>2</sub> – b-LiH</b>		583		
		626		
<b>4</b>	453	489	4.7	H <sub>2</sub>
<b>n-Mg(OH)<sub>2</sub> – m-LiH</b>		529		
		610		

As can be seen in Figure 4-4, TG-DTA results for ground Mg(OH)<sub>2</sub> – LiH mixtures show important differences between the bulk and the nanostructured samples. In fact, the reaction between milled lithium hydride and nanoplates of magnesium hydroxide results in a reduction in the onset temperature for hydrogen release to 453 K from 478 K for the bulk reagents. The dehydrogenation kinetics appear to be improved as well, reducing the total time over which hydrogen is evolved from the mixture. The TG-DTA data is in good agreement with the MS profiles (Figure 4-5): for Sample **3** (bulk) three distinct hydrogen releases can be identified. For Sample **4** (nano) also three hydrogen evolutions peaks can be observed. The temperature at which the dehydrogenation event occurs are in accordance with the differential thermal analysis results.

The weight loss appears to be closer to the theoretical 5.4% wt. H<sub>2</sub> when working with bulk materials. The use of nanostructured starting materials leads to a weight loss of 4.7 wt. % (87.0 % of the theoretical 5.4 %), suggesting that the dehydrogenation process starts during the milling, rather than during the thermal treatment. For the bulk materials the weight loss is 5.1 wt. % which is nearly 95% of the expected figure. The lower weight losses observed for both bulk and nanostructured materials may also be due to the presence of Li<sub>2</sub>O impurity in the LiH phases, leading to an inferior amount of hydrogen present in the system.

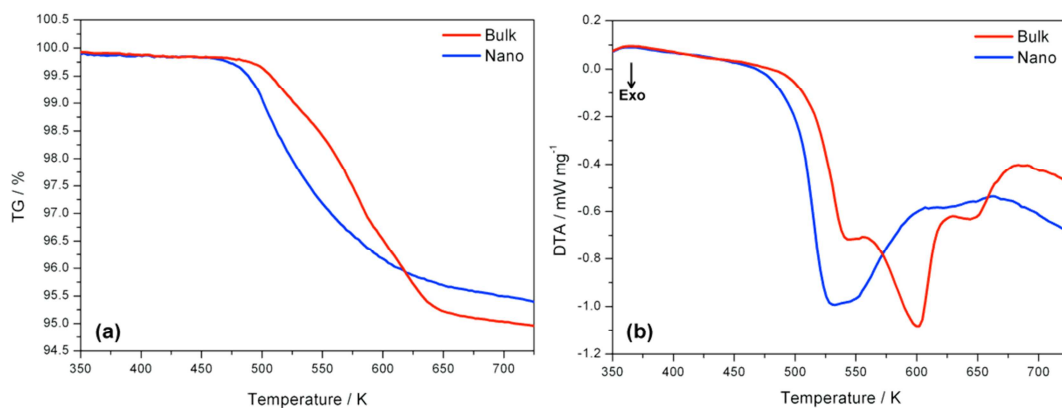


**Figure 4-4:** (a) TG and (b) DTA data comparison for bulk (3; red) and nanostructured (4; blue)  $\text{Mg}(\text{OH})_2 - \text{LiH}$  materials.

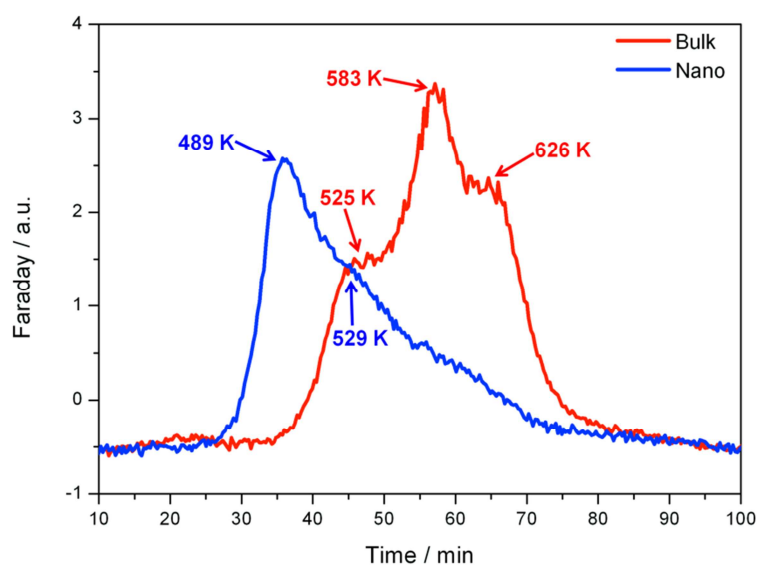


**Figure 4-5:** MS profiles Vs time for Sample 3 (bulk mixture, red line) and Sample 4 (nanostructured mixture, blue line).

Moreover, the TG-DTA data suggest that the dehydrogenation process is a multiple-step reaction. Once again, a noticeable difference can be observed between the nano and the bulk materials. Examination of the DTA profile suggests a three-step mechanism for the nanomaterials, with the first event starting at 453 K (with a temperature peak of 489 K) and the second thermal event occurring immediately afterwards with a peak temperature of 529 K and followed by the third event with a peak temperature of 610 K. The reaction of the bulk materials seems to follow a three-step mechanism as well. The dehydrogenation starts at 478 K and follows 3 consecutive thermal events, with a peak temperature of 525, 583 and 626 K respectively.

The use of nanostructured materials has led to better performances of the system and thus it was further investigated. The Kissinger plot for a nanostructured mixture prepared in an

identical procedure to **4** was obtained by performing TG-DTA experiments at different heating rates on Sample **6** (Figure 4-6). DTA profiles are reported in Appendix B.

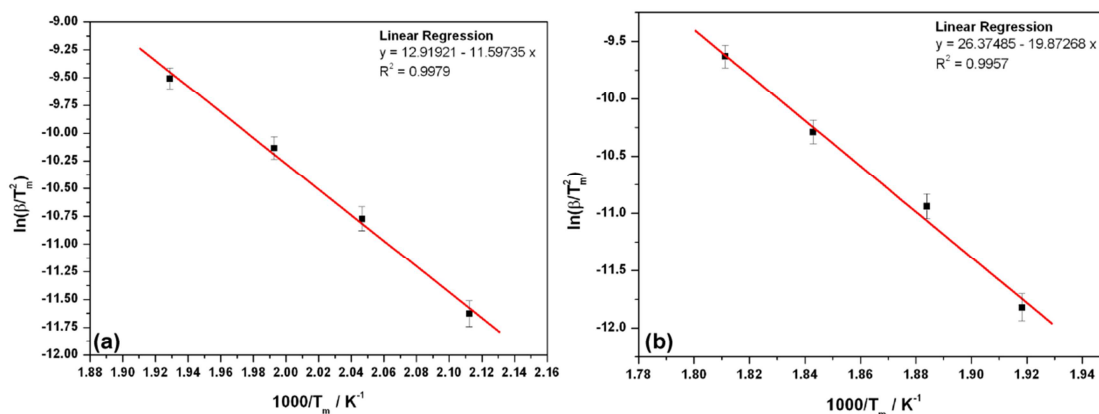


Figure 4-6: a) Kissinger plots for Samples 6: (a) plots calculated for the LT thermal event; (b) plots calculated for the HT thermal event.

Table 4-6: Kissinger plot data for Samples 6. Literature reported values for activation energy of  $\text{Mg}(\text{OH})_2$ , LiH and LiOH are given at the bottom of the table.

Sample	Thermal Event	$E_a / \text{kJ mol}^{-1}$
6	LT	$96 \pm 4$
	HT	$165 \pm 9$
<hr/>		
$E_{a\text{Mg}(\text{OH})_2} = 86 \text{ kJ mol}^{-1}$ Ref. 17		
$E_{a\text{Mg}(\text{OH})_2} = 98 \pm 6 \text{ kJ mol}^{-1}$ Ref. 18		
$E_{a\text{LiH}} = -6.7 \text{ kJ mol}^{-1}$ ; Ref 19		
$E_{a\text{LiOH}} = 123 \pm 4 \text{ kJ mol}^{-1}$ ; Ref. 20		

The activation energy for the low temperature event was found to be  $96 \pm 4 \text{ kJ mol}^{-1}$ . This value is in good agreement with the literature for the dehydration of magnesium hydroxide ( $E_{a\text{Mg}(\text{OH})_2} = 86 \text{ kJ mol}^{-1}$ ;  $E_{a\text{Mg}(\text{OH})_2} = 98 \pm 6 \text{ kJ mol}^{-1}$ )<sup>17,18</sup>. The  $E_a$  value for the high temperature event was calculated to be  $165 \pm 4 \text{ kJ mol}^{-1}$ . This is not in agreement with the  $E_a$  value found in the literature for the decomposition of LiH, which was found to be a barrierless reaction characterised by a negative value of activation energy ( $E_{a\text{LiH}} = -6.7 \text{ kJ mol}^{-1}$ )<sup>19</sup>. However, the value calculated for the LiH –  $\text{Mg}(\text{OH})_2$  system is higher when compared to the activation energy of lithium hydroxide decomposition ( $E_{a\text{LiOH}} = 123 \pm 4 \text{ kJ mol}^{-1}$ )<sup>20</sup>.

$\text{mol}^{-1})^{20}$ , suggesting that the HT event is somehow related to the presence of LiOH. The higher value may be due to the fact that an interaction between LiOH and LiH is occurring at that temperature range, so the activation energy would be related to that solid state reaction rather than LiH decomposition.

#### **4.3.1.3 *Ex-situ* PXD analysis and proposed mechanisms: an intermediate study of the nanostructured system**

Based on the STA results discussed in the previous Section, *ex-situ* PXD studies were performed on the nanostructured  $\text{Mg}(\text{OH})_2 - \text{LiH}$  system in order to propose a mechanism of hydrogen release indentifying the mechanistic steps of dehydrogenation. In order to try and isolate the intermediate species, TG-DTA-MS analyses were performed and intermediate temperature points in the profile were selected. The post STA products were collected and *ex-situ* PXD analysis carried out for each temperature point.

Experiments were performed at three different temperature points: 298, 513 and 873 K (Figure 4-7). No reaction apparently occurs between hydroxide and hydride during the manual mixing as since prior to the thermal treatment only  $\text{Mg}(\text{OH})_2$  and LiH are observed in the diffraction pattern. At 873 K the reaction has gone to completion as the only phases present are the respective oxides. In order to try and isolate intermediate species, TG-DTA-MS analysis was performed: Sample **5** was heated to 513 K at  $2 \text{ K min}^{-1}$ . PXD patterns reveal the presence of LiH,  $\text{Mg}(\text{OH})_2$ , MgO, LiOH and a small amount of  $\text{Li}_2\text{O}$ . Moreover, it is possible to note differences in peak widths for different phases: in particular the peaks assignable to Mg species (MgO) are very broad with respect to the lithium species: this may be due to the nanostructured nature of the material leading to a broadening of diffraction peaks.<sup>21,22</sup>

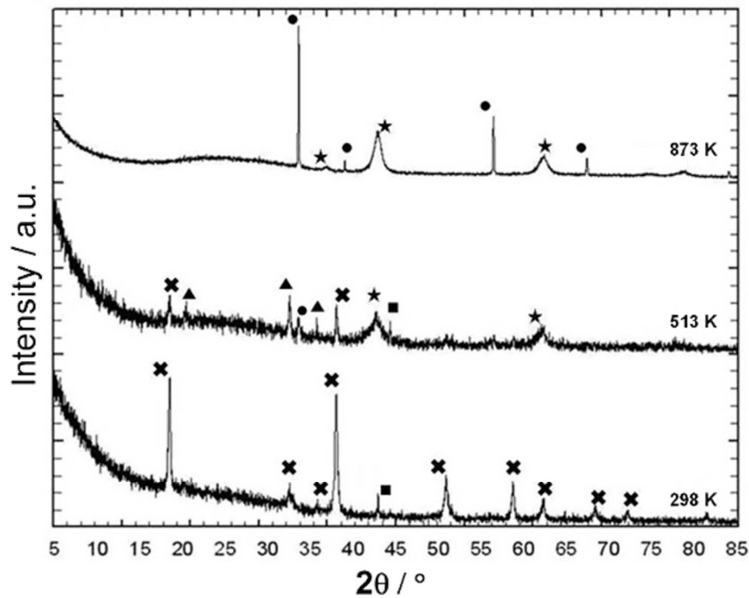
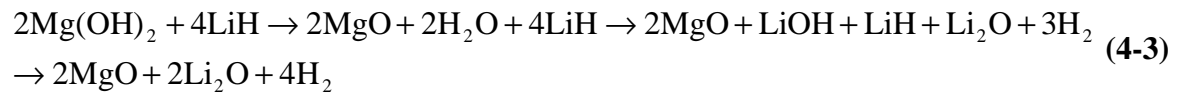


**Figure 4-7:** *Ex-situ* PXD patterns of Samples 4 and 5 compared to the mixture of starting materials at room temperature (PXD patterns of Sample 4 were collected at 298 K, prior to thermal treatment). Crosses denote  $\text{Mg}(\text{OH})_2$ , squares  $\text{LiH}$ , stars  $\text{MgO}$ , triangles  $\text{LiOH}$  and circles  $\text{Li}_2\text{O}$  respectively.

Based on the results shown in Sections 4.3.1.2 and 4.3.1.4, two alternative mechanisms of hydrogen release could be proposed. The first involves the release of gaseous water, the second would proceed entirely in the solid state.



In Equation 4-3 (Mechanism 1), the first thermal event is the endothermic decomposition of magnesium hydroxide ( $\Delta H = 84.2 \text{ KJ mol}^{-1}$ ) leading to the formation of magnesium oxide and the evolution of water. This is followed by the hydrolysis of two equivalents of the hydride ( $\Delta H = -178.3 \text{ KJ mol}^{-1}$ ) forming lithium hydroxide and lithium oxide. By analogy with the first step of the process, the last mechanistic step could involve the dehydration of  $\text{LiOH}$  to give  $\text{Li}_2\text{O}$  and release water with a subsequent hydrolysis of the remaining hydride. However, the last step of this mechanism is believed to be the solid state reaction between  $\text{LiOH}$  and the remaining  $\text{LiH}$  to form  $\text{Li}_2\text{O}$  ( $\Delta H = -9.4 \text{ KJ mol}^{-1}$ ).

This involves the combination of H<sub>2</sub> in the solid state form: Lu *et al.* suggested a similar reaction for the LiOH·H<sub>2</sub>O – LiH system, which proceeds through the initial dehydrogenation of the hydroxide and subsequent reaction of LiOH and LiH.<sup>7</sup> Moreover, for the last dehydrogenation step, a similar reaction pathway has been proposed by Drozd *et al.* for the NaBH<sub>4</sub> – Mg(OH)<sub>2</sub> system.<sup>23</sup> Recently Zhu *et al.* investigated the dehydrogenation behaviour of LiBH<sub>4</sub> mixed with alkali hydroxides, where a destabilization due to the interaction between H<sup>+</sup> from OH<sup>-</sup> and H<sup>-</sup> from the borohydride was hypothesised.<sup>24</sup> Based on this evidence, the first proposed reaction pathway, the mechanism of hydrogen release appears to be a three-step process.

In Equation 4-4 (Mechanism 2) instead, the formation of lithium hydroxide occurs simultaneously to the decomposition of magnesium hydroxide, implying that this process happens entirely in the solid state. This reaction is similar to dehydrogenation of LiNH<sub>2</sub> and LiH in the Li-N-H system, involving a proposed H<sub>2</sub> combination in the solid state.<sup>25</sup> The first step is then followed by the reaction of the remaining LiH with LiOH as for Equation 4-3. Hence, for this dehydrogenation process, the proposed reaction pathway involves a two-steps mechanism.

However, since it is very difficult to identify phases containing light elements such as lithium and hydrogen, the data collected has not been conclusive to identify one mechanism over the other. If Equation 4-3 was favoured, at 513 K magnesium hydroxide would not be present as it would dehydrate to MgO and the magnesium oxide – lithium hydride intermediate could be easily isolated before LiOH is formed. However, the reaction between the water evolved and LiH could be very fast. In fact, it is possible to draw an analogy with the Li-N-H system. In particular, for Li-N-H systems, it has been proposed that the amide decomposes to ammonia and this evolved NH<sub>3</sub> mediates the hydrogen release with an ultrafast reaction with LiH.<sup>26</sup> In the present case, it is not clear whether decomposition followed by hydrolysis is a prerequisite for the dehydrogenation process. *Ex-situ* PXD data would suggest that Equation 4-4 is favoured as it is not possible to isolate the MgO – LiH intermediate before LiOH is formed. Nevertheless, TG-DTA data previously discussed would seem to favour Equation 4-3: it is possible to identify three distinct thermal events which could be associated to Mg(OH)<sub>2</sub> dehydration, LiH hydrolysis and the LiH – LiOH solid state reaction respectively.

Moreover, the mass spectrometry coupled with differential thermogravimetric analysis has not given any conclusive evidence, since no rise in the detected water decomposition as might be expected from the hydroxide was observed.

In this sense, *in-situ* PND data combined with the data already obtained were considered crucial in elucidating the mechanism of H<sub>2</sub> release. The PND data collected are discussed in the following Section.

### 4.3.2 Powder neutron diffraction experiments

#### 4.3.2.1 Preparation and preliminary characterisation of the system

Deuterated reagents were prepared as discussed in Sections 4.2.1, 4.2.2 and 4.2.4. Nanostructured Mg(OD)<sub>2</sub> (Sample 7) was successfully synthesised, whereas nano LiD (Sample 8) was obtained by ball milling. As shown in Figures 4-8 and 4-9, deuterated magnesium hydroxide appears to be pure phase, whereas commercial lithium deuteride, after milling, indicates lithium oxide is present as an impurity. However, the Li<sub>2</sub>O impurity comes from the pre-milled commercial LiD.

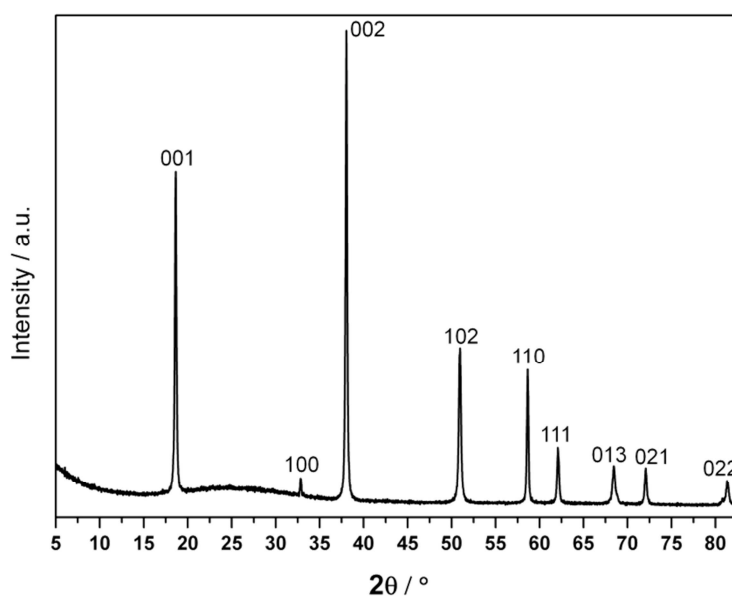
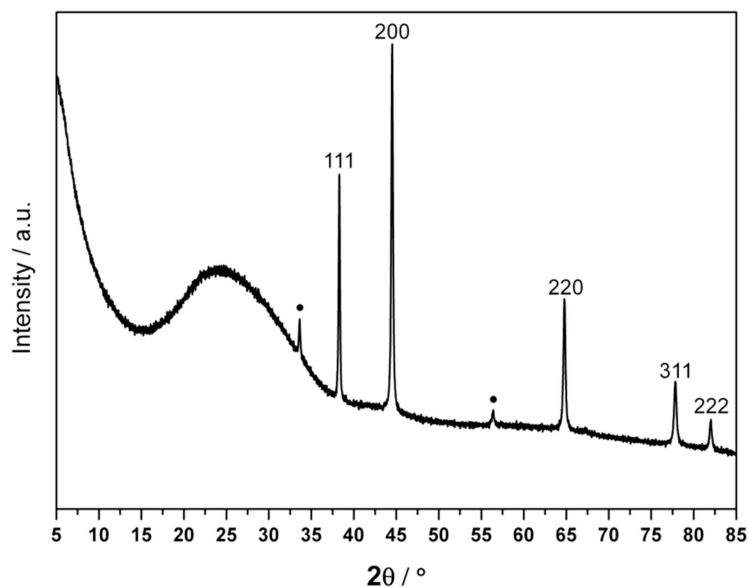


Figure 4-8: PXD pattern of Sample 7, synthesised nanostructured Mg(OD)<sub>2</sub>



**Figure 4-9: PXD analysis showing the experimental pattern of Sample 8, ball milled LiD. The black circles indicate the presence of  $\text{Li}_2\text{O}$ .**

TG-DTA analysis of the deuterated mixture was performed to determine any shift in the onset temperature of  $\text{D}_2$  release with respect to the hydrogenated materials. As shown in Figure 4-10, the results have been found to be consistent with the ones obtained for Sample **4** ( $\text{Mg}(\text{OH})_2 - \text{LiH}$ ) in terms of onset and peak temperatures of  $\text{H}_2/\text{D}_2$  release: TG-DTA profile for Sample **9** ( $\text{Mg}(\text{OD})_2 - \text{LiD}$ ) shows an onset temperature of  $\text{D}_2$  release of 442 K and peak temperatures of 495 and 528 K respectively. However, as opposed to Sample 4, it is not possible to identify the third thermal event when working with deuterated materials. In this sense, in-situ PND experiments are vital in order to completely clarify the mechanism of deuterium release for the  $\text{Mg}(\text{OD})_2 - \text{LiD}$  system. The higher weight loss of 8.8 wt. % is due to the use of deuterated materials (theoretical gravimetric capacity for the deuterated system is 10.2 wt. %  $\text{H}_2$ ). The lower mass change with respect to the theoretical figure is believed to be related to the presence of  $\text{Li}_2\text{O}$  impurity in the commercial LiD. Mass spectroscopy confirmed that the only gas evolved during the thermal treatment is  $\text{D}_2$ .

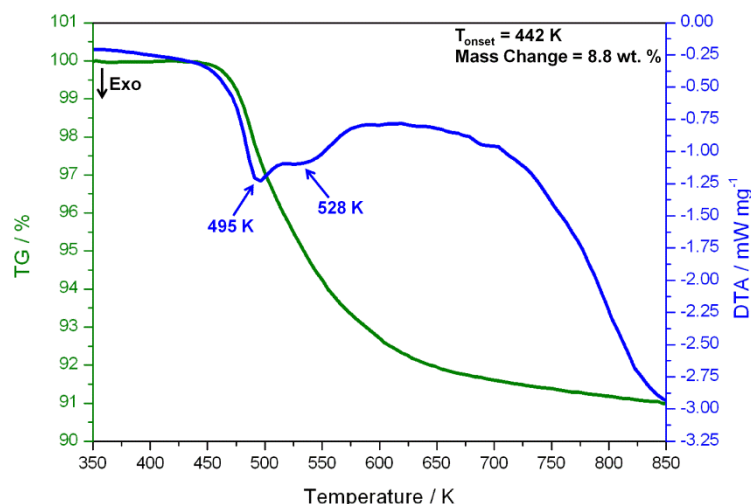


Figure 4-10: TG (green line) and DTA (blue line) data obtained for Sample 9.

### 4.3.3 The Polaris experiment

Initially, room temperature data were collected to ensure that no reaction occurred during the preparation of the PND sample. The sample was heated to 448 K. In order to avoid overshooting the set temperature small temperature increments were used. PND patterns were collected every 10 K up to a temperature of 548 K. The subsequent target temperatures were set to 573 K and then to 673 K. This was decided after a close analysis of the TG-DTA profile of the deuterated mixture (Figure 4-10), as the reaction should have gone to completion at *ca.* 673 K. Rietveld refinements were performed for each temperature point and the exact weight fraction was calculated for each phase at each temperature point to try to elucidate the mechanism of deuterium release.

An overview of the dehydrogenation process is given in Figure 4-11: data collected from Bank 5 (back scattered) during the *in-situ* PND experiment are presented. The phase changes involved when the  $\text{Mg}(\text{OD})_2$  – LiD system was heated can be clearly observed.

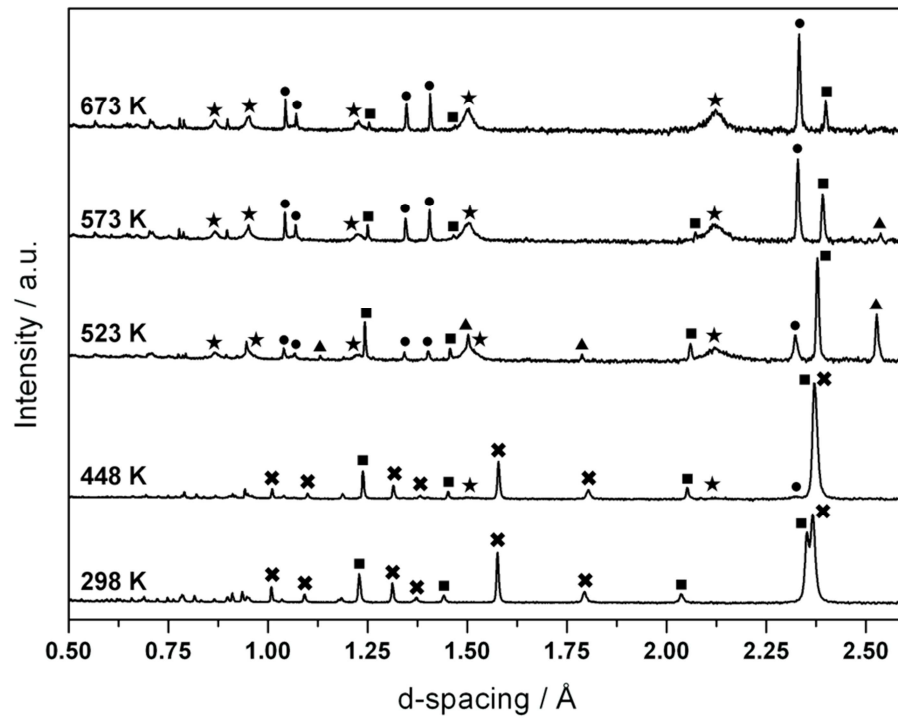


Figure 4-11: Bank 5 (back scattered) data obtained for the full temperature range showing the phase changes throughout the dehydrogenation process (Samples 11, 12, 20, 24 and 25). Crosses denote  $\text{Mg}(\text{OD})_2$ , squares LiD, stars MgO, triangles LiOD and circles  $\text{Li}_2\text{O}$  respectively.

A summary of the calculated weight fractions from the PND Rietveld refinement data for the phases present is given in Table 4-6.

Table 4-7: Calculated weight fractions from the PND Rietveld refinement data for the phases present in Samples 11, 12, 20, 24 and 25.

Sample	Collection Temperature / K	$\text{Mg}(\text{OD})_2$ wt. %	LiD wt. %	LiOD wt. %	$\text{Li}_2\text{O}$ wt. %	MgO wt. %
11	298	75.8(2)	24.2(3)	–	–	–
12	448	67.6(6)	21.9(5)	–	2.3(4)	8.2(1)
20	523	–	11.2(3)	14.6(5)	17.1(5)	57.1(5)
24	573	–	6.7(3)	6.3(4)	31.2(7)	55.8(8)
25	673	–	2.6(2)	–	42.3(9)	55.1(9)

At room temperature, the only phases present are  $\text{Mg}(\text{OD})_2$  and lithium deuteride: selected data from the PND Rietveld refinement are presented in Table 4-7 and Figure 4-12.

Table 4-8: Selected data from the PND Rietveld refinement for Sample 11 (298 K).

Empirical Formula	Mg(OD) <sub>2</sub>	LiD
<b>Crystal System</b>	Trigonal	Cubic
<b>Space Group</b>	<i>P-3m1</i>	<i>Fm-3m</i>
<b>Lattice Parameters</b>		
<i>a</i> / Å	3.1451(1)	4.0670(1)
<i>c</i> / Å	4.7526(1)	
<i>V</i> / Å <sup>3</sup>	40.712(2)	67.268(3)
<i>Z</i>	1	4
<b>Unit Cell Formula</b>		
<b>Weight / M<sub>w</sub></b>	60.331	35.820
<b>Density / g cm<sup>-3</sup></b>	2.461	0.884
<b>Wt. %</b>	75.8(2)	24.2(3)
<b>Temperature / K</b>		298
<b>No. of Variables</b>		73
<b>No. of Observations</b>		5807
<b>Rwp %</b>		2.49
<b>Rp %</b>		3.92
<b>χ<sup>2</sup></b>		1.80

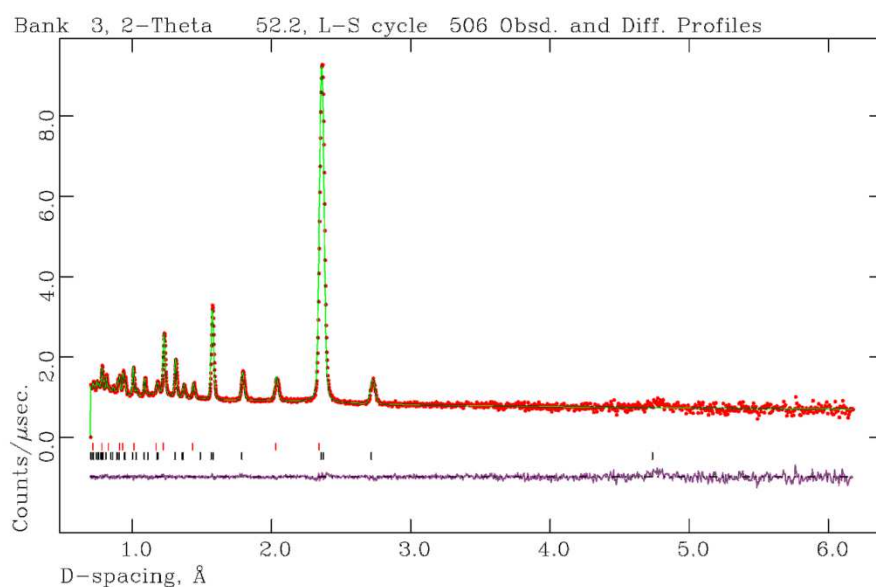
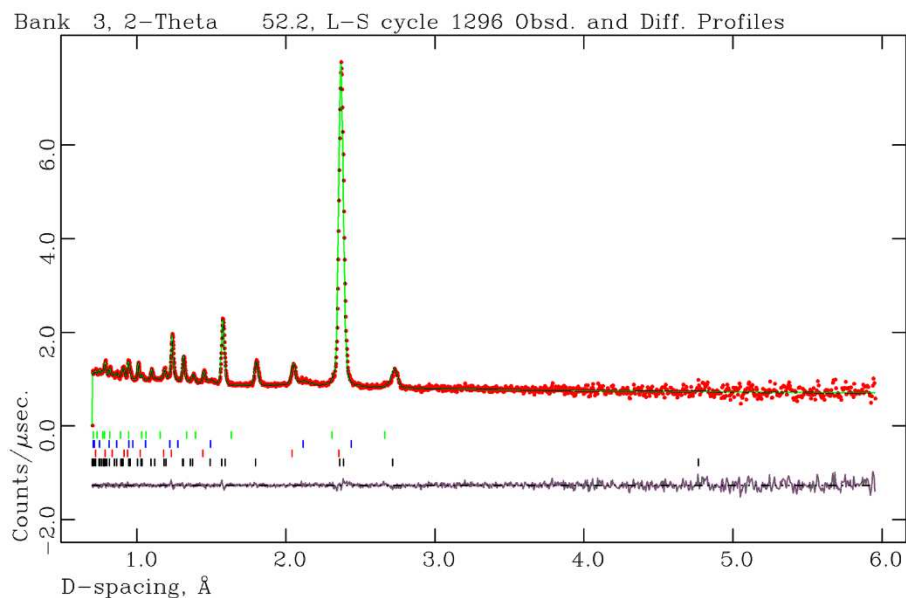


Figure 4-12: Observed, calculated and difference (OCD) plot from the PND Rietveld refinement for Sample 11 (298 K) from PND data, Bank 3 (low angle, 20° 40-67). The black and red tick marks indicate reflections from Mg(OD)<sub>2</sub> and LiD respectively.

A close look at the 448 K temperature point reveals the presence of very low intensity reflections assignable to both magnesium oxide and lithium oxide (Table 4-8 and Figure 4-13): the weight fractions of Mg(OD)<sub>2</sub> and LiD decrease with respect to the wt. % calculated for Sample 11 and new phases MgO and Li<sub>2</sub>O appear (weight fractions of 8.2 and 2.3 wt. % respectively).

**Table 4-9: Selected data from the PND Rietveld refinement for Sample 12 (448 K).**

<b>Empirical Formula</b>	<b>Mg(OD)<sub>2</sub></b>	<b>LiD</b>	<b>MgO</b>	<b>Li<sub>2</sub>O</b>
<b>Crystal System</b>	Trigonal	Cubic	Cubic	Cubic
<b>Space Group</b>	<i>P-3m1</i>	<i>Fm-3m</i>	<i>Fm-3m</i>	<i>Fm-3m</i>
<b>Lattice Parameters</b>				
<i>a</i> / Å	3.1459(1)	4.0919(1)	4.237(3)	4.630(1)
<i>c</i> / Å	4.7856(2)			
<i>V</i> / Å <sup>3</sup>	41.018(3)	68.514(5)	76.1(1)	99.24(9)
<i>Z</i>	1	4	4	4
<b>Unit Cell Formula</b>				
<b>Weight / M<sub>w</sub></b>	60.331	35.820	161.216	119.524
<b>Density / g cm<sup>-3</sup></b>	2.442	0.868	3.518	2.000
<b>Wt. %</b>	67.6(6)	21.9(5)	8.2(1)	2.3(4)
<b>Temperature / K</b>			448	
<b>No. of Variables</b>			94	
<b>No. of Observations</b>			5762	
<b>Rwp %</b>			2.84	
<b>Rp %</b>			4.32	
<b>χ<sup>2</sup></b>			1.58	



**Figure 4-13:** Observed, calculated and difference (OCD) plot from the PND Rietveld refinement for Sample 12 (448 K) from PND data, Bank 3 (low angle,  $2\theta^\circ$  40-67). The red, black, blue and green tick marks indicate reflections from LiD, Mg(OD)<sub>2</sub>, MgO and Li<sub>2</sub>O respectively.

As shown below in Table 4-9 and in Figure 4-14, at 523 K all the Mg(OD)<sub>2</sub> has converted to MgO, whose weight fraction has now risen to 57.1 wt. %. A new LiOD phase (14.6 wt. %) appears, whilst the intensity of the peaks assignable to LiD and Li<sub>2</sub>O decrease and increase respectively.

Table 4-10: Selected data from the PND Rietveld refinement of Sample 20 (523 K).

Empirical Formula	LiD	MgO	Li <sub>2</sub> O	LiOD
<b>Crystal System</b>	Cubic	Cubic	Cubic	Tetragonal
<b>Space Group</b>	<i>Fm-3m</i>	<i>Fm-3m</i>	<i>Fm-3m</i>	<i>P4/nmm</i>
<b>Lattice Parameters</b>				
<i>a</i> / Å	4.1133(1)	4.2398(3)	4.6394(2)	3.5695(2)
<i>c</i> / Å				4.3672(6)
<i>V</i> / Å <sup>3</sup>	69.593(7)	76.22(1)	99.86(1)	55.64(1)
<i>Z</i>	4	4	4	2
<b>Unit Cell Formula</b>				
Weight / M <sub>w</sub>	35.820	161.216	119.524	49.908
Density / g cm <sup>-3</sup>	0.855	3.512	1.998	1.489
Wt. %	11.2(3)	57.1(5)	17.1(5)	14.6(5)
<b>Temperature / K</b>			523	
<b>No. of Variables</b>			65	
<b>No. of Observations</b>			5458	
<b>Rwp %</b>			2.47	
<b>Rp %</b>			3.64	
<b>χ<sup>2</sup></b>			1.07	

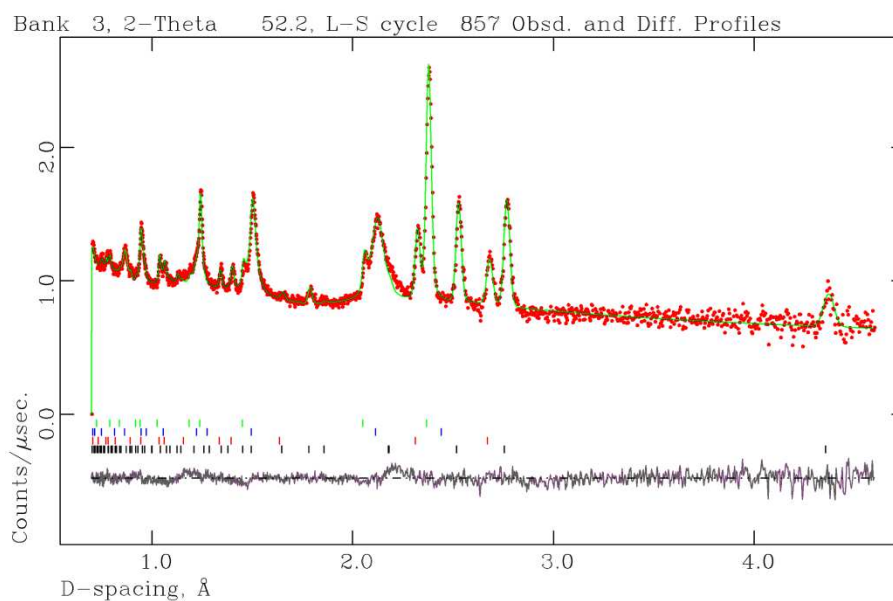
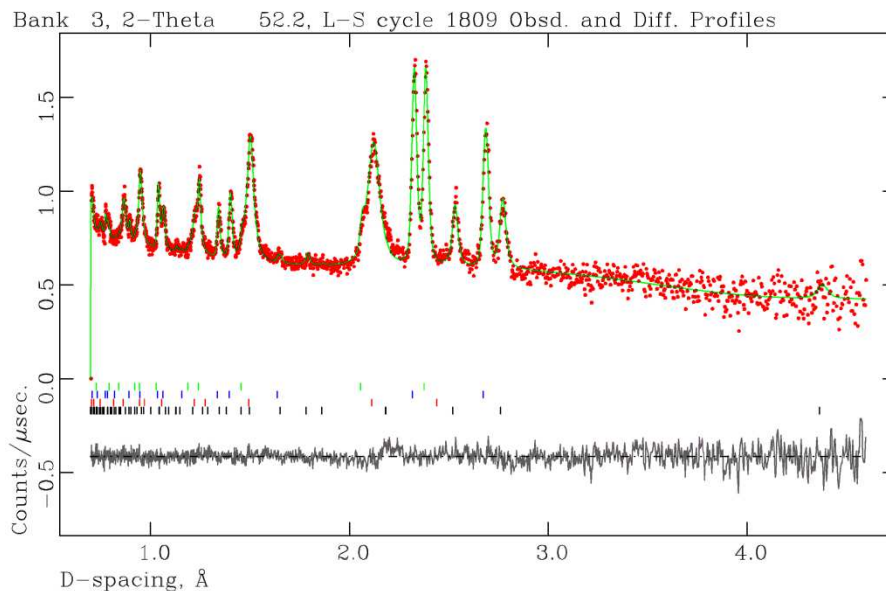


Figure 4-14: Observed, calculated and difference (OCD) plot from the PND Rietveld refinement for Sample 20 (523 K) from PND data, Bank 3 (low angle, 20° 40-67). The green, blue, red and black tick marks indicate reflections from LiD, MgO, Li<sub>2</sub>O and LiOD respectively.

At 573 K there is little variation in the amount of MgO from **20**, while the weight fractions of LiOD and lithium deuteride both decrease and lithium oxide increases. Selected data for this temperature point are presented in Table 4-10 and Figure 4-15.

**Table 4-11: Selected data from the PND Rietveld refinement for Sample 24 (573 K).**

<b>Empirical Formula</b>	<b>LiD</b>	<b>MgO</b>	<b>Li<sub>2</sub>O</b>	<b>LiOD</b>
<b>Crystal System</b>	Cubic	Cubic	Cubic	Tetragonal
<b>Space Group</b>	<i>Fm-3m</i>	<i>Fm-3m</i>	<i>Fm-3m</i>	<i>P4/nmm</i>
<b>Lattice Parameters</b>				
<i>a</i> / Å	4.1243(2)	4.2370(2)	4.6448(1)	3.5750(2)
<i>c</i> / Å				4.376(1)
<i>V</i> / Å <sup>3</sup>	70.155(8)	76.06(2)	100.208(8)	55.93(2)
<i>Z</i>	4	4	4	2
<b>Unit Cell Formula</b>				
<b>Weight / M<sub>w</sub></b>	35.820	161.216	119.524	49.908
<b>Density / g cm<sup>-3</sup></b>	0.848	3.520	1.981	1.482
<b>Wt. %</b>	6.7(3)	55.8(8)	31.2(7)	6.3(4)
<b>Temperature / K</b>			573	
<b>No. of Variables</b>			72	
<b>No. of Observations</b>			5438	
<b>Rwp %</b>			2.65	
<b>Rp %</b>			4.24	
<b>χ<sup>2</sup></b>			0.83	



**Figure 4-15: Observed, calculated and difference (OCD) plot from the PND Rietveld refinement for Sample 24 (573 K) from PND data, Bank 3 (low angle, 20° 40-67). The green, blue, red and black tick marks indicate reflections from LiD, Li<sub>2</sub>O, MgO and LiOD respectively.**

Once the mixture is heated to 673 K, there are no peaks assignable to LiOD, however a small amount of LiD is still present (2.6 wt. %). This may be due to the fact that a greater amount of sample has been employed during PND experiments with respect to the 500 mg scale; the mixing time was not entirely adequate anymore in order to obtain a homogeneous sample. In this sense, no reflections assignable to Mg(OD)<sub>2</sub> are identified due to the high target temperature: 673 K is abundantly above the dehydration temperature of magnesium hydroxide. Nonetheless, the main phases present are magnesium oxide and lithium oxide as expected. Rietveld refinement data for the PND data collected at 673 K are presented in Table 4-11 and Figure 4-16.

Table 4-12: Selected data from the PND Rietveld refinement for Sample 25 (673 K).

Empirical Formula	LiD	MgO	Li <sub>2</sub> O
<b>Crystal System</b>	Cubic	Cubic	Cubic
<b>Space Group</b>	<i>Fm-3m</i>	<i>Fm-3m</i>	<i>Fm-3m</i>
<b>Lattice Parameters</b>			
<i>a</i> / Å	4.1488(3)	4.2364(2)	4.6578(2)
<i>V</i> / Å <sup>3</sup>	71.41(2)	76.03(1)	101.05(1)
<i>Z</i>	4	4	4
<b>Unit Cell Formula</b>			
<b>Weight / M<sub>w</sub></b>	35.820	161.216	119.524
<b>Density / g cm<sup>-3</sup></b>	0.833	3.521	1.964
<b>Wt. %</b>	2.6(2)	55.1(9)	42.3(9)
<b>Temperature / K</b>		673	
<b>No. of Variables</b>		51	
<b>No. of Observations</b>		5425	
<b>Rwp %</b>		4.26	
<b>Rp %</b>		7.14	
<b>χ<sup>2</sup></b>		0.74	

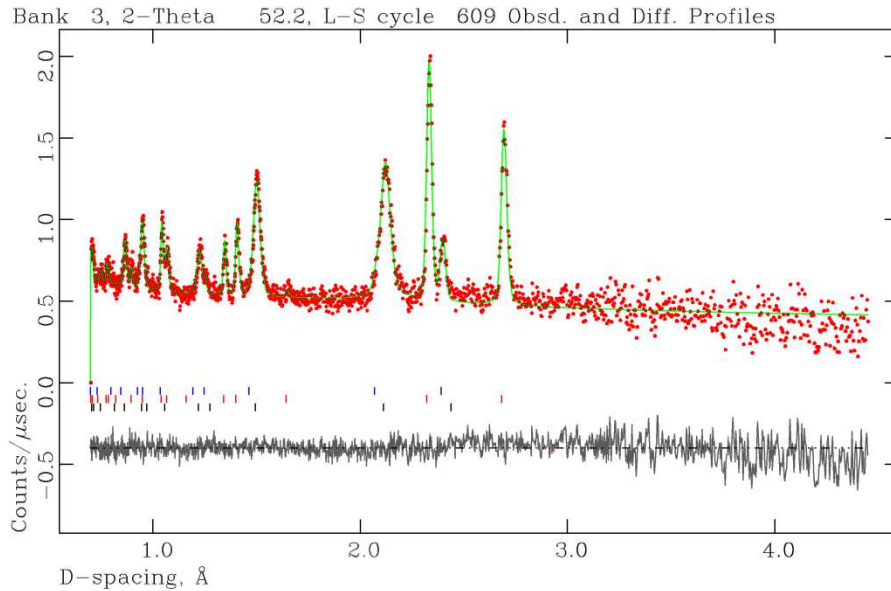
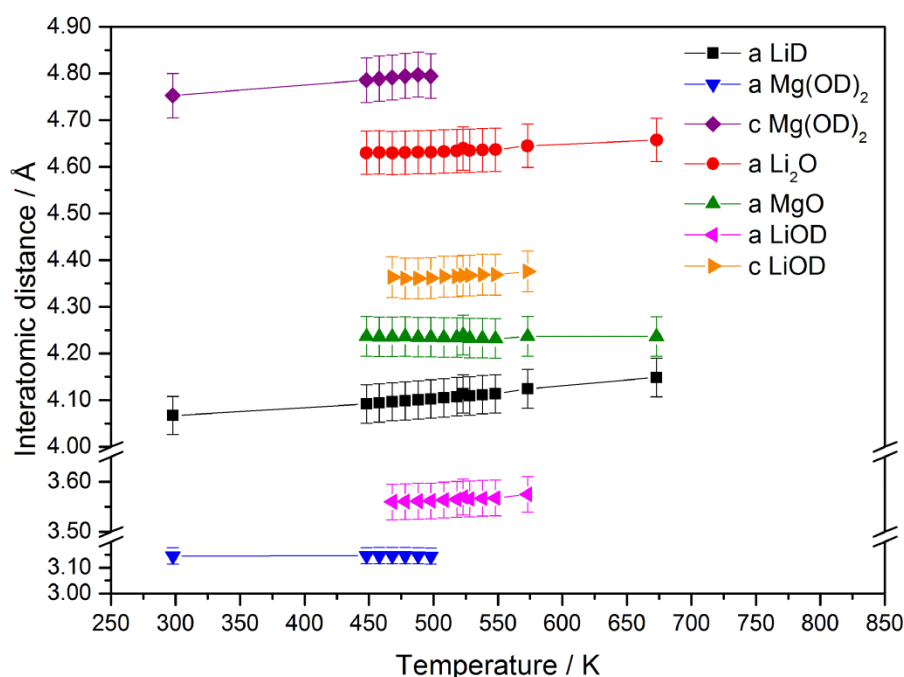


Figure 4-16: Observed, calculated and difference (OCD) plot from the PND Rietveld refinement for Sample 25 (673 K) from PND data, Bank 3 (low angle, 20° 40-67). The blue, red and black tick marks indicate reflections from LiD, Li<sub>2</sub>O and MgO respectively.

Therefore, at a first glance, it would appear that the system undergoes a two-step dehydrogenation process with the first step starting at 448 K and finishing at 523 K, when all the  $\text{Mg}(\text{OD})_2$  has reacted. The second step appears to start immediately after the first, involving the reaction between  $\text{LiD}$  and  $\text{LiOD}$ .

Further, no major structural changes can be observed for the phases throughout the whole reaction, however thermal expansion for  $\text{LiD}$ ,  $\text{Li}_2\text{O}$  and  $\text{Mg}(\text{OD})_2$  can be observed (Figure 4-17). The lattice parameters obtained from the Rietveld refined data in this study are in good agreement with the data present in the literature.<sup>27,28,29,30</sup>

An overview of the calculated weight fractions from the PND Rietveld refinement data for the phases present across the entire temperature range is given in Figure 4-18 (error bars omitted for clarity). It can be noted that the  $\text{MgO}$  weight fraction is decreased for the last two temperature points; this is believed to be attributable to a poor resolution of the experimental data. Beam issues were encountered during the acquisition of the 573 and 673 K temperature point, resulting in a higher signal to noise ratio and lower pattern resolution.



**Figure 4-17: Variation of lattice parameters Vs temperature obtained by Rietveld refinement across the complete temperature range.**

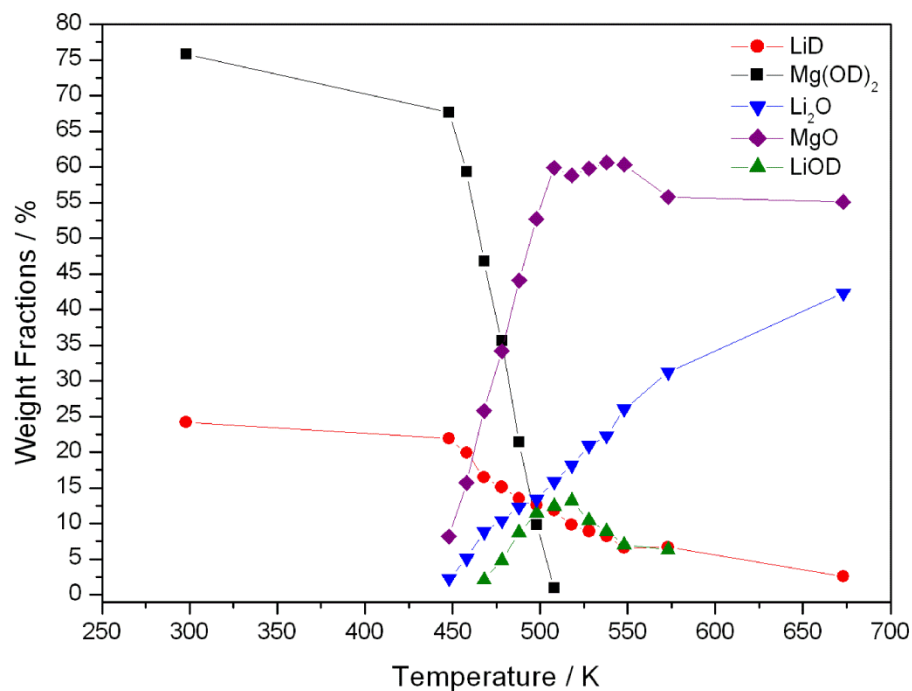


**Figure 4-18: Calculated weight fractions from the PND Rietveld refinement data for all phases present across the complete temperature range.**

#### **4.3.3.1 First mechanistic step: Mg(OD)<sub>2</sub> dehydration and LiD hydrolysis**

To understand the mechanism of hydrogen release more fully, the two dehydrogenation steps have been studied in detail. The data presented in this section focuses on the first reaction step that occurs in the 448 – 518 K range: PND patterns were collected every 10 K. Bank 5 (back scattered) data collected during the *in-situ* PND experiment are shown in Figure 4-19.

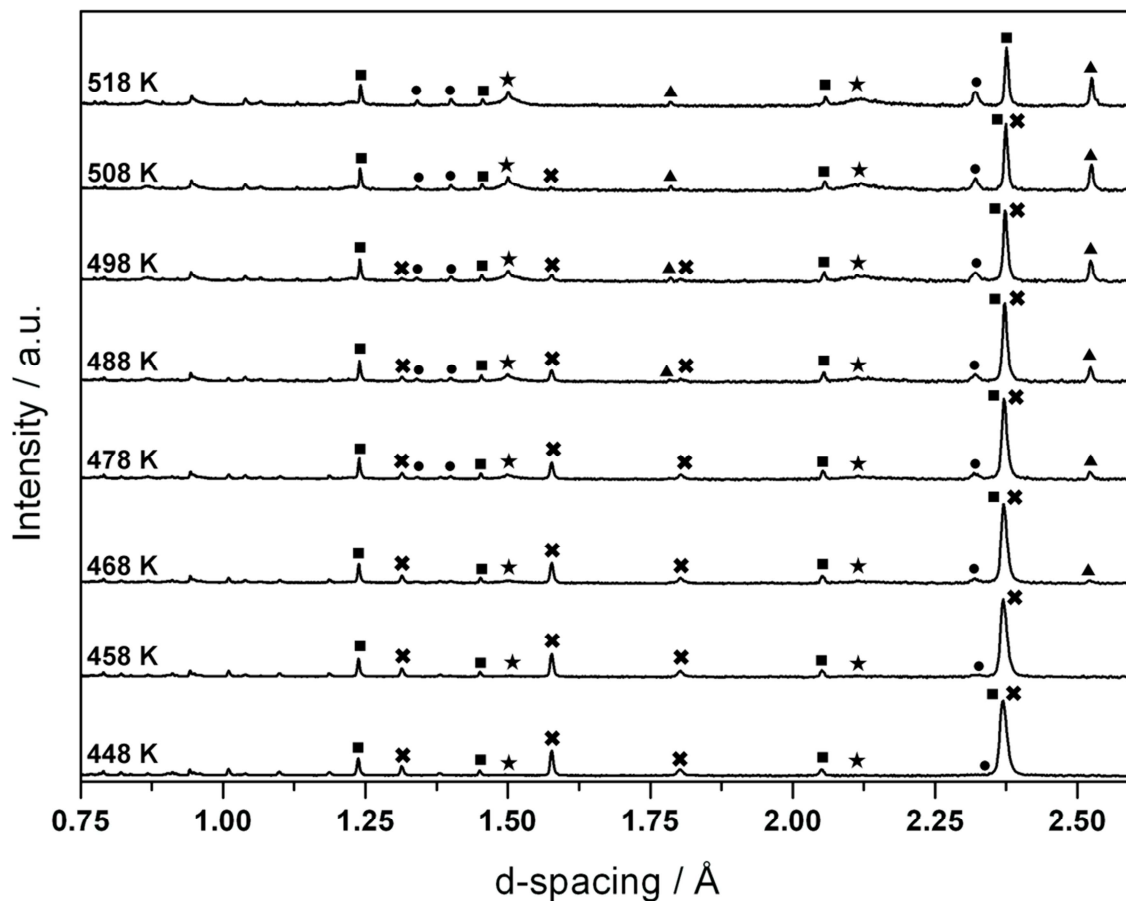


**Figure 4-19: Bank 5 (back scattered) data obtained over a temperature range of 448-518 K (Samples 12 to 19). Crosses denote  $\text{Mg}(\text{OD})_2$ , squares  $\text{LiD}$ , stars  $\text{MgO}$ , triangles  $\text{LiOD}$  and circles  $\text{Li}_2\text{O}$  respectively.**

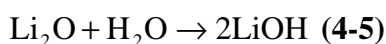
A summary of the calculated weight fractions from the PND Rietveld refinement data for the phases present is given in Table 4-12.

Selected Rietveld refinement data and all observed, calculated and difference (OCD) plots for all intermediate points are reported in Appendix B.

**Table 4-13: Calculated weight fractions from the PND Rietveld refinement data for the phases present in Samples 12 to 19.**

Sample	Collection	Mg(OD) <sub>2</sub>	LiD	MgO	Li <sub>2</sub> O	LiOD
	Temperature / K	wt. %	wt. %	wt. %	wt. %	wt. %
<b>12</b>	448	67.6(6)	21.9(5)	8.2(1)	2.3(4)	–
<b>13</b>	458	59.3(5)	19.9(4)	15.7(4)	5.1(4)	–
<b>14</b>	468	46.8(7)	16.5(4)	25.8(6)	8.8(4)	2.1(2)
<b>15</b>	478	35.6(8)	15.1(4)	34.2(8)	10.4(4)	4.8(3)
<b>16</b>	488	21.4(5)	13.5(4)	44.1(6)	12.3(5)	8.7(4)
<b>17</b>	498	9.8(4)	12.6(4)	52.7(8)	13.4(5)	11.5(5)
<b>18</b>	508	<1	11.8(4)	59.9(9)	15.9(7)	12.4(6)
<b>19</b>	518	–	9.8(2)	58.8(4)	18.2(3)	13.2(3)

From the data analysis, it would appear in fact that the first step of hydrogen release involves the dehydration of Mg(OD)<sub>2</sub>, which decomposes to MgO and releases D<sub>2</sub>O. This decomposition takes place at a lower temperature with respect to the data reported in the literature.<sup>4,31</sup> This may be due to the synergistic effect between the two reactants. In fact, the lower dehydrogenation temperature cannot be explained only by the fact that nanostructured materials are employed: as presented in Section 3.3.2, the decomposition of Mg(OH)<sub>2</sub> nanoplates alone starts at *ca.* 573 K. Nonetheless, in this system, the dehydration reaction starts at *ca.* 448 K. It can be proposed that the water evolved immediately hydrolyses two equivalents of LiD, leading to the formation of Li<sub>2</sub>O and LiOD. As reviewed by Haertling *et al.*, LiOH is the main product of LiH hydrolysis. However, it has been observed that a layer of Li<sub>2</sub>O forms between lithium hydroxide and lithium hydride (Equations 4-4 and 4-5).<sup>32</sup>



This hydrolysis reaction thus results in a multi-layered structure with a core of LiH and a two-layer shell formed by an inner layer of lithium oxide and a layer shell of lithium hydroxide at the interface with H<sub>2</sub>O.



**Figure 4-20: Layered structure for LiH hydrolysis**

The literature model for LiH hydrolysis is in good agreement with the PND data collected, where at first peaks assignable to  $\text{Li}_2\text{O}$  and  $\text{MgO}$  are found (448 and 458 K), followed by presence of  $\text{LiOD}$  peaks at higher temperatures (starting at 468 K). As the dehydration of  $\text{Mg}(\text{OD})_2$  proceeds, so does the hydrolysis of  $\text{LiD}$  to the point (518 K) at which all the  $\text{Mg}(\text{OD})_2$  has decomposed to  $\text{MgO}$  and the lithium species present are  $\text{LiD}$ ,  $\text{Li}_2\text{O}$  and  $\text{LiOD}$ .

#### **4.3.3.2 Second mechanistic step: reaction of the remaining LiD**

In this section, the data presented focuses on the second dehydrogenation step, starting at 528 K. Bank 5 (back scattered) data collected during the in-situ PND experiment are shown in Figure 4-21.

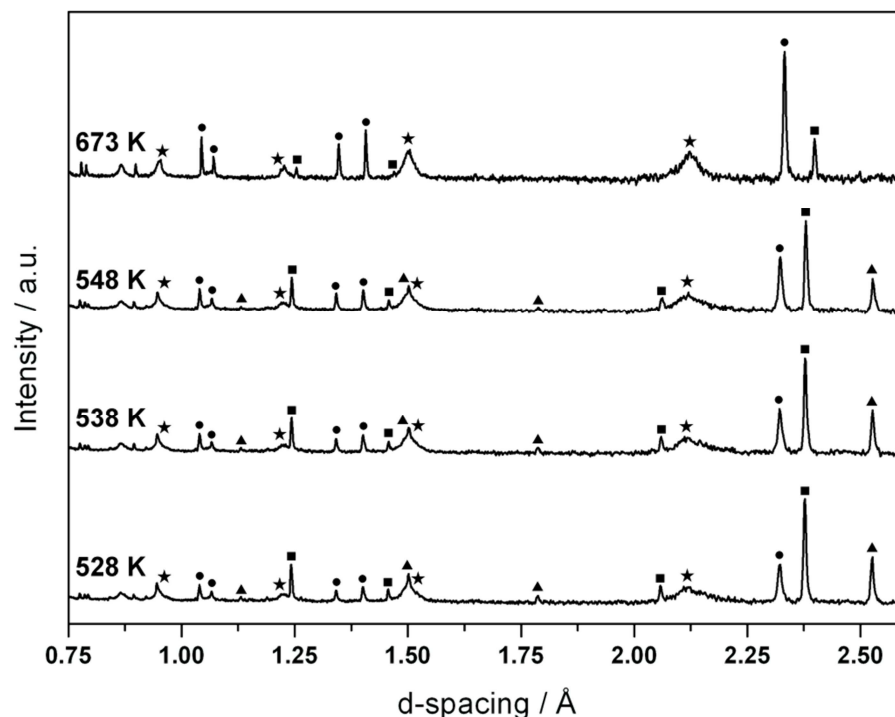


Figure 4-21: Bank 5 (back scattered) data obtained at 528-673 K, showing the phase changes throughout the dehydrogenation process (Samples 21, 22, 23 and 25). Squares denote LiD, stars MgO, triangles LiOD and circles Li<sub>2</sub>O respectively.

A summary of the calculated weight fractions from the PND Rietveld refinement data for the phases present is given in Table 4-20.

Selected Rietveld refinement data and all observed, calculated and difference (OCD) plots for all intermediate points are reported in Appendix B.

Table 4-14: Calculated wt. % from the PND Rietveld refinement data for the phases present in Samples 21-25.

	Collection	Mg(OD) <sub>2</sub>	LiD	MgO	Li <sub>2</sub> O	LiOD
Sample	Temperature / K	wt. %	wt. %	wt. %	wt. %	wt. %
21	528	–	8.9(3)	59.8(6)	20.9(6)	10.4(4)
22	538	–	8.2(3)	60.6(7)	22.3(7)	8.9(4)
23	548	–	6.6(4)	60.3(6)	26.1(5)	7.0(3)
24	573	–	6.7(3)	55.8(8)	31.2(7)	6.3(4)
25	673	–	2.6(2)	55.1(9)	42.3(9)	–

As already discussed in Section 4.3.3.1, at 673 K there are no peaks assignable to LiOD, but there is a small amount of LiD remaining (2.6 wt. %). The other phases present are magnesium oxide and lithium oxide as expected. The MgO weight fraction remains effectively constant throughout the whole temperature range of 528 – 673 K.

The data collected favour a second mechanistic step which involves reaction in the solid state between LiOD and LiD, where  $D^+$  and  $D^-$  combine together to form  $D_2$ . As mentioned in Section 4.3.1.4, a similar reaction pathway has been suggested by Drozd *et al.* for the  $NaBH_4 - Mg(OH)_2$  system<sup>23</sup> as well as by Lu *et al.* for the  $LiOH \cdot H_2O - LiH$  system, in which the second dehydrogenation step sees the solid state reaction between LiOH and LiH.<sup>7</sup>

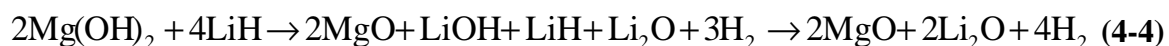
## 4.4 Conclusions

Nanostructured magnesium hydroxide has been successfully synthesised using the combination of hydrothermal treatment and microwave irradiation. This novel synthesis has resulted in the production of hexagonal nanoplates of  $Mg(OH)_2$  with a thickness of tenths of nanometres. The same synthetic route has been successfully used to produce nanostructured  $Mg(OD)_2$ , subsequently employed during *in-situ* powder neutron diffraction experiments at the Rutherford Appleton Laboratory in Didcot. Nanostructured LiH and LiD have been successfully obtained by mechanical milling of the bulk reactants.

The  $Mg(OH)_2 - LiH$  modular hydrogen release system has been studied in detail, comparing bulk as well as nanostructured materials. The system has been prepared by manually mixing stoichiometric amounts of the starting materials for 5 minutes. All manipulations have been carried out inside a recirculating glove box under inert atmosphere. For both systems, the theoretical weight loss of 5.4 wt. % of hydrogen was not achieved when heated to 873 K: the mass losses have found to be 5.1 wt. % and 4.7 % for bulk and nanomaterials respectively. However, using nanomaterials has resulted in a lowered onset temperature of hydrogen release (lowered from 478 K to 453 K) and a faster dehydrogenation process. Overall, nanomaterials have lead to better performances in terms of kinetics for the system. The calculated activation energy for the nanostructured system was found to be  $96 \pm 4 \text{ kJ mol}^{-1}$  for the first (low temperature) and  $165 \pm 9 \text{ kJ mol}^{-1}$  for the second (high temperature) step. Based on the calculated  $E_a$  values, the first event is believed to relate to  $Mg(OH)_2$  dehydration and the second event to the solid state reaction between LiOH and LiH.

Two mechanisms of hydrogen release were proposed: the first one involved the dehydration of magnesium hydroxide as initial step to form MgO, followed by the hydrolysis of 1 mole of lithium hydride and formation of lithium hydroxide, with the last step being the solid state reaction between the remaining LiH and LiOH. The second mechanism involves the solid state reaction between 2 equivalents of LiH and Mg(OH)<sub>2</sub> leading to the formation of magnesium oxide, lithium oxide and lithium hydroxide, with the second and last step of the reaction being the same as the final step of the first proposed mechanism. *Ex-situ* powder X-ray diffraction experiments have been performed in order to clarify the reaction pathway, although the studies were not conclusive. Therefore, *in-situ* PND data combined with the data already obtained were found to be pivotal to elucidate the mechanism of hydrogen release.

PND experiments were carried out over the complete temperature range of dehydrogenation, with short data collections over the crucial dehydrogenation temperatures to follow the reaction steps individually. Rietveld refinements against the collected PND ToF data were performed: the results confirm that the dehydrogenation process appears to follow the first proposed mechanism (Equation 4-3) rather than the second.



First the magnesium hydroxide undergoes a dehydration process forming MgO and releasing H<sub>2</sub>O. The evolved water then hydrolyses 1 mol of lithium hydride leading to H<sub>2</sub> release together with the formation of a layered structure with a core of LiH and a Li<sub>2</sub>O-LiOH double layer (Figure 4-25). These two steps happen almost simultaneously. The last reaction step involves the solid state reaction of the newly formed lithium hydroxide and the remaining hydride, which results in hydrogen evolution and formation of lithium oxide.

Future work should focus on further enhancing the performances of the nanostructured system. The use of additives or catalysts could be seen as a feasible option in order to improve the kinetics of hydrogen release. Disruption of the layered structure formed during the first dehydrogenation step should facilitate hydrogen evolution. Several catalysts and additives have been studied for promoting the hydrolysis process for magnesium hydride, although none of them has been tested in the presence of LiH. Based on studies published on MgH<sub>2</sub>, suitable candidates to be added to the magnesium hydroxide – lithium hydride modular system include graphite, silicon carbide as well as multi-valence titanium and vanadium based additives/catalysts.<sup>33,34,35,36,37</sup> Further studies in order to understand which additives and catalysts could be the most efficient are required.

## 4.5 References

1. Hanlon, J. M. Synthesis and characterisation of direct and indirect hydrogen storage materials. University of Glasgow, 2013.
2. Hanlon, J. M.; Balducci, G.; Bravo-Diaz, L.; Tapia-Ruiz, N.; Stobbs, B. A.; MacDonald, L.; Gregory, a. D. H., Nanostructured Mg(OH)<sub>2</sub> – LiH as a Hydrogen Release System. In *In Preparation*, 2015.
3. James M. Hanlon; Laura Bravo Diaz; Giulia Balducci; Blane A. Stobbs; Marek Bielewski; Chung, P.; Gregory, a. D. H., Rapid surfactant-free synthesis of Mg(OH)<sub>2</sub> nanoplates and pseudomorphic dehydration to MgO. *CrystEngComm* **2015**.
4. Turner, R. C.; Hoffman, I.; Chen, D., Thermogravimetry of the dehydration of Mg(OH)<sub>2</sub>. *Canadian Journal of Chemistry* **1963**, *41* (2), 243-251.
5. *CRC Handbook of Chemistry and Physics*. 95th Edition ed.; CRC Press: Boca Raton, Florida 33431, 1980-1981.
6. Vajo, J. J.; Skeith, S. L.; Mertens, F.; Jorgensen, S. W., Hydrogen-generating solid-state hydride/hydroxide reactions. *Journal of Alloys and Compounds* **2005**, *390* (1-2), 55-61.
7. Lu, J.; Fang, Z. Z.; Sohn, H. Y., A hybrid method for hydrogen storage and generation from water. *Journal of Power Sources* **2007**, *172* (2), 853-858.
8. Kissinger, H. E., Reaction Kinetics in Differential Thermal Analysis. *Analytical Chemistry* **1957**, *29* (11), 1702-1706.
9. Kissinger, H. E., Variation on Peak Temperature With Heating Rate in Differential Thermal Analysis. *Journal of Research of The National Bureau of Standards* **1956**, *57* (4), 5.
10. Inorganic Crystallographic Structure Database (ICSD). <http://cds.rsc.org/> (accessed 22<sup>nd</sup> May 2014).
11. Belsky, A.; Hellenbrandt, M.; Karen, V. L.; Luksch, P., New developments in the Inorganic Crystal Structure Database (ICSD): accessibility in support of materials research and design. *Acta Crystallographica Section B* **2002**, *58* (3 Part 1), 364-369.
12. The International Centre for Diffraction Data (ICDD). <http://www.icdd.com/> (accessed 22<sup>nd</sup> May 2014).
13. Information about the Mantid program. [www.mantidproject.org](http://www.mantidproject.org) (accessed 6<sup>th</sup> June 2014).
14. A. C. Larson, R. B. v. D. *General Structure Analysis System (GSAS)*; Los Alamos Laboratory: Los Alamos, NM, USA, 1995, 1995; pp 86-748.

15. Toby, B. H., EXPGUI, a graphical user interface for GSAS. *J. Appl. Crystallogr.* **2001**, *34*, 210-213.
16. R. B. Von Dreele, J. D. J. a. C. G. W., Rietveld Refinement with Spallation Neutron Powder Diffraction Data. *J. Appl. Crystallogr.* **0982**, *15*, 581-589.
17. Halikia, I.; Neou-Syngouna, P.; Kolitsa, D., Isothermal kinetic analysis of the thermal decomposition of magnesium hydroxide using thermogravimetric data. *Thermochimica Acta* **1998**, *320* (1–2), 75-88.
18. Leardini, F.; Ares, J. R.; Bodega, J.; Fernandez, J. F.; Ferrer, I. J.; Sanchez, C., Reaction pathways for hydrogen desorption from magnesium hydride/hydroxide composites: bulk and interface effects. *Phys. Chem. Chem. Phys.* **2010**, *12* (3), 572-577.
19. Leckey, J. H.; Nulf, L. E.; Kirkpatrick, J. R., Reaction of Lithium Hydride with Water. *Langmuir* **1996**, *12* (26), 6361-6367.
20. Kudo, H., The rates of thermal decomposition of LiOH<sub>(s)</sub>, LiOD<sub>(s)</sub> and LiOT<sub>(s)</sub>. *Journal of Nuclear Materials* **1979**, *87* (1), 185-188.
21. Harold P. Klug; Alexander, L. E., *X-Ray Diffraction Procedures for Polycrystalline and Amorphous Materials*. Sixth Edition ed.; John Wiley & Sons, Inc.: 1970.
22. Langford, J. I.; Wilson, A. J. C., Scherrer after sixty years: A survey and some new results in the determination of crystallite size. *J. Appl. Crystallogr.* **1978**, *11* (2), 102-113.
23. Drozd, V.; Saxena, S.; Garimella, S. V.; Durygin, A., Hydrogen release from a mixture of NaBH<sub>4</sub> and Mg(OH)<sub>2</sub>. *International Journal of Hydrogen Energy* **2007**, *32* (15), 3370-3375.
24. Cai, W.; Wang, H.; Sun, D.; Zhang, Q.; Yao, X.; Zhu, M., Destabilization of LiBH<sub>4</sub> dehydrogenation through H<sup>+</sup>-H<sup>-</sup> interactions by cooperating with alkali metal hydroxides. *RSC Advances* **2014**, *4* (6), 3082.
25. Isobe, S.; Ichikawa, T.; Hino, S.; Fujii, H., Hydrogen Desorption Mechanism in a Li-N-H System by Means of the Isotopic Exchange Technique. *The Journal of Physical Chemistry B* **2005**, *109* (31), 14855-14858.
26. Hu, Y. H.; Ruckenstein, E., Ultrafast reaction between LiH and NH<sub>3</sub> during H<sub>2</sub> storage in Li<sub>3</sub>N. *Journal of Physical Chemistry A* **2003**, *107* (46), 9737-9739.
27. Anderson, J. L.; Nasise, J.; Phillipson, K.; Pretzel, F. E., Isotopic effects on the thermal expansion of lithium hydride. *Journal of Physics and Chemistry of Solids* **1970**, *31* (4), 613-618.
28. Bowman Jr, R. C., Thermal expansion coefficients of lithium hydride. *Journal of Physics and Chemistry of Solids* **1973**, *34* (10), 1754-1756.

29. Taylor, D., Thermal-Expansion Data II. Binary Oxides with the Fluorite and Rutile Structures,  $\text{MO}_2$ , and the Antifluorite Structure,  $\text{M}_2\text{O}$ . *Transactions and Journal of the British Ceramic Society* **1984**, 83 (2), 32-37.
30. Xu, H.; Zhao, Y.; Hickmott, D.; Lane, N.; Vogel, S.; Zhang, J.; Daemen, L., High-temperature neutron diffraction study of deuterated brucite. *Phys Chem Minerals* **2013**, 40 (10), 799-810.
31. Nahdi, K.; Rouquerol, F.; Trabelsi Ayadi, M.,  $\text{Mg}(\text{OH})_2$  dehydroxylation: A kinetic study by controlled rate thermal analysis (CRTA). *Solid State Sciences* **2009**, 11 (5), 1028-1034.
32. Haertling, C.; Hanrahan, R. J.; Smith, R., A literature review of reactions and kinetics of lithium hydride hydrolysis. *Journal of Nuclear Materials* **2006**, 349 (1-2), 195-233.
33. Reardon, H. Synthesis, structure and characterisation of novel lightweight energy materials based on group I & II metal compounds. PhD Thesis, University of Glasgow, 2014.
34. Shahi, R. R.; Bhatnagar, A.; Pandey, S. K.; Dixit, V.; Srivastava, O. N., Effects of Ti-based catalysts and synergistic effect of SWCNTs- $\text{TiF}_3$  on hydrogen uptake and release from  $\text{MgH}_2$ . *International Journal of Hydrogen Energy* **2014**, 39 (26), 14255-14261.
35. Ren, C.; Fang, Z. Z.; Zhou, C. S.; Lu, J.; Ren, Y.; Zhang, X. Y., Hydrogen Storage Properties of Magnesium Hydride with V-Based Additives. *J. Phys. Chem. C* **2014**, 118 (38), 21778-21784.
36. da Conceicao, M. O. T.; dos Santos, D. S., Catalytic effect of chlorides compounds on hydrogen sorption properties of magnesium hydride. *Journal of Alloys and Compounds* **2014**, 615, S715-S718.
37. Cui, J.; Wang, H.; Liu, J.; Ouyang, L.; Zhang, Q.; Sun, D.; Yao, X.; Zhu, M., Remarkable enhancement in dehydrogenation of  $\text{MgH}_2$  by a nano-coating of multi-valence Ti-based catalysts. *Journal of Materials Chemistry A* **2013**, 1 (18), 5603-5611.

## 5 The magnesium hydride – lithium hydroxide ‘modular’ release system: H<sub>2</sub> desorption properties when working with anhydrous or monohydrate lithium hydroxide

### 5.1 Introduction

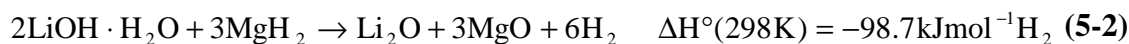
Lithium hydroxide has increasingly gained attention over the last decades in terms of hydrogen storage solutions. In fact its use has been proposed in several solid state hydrogen release systems in combination with different light metal hydrides. Firstly, in 2005 Vajo *et al.* proposed the use of LiOH, both anhydrous and as the monohydrate, in combination with two different light metal hydrides: lithium hydride, and lithium borohydride.<sup>1</sup> In 2007, Lu *et al.* published a detailed study of the lithium hydroxide – lithium hydride system using either LiOH or LiOH·H<sub>2</sub>O.<sup>2</sup> More recently Wang *et al.* studied the improved hydrogen storage and release properties of mechanically milled magnesium hydride when mixed with alkali hydroxides in catalytic amounts.<sup>3</sup> In 2014, based on the same idea Zhu *et al.* further investigated the destabilisation of LiBH<sub>4</sub> via its dehydrogenation through the H<sup>+</sup> – H<sup>-</sup> interaction between the hydride and light metal hydroxide (sodium, lithium and potassium hydroxides were employed).<sup>4</sup> Furthermore, the use of another light metal hydroxide, has been proposed to be used in these kind of systems, specifically the reaction between Mg(OH)<sub>2</sub> and Na(Li)BH<sub>4</sub> has been investigated.<sup>5,6</sup>

However, so far the lithium hydroxide – magnesium hydride hydrogen release system has not been studied. Two different systems can be proposed when employing these starting materials: both LiOH and LiOH·H<sub>2</sub>O can be mixed with MgH<sub>2</sub> to release H<sub>2</sub>.

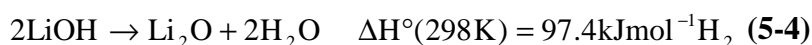
The LiOH – MgH<sub>2</sub> system, presented in Equation 5-1, is thermodynamically favourable and can theoretically release up to 5.9 wt. % of hydrogen. The starting materials react to yield magnesium oxide and lithium oxide together with the evolution of hydrogen.



When working with the monohydrate hydroxide, for the  $\text{LiOH}\cdot\text{H}_2\text{O} - \text{MgH}_2$  system (Equation 5-2) the theoretical thermogravimetric capacity of the whole system rises to 7.4 wt. %  $\text{H}_2$ . Once again the overall reaction is thermodynamically favourable and the starting materials react to yield magnesium oxide and lithium oxide, evolving hydrogen.



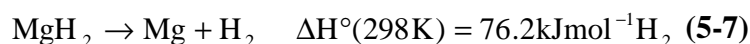
The decompositions of both anhydrous and lithium hydroxide monohydrate have been widely studied and are reported in Equations 5-3 and 5-4.<sup>7,8,9</sup>



Further, it is well known that under ambient atmosphere lithium hydroxide undergoes a carbonisation reaction by  $\text{CO}_2$ , leading to the formation of  $\text{Li}_2\text{CO}_3$  (Equations 5-5 and 5-6).<sup>10,11,12</sup> This phenomenon can be easily overcome by working under controlled atmosphere at all times: all  $\text{LiOH}(\cdot\text{H}_2\text{O})$  manipulations must be conducted under inert atmosphere.



The decomposition of  $\text{MgH}_2$  has been fully investigated. Magnesium hydride can theoretically release up to 7.6 wt. %  $\text{H}_2$ , although the kinetics and thermodynamics of the dehydrogenation process are not favourable (Equation 5-7) and the process is characterised by slow  $\text{H}_2$  desorption at high temperatures.<sup>13</sup>



The hydrolysis reaction of  $\text{MgH}_2$  meanwhile follows the reaction expressed in Equation 5-8.<sup>14</sup>



During this project  $\text{LiOH}\cdot\text{H}_2\text{O}$  and  $\text{MgH}_2$  have been used together to test their behaviour as solid state hydrogen release systems. A stoichiometric amount of the two reagents have been mixed together and the resulting mixture fully investigated.  $\text{LiOH} - \text{MgH}_2$  and  $\text{LiOH}\cdot\text{H}_2\text{O} - \text{MgH}_2$  mixtures have been prepared. Bulk, mechanically milled and nanostructured materials were used for each system. For the study of bulk systems, as-received  $\text{LiOH}\cdot\text{H}_2\text{O}$  and  $\text{MgH}_2$  have been manually ground together. Milled systems were prepared by mixing either anhydrous or hydrated mechanically milled lithium hydroxide with ball milled magnesium hydride. All starting materials were milled in order to reduce their particle size prior to mixing them together and testing their properties as hydrogen release systems.

Further, a feasible and facile route for the selective synthesis of nano  $\text{LiOH}\cdot\text{H}_2\text{O}$  has been successfully identified. Anhydrous lithium hydroxide nanosheets with a thickness of tens of nanometres were successfully obtained. Their behaviour as well as nanostructured  $\text{LiOH}\cdot\text{H}_2\text{O}$  when mixed with mechanically milled  $\text{MgH}_2$  was tested.

The aim of this chapter is to give an overview on the  $\text{LiOH}\cdot\text{H}_2\text{O} - \text{MgH}_2$  system: attention has been focused of the comparison of the dehydrogenation properties of chemically nanostructured and mechanically milled materials with respect to bulk reagents. In particular, the onset temperature of hydrogen release and associated weight loss has been fully studied for each system. Further, the role of structural water in  $\text{LiOH}\cdot\text{H}_2\text{O}$  was considered: the behaviour of lithium hydroxide monohydrate when mixed with  $\text{MgH}_2$  was investigated and compared to its corresponding anhydrous hydroxide. All materials were characterised using simultaneous thermogravimetric analysis (TG-DTA) with mass spectroscopy (MS), powder X-ray diffraction (PXRD) and scanning electron microscopy (SEM). TG-DTA-MS studies were conducted to obtain information on the onset and peak temperature of any thermal event occurring, weight loss percentage and nature and amount of the gas evolved during heating. *Ex-situ* PXRD was employed to propose a mechanism of hydrogen release for each studied system. SEM was used for morphology studies of both milled and nanostructured materials before and after heating.

## 5.2 Experimental

### 5.2.1 Preparation of the systems

Mixtures were prepared by manually mixing stoichiometric amounts of the starting materials for 5 minutes with an agate mortar and pestle. All preparations were conducted under an inert atmosphere inside either an Ar- or N<sub>2</sub>-filled recirculating glove box.

The amounts of starting materials mixed together for each system were:

- 180 mg of LiOH – 100 mg of MgH<sub>2</sub>
- 216 mg of LiOH·H<sub>2</sub>O – 100 mg of MgH<sub>2</sub>

For each hydroxide, three different kinds of systems were prepared and analysed:

- Bulk ‘modular’ system: mixtures of as-received LiOH(·H<sub>2</sub>O) (LiOH: Sigma-Aldrich, ≥ 98%; LiOH·H<sub>2</sub>O: Aldrich, 98%) and MgH<sub>2</sub> (Aldrich, hydrogen-storage grade, ≥ 96.5%). (b-LiOH, b-LiOH·H<sub>2</sub>O)
- Mechanically milled ‘modular’ system: mixtures of mechanically milled lithium hydroxide (m-LiOH(·H<sub>2</sub>O)) and mechanically milled magnesium hydride (m-MgH<sub>2</sub>).
- Nanostructured ‘modular’ system: mixtures of synthesised nanostructured LiOH(·H<sub>2</sub>O) (n-LiOH(·H<sub>2</sub>O)) and mechanically milled MgH<sub>2</sub> (m-MgH<sub>2</sub>).

### 5.2.2 Selective Synthesis of nanostructured LiOH(·H<sub>2</sub>O)

To prepare nanostructured LiOH(·H<sub>2</sub>O) (denoted n-LiOH and n-LiOH·H<sub>2</sub>O respectively), approximately 160 mg of lithium metal ribbon (Aldrich, Lithium ribbon, thickness × width 1.5 mm × 100 mm, 99.9%) was carefully cut into small chips inside an argon filled recirculating glove box and put inside a glass vial, which was sealed with parafilm prior to transfer out of the glove box. The metal was then quickly transferred to a 50 ml Schlenk flask and dissolved in 25 ml of deionised water, minimising the exposure of the lithium metal chips to moisture and air. Once the metal was completely dissolved, the flask was connected to the Schlenk apparatus and the evaporation process started. By carefully tuning the reaction conditions it was possible to synthesise the anhydrous LiOH and the monohydrate hydroxide selectively, exploiting the vacuum evaporation and thermal vacuum evaporation processes.<sup>15,16</sup>

Working in a high vacuum environment at room temperature allows evaporation of only the solvent water, yielding lithium hydroxide monohydrate. Conducting the evaporation process at higher temperature allowed to dehydrate the LiOH fully, resulting in the formation of the anhydrous hydroxide.

Specifically, to obtain LiOH, the process was conducted by immersing the flask in an oil bath heated to 343 K. The process was completed after *ca.* 120 minutes. For the synthesis of LiOH·H<sub>2</sub>O, vacuum evaporation was conducted at room temperature. The process took approximately 240 minutes to complete. For both synthetic procedures, the crystals were collected after the reaction flask was carefully sealed and transferred inside a glove box.

### 5.2.3 Ball milling of LiOH(·H<sub>2</sub>O)

Lithium hydroxides were mechanically milled broadly using the same conditions reported by Zhu *et al.*,<sup>4</sup> although a 40:1 ball-to-powder ratio was used as opposed to the 120:1 ratio employed by Zhu. During a typical milling experiment, 1 gram of LiOH(·H<sub>2</sub>O) (Sigma-Aldrich, 95%) was milled for 5 hours at 500 rpm, using 10 stainless steel balls. A 5 minute interval following every 5 minutes of milling was employed. The milling products are henceforth referred to as m-LiOH and m-LiOH·H<sub>2</sub>O.

### 5.2.4 Ball milling of MgH<sub>2</sub>

Nanostructured MgH<sub>2</sub> was produced by mechanically milling the as-received hydride (Aldrich, hydrogen-storage grade, ≥ 96.5%). 1 gram of MgH<sub>2</sub> was loaded into a 50 ml stainless steel jar using 10 stainless steel balls as a grinding medium. The process was typically conducted by milling the starting material for 5 hours at 450 rpm. A 5 minute interval following every 5 minutes of milling was used.<sup>17</sup> Milled MgH<sub>2</sub> is henceforth referred to as m-MgH<sub>2</sub>.

### 5.2.5 TG-DTA-MS studies

Thermogravimetric analysis coupled with mass spectroscopy studies were performed to obtain information on the onset and peak temperatures of the thermal events occurring during heating, the change in mass (wt. %) and nature of the gaseous species evolved during the thermal treatment. TG-DTA experiments were carried out using a Netzsch STA

409 PC instrument coupled to a Hiden HPR20 mass spectrometer as detailed in Section 2.3.4. All measurements were performed under a flow of argon and all manipulations were conducted under inert atmosphere inside glove boxes.

Initially correction files were created and then the samples analysed. First experiments were carried out heating the analysed material from room temperature to 873 K with a heating rate of 5 K min<sup>-1</sup> and holding that temperature for 1 hour before allowing the sample to cool naturally. Subsequent experiments were planned based on the results obtained and intermediate temperature points were studied to isolate any intermediate species forming and to propose a dehydrogenation mechanism. For each experiment, approximately 20-25 mg of sample were analysed.

Further, thermogravimetric analyses were performed in order to calculate the activation energy for every thermal event occurring during TG-DTA-MS experiments: this was done employing the Kissinger method.<sup>18,19</sup> Samples were heated to 773 K using heating rates of 2, 5, 10 and 20 K min<sup>-1</sup> (Table 5-5 and 5-9) and Kissinger plots were obtained.

### **5.2.6 Powder X-ray diffraction (PXD) experiments**

All starting materials and hydrogen release systems were analysed by PXD as described in Section 2.3.1.1. Due to the air sensitive nature of the materials employed, all X-ray diffraction patterns were collected with a Bruker d8 diffractometer using sealed capillaries. Typically, data were collected between  $5 \leq 2\theta^\circ \leq 85$  for 1 h for phase identification and for 12 h for structural refinement purposes.

PXD patterns obtained were compared with the appropriate reference patterns using the ICSD database<sup>20</sup> and generating calculated powder patterns with PowderCell.<sup>21</sup>

As already discussed in Section 2.3.3, Rietveld refinements against the PXD data were performed using the General Structure Analysis System (GSAS)<sup>22</sup> with the EXPGUI interface.<sup>23</sup> The background was successfully modelled using Function 8 (reciprocal interpolation function). This was followed by the refinement of the cell parameters, atomic positions, profile parameters and temperature factors. The peak shape was modelled using Function 2, which is a multi-term Simpson's integration of the Pseudo-Voigt function.

### 5.2.7 Scanning Electron Microscopy (SEM) imaging

Samples for SEM imaging were prepared as discussed in Section 2.3.5.1. All manipulations were carried out inside a recirculating argon- or nitrogen- filled glove box. A small amount of sample was deposited onto aluminium stubs using adhesive carbon tabs. The samples were put into glass vials and sealed before being transferred out of the glove box, to minimise the exposure to air and moisture. Since in this work materials were often found to charge under the beam, the samples were typically sputter-coated with a 10 nm layer of gold/palladium alloy in order to achieve better conductivity and increase the quality of the images. The samples were then placed inside the vacuum column of the microscope, which was shut using an air-tight door and evacuated.

Images have been acquired at the Imaging Spectroscopy and Analysis Centre (ISAAC), School of Geographical and Earth Sciences (GES) at the University of Glasgow. A Carl Zeiss Sigma Variable Pressure Analytical SEM with Oxford Microanalysis employing a Schottky thermal field emitter electron source was used with a working distance of typically 5-6 mm and an accelerating voltage of 15-25 kV and. All images were collected with the help of Dr Peter Chung.

### 5.2.8 Summary of samples and reactions

**Table 5-1: Summary of starting materials employed in the LiOH – MgH<sub>2</sub> hydrogen release systems.**

Sample	Material	Preparation Conditions	Heating program / K
1	n-LiOH	Schlenk Apparatus - 343 K	873 / 5 K min <sup>-1</sup> + 1 h dwell
2	n-LiOH·H <sub>2</sub> O	Schlenk Apparatus - 298 K	873 / 5 K min <sup>-1</sup> + 1 h dwell
3	m-LiOH	5 h milling @ 500 rpm (5/5)	873 / 5 K min <sup>-1</sup> + 1 h dwell
4	m-LiOH·H <sub>2</sub> O	5 h milling @ 500 rpm (5/5)	873 / 5 K min <sup>-1</sup> + 1 h dwell
5	m-MgH <sub>2</sub>	5 h milling @ 450 rpm (5/5)	873 / 5 K min <sup>-1</sup> + 1 h dwell

**Table 5-2: Summary of preparations carried out for the bulk LiOH – MgH<sub>2</sub> system.**

<b>Sample</b>	<b>Material</b>	<b>Preparation Conditions</b>	<b>Heating program / K</b>
<b>6</b>	b-LiOH – b-MgH <sub>2</sub>	5 min manual mixing	–
<b>7</b>	b-LiOH – b-MgH <sub>2</sub>	5 min manual mixing	873 / 5 K min <sup>-1</sup> + 1 h dwell
<b>8</b>	b-LiOH – b-MgH <sub>2</sub>	5 min manual mixing	673 / 5 K min <sup>-1</sup>
<b>9</b>	b-LiOH – b-MgH <sub>2</sub>	5 min manual mixing	758 / 5 K min <sup>-1</sup>
<b>10</b>	b-LiOH – b-MgH <sub>2</sub>	5 min manual mixing	773 / 5 K min <sup>-1</sup>

**Table 5-3: Summary of preparations carried out for the mechanically milled LiOH – MgH<sub>2</sub> system.**

<b>Sample</b>	<b>Material</b>	<b>Preparation Conditions</b>	<b>Heating program / K</b>
<b>11</b>	m-LiOH – m-MgH <sub>2</sub>	5 min manual mixing	–
<b>12</b>	m-LiOH – m-MgH <sub>2</sub>	5 min manual mixing	873 / 5 K min <sup>-1</sup> + 1 h dwell
<b>13</b>	m-LiOH – m-MgH <sub>2</sub>	5 min manual mixing	623 / 5 K min <sup>-1</sup>
<b>14</b>	m-LiOH – m-MgH <sub>2</sub>	5 min manual mixing	648 / 5 K min <sup>-1</sup>
<b>15</b>	m-LiOH – m-MgH <sub>2</sub>	5 min manual mixing	773 / 5 K min <sup>-1</sup>

**Table 5-4: Summary of preparations carried out for the nanostructured LiOH – MgH<sub>2</sub> system.**

<b>Sample</b>	<b>Material</b>	<b>Preparation Conditions</b>	<b>Heating program / K</b>
<b>16</b>	n-LiOH – m-MgH <sub>2</sub>	5 min manual mixing	–
<b>17</b>	n-LiOH – m-MgH <sub>2</sub>	5 min manual mixing	873 / 5 K min <sup>-1</sup> + 1 h dwell
<b>18</b>	n-LiOH – m-MgH <sub>2</sub>	5 min manual mixing	648 / 5 K min <sup>-1</sup>
<b>19</b>	n-LiOH – m-MgH <sub>2</sub>	5 min manual mixing	773 / 5 K min <sup>-1</sup>

**Table 5-5: Summary of preparations carried out for activation energy calculations for the LiOH – MgH<sub>2</sub> system.**

<b>Sample</b>	<b>Material</b>	<b>Preparation Conditions</b>	<b>Heating program / K</b>
<b>20</b>	b-LiOH – b-MgH <sub>2</sub>	5 min manual mixing	773 (2 K min <sup>-1</sup> )
			773 (5 K min <sup>-1</sup> )
			773 (10 K min <sup>-1</sup> )
			773 (20 K min <sup>-1</sup> )
<b>21</b>	m-LiOH – m-MgH <sub>2</sub>	5 min manual mixing	773 (2 K min <sup>-1</sup> )
			773 (5 K min <sup>-1</sup> )
			773 (10 K min <sup>-1</sup> )
			773 (20 K min <sup>-1</sup> )
<b>22</b>	n-LiOH – m-MgH <sub>2</sub>	5 min manual mixing	773 (2 K min <sup>-1</sup> )
			773 (5 K min <sup>-1</sup> )
			773 (10 K min <sup>-1</sup> )
			773 (20 K min <sup>-1</sup> )

**Table 5-6: Summary of preparations carried out for the bulk LiOH·H<sub>2</sub>O – MgH<sub>2</sub> system.**

<b>Sample</b>	<b>Material</b>	<b>Preparation Conditions</b>	<b>Heating program / K</b>
<b>23</b>	b-LiOH·H <sub>2</sub> O – b-MgH <sub>2</sub>	5 min manual mixing	–
<b>24</b>	b-LiOH·H <sub>2</sub> O – b-MgH <sub>2</sub>	5 min manual mixing	873 / 5 K min <sup>-1</sup> + 1 h dwell
<b>25</b>	b-LiOH·H <sub>2</sub> O – b-MgH <sub>2</sub>	5 min manual mixing	408 / 2 K min <sup>-1</sup>
<b>26</b>	b-LiOH·H <sub>2</sub> O – b-MgH <sub>2</sub>	5 min manual mixing	673 / 5 K min <sup>-1</sup>
<b>27</b>	b-LiOH·H <sub>2</sub> O – b-MgH <sub>2</sub>	5 min manual mixing	758 / 5 K min <sup>-1</sup>
<b>28</b>	b-LiOH·H <sub>2</sub> O – b-MgH <sub>2</sub>	5 min manual mixing	773 / 5 K min <sup>-1</sup>

**Table 5-7: Summary of preparations carried out for the mechanically milled LiOH·H<sub>2</sub>O – MgH<sub>2</sub> system.**

<b>Sample</b>	<b>Material</b>	<b>Preparation Conditions</b>	<b>Heating program / K</b>
<b>29</b>	m-LiOH·H <sub>2</sub> O – m-MgH <sub>2</sub>	5 min manual mixing	–
<b>30</b>	m-LiOH·H <sub>2</sub> O – m-MgH <sub>2</sub>	5 min manual mixing	873 / 5 K min <sup>-1</sup> + 1 h dwell
<b>31</b>	m-LiOH·H <sub>2</sub> O – m-MgH <sub>2</sub>	5 min manual mixing	408 / 2 K min <sup>-1</sup>
<b>32</b>	m-LiOH·H <sub>2</sub> O – m-MgH <sub>2</sub>	5 min manual mixing	573 / 5 K min <sup>-1</sup>
<b>33</b>	m-LiOH·H <sub>2</sub> O – m-MgH <sub>2</sub>	5 min manual mixing	673 / 5 K min <sup>-1</sup>
<b>34</b>	m-LiOH·H <sub>2</sub> O – m-MgH <sub>2</sub>	5 min manual mixing	773 / 5 K min <sup>-1</sup>

**Table 5-8: Summary of preparations carried out for the nanostructured LiOH·H<sub>2</sub>O – MgH<sub>2</sub> system.**

<b>Sample</b>	<b>Material</b>	<b>Preparation Conditions</b>	<b>Heating program / K</b>
<b>35</b>	n-LiOH·H <sub>2</sub> O – m-MgH <sub>2</sub>	5 min manual mixing	–
<b>36</b>	n-LiOH·H <sub>2</sub> O – m-MgH <sub>2</sub>	5 min manual mixing	873 / 5 K min <sup>-1</sup> + 1 h dwell
<b>37</b>	n-LiOH·H <sub>2</sub> O – m-MgH <sub>2</sub>	5 min manual mixing	408 / 2 K min <sup>-1</sup>
<b>38</b>	n-LiOH·H <sub>2</sub> O – m-MgH <sub>2</sub>	5 min manual mixing	623 / 5 K min <sup>-1</sup>
<b>39</b>	n-LiOH·H <sub>2</sub> O – m-MgH <sub>2</sub>	5 min manual mixing	773 / 5 K min <sup>-1</sup>

**Table 5-9: Summary of preparations carried out for activation energy calculations for the LiOH·H<sub>2</sub>O – MgH<sub>2</sub> system.**

<b>Sample</b>	<b>Material</b>	<b>Preparation Conditions</b>	<b>Heating program / K</b>
<b>40</b>	b-LiOH·H <sub>2</sub> O – b-MgH <sub>2</sub>	5 min manual mixing	773 (2 K min <sup>-1</sup> )
			773 (5 K min <sup>-1</sup> )
			773 (10 K min <sup>-1</sup> )
			773 (20 K min <sup>-1</sup> )
<b>41</b>	m-LiOH·H <sub>2</sub> O – m-MgH <sub>2</sub>	5 min manual mixing	773 (2 K min <sup>-1</sup> )
			773 (5 K min <sup>-1</sup> )
			773 (10 K min <sup>-1</sup> )
			773 (20 K min <sup>-1</sup> )
<b>42</b>	n-LiOH·H <sub>2</sub> O – m-MgH <sub>2</sub>	5 min manual mixing	773 (2 K min <sup>-1</sup> )
			773 (5 K min <sup>-1</sup> )
			773 (10 K min <sup>-1</sup> )
			773 (20 K min <sup>-1</sup> )

## 5.3 Results and Discussion

### 5.3.1 Preparation of the system components

#### 5.3.1.1 Nanostructured LiOH(·H<sub>2</sub>O)

Nanostructured LiOH(·H<sub>2</sub>O) (Samples **1** and **2**) were successfully obtained using the selective synthetic route described in Section 5.2.1. To obtain LiOH vacuum evaporation was conducted at 343 K, whereas for the synthesis of LiOH·H<sub>2</sub>O, the process was conducted at room temperature. For both synthetic procedures, the yield was found to be lower than the theoretical one: *ca.* 73% for both hydroxides. This may be due to the difficulty in collecting the entire amount of crystals from the Schlenk glassware. In particular, in a typical synthesis *ca.* 200 mg of LiOH and *ca.* 350 mg of LiOH·H<sub>2</sub>O were obtained with respect to the 274 mg and 480 mg theoretical figures for anhydrous and

monohydrate lithium hydroxide respectively. The synthesised nanostructured hydroxides were then characterised by PXD as well as SEM.

As shown in the PXD pattern for Sample 1 (Figure 5-1), pure phase LiOH was synthesised with no trace of either Li metal starting material or the monohydrate hydroxide present.

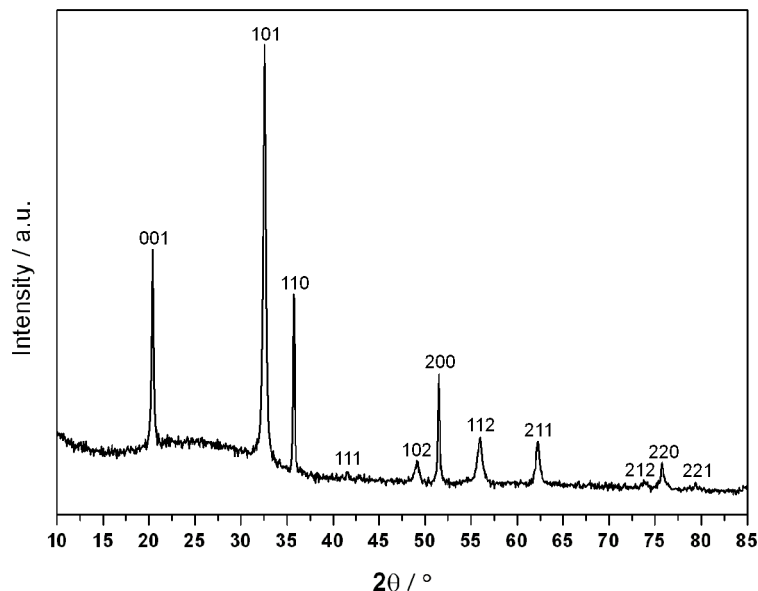


**Figure 5-1: PXD pattern for Sample 1, synthesised n-LiOH.**

SEM images of Sample 1 show a dramatic decrease of the particle size with respect to the as-received hydroxide (Figure 5-2). However, the particles show a non-uniform size distribution with particle size varying in the 40-80  $\mu\text{m}$  range. Nonetheless, a closer look at the morphology of the synthesised LiOH shows that the particles present a stacked sheet-like morphology with typical sheet thicknesses varying in the 30-50 nm range (Figure 5-3).

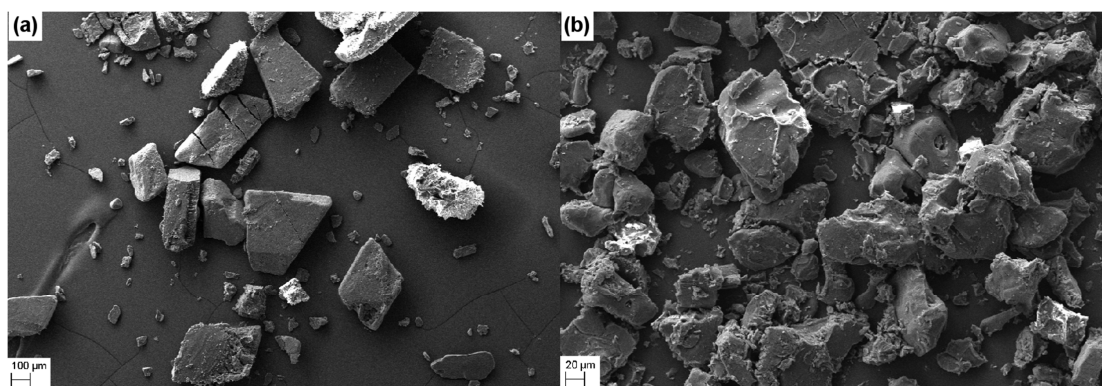


**Figure 5-2: Collected SEM images: a) commercial LiOH (100  $\mu\text{m}$  scale) and b) Sample 1 (20  $\mu\text{m}$  scale).**

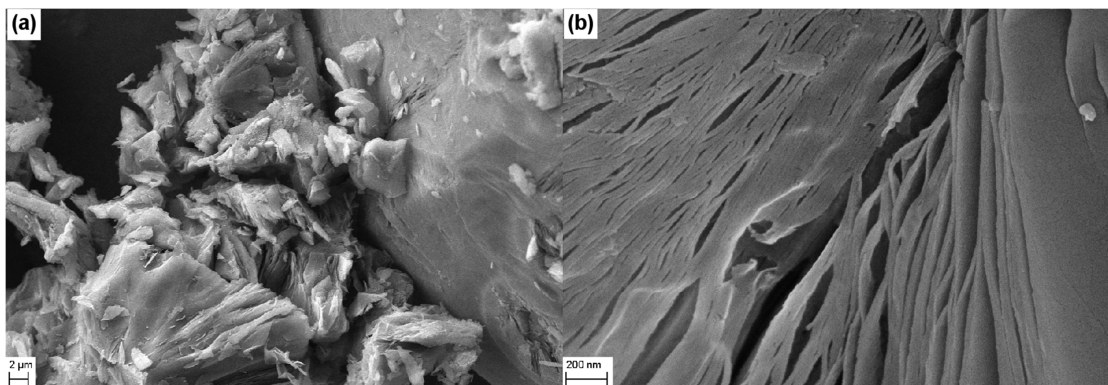


**Figure 5-3:** Collected SEM images for Sample 1: a) 2  $\mu\text{m}$  scale b) 200 nm scale.

Rietveld refinement was performed against PXD data with GSAS<sup>22</sup> using the EXPGUI<sup>23</sup> interface. Crystallographic data are presented in Table 5-10. These were found to be in good agreement with the literature values.<sup>24</sup> The observed, calculated and difference (OCD) plot from the PXD Rietveld refinement for Sample 1 is shown in Figure 5-4.

**Table 5-10:** Selected data from the PXD Rietveld refinement for Sample 1, synthesised nano LiOH.

<b>Empirical Formula</b>	<b>LiOH</b>
<b>Crystal System</b>	Tetragonal
<b>Space Group</b>	<i>P4/nmm</i>
<b>Lattice Parameters</b>	
<i>a</i> / Å	3.548(1)
<i>c</i> / Å	4.347(1)
<i>V</i> / Å <sup>3</sup>	54.71(5)
<i>Z</i>	2
<b>Unit Cell Formula</b>	47.896
<b>Weight / M<sub>w</sub></b>	
<b>Density / g cm<sup>-3</sup></b>	1.454
<b>No. of Variables</b>	23
<b>No. of Observations</b>	1056
<b>Rwp %</b>	9.51
<b>Rp %</b>	6.87
<b><math>\chi^2</math></b>	2.19

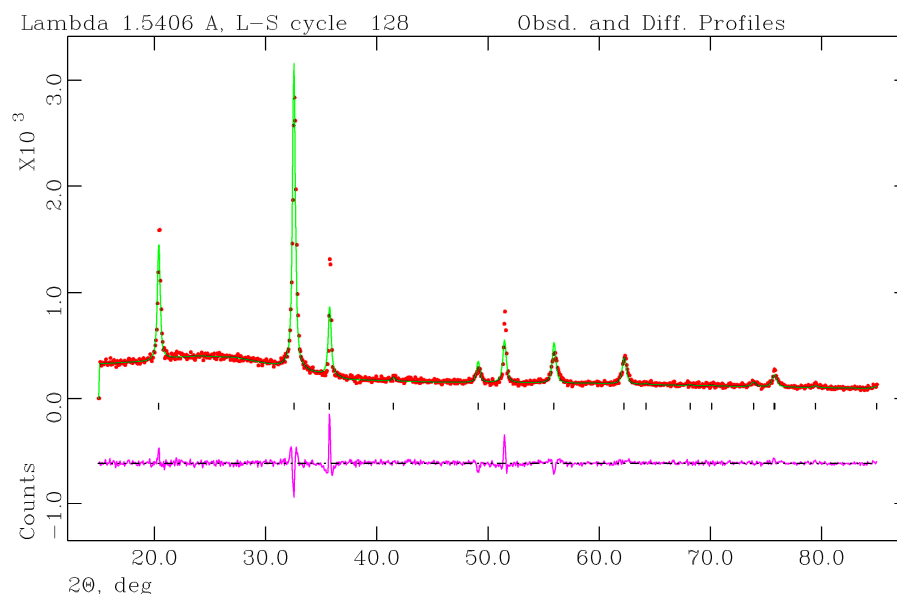


**Figure 5-4: Observed (green line), calculated (red dots) and difference (pink line) (OCD) plot from the PXD Rietveld refinement for Sample 1, synthesised n-LiOH. Black tick marks indicate n-LiOH reflections.**

As can be observed from the PXD pattern collected for Sample 2 (Figure 5-5), pure phase LiOH·H<sub>2</sub>O crystals were successfully obtained. No trace of either Li metal starting material or the anhydrous hydroxide can be identified in the diffraction pattern.

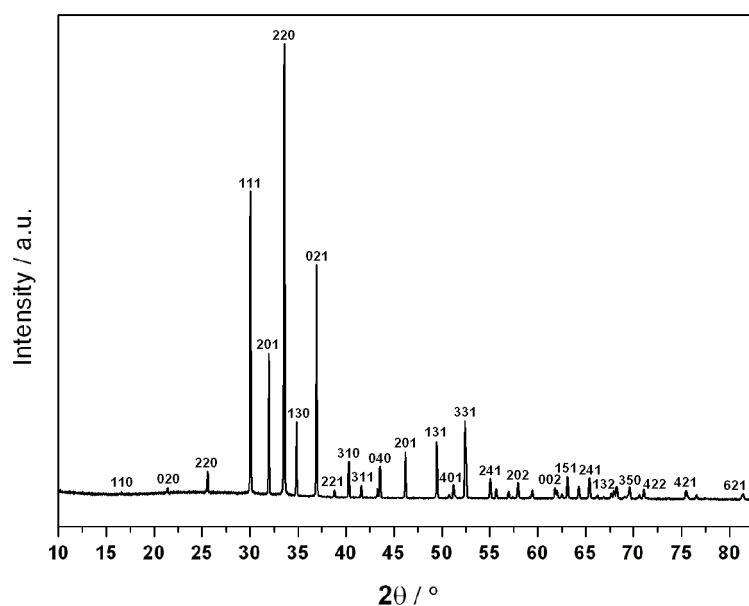


**Figure 5-5: PXD pattern for Sample 2, synthesised n-LiOH·H<sub>2</sub>O.**

Once again, SEM images were collected and they show a dramatic decrease of the particle size with respect to the as-received hydroxide (Figure 5-6), as previously observed for the anhydrous hydroxide. Also for the monohydrate compound, the particles do not show a uniform size distribution, which was found to vary in the 20-100 μm range. Images were

collected at higher magnification in order to identify the potential presence of a sheet-like morphology similar to that identified for n-LiOH. As shown in Figure 5-7, smaller particles in the 1-6  $\mu\text{m}$  range can be identified. Although it is not possible to identify any sheet-like morphology, the surface of the particle appears porous and textured.

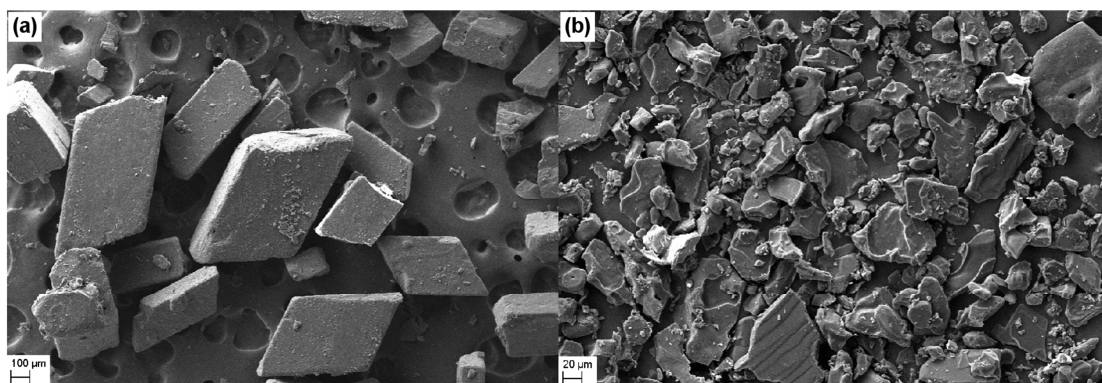


**Figure 5-6:** Collected SEM images: a) commercial LiOH (100  $\mu\text{m}$  scale) and b) Sample 2 (20  $\mu\text{m}$  scale).

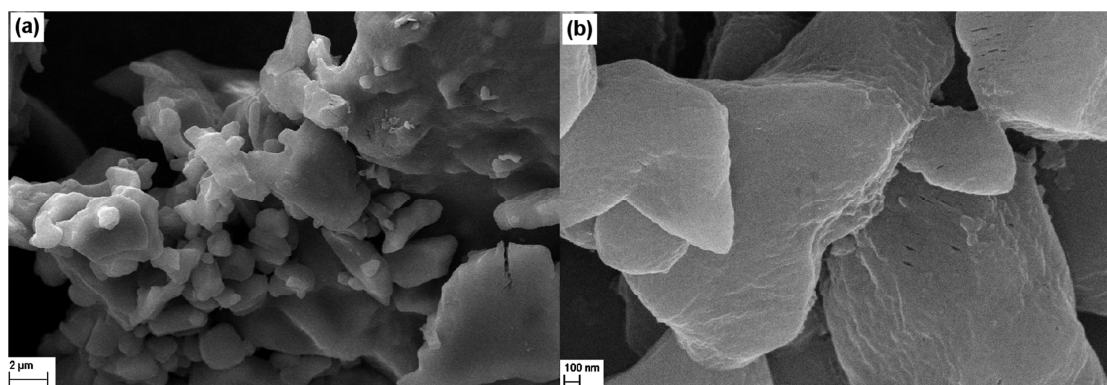


**Figure 5-7:** Collected SEM images for Sample 2: a) 2  $\mu\text{m}$  scale b) 100 nm scale.

Rietveld refinement was performed for Sample 2 against PXD data. Crystallographic data are reported in Table 5-11 and were found to be in good agreement with the literature values.<sup>25,26</sup> The observed, calculated and difference (OCD) plot from the PXD Rietveld Refinement for Sample 2 is presented in Figure 5-8.

Table 5-11: Selected data from the PXD Rietveld refinement for Sample 2, synthesised n-LiOH·H<sub>2</sub>O.

<b>Empirical Formula</b>	<b>LiOH·H<sub>2</sub>O</b>
<b>Crystal System</b>	Monoclinic
<b>Space Group</b>	<i>C2/m</i>
<b>Lattice Parameters</b>	
<i>a</i> / Å	7.4146(1)
<i>b</i> / Å	8.3051(1)
<i>c</i> / Å	3.1947(1)
<i>V</i> / Å <sup>3</sup>	184.742(6)
<i>Z</i>	4
<b>Unit Cell Formula</b>	
<b>Weight / M<sub>w</sub></b>	167.852
<b>Density / g cm<sup>-3</sup></b>	1.509
<b>No. of Variables</b>	33
<b>No. of Observations</b>	4423
<b>Rwp %</b>	6.45
<b>Rp %</b>	4.95
<b>χ<sup>2</sup></b>	1.73

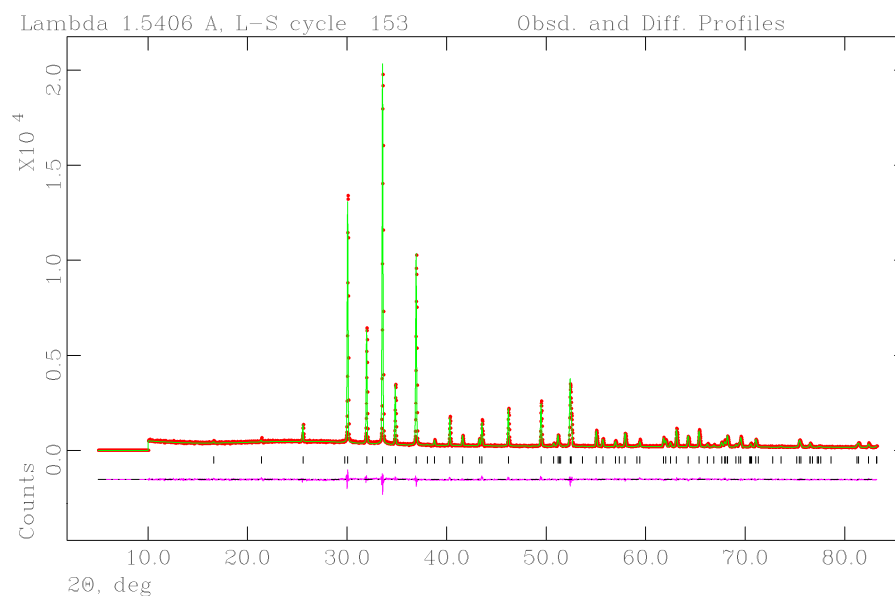


Figure 5-8: Observed (green line), calculated (red dots) and difference (pink line) (OCD) plot from the PXD Rietveld refinement for Sample 2, synthesised n-LiOH·H<sub>2</sub>O. Black tick marks indicate n-LiOH·H<sub>2</sub>O reflections.

### 5.3.1.2 Ball milled LiOH( $\cdot$ H<sub>2</sub>O)

Anhydrous lithium hydroxide (Sample 3) and lithium hydroxide monohydrate (Sample 4) were ball milled for 5 h at 500 rpm. As shown in Figures 5-9 and 5-10, the post-milling products are still single phase LiOH( $\cdot$ H<sub>2</sub>O).

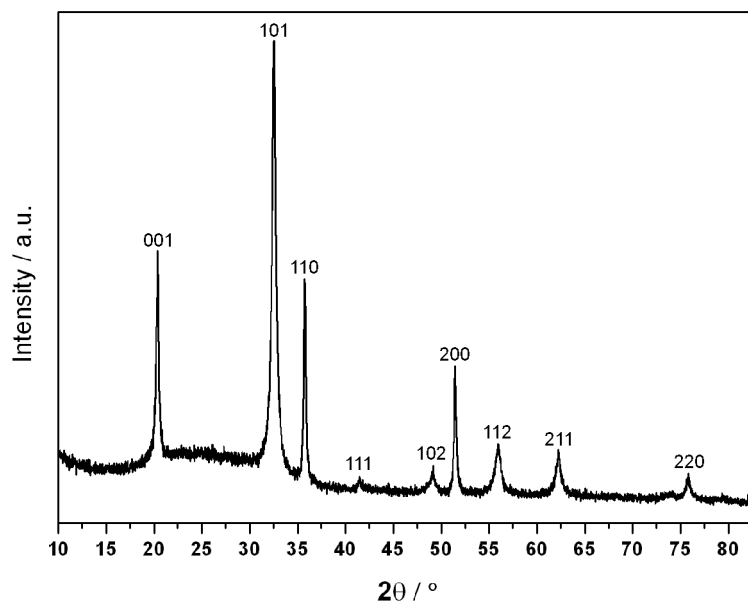


Figure 5-9: PXD pattern for Sample 3, ball m-LiOH.

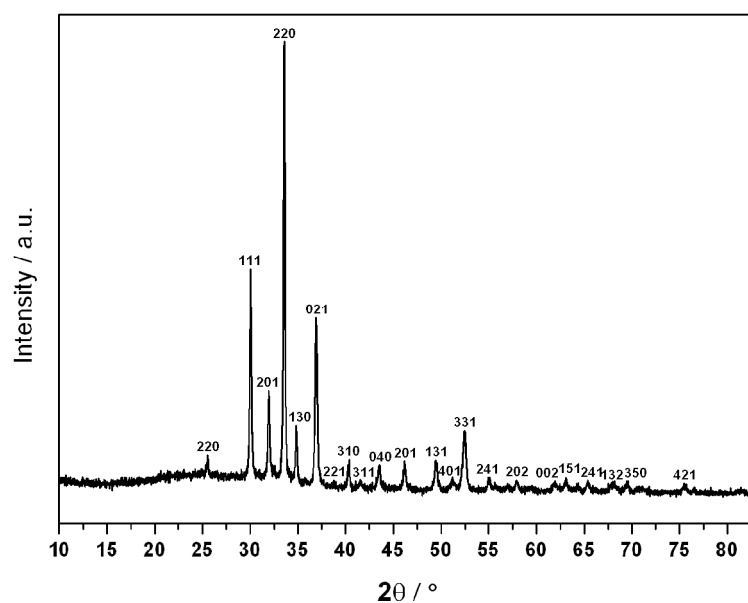


Figure 5-10: PXD pattern for Sample 4, m-LiOH $\cdot$ H<sub>2</sub>O.

SEM images for both milled hydroxides have been collected (Figures 5-11 and 5-12). The milled materials present similar typical particle size of 2-8  $\mu$ m in diameter. However, unlike as previously observed for milled Mg(OH)<sub>2</sub> (Section 3.3.1.2), milled LiOH( $\cdot$ H<sub>2</sub>O)

particles do not tend to agglomerate into bigger clusters, resulting in a homogeneous distribution of the particles throughout the whole sample.

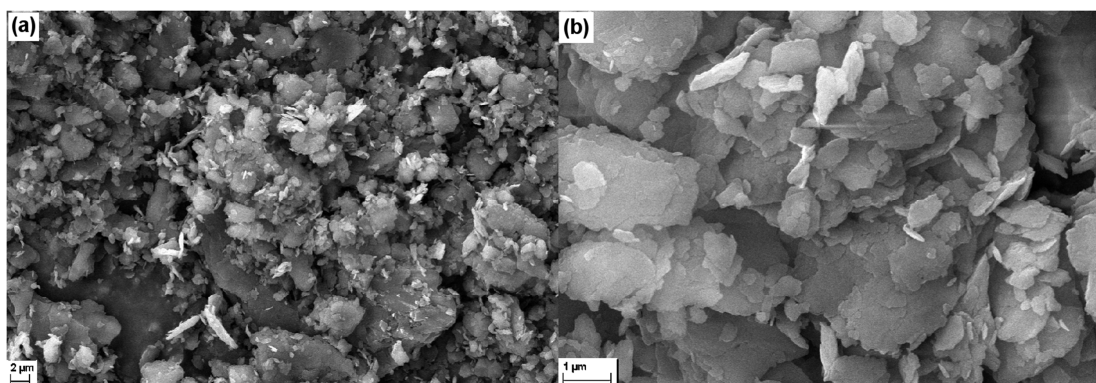


Figure 5-11: Collected SEM images for Sample 3: a) 2  $\mu\text{m}$  scale b) 1  $\mu\text{m}$  scale.

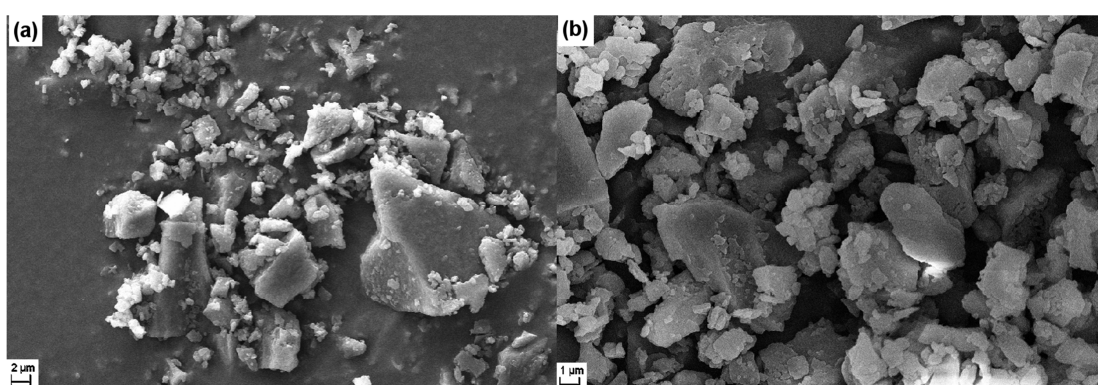


Figure 5-12: Collected SEM images for Sample 4: a) 2  $\mu\text{m}$  scale b) 1  $\mu\text{m}$  scale.

### 5.3.1.3 Ball milled $\text{MgH}_2$

Magnesium hydride (Sample 5) was ball milled for 5 h at 450 rpm. The PXD pattern collected after the milling procedure was carried out confirms that shows that no major reaction occurs during the milling time:  $\beta\text{-MgH}_2$  is still the main phase present and reflections assignable to  $\gamma\text{-MgH}_2$  and Mg metal can be identified as minor phases. A detailed discussion of ball milled  $\text{MgH}_2$  can be found in Section 3.3.1.3.

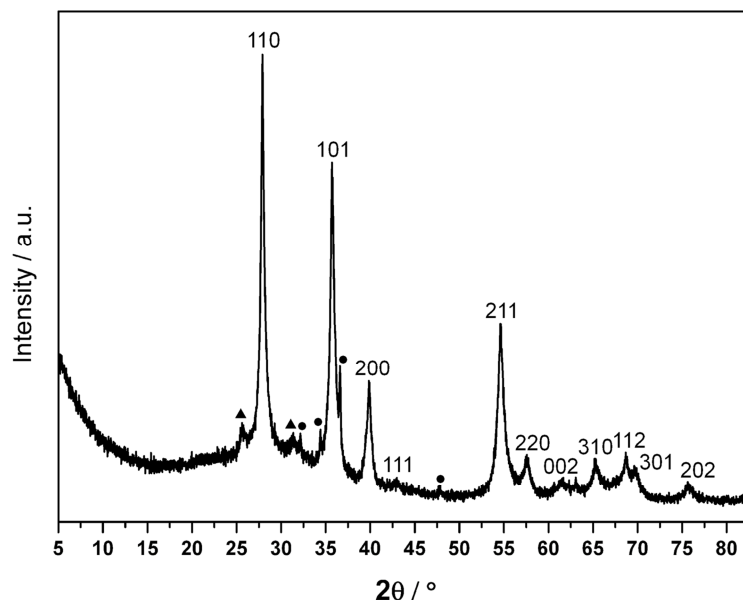


Figure 5-13: PXD pattern for Sample 5, ball milled magnesium hydride ( $\beta$ -MgH<sub>2</sub>). Triangles and circles indicate  $\gamma$ -MgH<sub>2</sub> and Mg metal respectively.

## 5.3.2 TG-DTA-MS data

### 5.3.2.1 Starting Materials

Similarly to the magnesium hydroxide – magnesium hydride system already presented in Chapter 3, prior to the study of the ‘modular’ release system, TG-DTA-MS studies were carried out on the starting materials. Samples **1**, **2**, **3**, and **4**, the commercial anhydrous as well as monohydrate lithium hydroxide were investigated individually. Sample **5** and as-received MgH<sub>2</sub> were also studied individually. This allowed a comparison of onset and peak temperatures of dehydration and dehydrogenation for LiOH( $\cdot$ H<sub>2</sub>O) and MgH<sub>2</sub> respectively, as well as weight losses and an assessment of the gaseous species evolved during heating. A summary of the results obtained for anhydrous lithium hydroxide is reported in Table 5-12.

**Table 5-12: Onset temperature, peak temperatures, weight losses and identified released gaseous species for Sample 1 (n-LiOH), Sample 3 (m-LiOH) and as-received LiOH (b-LiOH).**

Sample	Onset T / K	Peak T / K	Weight Loss / %	Evolved Gases
<b>1</b> n-LiOH	709	747	27.7	H <sub>2</sub> O
<b>3</b> m-LiOH	713	751	35.2	H <sub>2</sub> O
<b>Commercial</b> LiOH	711	751	36.2	H <sub>2</sub> O

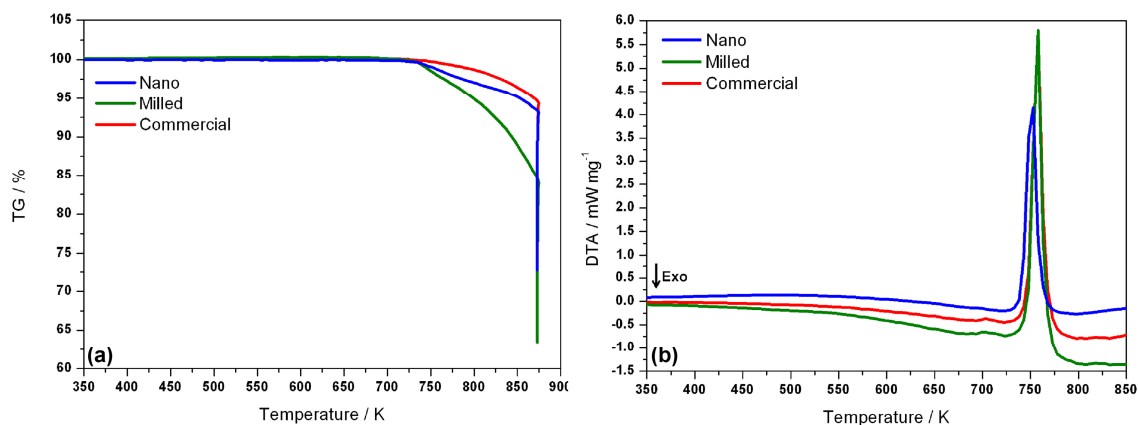


**Figure 5-14: (a) TG and (b) DTA data comparison for commercial (red), nanostructured (1; blue) and milled (2, green) anhydrous lithium hydroxide.**

Figure 5-14 presents the TG-DTA data collected for Sample 1 (n-LiOH), 3 (m-LiOH) and as-received LiOH (b-LiOH). From both TG and DTA profile it is possible to identify one single thermal event. The temperature of this endothermic event is consistent throughout all three samples with the dehydration and melting of LiOH beginning at 709, 713 and 711 K and reaching a peak temperature of 747 K for nano and 751 K for both milled and commercial materials respectively. These data are consistent with the melting of LiOH, which is supposed to occur at 723 K according to the Handbook of Chemistry and Physics.<sup>27</sup> However, the TG profiles show differences between materials. Nanostructured LiOH (Sample 1) displays a weight change of 27.7 %, which corresponds to *ca.* 75% of the theoretical mass loss of 37.6%. The thermal treatment of Sample 3 results in a mass loss of 35.2 % (93.6 % of the theoretical one), whilst the commercial LiOH dehydration process

yields a weight loss of 36.2 % (96.3 % with respect to the theoretical figure). It was not possible to retrieve any sample after the thermal treatment, as the powder melted inside the sample holder inside the STA apparatus. It is interesting to note that all mass losses start close to the melting point of the material and take place mostly during the 1 h holding time at 873 K. It is possible to hypothesise that if the temperature of holding was held for a longer time, this would have resulted in mass losses nearer to the theoretical value of 37.6%.

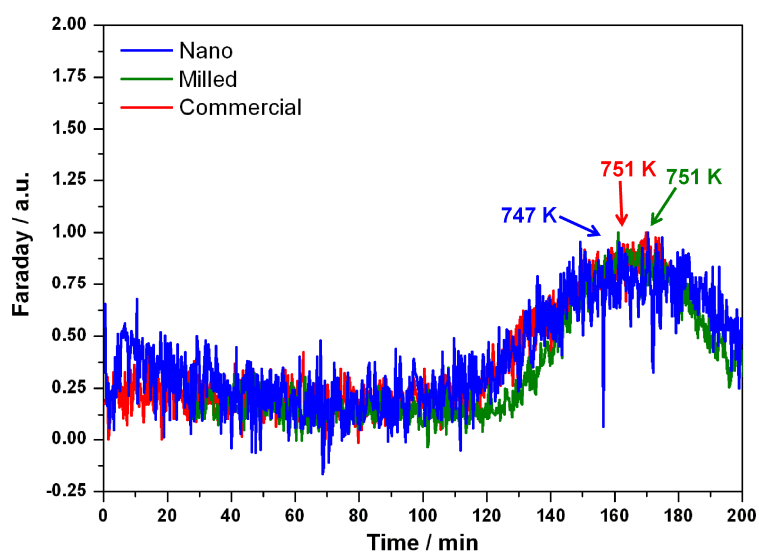


**Figure 5-15: MS profiles Vs time for commercial (red), nanostructured (1; blue) and milled (3, green) anhydrous lithium hydroxide.**

The only gaseous species detected appears to be water as expected. As can be seen in Figure 5-15, the H<sub>2</sub>O release appears to be a single event, with the mass losses take places during the holding time. Further, the MS peak shape from the H<sub>2</sub>O release is not well-defined, suggesting that the water release was still an ongoing process at the time the measurement ended.

Data obtained for lithium hydroxide monohydrate are summarised in Table 5-13. The TG-DTA data collected for Sample 2 (n-LiOH·H<sub>2</sub>O), Sample 4 (m-LiOH·H<sub>2</sub>O) and as-received LiOH·H<sub>2</sub>O (b-LiOH·H<sub>2</sub>O) are presented in Figure 5-16.

**Table 5-13: Onset temperature, peak temperatures, weight losses and identified released gaseous species for Sample 2 (n-LiOH·H<sub>2</sub>O), Sample 4 (m-LiOH·H<sub>2</sub>O) and as-received LiOH·H<sub>2</sub>O (b-LiOH·H<sub>2</sub>O).**

Sample	Onset T / K	Peak T / K	Weight Loss / %	Evolved Gases
<b>2</b> n- LiOH·H <sub>2</sub> O	331	383	63.5	H <sub>2</sub> O
	716	745		
<b>4</b> m- LiOH·H <sub>2</sub> O	324	378	62.7	H <sub>2</sub> O
	716	744		
<b>Commercial</b> LiOH·H <sub>2</sub> O	330	390	63.4	H <sub>2</sub> O
	724	746		

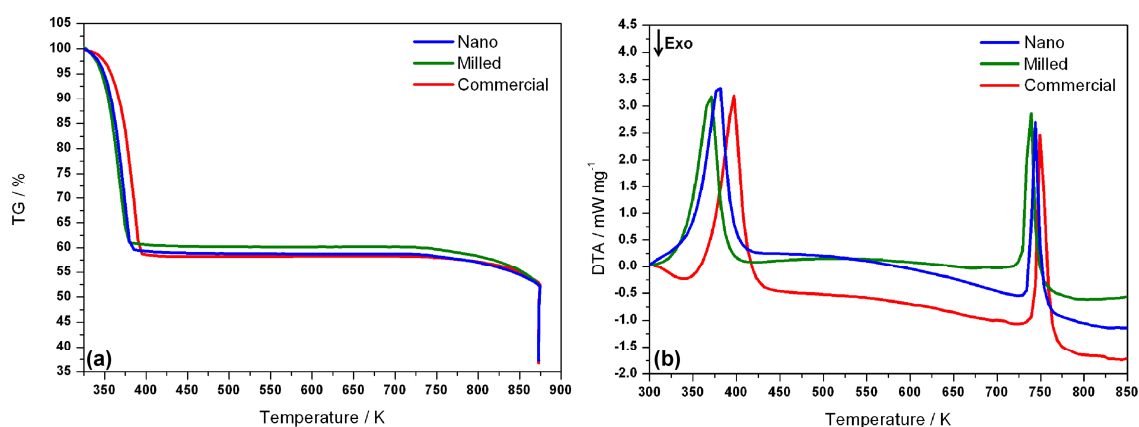


**Figure 5-16: (a) TG and (b) DTA data comparison for commercial (red), nanostructured (3; blue) and milled (4, green) lithium hydroxide monohydrate.**

From both TG and DTA profiles is possible to identify two different thermal events taking place. The first endothermic event is believed to relate to the loss of structural water, leading to the formation of LiOH from LiOH·H<sub>2</sub>O. The onset temperature for this first event was found to be 331, 324 and 330 K with a peak temperatures of 383, 378 and 390 K for Sample **2** (nano), **4** (milled) and commercial LiOH respectively. The second endothermic event can be attributed once again to the final dehydration and melting of the remaining LiOH. The onset temperature of this process was found to be consistent with Sample **1**, **3** and commercial LiOH and was found to be 716 K for nanostructured and milled LiOH·H<sub>2</sub>O and 724 K for as-received LiOH·H<sub>2</sub>O, with the peak temperatures being

746, 744 and 745 K for commercial, milled and nanostructured LiOH·H<sub>2</sub>O respectively. This values are once again in agreement with the melting point value given in the Handbook of Chemistry and Physics.<sup>27</sup> Further, all mass losses appear to be consistent; the lowest is related to the milled LiOH·H<sub>2</sub>O (Sample 4), where a weight change of 62.7 % corresponding to 97.4 % with the theoretical figure is observed. Thermal treatment of a nanostructure lithium hydroxide monohydrate results in a weight loss of 63.5 %, which is 98.6% of the theoretical 64.4 % loss. This value is found to be similar to the mass loss observed for the as-received LiOH·H<sub>2</sub>O, whose weight change was found to be 63.4 % (98.4 % of the theoretical figure).

Although the theoretical weight losses are closer to the theoretical figure than was the case with anhydrous lithium hydroxide, the combination of TG and DTA profile once again suggests that by holding the temperature of 873 K for a longer period of time, it would be possible to completely dehydrate and melt the material. Similarly to LiOH, it was not possible to collect any LiOH·H<sub>2</sub>O powder after the STA analysis.

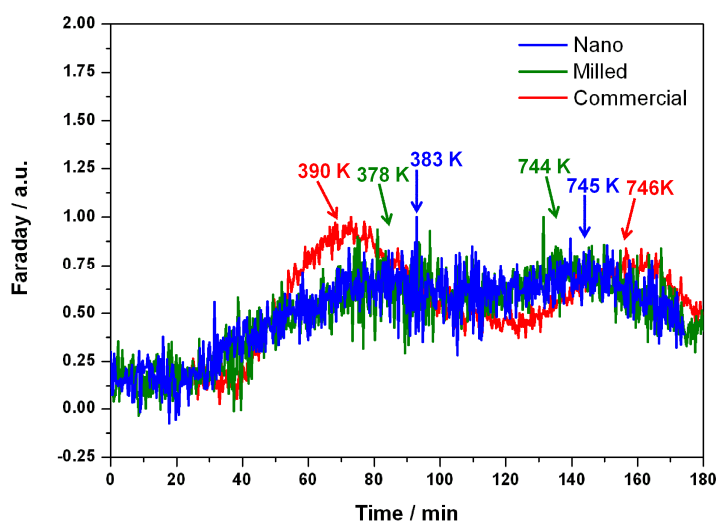


**Figure 5-17: MS profiles Vs time for commercial (red), nanostructured (2; blue) and milled (4, green) lithium hydroxide monohydrate.**

MS spectra (Figure 5-17) present two events which can be related to the release of structural water and the dehydration/melting of the remaining LiOH respectively. Similarly to LiOH, mass losses are found to take place after the peak temperature of the respective thermal event is reached in the MS spectra: 390, 378 and 383 K for the first event and 746, 744 and 745 K for the second event for commercial, milled and nanostructured LiOH·H<sub>2</sub>O respectively. As for the anhydrous LiOH, the peak shape of the second water release is not completely defined, suggesting that some H<sub>2</sub>O was still being evolved from the material during the holding time of the 873 K temperature point.

As for the studies of MgH<sub>2</sub> starting material, a detailed discussion of the TG-DTA-MS studied performed on both ball milled and as-received magnesium hydride can be found in Section 3.3.1.4. A summary of the data obtained is given in Table 5-14.

**Table 5-14: Onset temperature, peak temperatures, weight losses and identified released gaseous species for Sample 5 (milled MgH<sub>2</sub>) and for as-received MgH<sub>2</sub>.**

Sample	Onset T / K	Peak T / K	Weight Loss / %	Evolved Gases
<b>5</b> <b>m-MgH<sub>2</sub></b>	580	625	6.4	H <sub>2</sub>
<b>Commercial</b> <b>MgH<sub>2</sub></b>	667	696	6.9	H <sub>2</sub>

### 5.3.2.2 LiOH – MgH<sub>2</sub> system

Initial TG-DTA-MS experiments were performed on Samples **7**, **12** and **17** to determine the onset temperature as well as the peak temperature of possible hydrogen release and the weight loss for bulk, milled and nanostructured systems (Figures 5-18 and 5-19). The results obtained are summarised in Table 5-15. The three mixtures were heated to 873 K and that temperature held for one hour.

**Table 5-15: Onset temperature, peak temperatures, weight losses and identified released gaseous species for Samples 7, 12 and 17.**

Sample	Onset T / K	Peak T / K	Weight Loss / %	Evolved Gases
<b>7</b> <b>b-LiOH – b-MgH<sub>2</sub></b>	598	673 702 735	10.1	H <sub>2</sub>
<b>12</b> <b>m-LiOH – m-MgH<sub>2</sub></b>	509 629	598 648 711	5.2	H <sub>2</sub>
<b>17</b> <b>n-LiOH – m-MgH<sub>2</sub></b>	512 635	606 649 720	5.2	H <sub>2</sub>

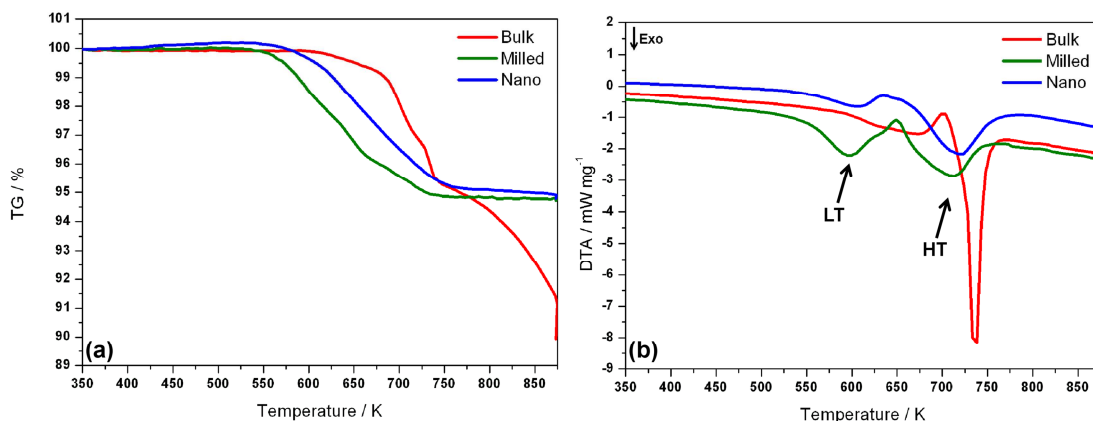


**Figure 5-18: (a) TG and (b) DTA data comparison for Sample 7 (bulk; red), Sample 12 (milled; green) and Sample 17 (nano; blue).**

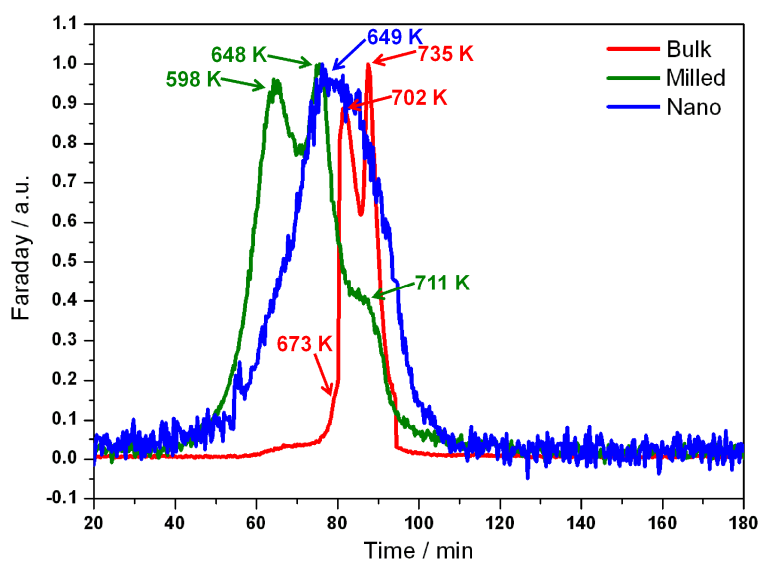


**Figure 5-19: MS profiles Vs time for Sample 7 (bulk), Sample 12 (milled) and Sample 17 (nano).**

As can be observed from Figure 5-18, interesting differences can be appreciated amongst bulk, milled and nanostructured systems in particular in terms of both weight losses and DTA profiles. It is possible to note how the onset temperature of hydrogen release is dramatically decreased by nearly 100 K when working with both milled and nanostructured materials. The onset T was found to be 509 K and 512 K for Sample 12 (milled) and Sample 17 (nano) respectively, whilst for Sample 7 (bulk) it was found to be as high as 598 K. DTA profiles for all samples show the presence of 2 main endothermic events occurring one immediately after the other. Although a closer look at both TG and first derivative of the DTA data suggest the second event to be a combination of two. The peak temperatures of the three events were found to be 673, 702 and 735 K for Sample 7

(bulk); 598, 648 and 711 K for Sample **12** (milled) and 606, 649 and 720 for Sample **17** (nano).

In terms of thermogravimetric capacity, according to Equation 5-1, the LiOH – MgH<sub>2</sub> system can theoretically release 5.9 wt. % of H<sub>2</sub>. However, the weight change for Sample **7** (bulk) was found to be 10.1 wt %, which is a higher value than expected, whereas mass losses for Sample **12** and Sample **17** were consistent for both systems and they were found to be 5.2 wt. %, nearly 90 % of the theoretical figure.

If the thermal profile followed the independent decomposition of the two starting materials then two distinct thermal events would be expected and the TG-DTA profile would appear different from the experimental one (and no third event would be identified). Further, the system would release 24.3 wt. % H<sub>2</sub>O from the decomposition of LiOH and 2.7 wt. % of H<sub>2</sub> from the decomposition of MgH<sub>2</sub>, for a total weight loss of 27.0 %. This is not in agreement with the experimental data. In this sense, it is believed that the two starting materials interact with each other rather than react individually.

The differential thermogravimetric analysis data for Sample **7** (bulk) suggest that an initial solid state reaction between LiOH and MgH<sub>2</sub> to yield Li<sub>2</sub>O and MgO accompanied by hydrogen evolution and driven by an H<sup>+</sup> – H<sup>-</sup> interaction. In fact, if the first event were related to the decomposition of either LiOH or MgH<sub>2</sub>, the onset temperature of the thermal event would be higher (711 and 667 K for LiOH and MgH<sub>2</sub> respectively). However, the reaction may lead to the formation of MgO and Li<sub>2</sub>O on the surface of MgH<sub>2</sub> and LiOH respectively, preventing the interaction between the two starting materials as the reaction proceeds. The dehydrogenation process then proceeds with the decomposition of the remaining hydride to evolve hydrogen and give magnesium metal, with the last event being the dehydration of the remaining lithium hydroxide to release water, which will react with the Mg obtained from the hydride decomposition. These three reaction steps are assignable to three different mass losses for a total of 4.8 wt. %. This is followed by another 5.3 wt. % of mass loss during the holding time. Considering the data obtained from the analysis of LiOH by itself (Section 5.3.2.1), this is consistent with the decomposition of LiOH, and a mass change that occurs during the holding time. Ultimately, the higher mass loss may be imputed to the release of gaseous water from LiOH which has not reacted with MgH<sub>2</sub> during the thermal treatment. Although, this is in contrast with the collected MS data (Figure 5-19), where the only gaseous species detected during the analysis was hydrogen.

Sample **12** (milled) and Sample **17** (nano) present the same mass loss of 5.2 wt. % and a similar DTA profile. Further, no mass loss is recorded during the holding time of 1 h at 873 K, suggesting that the reaction has gone to completion when reaching the final target temperature is reached. A similar reaction pathway can be therefore proposed for both **12** and **17**. The reaction is believed to start with the solid state reaction between  $\text{MgH}_2$  and  $\text{LiOH}$  to give  $\text{Li}_2\text{O}$  and  $\text{MgO}$  and evolve hydrogen. The reaction should then proceed with the decomposition of the remaining hydride to evolve hydrogen and yield magnesium metal. The difference between bulk and milled/nanostructured materials resides in the fact that this reaction is believed to be simultaneous to the decomposition of both the remaining magnesium hydride and lithium hydroxide. The Mg metal obtained from the hydride decomposition will immediately react with the water released from the hydroxide decomposition resulting in the formation of  $\text{MgO}$  and evolution of hydrogen.

MS data are presented in Figure 5-19. The only gaseous species detected for all samples was found to be hydrogen and evolution of water was not observed during any of the thermal treatments. However, this is not completely in agreement with the mass change observed for Sample **7** (bulk): this may be due to the fact that a very small amount of water is released from the dehydration of the remaining  $\text{LiOH}$ , still partly occurring when the measurement was stopped. This is consistent also with the MS profiles of  $\text{LiOH}$  starting material. Moreover, there are some subtle differences for the nanostructured system compared to the bulk with respect to the differential thermogravimetric analysis results. In particular, for Sample **7** (bulk) and Sample **12** (milled) the MS profile shows the presence of three distinct hydrogen releases. For the bulk materials most hydrogen appears to be evolved during the second and third event with only a small amount of  $\text{H}_2$  being released during the first event. For milled materials most  $\text{H}_2$  appears to be released during the first two events with a small amount of gas evolved during the last endothermic event. The mass spectrum for Sample **17** (nano) suggests hydrogen release takes place in a single event and it is not possible to discriminate amongst different  $\text{H}_2$  release peaks. A slightly higher onset T of  $\text{H}_2$  release and peak temperature throughout the whole dehydrogenation process suggests the hydrogen evolution from the nanostructured system to be subjected to slower kinetics with respect to the milled system.

The Kissinger method was employed for calculating the activation energies relative to the two main thermal events.<sup>18,19</sup> The first one a low temperature (LT), believed to relate to the solid state reaction between  $\text{LiOH}$  and  $\text{MgH}_2$  and the one at high temperature (HT), believed to correspond to the decomposition of the remaining  $\text{MgH}_2$  and simultaneous

dehydration of the remaining LiOH to yield MgO and Li<sub>2</sub>O and evolve H<sub>2</sub>. Data for Kissinger analysis were collected for bulk, milled and nanostructured mixtures (Samples **20**, **21** and **22**) prepared using the exact same procedure to **6**, **11** and **16** and analysed as previously stated in Section 5.2.5. Kissinger plots for both thermal events are shown in Figure 5-20 (error bars omitted for clarity) and a summary of the activation energies is given in Table 5-16. Single Kissinger plots with relative error bars and DTA profiles can be found in Appendix C. It is important to note that at greater heating rates it was not possible to discriminate between the second two thermal events. Hence it was not possible to collect enough data points to construct a Kissinger plot for postulated MgH<sub>2</sub> decomposition and LiOH dehydration reactions.

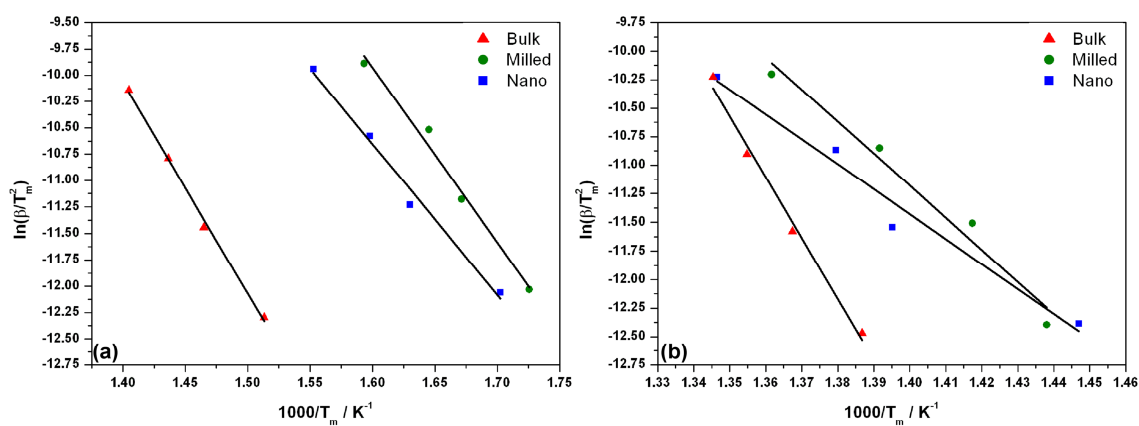


**Figure 5-20: Kissinger plots for Samples 20 (bulk; red triangles), 21 (milled; green circles) and 22 (nano; blue squares): (a) plots calculated for the LT thermal event; (b) plots calculated for the HT thermal event.**

**Table 5-16: Calculated activation energies for Samples 20, 21 and 22. Literature reported values for activation energy for LiOH and MgH<sub>2</sub> are given at the bottom of the table.**

Sample	Thermal Event	E <sub>a</sub> / kJ mol <sup>-1</sup>
<b>20</b>	LT	166±6
	HT	442±9
<b>21</b>	LT	137±9
	HT	232±8
<b>22</b>	LT	118±9
	HT	181±8
E <sub>aLiOH</sub> = 123±4 kJ mol <sup>-1</sup> ; Ref. 28		
E <sub>a bulk MgH<sub>2</sub></sub> = 156 kJ mol <sup>-1</sup> ; Ref 29		
E <sub>a milled MgH<sub>2</sub></sub> = 120 kJ mol <sup>-1</sup> ; Ref 29		

The activation energy for the LT thermal event (proposed solid state reaction between LiOH and MgH<sub>2</sub>) was found to be 166±6, 137±9 and 118±9 kJ mol<sup>-1</sup> for Sample **20**, **21** and **22** respectively.

The activation energy values for the HT thermal event were found to be 442±9, 232±8 and 181±8 kJ mol<sup>-1</sup> for Sample **20**, **21** and **22** respectively. It is possible to observe a trend in the activation energy values associated with the HT event: from bulk to milled materials the value of E<sub>a</sub> is nearly halved, whereas between nanostructured and milled materials the values are found to be similar, although slightly decreased when working with nanomaterials. This could be explained by the fact that milled as well as nano systems present a smaller particle size with respect to the bulk system: in fact, reducing the particle size of the starting materials results in an increased surface area and reactivity of the materials resulting in better dehydrogenation kinetics and thus decreased values of activation energies.

### 5.3.2.3 LiOH·H<sub>2</sub>O – MgH<sub>2</sub> system

Samples **24**, **30** and **36** were analysed using TG-DTA-MS to determine the onset temperature as well as the peak temperature of hydrogen release and the weight loss for bulk, milled and nanostructured systems (Figures 5-21 and 5-22). The bulk, milled and nanostructured mixtures were heated to 873 K and that temperature was held for one hour. The results obtained are summarised in Table 5-17.

**Table 5-17: Onset temperature, peak temperatures, weight losses and identified released gaseous species for Samples 24, 30 and 36. If not otherwise specified, the thermal events are endothermic.**

Sample	Onset T / K	Peak T / K	Weight Loss / %	Evolved Gases
<b>24</b>	331	383	33.6	H <sub>2</sub> ; H <sub>2</sub> O
<b>b-LiOH·H<sub>2</sub>O – b-MgH<sub>2</sub></b>	669	708 732		
<b>30</b>	323	358 (exo)	25.2	H <sub>2</sub> ; H <sub>2</sub> O
<b>m-LiOH·H<sub>2</sub>O – m-MgH<sub>2</sub></b>	490	566 615 672		
<b>36</b>	313	358 (exo)	22.8	H <sub>2</sub> ; H <sub>2</sub> O
<b>n-LiOH·H<sub>2</sub>O – m-MgH<sub>2</sub></b>	473	573 627 713		

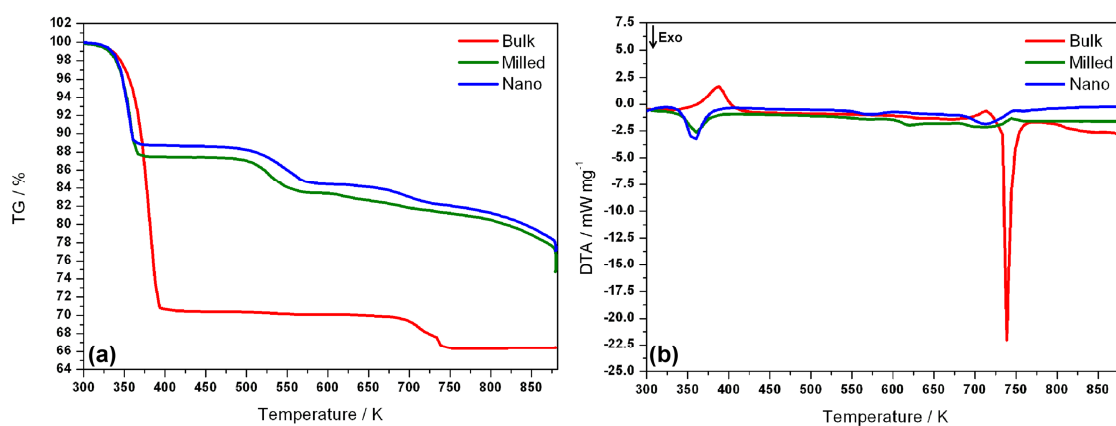


**Figure 5-21: (a) TG and (b) DTA data comparison for Sample 24 (bulk; red), Sample 30 (milled; green) and Sample 36 (nano; blue).**

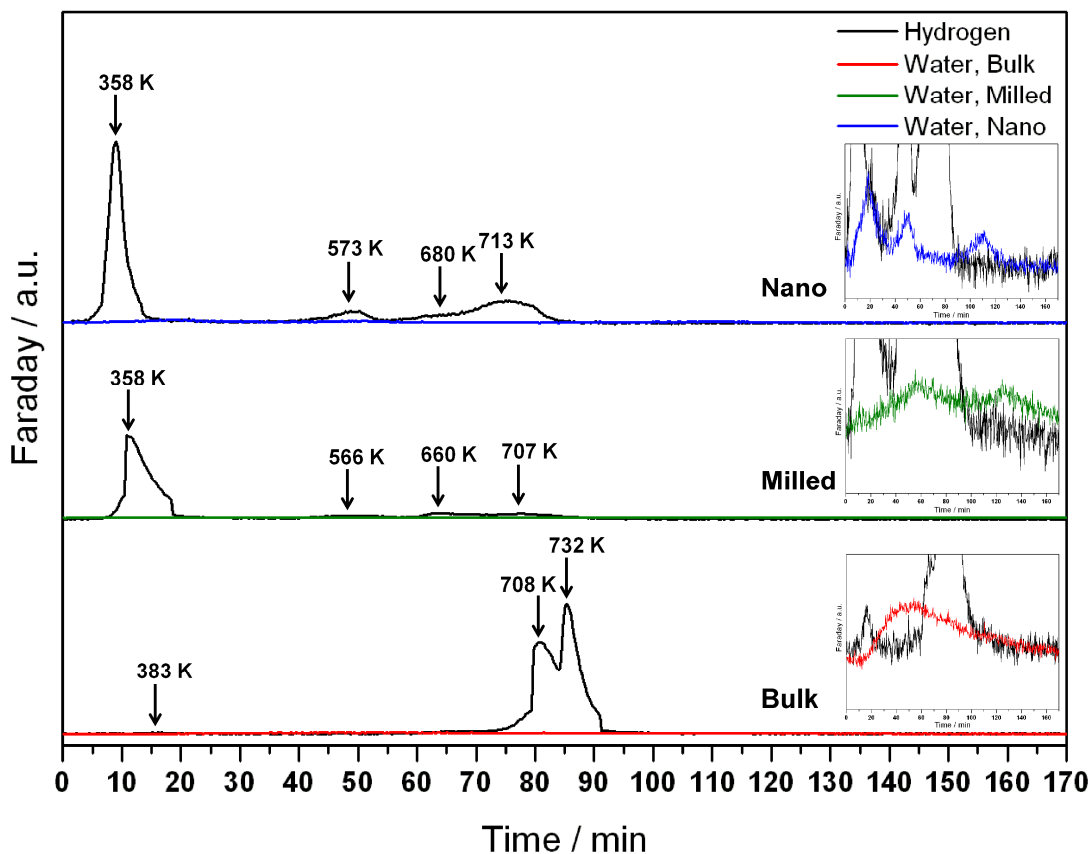


Figure 5-22: MS profiles Vs time for Sample 24 (bulk), Sample 30 (milled) and Sample 36 (nano). Black line denotes hydrogen release. In the inserts, water release for bulk, milled and nanostructured materials is denoted by red, green and blue lines respectively.

As can be observed from Figure 5-21, great differences can be appreciated amongst the three systems in terms of both mass change and DTA profiles.

TGA profiles show that the weight losses are higher than the expected 7.4 wt. %: the observed mass changes were found to be 33.6, 25.2 and 22.8 wt. % for Sample **24** (bulk), **30** (milled) and **36** (nano) respectively. Again, if the decomposition of the starting materials were due to distinct independent events such as the dehydration of  $\text{LiOH}\cdot\text{H}_2\text{O}$  and the decomposition of  $\text{MgH}_2$ , the theoretical weight change of the system would be of 38.5 wt. %: 34.6 wt. %  $\text{H}_2\text{O}$  from  $\text{LiOH}\cdot\text{H}_2\text{O}$  (23.1 wt. % from the structural water and 11.5 wt. % from  $\text{LiOH}$  dehydration) and 3.9 wt. %  $\text{H}_2$  from magnesium hydride. The differences in terms of TG-DTA profiles could be explained by taking into account the MS spectra showing the gaseous species evolved during the thermal treatment of each sample (Figure 5-22).

The most interesting feature in terms of the differential thermal analysis is related to the thermodynamic nature of the first thermal events occurring and the release of the gaseous species associated with them. For Sample **24** (bulk) the first thermal event was found to be endothermic, starting at 331 K and with a peak temperature of 383 K, which is assignable to the loss of structural water from  $\text{LiOH}\cdot\text{H}_2\text{O}$  as  $\text{H}_2\text{O}$  is the main species detected in the mass spectra, however a very small amount of hydrogen could be detected as well. This could explain the first weight loss of 29.5 %, which may be due both the loss of structural water from the hydroxide together with a slight release of  $\text{H}_2$  from the surface of the newly formed anhydrous  $\text{LiOH}$ . The dehydrogenation process is then believed to follow the same reaction pathway as Sample **7**, the anhydrous lithium hydroxide – magnesium hydride already discussed in Section 3.3.2.2, with the only gaseous species detected being  $\text{H}_2$ . The subsequent thermal event was found to have an onset temperature of 669 K and a peak temperature of 708 K and it is immediately followed by the last event with a peak temperature of 732 K.

TG-DTA data suggest a different dehydrogenation reaction occurring when employing milled and nanostructured materials. Sample **30** (milled) and Sample **36** (nano) present similar weight change and similar differential thermogravimetric profiles and therefore it is hypothesised that they follow similar mechanistic steps in terms of hydrogen release. The major difference with respect to bulk materials is that for both milled and nanostructured materials the first event appears to be exothermic, suggesting the reaction to be a simultaneous loss of structural water from  $\text{LiOH}\cdot\text{H}_2\text{O}$  and  $\text{MgH}_2$  hydrolysis to yield magnesium hydroxide and evolve hydrogen rather than water, starting at temperatures as low as 323 and 313 K (with peak temperatures of 358 K for both systems) for Sample **30** (milled) and **36** (nano) respectively. This event is related to mass changes of 12.5 wt. % and 11.3 wt. % for milled and nanostructured systems respectively. If only water was evolved that weight loss would be higher and the evidence suggests instead that water release is accompanied by hydrogen evolution. The collected MS data are in good agreement with the TG-DTA profiles, showing that mostly hydrogen is released during this event, together with the presence of a small amount of water vapour. Both Samples **30** (milled) and **36** (nano) then appear to be subjected to three more reaction steps associated with hydrogen and water release throughout the whole thermal treatment.

In particular, the next event for Sample **30** (milled) was found to start at 490 K with a peak temperature of 566 K and is immediately followed by the third thermal event, with a peak temperature of 615 K. The fourth and last event was found to have an onset temperature of

672 K and a peak temperature of 707 K. The mass loss associated with the 3 events was found to be 12.7 wt. %, suggesting once again that both H<sub>2</sub> and H<sub>2</sub>O are evolved during the thermal treatment. A similar TG-DTA profile was observed for Sample **36** (nano), which present temperatures consistent with the milled materials. For nanostructured materials the second event was found to start at 473 K and to have a peak temperature of 573 K. For nanostructured materials, it was also possible to identify the onset temperature of the third event, which was found to be 627 K with a peak temperature of 680 K with the fourth and last event following immediately with a peak temperature of 713 K. These 3 events are associated with a weight change of 11.6 %, suggesting as for milled materials, that both hydrogen and gaseous water are being evolved. This is confirmed by the mass spectra.

Based on the TG-DTA-MS data collected it is possible to hypothesise that milled and nano materials follow the same reaction pathway. The first step would correspond to the simultaneous loss of structural water from LiOH·H<sub>2</sub>O and hydrolysis of 1 mole of MgH<sub>2</sub> to yield Mg(OH)<sub>2</sub>, LiOH and evolution of both H<sub>2</sub> and H<sub>2</sub>O. Then the reaction is believed to proceed via the dehydration of Mg(OH)<sub>2</sub> to evolve water, which hydrolyses another mole of the hydride and at the same time evolves more water and hydrogen. This is then followed by the decomposition of the remaining mole of magnesium hydride to give Mg, evolving H<sub>2</sub>. The last step of the reaction mechanism is believed to be the decomposition of the remaining lithium hydroxide to release water, which will partially react with the magnesium metal formed during the decomposition of the hydride to yield Mg(OH)<sub>2</sub>, which then almost instantly forms MgO and evolves H<sub>2</sub>.

Similarly, the Kissinger method was used to obtain the activation energies for the different thermal events for the LiOH·H<sub>2</sub>O – MgH<sub>2</sub> system.<sup>18,19</sup> Data for obtaining Kissinger plots were collected for bulk, milled and nanostructured mixtures (Samples **40**, **41** and **42**) prepared using the same procedure to **23**, **29** and **35** and analysed as previously stated in Section 5.2.5. Specifically, it was possible to calculate the activation energies for the 3 events occurring during the thermal treatment of Sample **40** and for the 4 events occurring during thermal treatment of Sample **41** and Sample **42**. Kissinger plots for all thermal events are shown in Figure 5-23 (error bars omitted for clarity) and a summary of the activation energies given in Table 5-18. Single Kissinger plots with relative error bars and DTA profiles are presented in Appendix C.

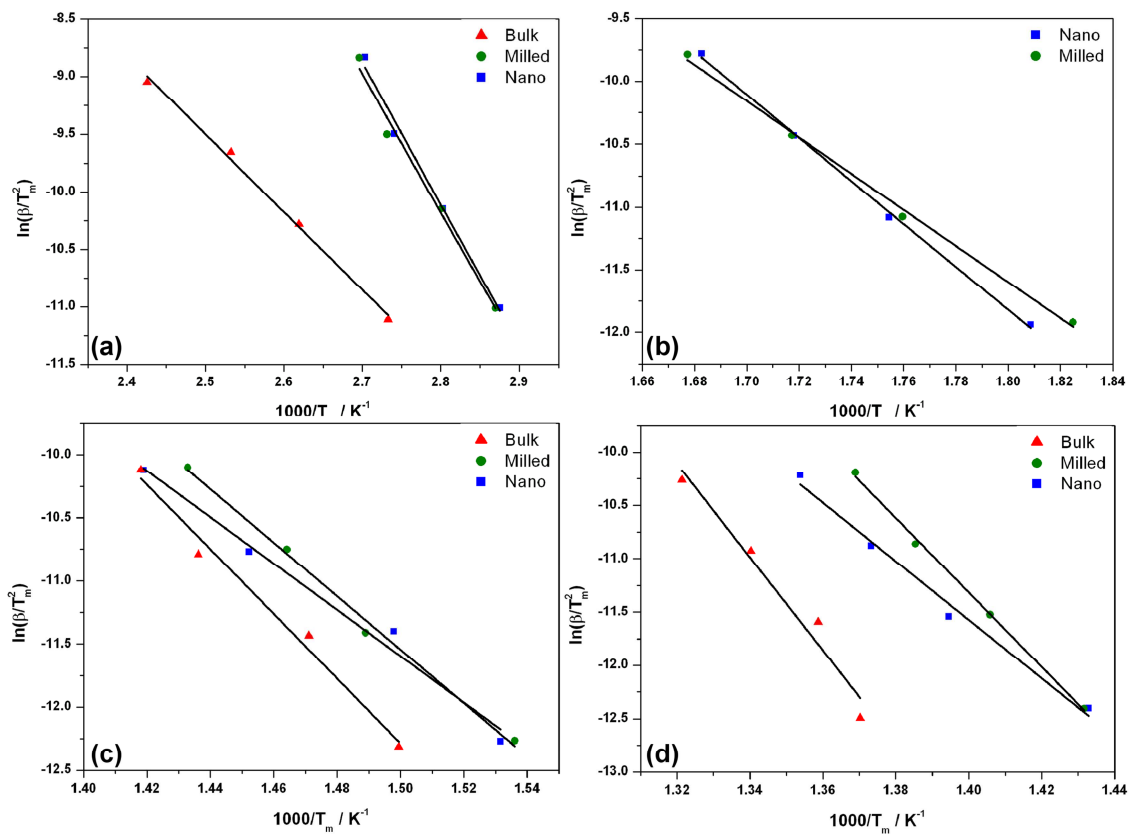


**Figure 5-23: Kissinger plots for Samples 40 (bulk; red triangles), 41 (milled; green dots) and 42 (nano; blue squares): (a) plots calculated for thermal event 1; (b) plots calculated for thermal event 2; (c) plots calculated for thermal event 3; (d) plots calculated for thermal event 4.**

**Table 5-18: Calculated activation energies for Samples 40, 41 and 42. Literature reported values for activation energy for LiOH·H<sub>2</sub>O, Mg(OH)<sub>2</sub>, LiOH and MgH<sub>2</sub> are given at the bottom of the table.**

Sample	Thermal Event	E <sub>a</sub> / kJ mol <sup>-1</sup>
<b>40</b>	1	56±2
	2	212±7
	3	363±9
<b>41</b>	1	100±8
	2	120±4
	3	176±9
	4	290±8
<b>42</b>	1	102±7
	2	142±4
	3	152±9
	4	228±9

---

E<sub>a</sub><sub>LiOH·H<sub>2</sub>O</sub> = 52 kJ mol<sup>-1</sup>; Ref. 30

E<sub>a</sub><sub>LiOH</sub> = 123±4 kJ mol<sup>-1</sup>; Ref. 28

E<sub>a</sub><sub>Mg(OH)<sub>2</sub></sub> = 123±5 kJ mol<sup>-1</sup>; Ref 31

E<sub>a</sub><sub>bulk MgH<sub>2</sub></sub> = 156 kJ mol<sup>-1</sup>; Ref 29

E<sub>a</sub><sub>milled MgH<sub>2</sub></sub> = 120 kJ mol<sup>-1</sup>; Ref 29

---

The activation energy values for the thermal event 1 were found to be 56±2, 100±8 and 102±7 kJ mol<sup>-1</sup> for Sample **40** (bulk), **41** (milled) and **42** (nano) respectively. This event is believed to be related to the loss of structural water from the hydroxide (and partial hydrolysis of MgH<sub>2</sub> for milled and nano materials). In fact, the E<sub>a</sub> value found for bulk materials is in good agreement with the literature for the first dehydration step of LiOH·H<sub>2</sub>O (E<sub>a</sub> = 52 kJ mol<sup>-1</sup>)<sup>30</sup>. The values are higher in case of milled and nano systems. This is likely to be due to the fact that a simultaneous dehydration – hydrolysis process is believed to be taking place, resulting in an overall increased activation energy.

The second event for milled and nanostructured materials presents an activation energy of 120±4 and 142±4 kJ mol<sup>-1</sup> for Sample **41** (milled) and **42** (nano) respectively: this is believed to be related to the dehydration of magnesium hydroxide formed during the first

step of the dehydrogenation process: the calculated values were found to be in good agreement with the one reported by Leardini *et al* (Ea value of Mg(OH)<sub>2</sub> dehydration 123±5 kJ mol<sup>-1</sup>).<sup>31</sup>

The second event for Sample **40** (bulk) relates to the third event for Samples **41** (milled) and **42** (nano) yielding activation energies of 212±6, 176±9 and 152±9 kJ mol<sup>-1</sup> respectively. A trend can be seen, with the values of Ea decreasing from bulk to nanomaterials. This event is believed to relate to the decomposition of MgH<sub>2</sub>. Although the calculated value for Sample **40** (bulk) is high when compared to the activation energy values reported in the literature. The calculated Ea for both Sample **41** (milled) and **42** (nano) materials are in good agreement with the values reported for the decomposition of both bulk and milled magnesium hydride (Ea<sub>bulk MgH<sub>2</sub></sub> = 156 kJ mol<sup>-1</sup>; Ea<sub>milled MgH<sub>2</sub></sub> = 120 kJ mol<sup>-1</sup>).<sup>29</sup> The higher value for bulk materials can be explained if the event is considered as a combination of the solid state reaction between LiOH and MgH<sub>2</sub> with the decomposition of the remaining hydride.

The activation energies for the thermal event taking place at the highest temperature, believed to correspond to the dehydration of the remaining LiOH, were found to be 363±9, 290±8 and 228±8 kJ mol<sup>-1</sup> for Sample **40**, **41** and **42** respectively. For all samples, the calculated Ea appears to be higher than the equivalent values given in the literature (Ea<sub>LiOH</sub> = 123±4 kJ mol<sup>-1</sup>).<sup>28</sup> This may be due to the fact that in the system described in the present work, the reaction of Mg yielded from MgH<sub>2</sub> decomposition is simultaneously reacting with the water released from lithium hydroxide, which thus represents a different, more complex process.

### 5.3.3 Ex-situ PXD and Proposed Mechanisms

*Ex-situ* PXD studies were performed for each studied system in order to propose a mechanism of hydrogen release as well as identify any differences in terms of the mechanistic steps of dehydrogenation when using different starting materials. Based on the STA results discussed in the previous Section, bulk, milled and nanostructured systems were fully studied individually for both the LiOH – MgH<sub>2</sub> and LiOH·H<sub>2</sub>O – MgH<sub>2</sub> systems. In order to try and isolate the intermediate species, TG-DTA-MS analyses were performed and intermediate temperature points in the profile were selected. The post STA products were collected and *ex-situ* PXD analysis carried out for each temperature point.

### 5.3.3.1 LiOH – MgH<sub>2</sub> system

#### 5.3.3.1.1 Bulk system

Figure 3-17 illustrates the DT-TGA profile for Sample 7 and the intermediate temperature points selected. Samples from five different temperatures points were studied (see Table 5-2): 298, 673, 758, 773 and 873 K. The collected X-ray diffraction patterns are presented in Figure 5-25. TG-DTA plots for the intermediate points of reaction are presented in Appendix C.

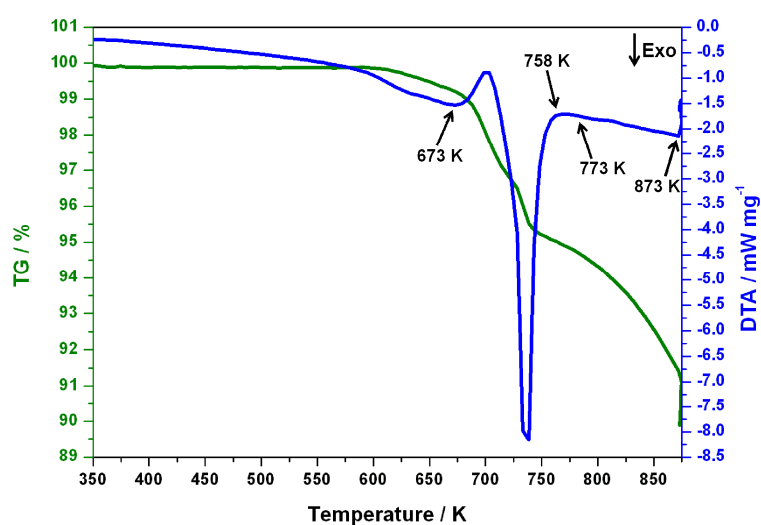


Figure 5-24: TG (green line) and DTA (blue line) data obtained for Sample 7.

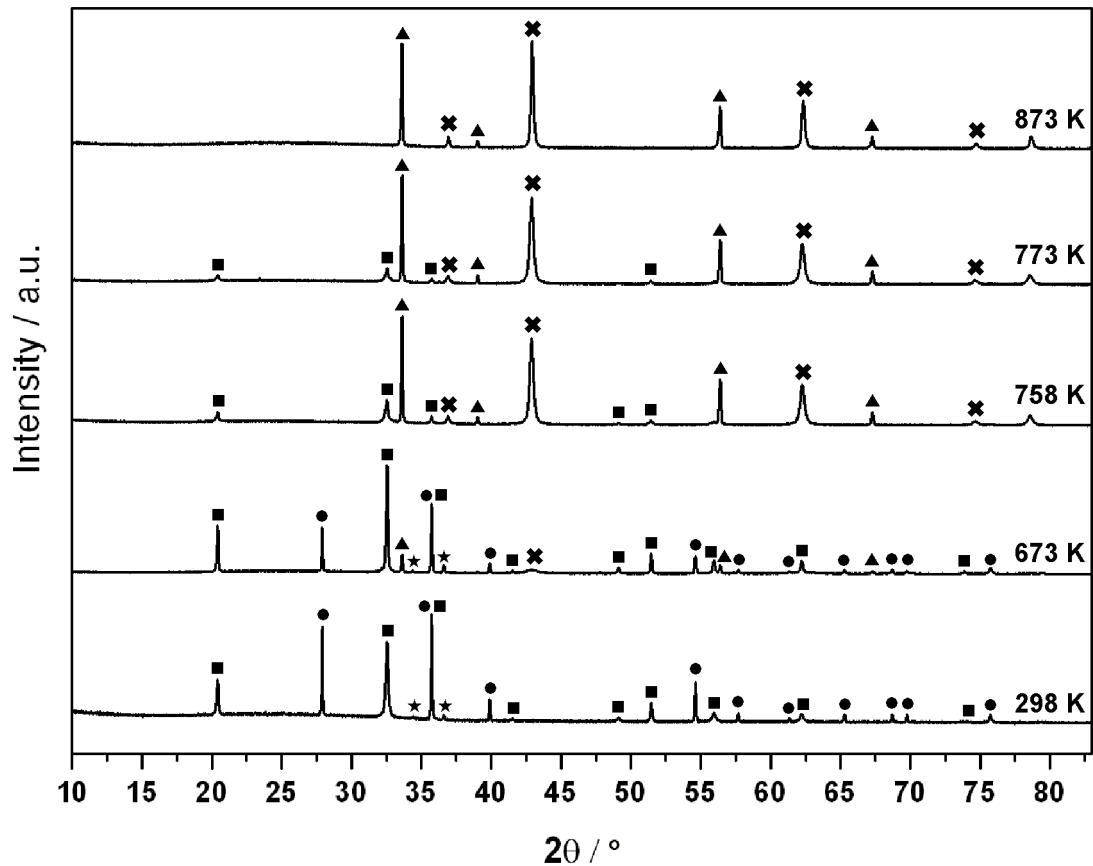


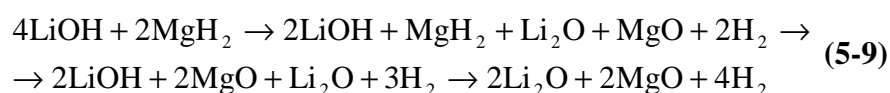
Figure 5-25: *Ex-situ* PXD patterns for Samples 6, 7, 8, 9 and 10 collected at 298, 873, 673, 758 and 773 K respectively. Squares denote LiOH, circles MgH<sub>2</sub>, stars Mg, triangles Li<sub>2</sub>O and crosses MgO respectively.

During manual mixing, no reaction occurs between hydroxide and hydride prior to thermal treatment and MgH<sub>2</sub> and LiOH were found to be the only phases observed in the diffraction pattern together with Mg impurity from the MgH<sub>2</sub> starting material. At 873 K the reaction has gone to completion as the only phases present are Li<sub>2</sub>O and MgO. The PXD pattern collected at 673 K reveals the presence of LiOH, MgH<sub>2</sub> and Mg together with low intensity reflections assignable to Li<sub>2</sub>O and MgO. The 758 K point sees the absence of reflections attributable to magnesium hydride and magnesium metal. The relative intensities of reflections from MgO and Li<sub>2</sub>O increase, while the LiOH peaks are found to decrease in intensity. At 773 K the main phases present are still magnesium oxide and lithium oxide with weak intensity peaks attributable to LiOH. A summary of the phases present at each temperature point is given in Table 5-19.

**Table 5-19: Summary of the temperature points and respective phases present for *ex-situ* PXD analysis for Samples 6, 7, 8, 9 and 10.**

<b>Sample</b>	<b>Temperature / K</b>	<b>Present Phases</b>
<b>6</b>	298	LiOH, MgH <sub>2</sub> , Mg
<b>8</b>	623	LiOH, MgH <sub>2</sub> , Mg, Li <sub>2</sub> O, MgO
<b>9</b>	648	Li <sub>2</sub> O, LiOH, MgO
<b>10</b>	773	Li <sub>2</sub> O, LiOH, MgO
<b>7</b>	873	MgO, Li <sub>2</sub> O

Based on the results shown in Sections 5.3.2.2 and 5.3.3.1.1, the following mechanisms of hydrogen release can be proposed (Equation 5-9):



In the proposed mechanism, the first thermal event is the reaction between LiOH and MgH<sub>2</sub> leading to the formation of magnesium oxide and lithium oxide accompanied by the evolution of hydrogen. This is followed by the decomposition of the remaining magnesium hydride ( $\Delta H = 76.2 \text{ KJ mol}^{-1} \text{ H}_2$ ) to yield magnesium metal and the evolution of H<sub>2</sub>. This step would also involve immediate reaction of Mg with H<sub>2</sub>O to give MgO. The last step of the reaction is believed to be the decomposition of the remaining LiOH to yield Li<sub>2</sub>O ( $\Delta H = 97.4 \text{ KJ mol}^{-1} \text{ H}_2\text{O}$ ).

### **5.3.3.1.2 Milled system**

Based on the results reported for Sample **12**, samples from five temperature points were studied: 298, 623, 648, 773, and 873 K (Table 5-3). Figure 5-26 shows the TG-DTA profile for Sample **12** as well as the intermediate temperature points. TG-DTA plots for the intermediates studied can be found in Appendix C. The collected *ex-situ* PXD patterns are presented in Figure 5-20.

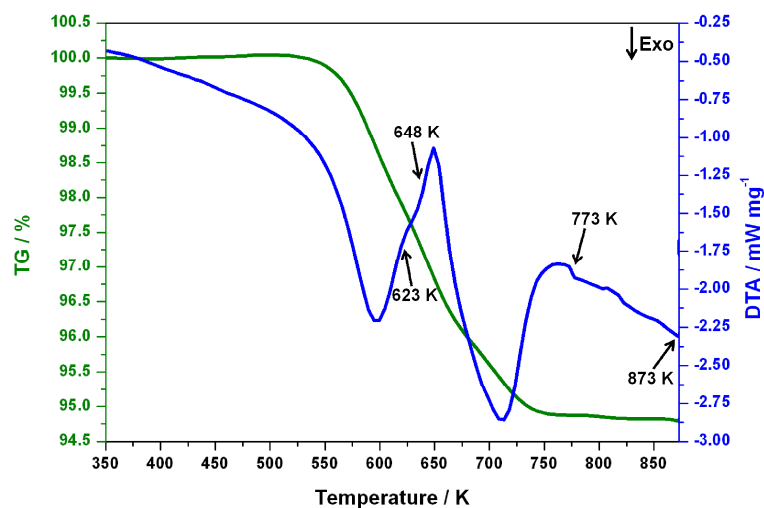


Figure 5-26: TG (green line) and DTA (blue line) data obtained for Sample 12.

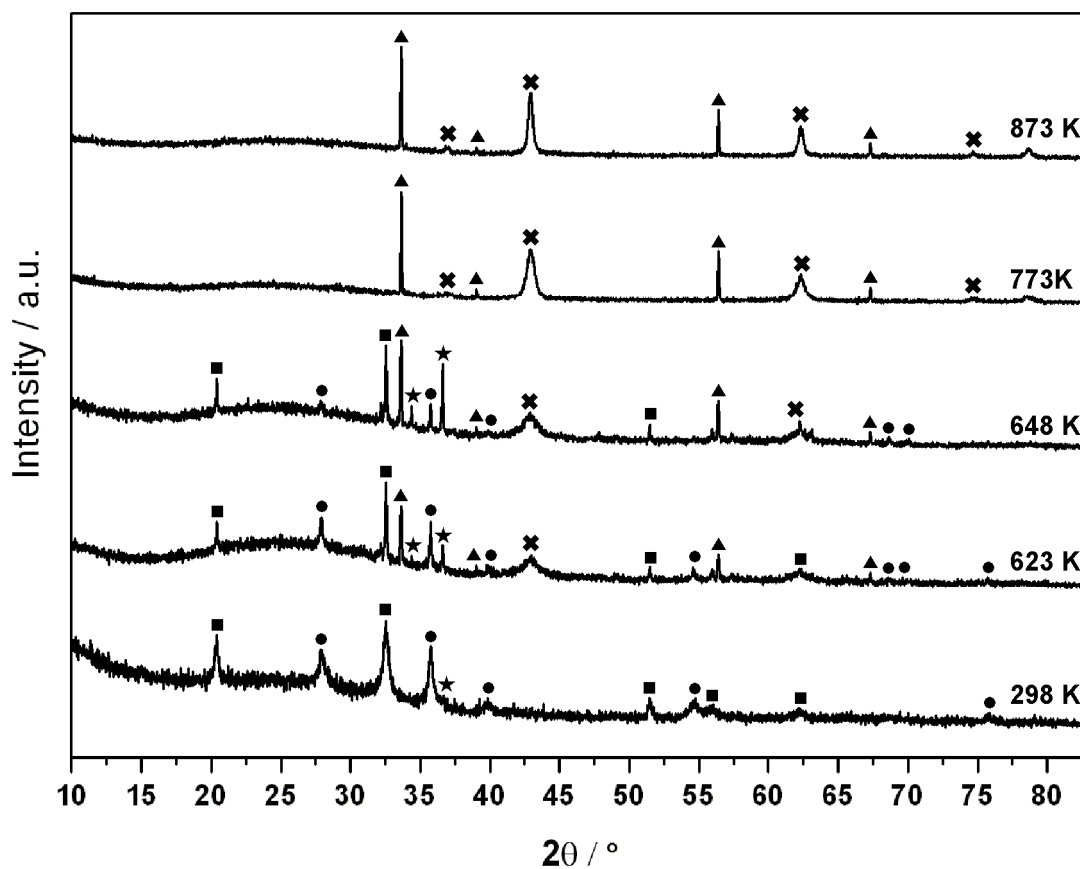


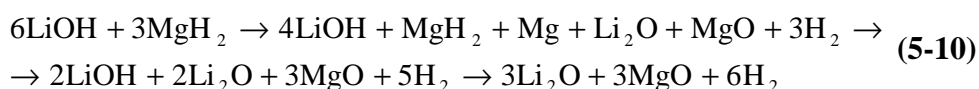
Figure 5-27: *Ex-situ* PXD patterns for Samples 11, 12, 13, 14 and 15 collected at 298, 873, 623, 648 and 773 K respectively. Squares denote LiOH, circles MgH<sub>2</sub>, stars Mg, triangles Li<sub>2</sub>O and crosses MgO respectively.

The PXD pattern collected at 298 K, after hand mixing and prior to thermal treatment, shows that no reaction occurs between hydroxide and hydride as the only reflections present are assignable to LiOH and MgH<sub>2</sub> (with Mg metal being the impurity from the commercial magnesium hydride). Similarly to bulk materials, the reaction has gone to completion at 873 K with the phases present being MgO and Li<sub>2</sub>O. X-ray diffraction patterns collected at 623 and 648 K show the presence of the same species: LiOH and MgH<sub>2</sub> starting materials are present, together with Mg metal, MgO and Li<sub>2</sub>O. As the reaction proceeds, the intensity of LiOH and MgH<sub>2</sub> reflections decreases, whereas the intensity of the reflections attributable to Mg, MgO and Li<sub>2</sub>O increases. Reaching the 773 K temperature point results in the absence of any peak assignable to the starting materials, with the only phases present being MgO and Li<sub>2</sub>O, suggesting that the reaction has gone to completion by that temperature. A summary of the phases identified at each temperature point is given in Table 5-20.

**Table 5-20: Summary of the temperature points and respective phases present for *ex-situ* PXD analysis for Samples 11, 12, 13, 14 and 15.**

Sample	Temperature / K	Present Phases
11	298	LiOH, MgH <sub>2</sub> , Mg
13	623	LiOH, MgH <sub>2</sub> , Mg, Li <sub>2</sub> O, MgO
14	648	LiOH, MgH <sub>2</sub> , Mg, Li <sub>2</sub> O, MgO
15	773	Li <sub>2</sub> O, MgO
12	873	Li <sub>2</sub> O, MgO

For milled materials, the hypothesised mechanism of hydrogen release is presented in Equation 5-10:



The reaction appears to start with the interaction between lithium hydroxide and most magnesium hydride, yielding magnesium oxide and lithium oxide accompanied by the evolution of hydrogen. This is followed by the decomposition of the remaining magnesium hydride ( $\Delta H = 76.2 \text{ KJ mol}^{-1}\text{H}_2$ ) to yield magnesium and the evolution of H<sub>2</sub>, which is believed to take place simultaneously to the decomposition of the remaining LiOH associated with H<sub>2</sub>O evolution ( $\Delta H = 97.4 \text{ KJ mol}^{-1}\text{H}_2\text{O}$ ). The water is believed to react with Mg to give MgO. The reaction appears to be completed at 773 K.

### 5.3.3.1.3 Nanostructured system

TG-DTA-MS analyses were performed and intermediate temperature points collected as reported in Table 5-4. Samples for four temperatures points were studied: 298, 648, 773 and 873 K. *Ex-situ* PXD patterns were collected at each temperature point and the phases present identified (Figure 5-29). The DT-TGA profile for Sample 17 is shown in Figure 5-28, whereas TG-DTA plots for the intermediate temperature points are reported in Appendix C.

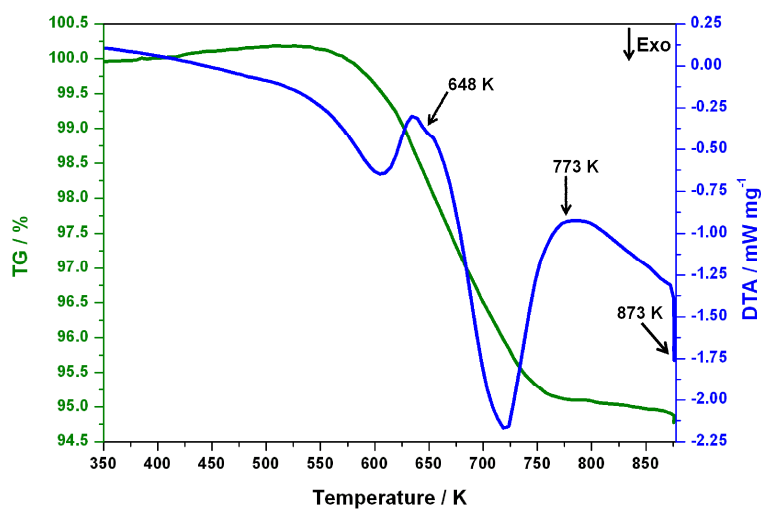


Figure 5-28: TG (green line) and DTA (blue line) data obtained for Sample 17.

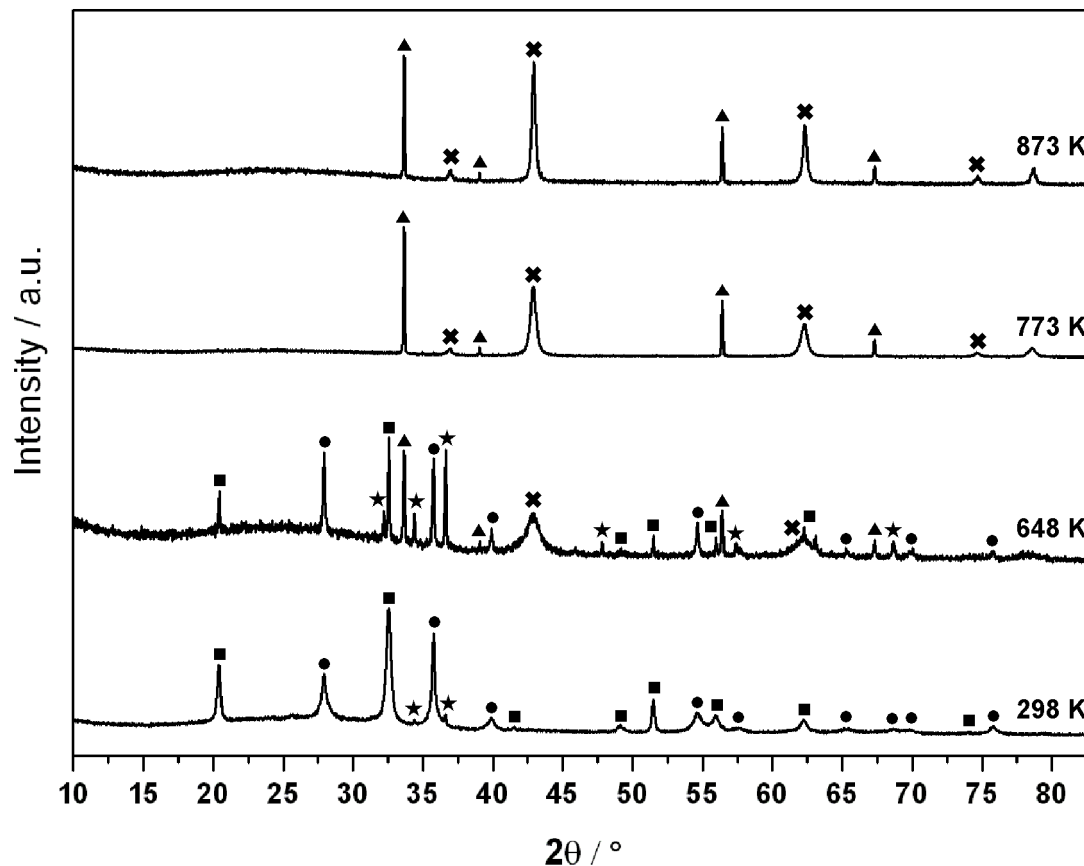


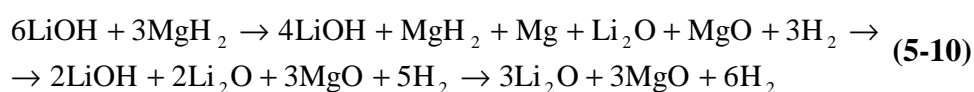
Figure 5-29: *Ex-situ* PXD patterns for Samples 16, 17, 18 and 19 collected at 298, 873, 648 and 773 K respectively. Squares denote LiOH, circles MgH<sub>2</sub>, stars Mg, triangles Li<sub>2</sub>O and crosses MgO respectively.

Similarly to the bulk and milled systems, no reaction occurs during the manual mixing and the PXD pattern collected at 298 K prior to thermal treatment confirms that the only phases present in the mixture are LiOH and MgH<sub>2</sub> together with Mg present as impurity from the as-received hydride. Again, the pattern collected after heating to 873 K shows that the only phases present are magnesium oxide and lithium oxide, confirming that the reaction has gone to completion. At 648 K it is possible to observe the presence of new reflections assignable to MgO and Li<sub>2</sub>O, together with the presence of peaks attributable to LiOH, MgH<sub>2</sub> and Mg metal. It is interesting to note that the intensity of the peaks assignable to magnesium metal has considerably increased in intensity with respect to the other phases present, suggesting that it is possible that the hydride has almost completely decomposed by that temperature. At 773 K the reflections relative to any of the starting materials are completely absent, while MgO and Li<sub>2</sub>O reflections are present, suggesting as for the milled materials that the reaction is completed at 773 K. A summary of the phases present at each intermediate temperature point is presented in Table 5-21.

**Table 5-21: Summary of the temperature points and respective phases present for *ex-situ* PXD analysis for Samples 16, 17, 18 and 19.**

<b>Sample</b>	<b>Temperature / K</b>	<b>Present Phases</b>
<b>16</b>	298	LiOH, MgH <sub>2</sub> , Mg
<b>18</b>	648	LiOH, MgH <sub>2</sub> , Mg, Li <sub>2</sub> O, MgO
<b>19</b>	773	Li <sub>2</sub> O, MgO
<b>17</b>	873	Li <sub>2</sub> O, MgO

Nanostructured materials are believed to follow an almost identical pathway to the milled materials (Equation 5-10), with the first dehydrogenation step being the solid state reaction between LiOH and MgH<sub>2</sub> to yield MgO, Li<sub>2</sub>O and H<sub>2</sub>. This is once again believed to be followed by the decomposition of the remaining hydride ( $\Delta H = 76.2 \text{ KJ mol}^{-1} \text{ H}_2$ ) to evolve hydrogen and form Mg, being simultaneous to the dehydration of the remaining hydroxide ( $\Delta H = 97.4 \text{ KJ mol}^{-1} \text{ H}_2\text{O}$ ). The water evolved from LiOH will immediately react with Mg, ultimately leading to the formation of Li<sub>2</sub>O and MgO final products. Similarly to milled materials, the reaction is completed at 773 K.



SEM images were collected after thermal treatment in order to ascertain whether the sheet-like morphology of LiOH was retained. As can be seen in Figure 5-30, the sample is composed of particles with a typical size distribution of 100-300 nm and it is not possible to still identify any specific morphology. This may be due to the fact that the temperature employed during the thermal treatment is above the melting point of LiOH, resulting in a post STA product composed of agglomerated clusters of MgO mixed with melted Li<sub>2</sub>O particles.

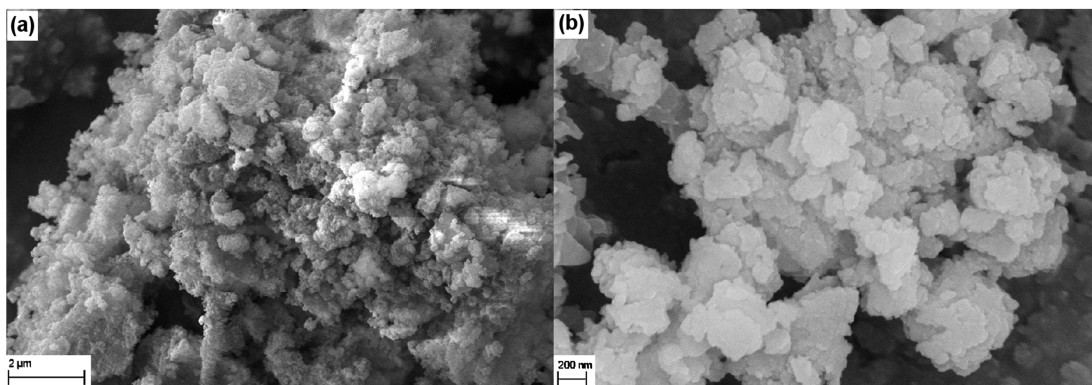


Figure 5-30: Collected SEM images for Sample 17: a) 2  $\mu\text{m}$  scale b) 200 nm scale.

### 5.3.3.2 $\text{LiOH}\cdot\text{H}_2\text{O} - \text{MgH}_2$ system

#### 5.3.3.2.1 Bulk system

Based on the results reported for Sample **24**, sample for six temperatures points were studied: 298, 408, 673, 758, 773, and 873 K (Table 5-6). Figure 5-31 illustrates the TG-DTA profile for Sample **24** and the collected intermediate temperature points. TG-DTA plots for the intermediate temperature points are presented in Appendix C. The collected *ex-situ* PXD patterns are presented in Figure 5-32.

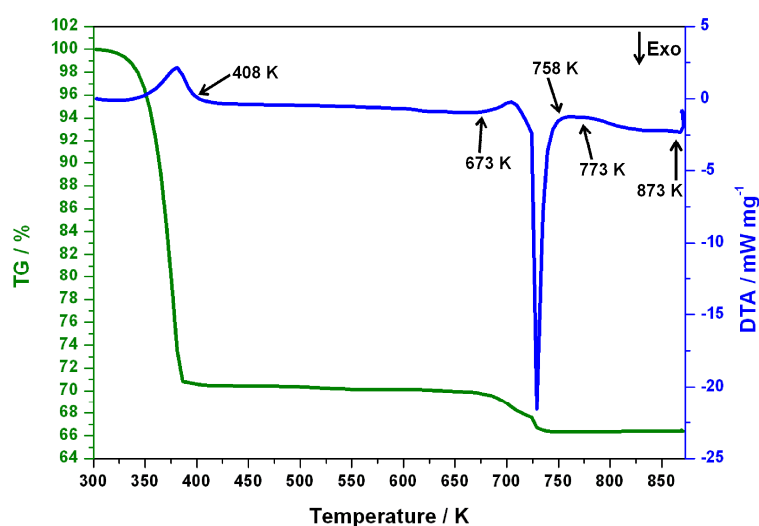


Figure 5-31: TG (green line) and DTA (blue line) data obtained for Sample **24**.

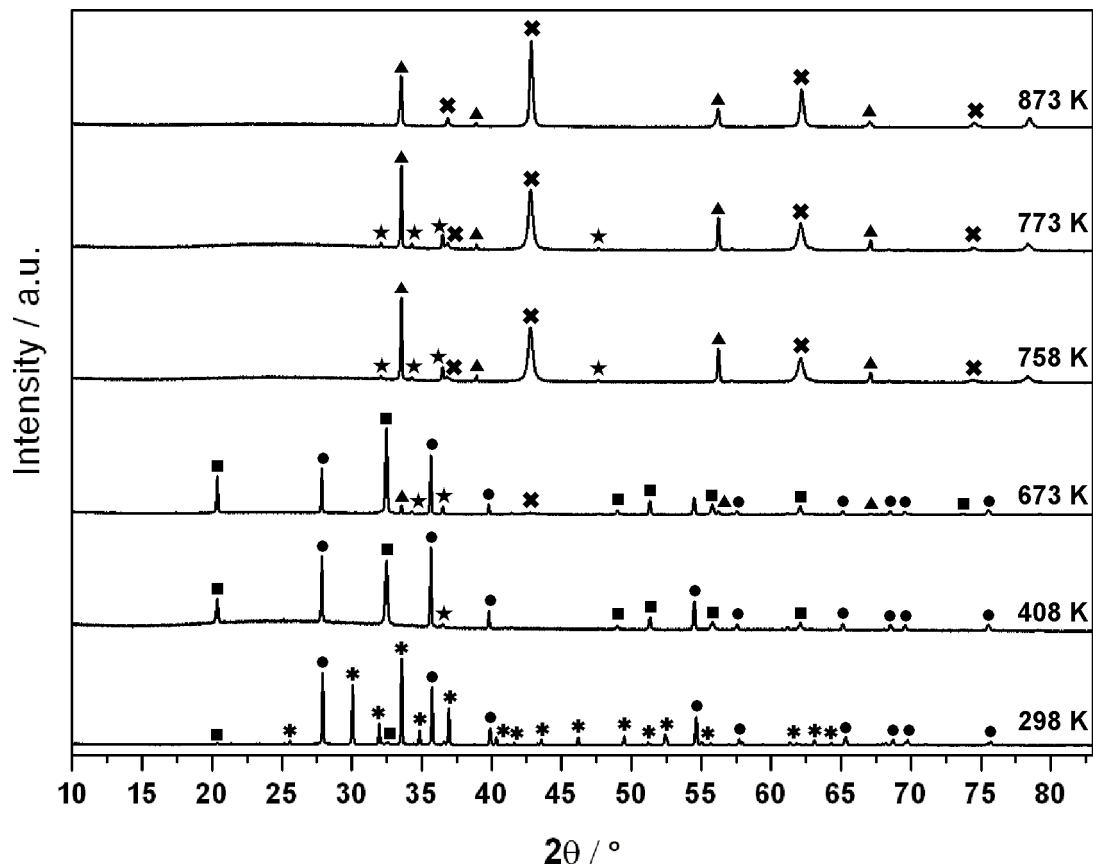


Figure 5-32: *Ex-situ* PXD patterns for Samples 23, 24, 25, 26, 27 and 28 collected at 298, 873, 408, 673, 758 and 773 K respectively. Asterisks denote  $\text{LiOH}\cdot\text{H}_2\text{O}$ , squares  $\text{LiOH}$ , circles  $\text{MgH}_2$ , stars  $\text{Mg}$ , triangles  $\text{Li}_2\text{O}$  and crosses  $\text{MgO}$  respectively.

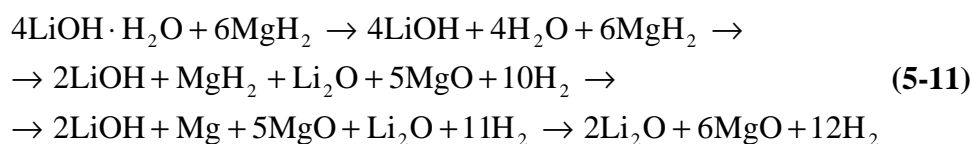
During manual mixing, no major reaction occurs between hydroxide and hydride prior to thermal treatment and  $\text{MgH}_2$  and  $\text{LiOH}\cdot\text{H}_2\text{O}$  were found to be the main phases present in the PXD pattern. Nonetheless, it is possible to identify peaks assignable to  $\text{LiOH}$ , although their intensity is very weak. At 873 K the reaction has gone to completion as the only phases present were found to be magnesium oxide and lithium oxide. The 408 K point sees the presence of only  $\text{LiOH}$  and  $\text{MgH}_2$  together with  $\text{Mg}$  metal as impurity from the as-received hydride. At 673 K the presence of new reflections assignable to  $\text{MgO}$  and  $\text{Li}_2\text{O}$  can be observed, together with  $\text{LiOH}$ ,  $\text{MgH}_2$  and  $\text{Mg}$  metal. The 758 K point sees the absence of peaks assignable to lithium hydroxide and magnesium hydride and the only phases present were found to be lithium oxide, magnesium oxide and magnesium metal. These phases remain at 773 K.

A summary of the phases present at each temperature point is given in Table 5-22.

**Table 5-22: Summary of the temperature points and respective phases present for *ex-situ* PXD analysis for Samples 23, 24, 25, 26, 27 and 28.**

<b>Sample</b>	<b>Temperature / K</b>	<b>Present Phases</b>
<b>23</b>	298	LiOH·H <sub>2</sub> O, LiOH, MgH <sub>2</sub> , Mg
<b>25</b>	408	LiOH, MgH <sub>2</sub> , Mg
<b>26</b>	673	LiOH, MgH <sub>2</sub> , Mg, Li <sub>2</sub> O, MgO
<b>27</b>	758	Li <sub>2</sub> O, Mg, MgO
<b>28</b>	773	Li <sub>2</sub> O, Mg, MgO
<b>24</b>	873	MgO, Li <sub>2</sub> O

Based on the results shown in Sections 5.3.2.3 and 5.3.3.2.1, the following mechanisms of hydrogen release can be proposed (Equation 5-11):



In the proposed mechanism, the first thermal event is the loss of structural water leading to LiOH and MgH<sub>2</sub> with release of water ( $\Delta H = 53.1 \text{ KJ mol}^{-1}\text{H}_2\text{O}$ ). The system then undergoes the same dehydrogenation process as the bulk anhydrous lithium hydroxide – magnesium hydride system. The first step is followed by the solid state reaction between LiOH and MgH<sub>2</sub> leading to the formation of MgO and Li<sub>2</sub>O and release H<sub>2</sub>. This is followed by the decomposition of the remaining magnesium hydride ( $\Delta H = 76.2 \text{ KJ mol}^{-1}\text{H}_2$ ) to yield magnesium and the evolution of H<sub>2</sub>, with the last step of the reaction being the decomposition of the remaining LiOH to give Li<sub>2</sub>O and water ( $\Delta H = 97.4 \text{ KJ mol}^{-1}\text{H}_2\text{O}$ ). The H<sub>2</sub>O released from the last step of the reaction reacts with the Mg present, leading to the formation of MgO and evolution of the last mole of H<sub>2</sub>.

### 5.3.3.2.2 Milled system

Simultaneous thermogravimetric analyses were performed and samples at intermediate temperature points collected as reported in Table 5-7. The TG-DTA profile for Sample **30** is shown in Figure 5-28, whilst TG-DTA plots for the intermediates are reported in Appendix C. Six temperatures points were studied: 298, 408, 573, 673, 773 and 873 K. *Ex-*

*situ* PXD patterns were collected at each temperature point in order to identify all the phases present (Figure 5-29).

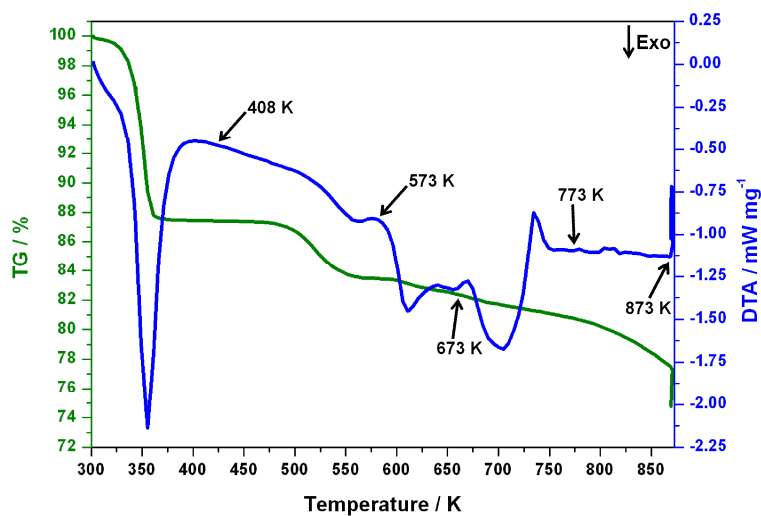


Figure 5-33: TG (green line) and DTA (blue line) data obtained for Sample 30.

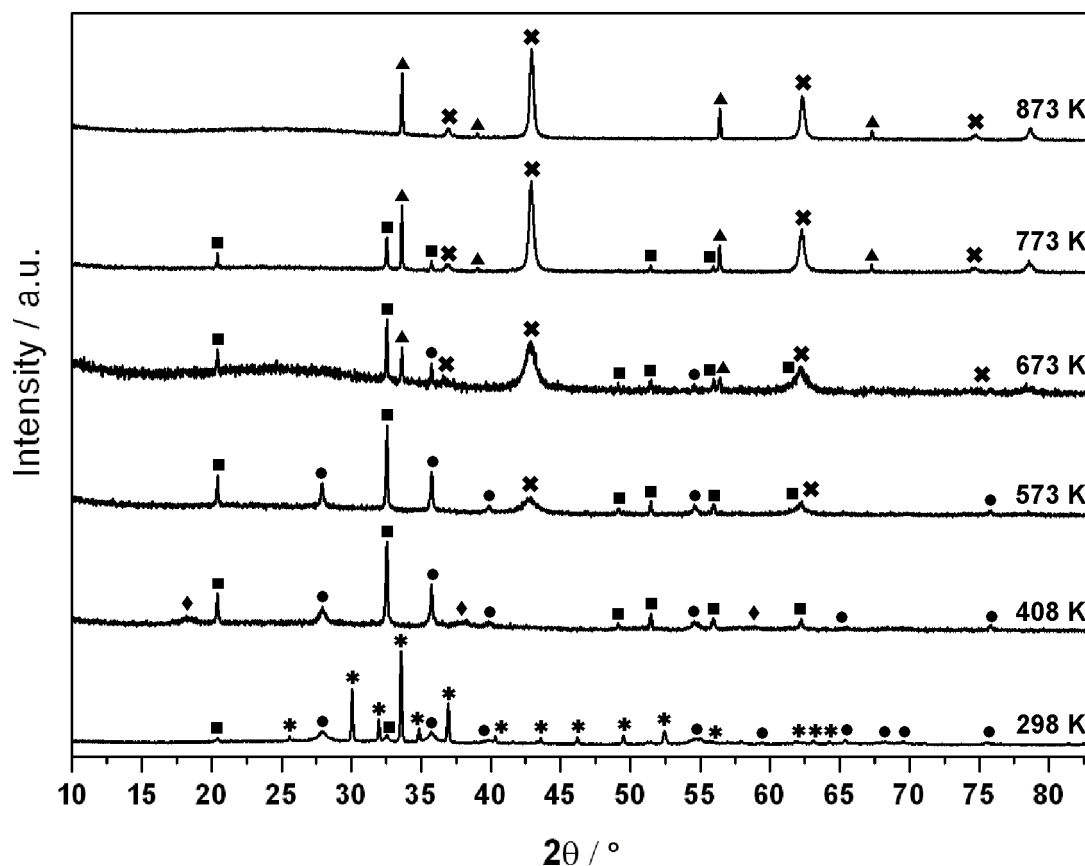


Figure 5-34: *Ex-situ* PXD patterns for Samples 29, 30, 31, 32, 33 and 34 collected at 298, 873, 408, 573, 673 and 773 K respectively. Asterisks denote  $\text{LiOH}\cdot\text{H}_2\text{O}$ , squares  $\text{LiOH}$ , circles  $\text{MgH}_2$ , rhombuses  $\text{Mg}(\text{OH})_2$ , triangles  $\text{Li}_2\text{O}$  and crosses  $\text{MgO}$  respectively.

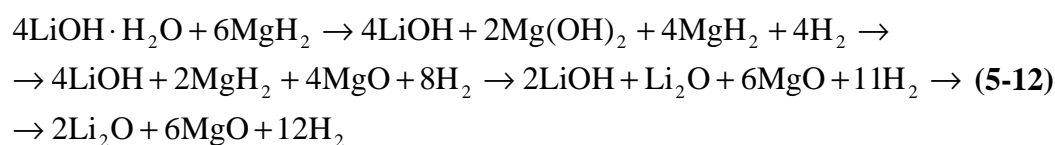
The PXD pattern collected at 298 K, after mixing and prior to thermal treatment, shows that no major reaction occurs between hydroxide and hydride as only reflections present are assignable to LiOH·H<sub>2</sub>O and MgH<sub>2</sub>, however very weak peaks assignable to LiOH can be identified. At 873 K the reaction has gone to completion as the only phases present were found to be magnesium oxide and lithium oxide. At the 408 K point, the phases present were found to be LiOH, MgH<sub>2</sub> and Mg(OH)<sub>2</sub>. At 573 K new reflections assignable to MgO and Li<sub>2</sub>O are observed, together with LiOH and MgH<sub>2</sub>. Moreover, at this temperature it is not possible to observe reflections assignable to magnesium hydroxide. The 673 K point sees the absence of peaks assignable to magnesium hydride with the only phases present being lithium hydroxide, lithium oxide and magnesium oxide. The same composition can be observed at 773 K, where Li<sub>2</sub>O and MgO are present together with LiOH as minor phase.

The phases present at each temperature point are summarised in Table 5-23.

**Table 5-23: Summary of the temperature points and respective phases present for *ex-situ* PXD analysis for Samples 29, 30, 31, 32, 33 and 34.**

Sample	Temperature / K	Present Phases
29	298	LiOH·H <sub>2</sub> O, LiOH, MgH <sub>2</sub>
31	408	LiOH, MgH <sub>2</sub> , Mg(OH) <sub>2</sub>
32	573	LiOH, MgH <sub>2</sub> , Li <sub>2</sub> O, MgO
33	673	LiOH, Li <sub>2</sub> O, MgO
34	773	Li <sub>2</sub> O, MgO, LiOH
30	873	Li <sub>2</sub> O, MgO

Milled materials seem to be subjected to a different dehydrogenation process with respect to the bulk materials. The hypothesised mechanism of hydrogen release is presented in Equation 5-12:



The reaction appears to start with the simultaneous loss of structural water from  $\text{LiOH}\cdot\text{H}_2\text{O}$  ( $\Delta H = 53.1 \text{ KJ mol}^{-1}\text{H}_2\text{O}$ ) and  $\text{MgH}_2$  hydrolysis ( $\Delta H = -138.5 \text{ KJ mol}^{-1}\text{H}_2\text{O}$ ) to yield  $\text{Mg}(\text{OH})_2$ ,  $\text{LiOH}$  and evolve  $\text{H}_2$ . This is then followed by the dehydration of the newly formed magnesium hydroxide ( $\Delta H = 84.2 \text{ KJ mol}^{-1}\text{H}_2\text{O}$ ), whose released water is believed to hydrolyse another mole of  $\text{MgH}_2$ . The next step is believed to be the decomposition of the remaining magnesium hydride ( $\Delta H = 76.2 \text{ KJ mol}^{-1}\text{H}_2$ ) to yield  $\text{Mg}$  and  $\text{H}_2$ . This is immediately followed by the dehydration of the remaining  $\text{LiOH}$  associated with evolution of  $\text{H}_2\text{O}$  ( $\Delta H = 97.4 \text{ KJ mol}^{-1}\text{H}_2\text{O}$ ), which is believed to react with  $\text{Mg}$  to give  $\text{MgO}$  and  $\text{H}_2$ .

### 5.3.3.2.3 Nanostructured system

Figure 5-35 illustrates the DT-TGA profile for Sample **36** and the intermediate temperature points collected. Samples from five different temperatures points were studied (Table 5-8): 298, 408, 623, 773 and 873 K. The collected PXD patterns are presented in Figure 5-25. TG-DTA plots of the intermediate temperature point are presented in Appendix C.

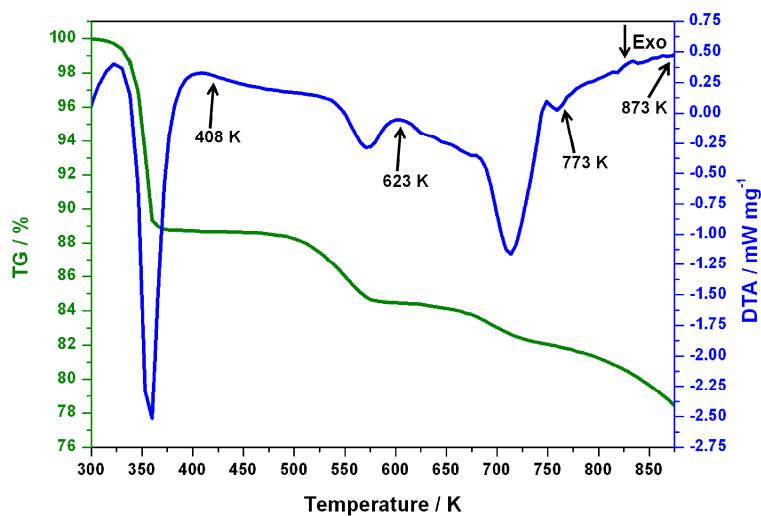


Figure 5-35: TG (green line) and DTA (blue line) data obtained for Sample **36**.

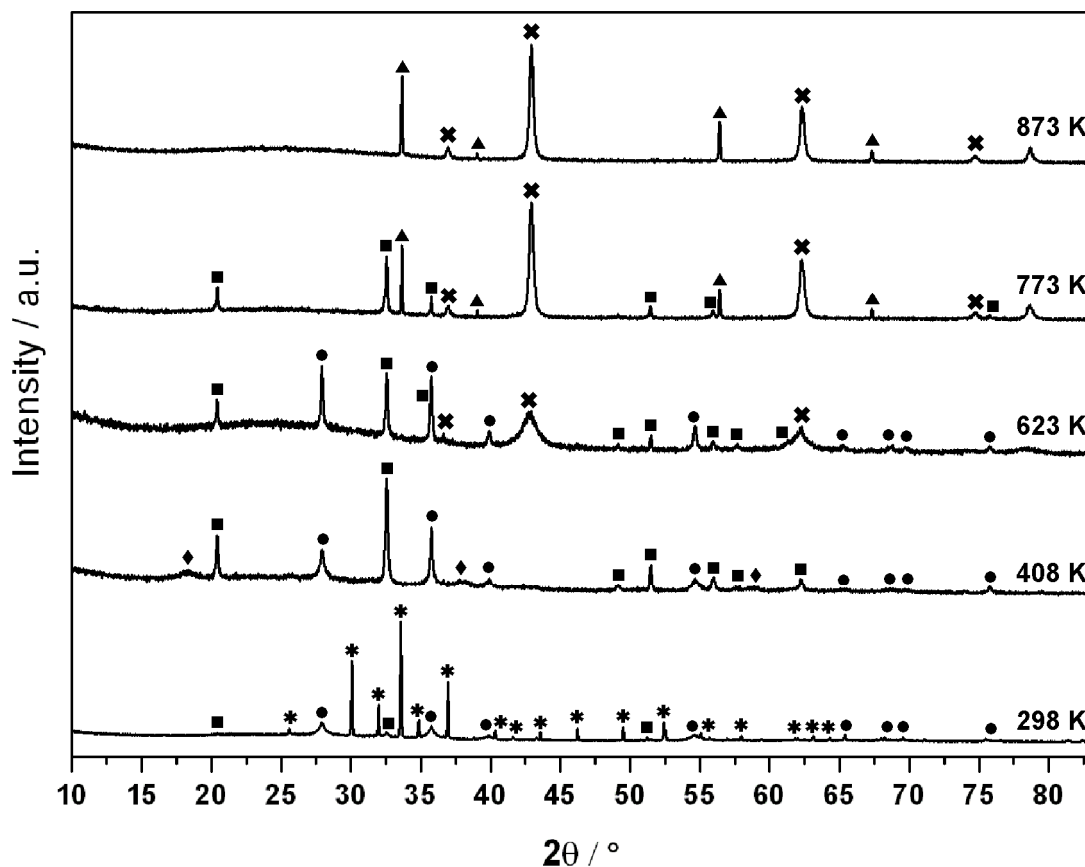


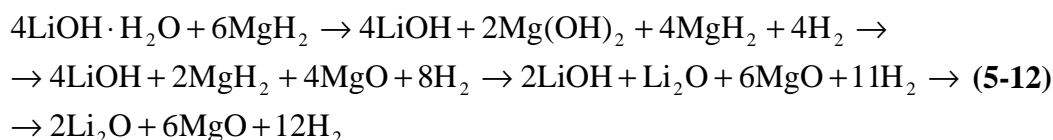
Figure 5-36: *Ex-situ* PXD patterns for Samples 35, 36, 37, 38 and 39 collected at 298, 873, 408, 623 and 773 K respectively. Asterisks denote  $\text{LiOH}\cdot\text{H}_2\text{O}$ , squares  $\text{LiOH}$ , circles  $\text{MgH}_2$ , rhombuses  $\text{Mg(OH)}_2$ , triangles  $\text{Li}_2\text{O}$  and crosses  $\text{MgO}$  respectively.

As previously observed for bulk and milled systems, no major reaction occurs between the starting material during the mixing and before the thermal treatment: the main phases were still found to be  $\text{LiOH}\cdot\text{H}_2\text{O}$  and  $\text{MgH}_2$ , although once again weak reflections attributable to  $\text{LiOH}$  can be identified. At 873 K the only phases present were found to be lithium oxide and magnesium oxide, indicating that the reaction has gone to completion. Similarly to the milled systems at 408 K the phases present were found to be  $\text{LiOH}$ ,  $\text{MgH}_2$  and  $\text{Mg(OH)}_2$ . At 623 K it is possible to observe reflections attributable to  $\text{MgO}$  and  $\text{Li}_2\text{O}$ , together with  $\text{LiOH}$  and  $\text{MgH}_2$ .  $\text{Mg(OH)}_2$  reflections are completely absent at this temperature. At 773 K it is possible to observe the presence of reflections relative to  $\text{LiOH}$ ,  $\text{Li}_2\text{O}$  and  $\text{MgO}$  and the absence of  $\text{MgH}_2$  peaks.

**Table 5-24: Summary of the temperature points and respective phases present for *ex-situ* PXD analysis for Samples 35, 36, 37, 38 and 39.**

Sample	Temperature / K	Present Phases
35	298	LiOH·H <sub>2</sub> O, LiOH, MgH <sub>2</sub>
37	408	LiOH, MgH <sub>2</sub> , Mg(OH) <sub>2</sub>
38	623	LiOH, MgH <sub>2</sub> , Li <sub>2</sub> O, MgO
39	773	LiOH, Li <sub>2</sub> O, MgO
36	873	Li <sub>2</sub> O, MgO

Nanostructured materials are believed to follow an almost identical reaction pathway as milled materials (Equation 5-12). Initially simultaneous loss of structural water from LiOH·H<sub>2</sub>O ( $\Delta H = 53.1 \text{ KJ mol}^{-1}\text{H}_2\text{O}$ ) and hydrolysis of 1 mole of MgH<sub>2</sub> ( $\Delta H = -138.5 \text{ KJ mol}^{-1}\text{H}_2\text{O}$ ) occurs to yield Mg(OH)<sub>2</sub>, LiOH and evolve H<sub>2</sub>. The next mechanistic step is once again believed to be the decomposition of Mg(OH)<sub>2</sub> ( $\Delta H = 76.2 \text{ KJ mol}^{-1}\text{H}_2$ ), with the water evolved from this step believed to hydrolyse a second mole of MgH<sub>2</sub> resulting in the formation of MgO and H<sub>2</sub>. This is then followed by the decomposition of the last mole of magnesium hydride ( $\Delta H = 76.2 \text{ KJ mol}^{-1}\text{H}_2$ ) and dehydration of LiOH ( $\Delta H = 97.4 \text{ KJ mol}^{-1}\text{H}_2\text{O}$ ), which ultimately leads to the formation of the final products Li<sub>2</sub>O and MgO together with H<sub>2</sub> evolution (Equation 5-12).



Again for Sample **36**, SEM images have been collected after TG-DTA-MS analysis to determine if the morphology of LiOH·H<sub>2</sub>O was retained. Figure 5-30 illustrates that it is not possible to identify any specific morphology. Further, it is possible to observe particles with a typical size distribution of 100-500 nm in diameter. Similar to the LiOH – MgH<sub>2</sub> nanostructured system, this is believed to be a result of the high temperature employed during the thermal treatment of the system. The melting point of lithium hydroxide is exceeded which is believed to result in a partial melting of the post-STA product. This is thus proposed to be composed of agglomerated clusters of MgO particles and partially melted Li<sub>2</sub>O particles.

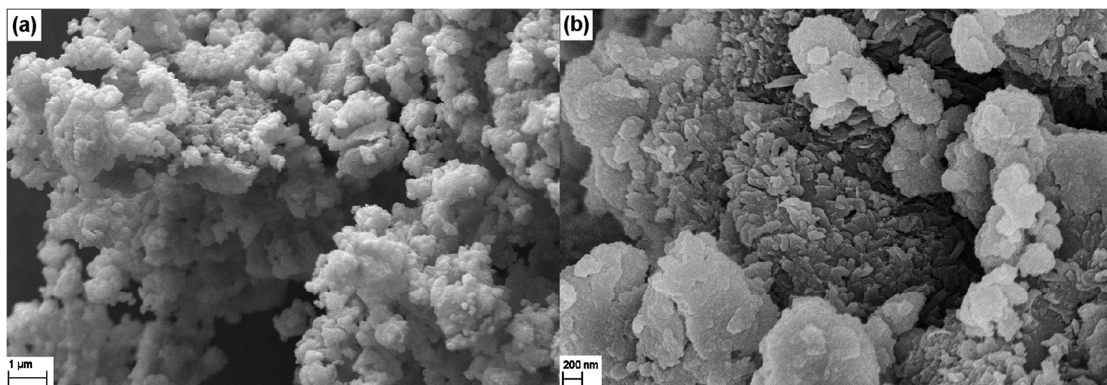


**Figure 5-37: Collected SEM images for Sample 36: a) 1  $\mu\text{m}$  scale b) 200 nm scale.**

## 5.4 Conclusions and Future Work

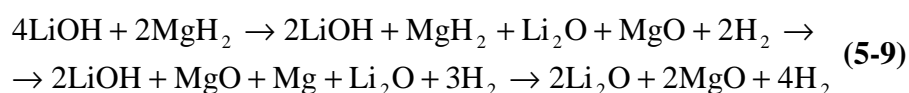
A selective synthesis for yielding nanostructured anhydrous and monohydrate LiOH was successfully identified. Pure LiOH( $\cdot\text{H}_2\text{O}$ ) was synthesised and fully characterised. Rietveld refinements were performed on the synthesised hydroxides and lattice parameters were calculated. These were found to be in good agreement with the literature values for both LiOH and LiOH $\cdot\text{H}_2\text{O}$  respectively.<sup>24,25,26</sup> Collected SEM images show that the nanostructuring process results in a dramatic decrease of the particle size with respect to the commercial hydroxides. In particular, the synthesis of LiOH results in the production of hydroxide with a non-uniform morphology and size distribution with the particle size varying in the 40-80  $\mu\text{m}$  range. Further, SEM images collected at higher magnification show a sheet-like morphology present at the surface of the synthesised particles, with a typical sheet thickness varying in the 30-50 nm range. The synthesis of LiOH $\cdot\text{H}_2\text{O}$  results in particles with a diameter varying in the 20-100  $\mu\text{m}$  range, again with a non-uniform size distribution. Images were collected at higher magnification in order to determine the presence of any sheet-like morphology. Smaller particles in the 1-6  $\mu\text{m}$  range can be identified, however it was not possible to observe the presence of sheets. Nonetheless the surface of the particles appeared textured and porous.

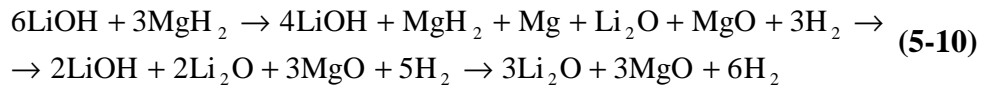
Physical reduction of the particle size of as-received anhydrous and hydrated lithium hydroxides and magnesium hydride has been successfully achieved by mechanically milling the commercial reactants. For both anhydrous and hydrated LiOH, the typical size distribution of particles was found to be a range between 2-8  $\mu\text{m}$  in diameter. The milling process for MgH<sub>2</sub> resulted in a decreased particle size distribution with respect to the bulk material, with a typical particle size in the 70-200 nm range.

The LiOH( $\cdot$ H<sub>2</sub>O) – MgH<sub>2</sub> systems were studied in detail comparing bulk, milled and nanostructured materials. All samples were prepared by manually mixing stoichiometric amounts of the starting material for 5 minutes inside a recirculating Ar- or N<sub>2</sub>-filled glove box under an inert atmosphere.

Results obtained for the LiOH – MgH<sub>2</sub> system, show a dramatic decrease in the onset temperature of H<sub>2</sub> release of nearly 100 K when working with milled and nanostructured materials with respect to bulk reagents (an onset T of 509 K and 512 K for milled and nano systems respectively, whereas it was found to be 598 K for bulk materials). TG-DTA profiles of all samples show the presence of 2 main endothermic events occurring immediately one after the other, although a closer look at the data suggests the second event to be a combination of two processes occurring close in temperature. It is believed that the first event is a solid state reaction between LiOH and MgH<sub>2</sub>, followed by the decomposition of the remaining hydride, with the last mechanistic step being the dehydration of the remaining LiOH. The LiOH – MgH<sub>2</sub> system can theoretically release up to 5.9 wt. % H<sub>2</sub>. However, after thermal treatment to 873 K the weight losses were found to be 10.1 % for bulk materials and 5.2 wt. % for both milled and nano systems. The higher mass loss observed for bulk materials may be due to the release of gaseous water from LiOH, which has not reacted with MgH<sub>2</sub> during the thermal treatment. For milled and nano systems no mass loss is recorded during the holding time of 1 h at the 873 K temperature point during TG-DTA-MS analyses, suggesting that the reaction has gone to completion when reaching the final target temperature. The last step of the reaction is believed to be the simultaneous final LiOH dehydration and reaction of the Mg metal formed from the decomposition of MgH<sub>2</sub>. Activation energies were calculated for the two main thermal events for each system: these were found to be 166 $\pm$ 6, 137 $\pm$ 9 and 118 $\pm$ 9 kJ mol<sup>-1</sup> for the low temperature event for bulk, milled and nano system respectively. The activation energies for the second HT event were found to be 442 $\pm$ 9, 232 $\pm$ 8 and 181 $\pm$ 8 kJ mol<sup>-1</sup> for bulk, milled and nano materials respectively.

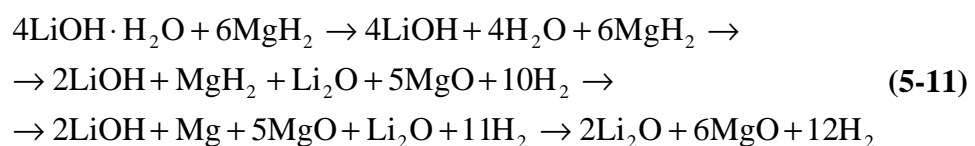
Ex-situ PXD analyses were performed to elucidate the mechanism of hydrogen release for each system. It was possible to propose two different dehydrogenation pathways: one for the bulk materials and one for both the milled and nanostructured systems. The two reaction mechanisms are presented in Equation 5-9 and 5-10 respectively.

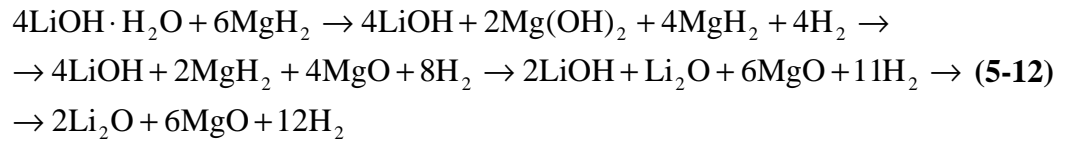




Results obtained for the LiOH·H<sub>2</sub>O – MgH<sub>2</sub> system show important differences in the TG-DTA profiles and mass spectra when reducing the particle size from the bulk to the nanometric scale. In particular, when working with bulk materials only endothermic peaks can be observed and the system releases both water and hydrogen. The first event was found to relate to the loss of structural water from LiOH·H<sub>2</sub>O, after which the system was found to behave as the bulk LiOH – MgH<sub>2</sub> system. Using milled or nanostructured materials results in an initial exothermic process followed by three endothermic events. Data suggest the first event to be the simultaneous dehydration of LiOH·H<sub>2</sub>O to yield LiOH and hydrolysis of MgH<sub>2</sub> to give Mg(OH)<sub>2</sub>. This is associated with hydrogen release and evolution of a small amount of water. The onset temperature of H<sub>2</sub> is drastically lowered to 323 and 313 K for milled and nano systems respectively, whereas the first major H<sub>2</sub> release for bulk system was found to start at 669 K. Further, the weight changes for all systems were found to be higher than the theoretical 7.4 wt. % H<sub>2</sub> figure: in particular the bulk, milled and nano systems were found to lose 33.6, 25.2 and 22.8 wt. % with most of the weight being lost during the first dehydration step of LiOH·H<sub>2</sub>O, suggesting that both H<sub>2</sub>O and H<sub>2</sub> are evolved from all systems. Although the onset temperature of hydrogen release is dramatically lowered to nearly ambient temperature when working with milled and nanosized reactants, the thermal treatment of such materials always results in the evolution of H<sub>2</sub>O together with H<sub>2</sub>. This could make the employment of lithium hydroxide monohydrate – magnesium hydride system difficult to in operational fuel cells. Activation energies were calculated for all the thermal events for each system. For bulk materials these were found to be 56±2, 212±7 and 363±9 kJ mol<sup>-1</sup>. Milled and nano systems present four thermal events each. The values of E<sub>a</sub> were calculated to be 100±8, 120±4, 176±9 and 290±8 kJ mol<sup>-1</sup> for the milled system and 102±7, 142±4, 152±9 and 228±9 kJ mol<sup>-1</sup> for the nano system.

It was possible to propose two different dehydrogenation reaction pathways; one for the bulk materials and one for the milled and nanostructured systems. The mechanisms are reported in Equations 5-11 and 5-12 for bulk and milled/nanostructured materials respectively.





Overall, the most promising systems have been identified in the LiOH – MgH<sub>2</sub> system employing nanosized materials. Hence, efforts should be focused on further enhancing the performances of such systems. First, elucidating the exact reaction mechanism of hydrogen release is pivotal in order to understand and improve the system. In this sense, *In-situ* PXD and PND experiments should also be performed in order to confirm the proposed mechanism of hydrogen release for both bulk and milled materials. The use of catalysts and additives should be fully investigated. Finding a suitable candidate for favouring the solid-state reaction between LiOH and MgH<sub>2</sub> could result in a single event of hydrogen release at temperature suitable for fuel cells operating at low or intermediate temperatures. Moreover, completing the reaction in a single step would result in the release of hydrogen as the only gaseous species evolved, suppressing the release of water as by-product of the LiOH dehydration reaction. A wide range of additives and catalysts have been tested in order to enhance the dehydrogenation properties of magnesium hydride by itself, although no-one of them has been tested in the presence of both MgH<sub>2</sub> and LiOH. These include calcium, lithium and sodium hydrides to yield ternary hydrides and composites<sup>29,32</sup>, graphite and/or silicon carbide<sup>17</sup> as well as transition metals and multi-valence vanadium- and titanium-based materials.<sup>33,34,35,36</sup> They all could be seen as suitable candidates to be tested on the LiOH – MgH<sub>2</sub> system.

Studies for the further development of the system are needed.

## 5.5 References

1. Vajo, J. J.; Skeith, S. L.; Mertens, F.; Jorgensen, S. W., Hydrogen-generating solid-state hydride/hydroxide reactions. *Journal of Alloys and Compounds* **2005**, 390 (1-2), 55-61.
2. Lu, J.; Fang, Z. Z.; Sohn, H. Y., A hybrid method for hydrogen storage and generation from water. *Journal of Power Sources* **2007**, 172 (2), 853-858.
3. Wang, H.; Zhang, J.; Liu, J. W.; Ouyang, L. Z.; Zhu, M., Improving hydrogen storage properties of MgH<sub>2</sub> by addition of alkali hydroxides. *International Journal of Hydrogen Energy* **2013**, 38 (25), 10932-10938.

4. Cai, W.; Wang, H.; Sun, D.; Zhang, Q.; Yao, X.; Zhu, M., Destabilization of  $\text{LiBH}_4$  dehydrogenation through  $\text{H}^+ - \text{H}^-$  interactions by cooperating with alkali metal hydroxides. *RSC Advances* **2014**, *4* (6), 3082.
5. Varin, R. A.; Parviz, R., Hydrogen generation from the ball milled composites of sodium and lithium borohydride ( $\text{NaBH}_4/\text{LiBH}_4$ ) and magnesium hydroxide ( $\text{Mg}(\text{OH})_2$ ) without and with the nanometric nickel (Ni) additive. *International Journal of Hydrogen Energy* **2012**, *37* (2), 1584-1593.
6. Drozd, V.; Saxena, S.; Garimella, S. V.; Durygin, A., Hydrogen release from a mixture of  $\text{NaBH}_4$  and  $\text{Mg}(\text{OH})_2$ . *International Journal of Hydrogen Energy* **2007**, *32* (15), 3370-3375.
7. Monnin, C.; Dubois, M., Thermodynamics of the  $\text{LiOH} + \text{H}_2\text{O}$  System. *Journal of Chemical & Engineering Data* **2005**, *50* (4), 1109-1113.
8. Dinh, L. N.; McLean Li, W.; Schildbach, M. A.; LeMay, J. D.; Siekhaus, W. J.; Balooch, M., The nature and effects of the thermal stability of lithium hydroxide. *Journal of Nuclear Materials* **2003**, *317* (2-3), 175-188.
9. Popescu, C.; Jianu, V.; Alexandrescu, R.; Mihăilescu, I. N.; Morjan, I.; Pascu, M. L., Dehydration of some inorganic compounds by CW  $\text{CO}_2$  laser irradiation and thermal heating: A comparative study. *Thermochimica Acta* **1988**, *129* (2), 269-276.
10. Zho, Z.; Chashchin, V. A.; Vishnyakov, A. V., Carbonization kinetics of lithium hydroxide and its monohydrate. *Theoretical Foundations of Chemical Engineering* **2007**, *41* (5), 577-584.
11. Zhao, Z.; Fu, P.; Zhao, B. In Investigation into Reaction Kinetics of  $\text{LiOH} \cdot \text{H}_2\text{O}$  and  $\text{CO}_2$ , *Power and Energy Engineering Conference*, 2009. APPEEC 2009. Asia-Pacific, 27-31 March 2009; 2009; pp 1-4.
12. Noda, Y.; Koga, N., Phenomenological Kinetics of the Carbonation Reaction of Lithium Hydroxide Monohydrate: Role of Surface Product Layer and Possible Existence of a Liquid Phase. *The Journal of Physical Chemistry C* **2014**, *118* (10), 5424-5436.
13. Züttel, A., Materials for hydrogen storage. *Materials Today* **2003**, *6* (9), 24-33.
14. Tayeh, T.; Awad, A. S.; Nakhil, M.; Zakhour, M.; Silvain, J. F.; Bobet, J. L., Production of hydrogen from magnesium hydrides hydrolysis. *International Journal of Hydrogen Energy* **2014**, *39* (7), 3109-3117.
15. Mattox, D. M., 5 - Vacuum Evaporation and Vacuum Deposition. In *Handbook of Physical Vapor Deposition (PVD) Processing*, Mattox, D. M., Ed. William Andrew Publishing: Westwood, NJ, 1998; pp 288-342.
16. Sadtler, P. B., Vacuum evaporation. *J. Ind. Eng. Chem.* **1909**, *1*, 644-653.

17. Reardon, H. Synthesis, structure and characterisation of novel lightweight energy materials based on group I & II metal compounds. PhD Thesis, University of Glasgow, 2014.
18. Kissinger, H. E., Reaction Kinetics in Differential Thermal Analysis. *Analytical Chemistry* **1957**, 29 (11), 1702-1706.
19. Kissinger, H. E., Variation on Peak Temperature With Heating Rate in Differential Thermal Analysis. *Journal of Research of The National Bureau of Standards* **1956**, 57 (4), 5.
20. Inorganic Crystallographic Structure Database (ICSD). <http://cds.rsc.org/> (accessed 22<sup>nd</sup> May 2014).
21. Belsky, A.; Hellenbrandt, M.; Karen, V. L.; Luksch, P., New developments in the Inorganic Crystal Structure Database (ICSD): accessibility in support of materials research and design. *Acta Crystallographica Section B* **2002**, 58 (3 Part 1), 364-369.
22. A. C. Larson, R. B. v. D. *General Structure Analysis System (GSAS)*; Los Alamos Laboratory: Los Alamos, NM, USA, 1995, 1995; pp 86-748.
23. Toby, B. H., EXPGUI, a graphical user interface for GSAS. *J. Appl. Crystallogr.* **2001**, 34, 210-213.
24. Ernst, T., Description and crystal structure of lithium hydroxide. *Z. Phys. Chem. B-Chem. Elem. Aufbau. Mater.* **1933**, 20 (1/2), 65-88.
25. Pepinsky, R., Crystal structure of lithium hydroxide monohydrate. *Z. Kristall.* **1939**, 102 (2), 119-131.
26. Alcock, N. W., Rrefinement of crystal structure of lithium hydroxide monohydrate. *Acta Crystallographica Section B-Structural Crystallography and Crystal Chemistry* **1971**, B 27 (AUG15), 1682-&.
27. *CRC Handbook of Chemistry and Physics*. 95th Edition ed.; CRC Press: Boca Raton, Florida 33431, 1980-1981.
28. Kudo, H., The rates of thermal decomposition of LiOH(s), LiOD(s) and LiOT(s). *Journal of Nuclear Materials* **1979**, 87 (1), 185-188.
29. Huot, J.; Liang, G.; Boily, S.; Van Neste, A.; Schulz, R., Structural study and hydrogen sorption kinetics of ball-milled magnesium hydride. *Journal of Alloys and Compounds* **1999**, 293–295 (0), 495-500.
30. Mitushiro Kubota, S. M., Hitoki Matsuda, Hong Yu Huang, Zhao Hong He, Xi Xian Yang, Chemical Heat Storage with LiOH/LiOH·H<sub>2</sub>O Reaction for Low-Temperature Heat below 373 K. *Advanced Materials Research* **2014**, 757, 757-760.

31. Leardini, F.; Ares, J. R.; Bodega, J.; Fernandez, J. F.; Ferrer, I. J.; Sanchez, C., Reaction pathways for hydrogen desorption from magnesium hydride/hydroxide composites: bulk and interface effects. *Phys. Chem. Chem. Phys.* **2010**, *12* (3), 572-577.
32. Tessier, J. P.; Palau, P.; Huot, J.; Schulz, R.; Guay, D., Hydrogen production and crystal structure of ball-milled  $\text{MgH}_2\text{-Ca}$  and  $\text{MgH}_2\text{-CaH}_2$  mixtures. *Journal of Alloys and Compounds* **2004**, *376* (1-2), 180-185.
33. Bazzanella, N.; Checchetto, R.; Miotello, A., Atoms and Nanoparticles of Transition Metals as Catalysts for Hydrogen Desorption from Magnesium Hydride. *Journal of Nanomaterials* **2011**, *2011*, 1-11.
34. Ren, C.; Fang, Z. Z.; Zhou, C. S.; Lu, J.; Ren, Y.; Zhang, X. Y., Hydrogen Storage Properties of Magnesium Hydride with V-Based Additives. *J. Phys. Chem. C* **2014**, *118* (38), 21778-21784.
35. Cui, J.; Wang, H.; Liu, J.; Ouyang, L.; Zhang, Q.; Sun, D.; Yao, X.; Zhu, M., Remarkable enhancement in dehydrogenation of  $\text{MgH}_2$  by a nano-coating of multi-valence Ti-based catalysts. *Journal of Materials Chemistry A* **2013**, *1* (18), 5603-5611.
36. Shahi, R. R.; Bhatnagar, A.; Pandey, S. K.; Dixit, V.; Srivastava, O. N., Effects of Ti-based catalysts and synergistic effect of SWCNTs- $\text{TiF}_3$  on hydrogen uptake and release from  $\text{MgH}_2$ . *International Journal of Hydrogen Energy* **2014**, *39* (26), 14255-14261.

## 6 Conclusions and Future Work

### 6.1 Conclusions

This thesis describes the preparation and characterisation of potential ‘modular’ solid state hydrogen storage solutions for on-board applications. The systems investigated throughout this work are based on reactions between light weight hydroxides and hydrides. In particular, three main systems were fully investigated:

- $\text{Mg(OH)}_2 - \text{MgH}_2$  system
- $\text{Mg(OH)}_2 - \text{LiH}$  system
- $\text{LiOH} \cdot \text{H}_2\text{O} - \text{MgH}_2$  system (both anhydrous and monohydrate LiOH were used)

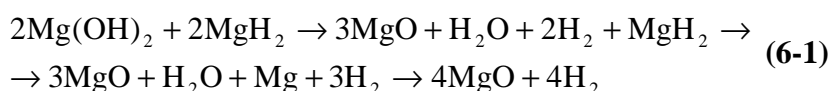
Mixtures of hydroxides and hydrides were prepared by manually grinding stoichiometric amounts of the starting materials under inert atmosphere. Further, nanostructuring the reactants was investigated as a means to improve the dehydrogenation process. All systems were characterised by Powder X-ray diffraction (PXD) and simultaneous thermogravimetric analysis (TG-DTA) mass spectroscopy (MS) and scanning electron microscopy (SEM). Each system was then studied in detail comparing bulk and nanosized materials. The most promising systems were identified.

Chemically nanostructured  $\text{Mg(OH)}_2$  and  $\text{LiOH} \cdot \text{H}_2\text{O}$  were successfully obtained using both new and conventional synthetic routes. Specifically, using a new synthetic procedure that combines microwave irradiation and hydrothermal treatment,  $\text{Mg(OH)}_2$  hexagonal nanoplates were successfully obtained. Further, a selective synthesis for yielding nanostructured anhydrous LiOH and its monohydrate was successfully identified. Physical reduction of the particle size of magnesium hydroxide, lithium hydroxides, lithium hydride and magnesium hydride was successfully achieved by mechanically milling the commercial reactants.

#### *$\text{Mg(OH)}_2 - \text{MgH}_2$ system*

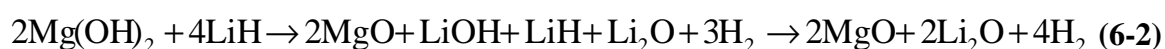
Amongst the Mg-O-H systems, the most promising was found to be the nanostructured  $\text{Mg(OH)}_2 - \text{MgH}_2$  system. Although the onset temperature is not dramatically lowered when working with nanostructured materials (530 K) when compared to bulk reactants (567 K), it is interesting to note that, with respect to the results published by Leardini *et al.*, the onset T of  $\text{H}_2$  release is lowered of nearly 100 K (first main hydrogen release event was

reported to occur at 623 K).<sup>1</sup> Further, important differences were observed when employing nanomaterials instead of bulk reagents. In particular, using nanostructured materials resulted in an initial exothermic event, attributed to a simultaneous decomposition of both Mg(OH)<sub>2</sub> and MgH<sub>2</sub>, followed by the dehydrogenation of the remaining hydride. The major drawback is that both water and hydrogen were evolved from the nano systems, resulting in a dilution of the FC hydrogen fuel, which can result in a decreased efficiency of the fuel cell apparatus. However, the water signal was found to be very weak. This is in agreement with the weight losses observed for the system; after thermal treatment to 873 K the mass change was found to be 7.9 wt. % for nano materials, which is higher than the theoretical 4.7 wt. % H<sub>2</sub>. Based on the obtained STA results, *ex-situ* PXD experiments were performed in order to propose a mechanism of dehydrogenation (Equation 6-1).



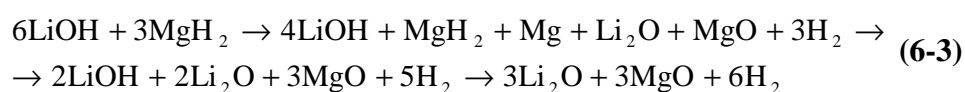
### Mg(OH)<sub>2</sub> – LiH system

Nanomaterials have lead to better performance for the system and were further studied. The use of nanostructured materials resulted in a reduced onset temperature of hydrogen release (lowered from 478 K to 453 K) and faster kinetics, although the mass loss was found to be 4.7 wt. %, lower than to the theoretical 5.4 wt. % H<sub>2</sub>. Based on *ex-situ* PXD experiments performed, two mechanisms of hydrogen release were proposed: the first involved the release of gaseous water from the dehydration of Mg(OH)<sub>2</sub> as an initial step, whilst the second proposed mechanism involved the reaction in the solid state between magnesium hydroxide and lithium hydride to form their respective oxides and LiOH. *In-situ* PND data combined with the data already obtained were found to be essential for elucidating the mechanistic steps of hydrogen release. *In-situ* PND experiments were carried out over the complete temperature range, with short data collections over the crucial dehydrogenation temperatures to follow the reaction steps individually. Rietveld refinements against the collected PND ToF data were performed. Data analysis confirms that the system follows the mechanism presented in Equation 6-2.



### LiOH(H<sub>2</sub>O) – MgH<sub>2</sub> system

The most promising system was identified as the nanostructured LiOH – MgH<sub>2</sub>; it shows a dramatic decrease of the onset temperature of H<sub>2</sub> release of nearly 100 K with respect to bulk materials (from 598 K to 512 K) and the weight loss was found to be 5.2 wt. % (88% of the theoretical 5.9 wt. % H<sub>2</sub>). The dehydrogenation pathway is believed to start with the solid state reaction between LiOH and MgH<sub>2</sub> to yield the respective oxides and evolve H<sub>2</sub>. This results in the formation of MgO and Li<sub>2</sub>O at the surface MgH<sub>2</sub> and LiOH respectively, preventing a further interaction between the two starting materials. The next step is believed to be the decomposition of the remaining hydride, followed by the dehydration of the remaining LiOH (Equation 6-3).



Results obtained for the LiOH·H<sub>2</sub>O – MgH<sub>2</sub> system show important differences when reducing the particle size to the nanometric scale. Bulk materials appear to first release the structural water from LiOH·H<sub>2</sub>O, after which the system was found to behave as the bulk LiOH – MgH<sub>2</sub> composite. The use of milled or nanostructured materials results in a first exothermic event which is believed to relate to a simultaneous loss of structural water from lithium hydroxide and partial hydrolysis of MgH<sub>2</sub>, associated with water and hydrogen release. The onset temperature of H<sub>2</sub> release for nanosized material is drastically lowered to 323 and 313 K for milled and nano systems respectively, whereas the first major H<sub>2</sub> release for bulk system was found to start at nearly 670 K. Further, the weight changes for all systems were found to be higher than the theoretical 7.4 wt. % H<sub>2</sub> (33.6, 25.2 and 22.8 wt. % for bulk, milled and nano materials respectively), confirming that both hydrogen and water are evolved from all systems. The evolution of H<sub>2</sub>O together with H<sub>2</sub> renders the employment of lithium hydroxide monohydrate difficult in operative low temperature fuel cells, as it dilutes the cell fuel reducing the efficiency of the PEMFC.

### Comparison of Li-Mg-O-H systems

It is possible to compare the dehydrogenation performances of the nanostructured MgH<sub>2</sub> – LiOH and the LiH – Mg(OH)<sub>2</sub> systems. They present similar theoretical gravimetric capacity (5.9 wt. % H<sub>2</sub> for the MgH<sub>2</sub>-based and 5.4 wt. % H<sub>2</sub> for the LiH-based). Although the onset temperature of hydrogen release for the MgH<sub>2</sub> – LiOH system is higher with respect to the LiH – Mg(OH)<sub>2</sub> system (512 K Vs 453 K), the weight change associated with hydrogen release was higher: it was possible to evolve 5.2 wt. % H<sub>2</sub> when working

with  $\text{MgH}_2 - \text{LiOH}$  composite, whereas only 4.7 wt. %  $\text{H}_2$  was released when working with the  $\text{LiH} - \text{Mg(OH)}_2$  system. The higher onset temperature of hydrogen release is believed to be related to the ionic nature of the hydride: being  $\text{LiH}$  more ionic than  $\text{MgH}_2$ , it is more effectively destabilised by the interaction with the hydroxide, resulting in a decreased onset T. The two systems were also found to follow different reaction pathways. In the  $\text{MgH}_2 - \text{LiOH}$  the reaction starts with a solid state reaction between the two reagents driven by a  $\text{H}^+ - \text{H}^-$  interaction, whereas in the  $\text{LiH} - \text{Mg(OH)}_2$  system the reactions begins with the independent decomposition of the two starting materials ( $\text{Mg(OH)}_2$  dehydration and  $\text{LiH}$  hydrolysis). The major drawback for both systems is that the hydrogen evolution is a multi-step reaction and efforts should be focused on having a single  $\text{H}_2$  release event. Overall, the magnesium hydride – anhydrous lithium hydroxide system appears to be the most promising one and should be further investigated.

Moreover, it is possible to draw a comparison between the systems studied during this work and the systems already reported in the literature.

When magnesium hydroxide is used as component for ‘modular’ hydrogen release systems, it is interesting to note that the results obtained when employing  $\text{LiH}$  are similar to the one obtained when using  $\text{LiBH}_4$ . In fact, in the present work the onset temperature of hydrogen release for the nanostructured  $\text{LiH} - \text{Mg(OH)}_2$  system was found to be 478 K with a mass loss of 4.7 wt. %  $\text{H}_2$ . For the  $\text{LiBH}_4 - \text{Mg(OH)}_2$  system, the onset T reported by Varin *et al.* was found to be 473 K and the hydrogen release was associated with a mass change of 4.5%.<sup>2</sup> In 2014 however, Pan *et al.* reported a mass loss of 9.6 wt. % with an onset temperature of  $\text{H}_2$  release lowered to 373 K when working with a non stoichiometric ratio of 1  $\text{LiBH}_4$  to 0.35  $\text{Mg(OH)}_2$ .<sup>3</sup> In the light of these results,  $\text{LiH} - \text{Mg(OH)}_2$  non-stoichiometric mixtures should be investigated as well.

Further, as previously discussed in Section 5.1,  $\text{LiOH}$  has increasingly gained attention as a component of solid state hydrogen storage solutions and its use has been proposed in several systems. Its dehydrogenation properties have been tested in the presence of several light metal hydrides such as lithium hydride and lithium borohydride. With respect to both onset temperature of hydrogen release and weight change, data obtained in this work are consistent with the results already reported in the literature. When working with the  $\text{LiOH} - \text{LiH}$  composite, Vajo *et al.* and Lu *et al.* reported a mass loss of 5.5 and 6.6 wt. %  $\text{H}_2$  with onset temperatures of hydrogen release of respectively 523 and 473 K.<sup>4,5</sup> Interestingly, the same onset T of 523 K was observed by Vajo *et al.* when employing  $\text{LiOH}$  together with  $\text{LiBH}_4$ , although the observed weight change in this case was 6.6 wt.

% H<sub>2</sub>.<sup>4</sup> Zhu *et al.* further investigated the LiBH<sub>4</sub> – LiOH system using different stoichiometric ratios: when working with a 1:4 ratio, the system was found to release 6.5 wt. % H<sub>2</sub> with an onset T of H<sub>2</sub> release as high as the one reported by Vajo *et al.* in 2004 (523 K).<sup>6</sup> These temperatures are similar to the onset temperature of hydrogen release observed for the LiOH – MgH<sub>2</sub> system studied during this project (512 K), which is however characterised by a lower mass change of 5.2 wt. % of hydrogen. When working with lithium hydroxide monohydrate, the onset temperatures of hydrogen release were found to be consistent with the ones obtained for other systems: both Vajo *et al.* and Lu *et al.* reported an onset temperature of hydrogen release of 313 K when employing LiOH·H<sub>2</sub>O with LiBH<sub>4</sub> and LiH respectively.<sup>4,5</sup> A difference can be observed in the mass changes of such systems: for the LiOH·H<sub>2</sub>O – MgH<sub>2</sub> system a weight change of 22.8 wt. % due to the release of both H<sub>2</sub> and H<sub>2</sub>O was observed, while the mass loss was found to be 10 and 8.8 wt. % for the LiOH·H<sub>2</sub>O – LiBH<sub>4</sub> and LiOH·H<sub>2</sub>O – LiH systems respectively and they were related to the release of only hydrogen.

## 6.2 Future Work

From the experimental evidence, it is clear that the most promising systems in terms of hydrogen release properties are the nanostructured Mg(OH)<sub>2</sub> – MgH<sub>2</sub>, the Mg(OH)<sub>2</sub> – LiH and the LiOH – MgH<sub>2</sub> systems. Future work should focus on further improving their performance. Attention should be also focused on developing the system in order to have one single hydrogen release event and at the same time avoiding the release of water. A viable approach could be seen in the use of additives or catalysts, which could lead to improved performances of hydrogen release. In this sense, magnesium hydride has been extensively studied and a wide range of catalysts and additives have been investigated in order to improve its dehydrogenation performances. However, none of them has been tested in the presence of both lithium hydroxide and magnesium hydride. On the contrary, lithium hydride has been studied mostly as a component of solid state hydrogen release systems (*i.e.* Li-N-H systems) because of its very high decomposition temperature. Nonetheless suitable catalysts and additives for promoting the interaction between hydride and hydroxide could be seen in calcium, lithium and sodium hydride to yield ternary hydrides and composites<sup>7,8</sup> as well as transition metals including multi-valence vanadium- and titanium-based materials.<sup>9,10,11,12,13</sup> Two different strategies could be followed: composites could be prepared by adding the appropriate wt. % of catalyst/additives (5 to 20 wt. %) to the as-received hydrides before the milling procedure is carried out. The

milled hydride is then mixed with the hydroxide and the resulting system characterised by thermogravimetric analysis, PXD and SEM. The other approach could consist in adding the catalyst/additives to the system prior manual mixing and after the milling of the starting materials: mixtures could be prepared by adding appropriate wt. % of additive/catalyst to the stoichiometric amounts of nanostructured hydride and hydroxide. The three components will then be manually ground together under inert atmosphere and the resulting composite characterised by TG-DTA-MS, PXD and SEM. However, destabilising the hydride could also lead in a prevented interaction between hydride and hydroxide. Moreover, catalysts or additives to be employed must be carefully chosen: they must not interact with the hydroxide and they must not react or be deactivated by the presence of the smallest amount of water that could be released during the dehydrogenation process. Additional studies in order to understand which additives and catalysts could be the most efficient are required.

Moreover, future studies should focus on the recyclability of each system. In particular, for the  $\text{Mg(OH)}_2 - \text{MgH}_2$  system, the main phase present after the dehydrogenation process was found to be MgO with magnesium metal as impurity. Thus, MgO should be fully investigated as potentially recyclable starting material for the synthesis of new nanostructured  $\text{Mg(OH)}_2$  to be employed in a new dehydrogenation cycle. Further, the morphology of the synthesised nano  $\text{Mg(OH)}_2$  is not dependant on the morphology of the starting material employed. For Mg-Li-O-H systems the study of the recyclability is intrinsically more complicated as the final dehydrogenation product is a mixture of magnesium oxide and lithium oxide for both  $\text{Mg(OH)}_2 - \text{LiH}$  and  $\text{LiOH} - \text{MgH}_2$  systems. Different recycling strategies should be investigated: MgO and  $\text{Li}_2\text{O}$  could be separated with a thermal treatment basing on their melting point (3125 and 1711 K for MgO and  $\text{Li}_2\text{O}$  respectively)<sup>14</sup>. Solubility tests could be performed to identify one or more solvents in which either MgO or  $\text{Li}_2\text{O}$  is soluble and therefore selectively precipitate MgO or  $\text{Li}_2\text{O}$ . MgO could then be used to regenerate nanostructured  $\text{Mg(OH)}_2$ , whilst lithium oxide could be employed for the regeneration of LiOH starting material via reaction with water. Further, working with the  $\text{LiOH} - \text{MgH}_2$  system could prove problematic because the dehydrogenation product consist in clusters of MgO particles mixed partially melted  $\text{Li}_2\text{O}$ : studies are required in order to understand whether it is possible to retain the morphology and the particle size after the recycling process. Additional studies are required to identify a viable approach for the separation of magnesium oxide and lithium oxide and subsequent regeneration to starting materials that would result in an overall energy- and cost-efficient cycle.

Further, elucidating the exact reaction pathway is indeed pivotal to achieve a better insight in order to improve dehydrogenation properties of each system. In this respect, similar to the  $\text{Mg}(\text{OH})_2 - \text{LiH}$  system, *in-situ* PXD and PND experiments should be performed on  $\text{Mg}(\text{OH})_2 - \text{MgH}_2$  and  $\text{LiOH} - \text{MgH}_2$  systems to confirm the proposed mechanism of hydrogen release.

### 6.3 References

1. Leardini, F.; Ares, J. R.; Bodega, J.; Fernandez, J. F.; Ferrer, I. J.; Sanchez, C., Reaction pathways for hydrogen desorption from magnesium hydride/hydroxide composites: bulk and interface effects. *Phys. Chem. Chem. Phys.* **2010**, *12* (3), 572-577.
2. Varin, R. A.; Parviz, R., Hydrogen generation from the ball milled composites of sodium and lithium borohydride ( $\text{NaBH}_4/\text{LiBH}_4$ ) and magnesium hydroxide ( $\text{Mg}(\text{OH})_2$ ) without and with the nanometric nickel (Ni) additive. *International Journal of Hydrogen Energy* **2012**, *37* (2), 1584-1593.
3. Liu, Y.; Zhang, Y.; Zhou, H.; Zhang, Y.; Gao, M.; Pan, H., Reversible hydrogen storage behavior of  $\text{LiBH}_4\text{-Mg}(\text{OH})_2$  composites. *International Journal of Hydrogen Energy* **2014**, *39* (15), 7868-7875.
4. Vajo, J. J.; Skeith, S. L.; Mertens, F.; Jorgensen, S. W., Hydrogen-generating solid-state hydride/hydroxide reactions. *Journal of Alloys and Compounds* **2005**, *390* (1-2), 55-61.
5. Lu, J.; Fang, Z. Z.; Sohn, H. Y., A hybrid method for hydrogen storage and generation from water. *Journal of Power Sources* **2007**, *172* (2), 853-858.
6. Cai, W.; Wang, H.; Sun, D.; Zhang, Q.; Yao, X.; Zhu, M., Destabilization of  $\text{LiBH}_4$  dehydrogenation through  $\text{H}^+ - \text{H}^-$  interactions by cooperating with alkali metal hydroxides. *RSC Advances* **2014**, *4* (6), 3082.
7. Huot, J.; Liang, G.; Boily, S.; Van Neste, A.; Schulz, R., Structural study and hydrogen sorption kinetics of ball-milled magnesium hydride. *Journal of Alloys and Compounds* **1999**, *293-295* (0), 495-500.
8. Tessier, J. P.; Palau, P.; Huot, J.; Schulz, R.; Guay, D., Hydrogen production and crystal structure of ball-milled  $\text{MgH}_2\text{-Ca}$  and  $\text{MgH}_2\text{-CaH}_2$  mixtures. *Journal of Alloys and Compounds* **2004**, *376* (1-2), 180-185.
9. Bazzanella, N.; Checchetto, R.; Miotello, A., Atoms and Nanoparticles of Transition Metals as Catalysts for Hydrogen Desorption from Magnesium Hydride. *Journal of Nanomaterials* **2011**, *2011*, 1-11.

10. Ren, C.; Fang, Z. Z.; Zhou, C. S.; Lu, J.; Ren, Y.; Zhang, X. Y., Hydrogen Storage Properties of Magnesium Hydride with V-Based Additives. *J. Phys. Chem. C* **2014**, *118* (38), 21778-21784.
11. Cui, J.; Wang, H.; Liu, J.; Ouyang, L.; Zhang, Q.; Sun, D.; Yao, X.; Zhu, M., Remarkable enhancement in dehydrogenation of MgH<sub>2</sub> by a nano-coating of multi-valence Ti-based catalysts. *Journal of Materials Chemistry A* **2013**, *1* (18), 5603-5611.
12. Shahi, R. R.; Bhatnagar, A.; Pandey, S. K.; Dixit, V.; Srivastava, O. N., Effects of Ti-based catalysts and synergistic effect of SWCNTs-TiF<sub>3</sub> on hydrogen uptake and release from MgH<sub>2</sub>. *International Journal of Hydrogen Energy* **2014**, *39* (26), 14255-14261.
13. da Conceicao, M. O. T.; dos Santos, D. S., Catalytic effect of chlorides compounds on hydrogen sorption properties of magnesium hydride. *Journal of Alloys and Compounds* **2014**, *615*, S715-S718.
14. *CRC Handbook of Chemistry and Physics*. 95<sup>th</sup> Edition ed.; CRC Press: Boca Raton, Florida 33431, 1980-1981.

## 7 Appendices

### 7.1 Appendix A: Tables and Figures for Chapter 3

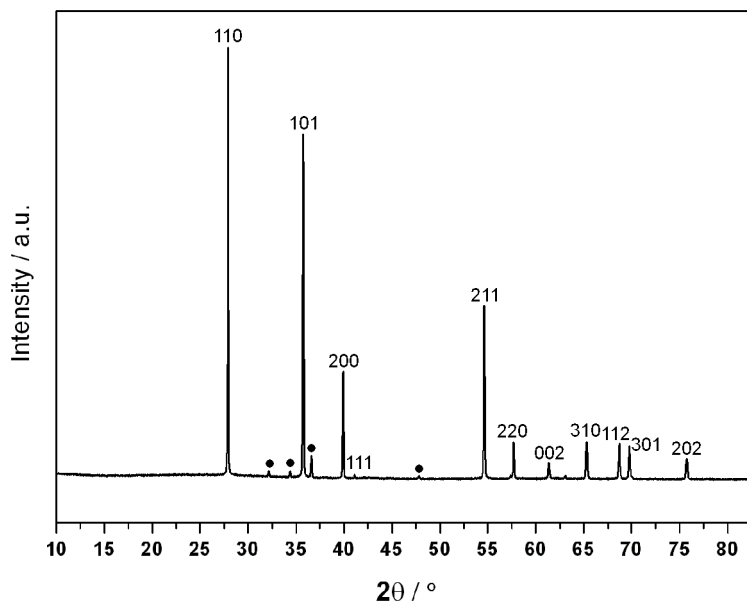


Figure 7-1: PXD pattern for commercial  $\beta$ -MgH<sub>2</sub>. Circles indicate Mg metal.

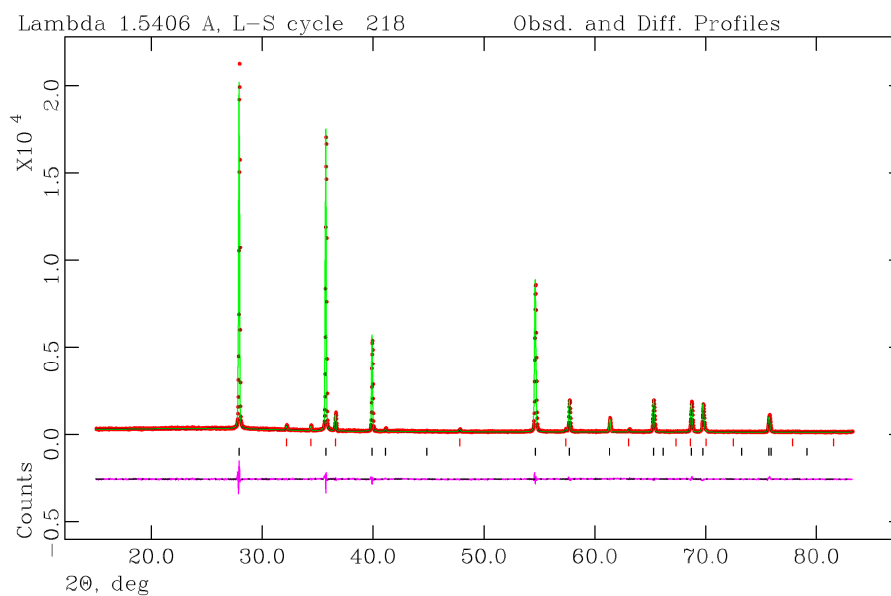


Figure 7-2: Observed, calculated and difference (OCD) plot from the PXD Rietveld refinement for commercial  $\beta$ -MgH<sub>2</sub>. The black and red tick marks indicate reflections from MgH<sub>2</sub> and Mg respectively.

Table 7-1: Selected data from the PXD Rietveld refinement for commercial  $\beta$ -MgH<sub>2</sub>.

Empirical Formula	MgH <sub>2</sub>	Mg
<b>Crystal System</b>	Tetragonal	Hexagonal
<b>Space Group</b>	<i>P4/mmm</i>	<i>P6<sub>3</sub>/mmc</i>
<b>Lattice Parameters</b>		
<i>a</i> / Å	4.51639(5)	3.2101(2)
<i>c</i> / Å	3.02074(3)	5.2117(4)
<i>V</i> / Å <sup>3</sup>	61.616(2)	46.510(6)
<i>Z</i>	2	2
<b>Unit Cell Formula</b>		
<b>Weight / M<sub>w</sub></b>	52.642	48.610
<b>Density / g cm<sup>-3</sup></b>	1.419	1.735
<b>Wt. %</b>	96(1)	4(1)
<b>No. of Variables</b>		30
<b>No. of Observations</b>		4423
<b>Rwp %</b>		7.29
<b>Rp %</b>		5.54
<b><math>\chi^2</math></b>		1.74

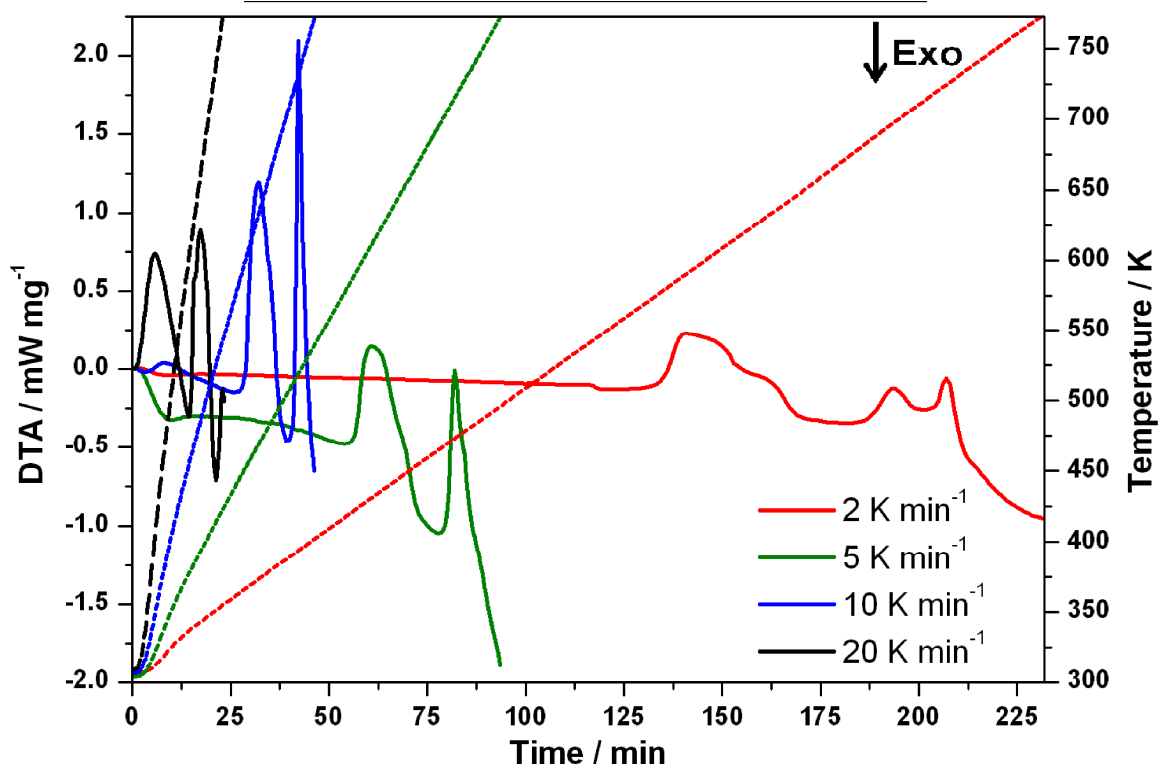


Figure 7-3: DTA profiles used to obtain Kissinger plots for Sample 18 (bulk). Dashed and full lines indicate temperature and DTA profiles respectively.

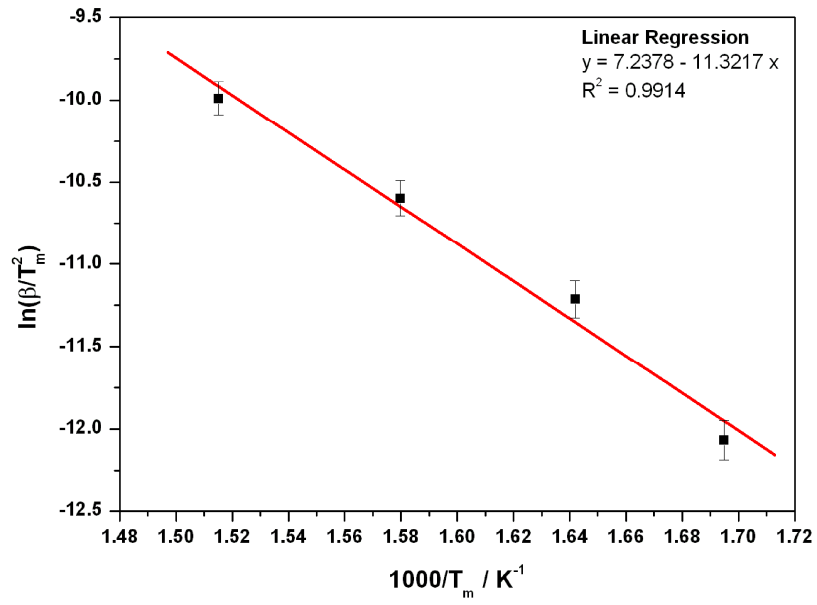


Figure 7-4: Kissinger plot for the LT thermal event for Sample 18 (bulk).

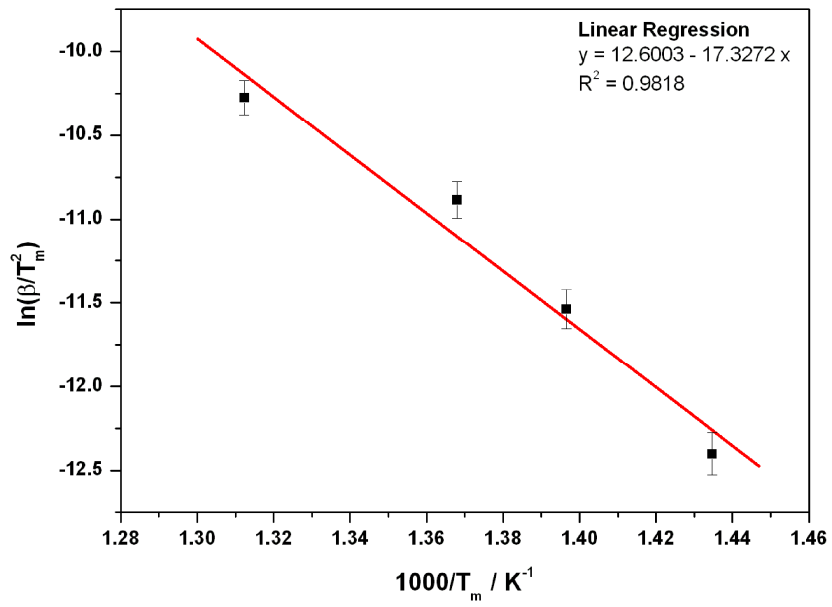


Figure 7-5: Kissinger plot for the HT thermal event for Sample 18 (bulk).

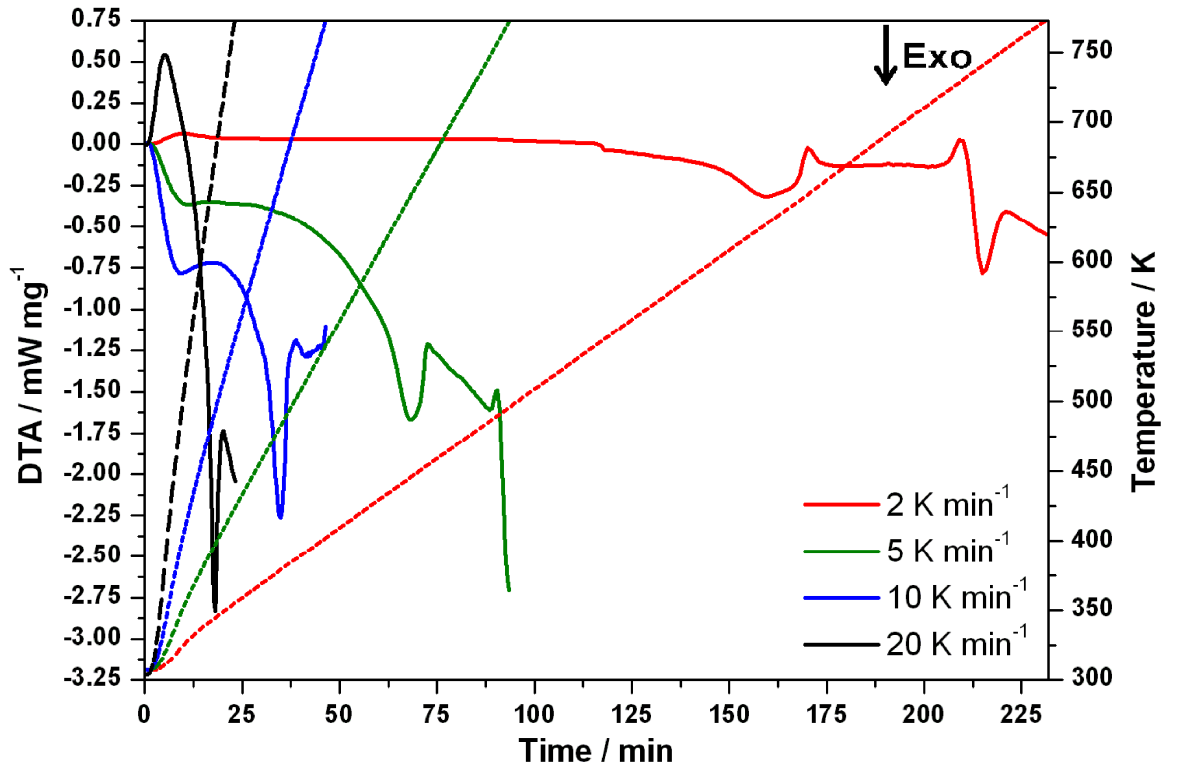


Figure 7-6: DTA profiles used to obtain Kissinger plots for Sample 19 (milled). Dashed and full lines indicate temperature and DTA profiles respectively.

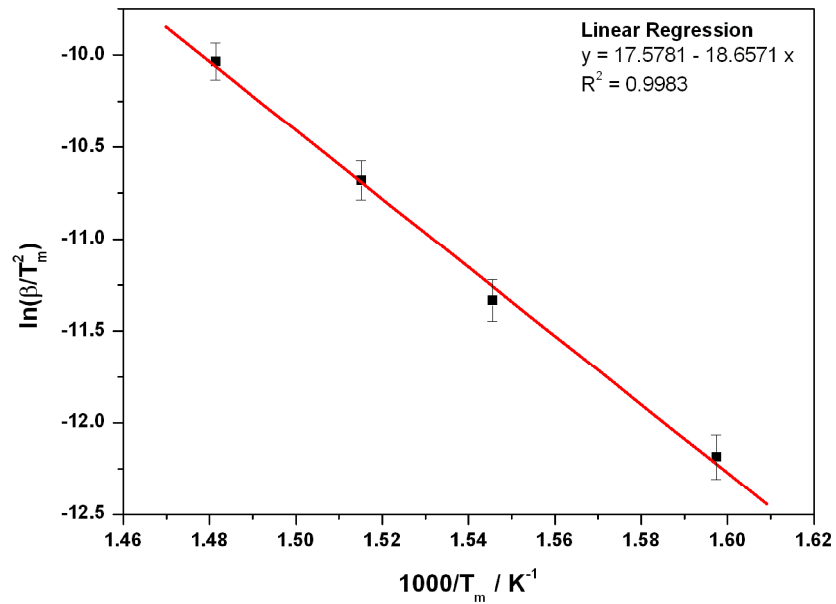


Figure 7-7: Kissinger plot for the LT thermal event for Sample 19 (milled).

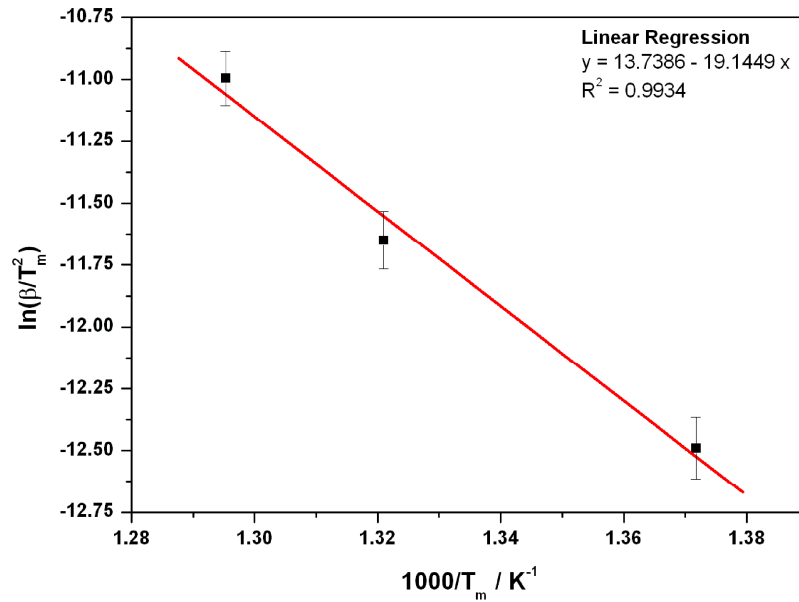


Figure 7-8: Kissinger plot for the HT thermal event for Sample 19 (milled).

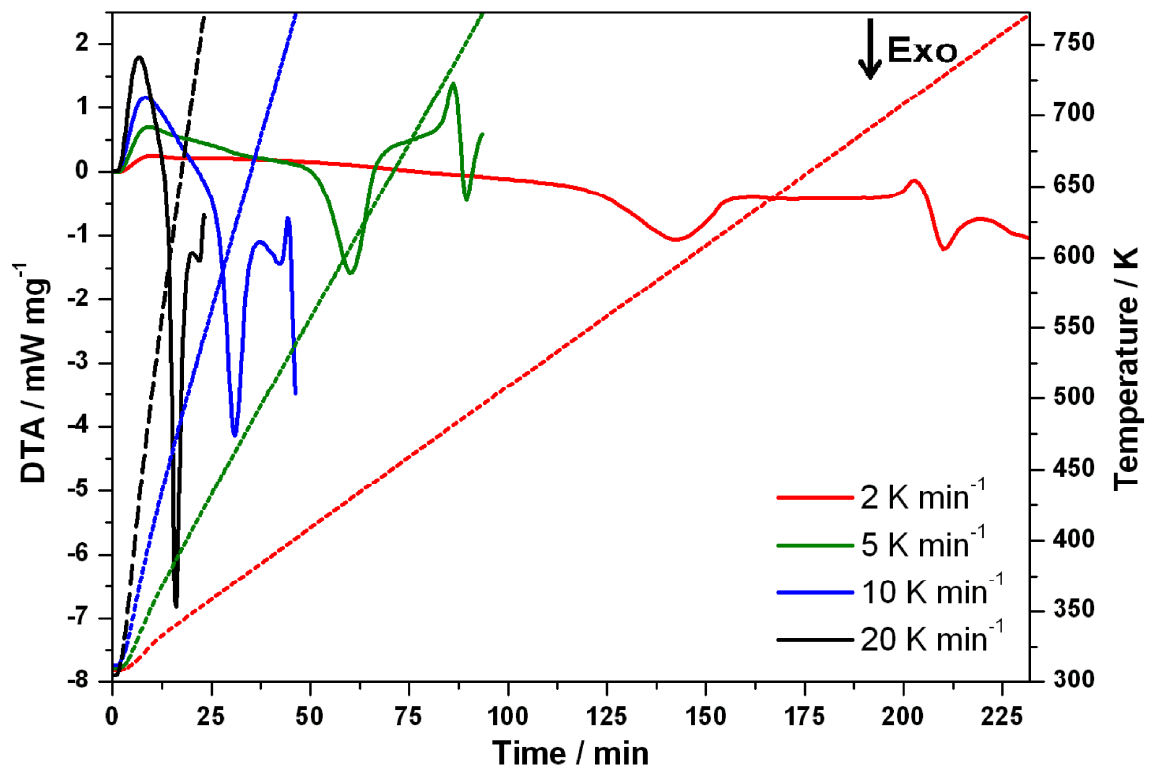


Figure 7-9: DTA profiles used to obtain Kissinger plots for Sample 20 (nano). Dashed and full lines indicate temperature and DTA profiles respectively.

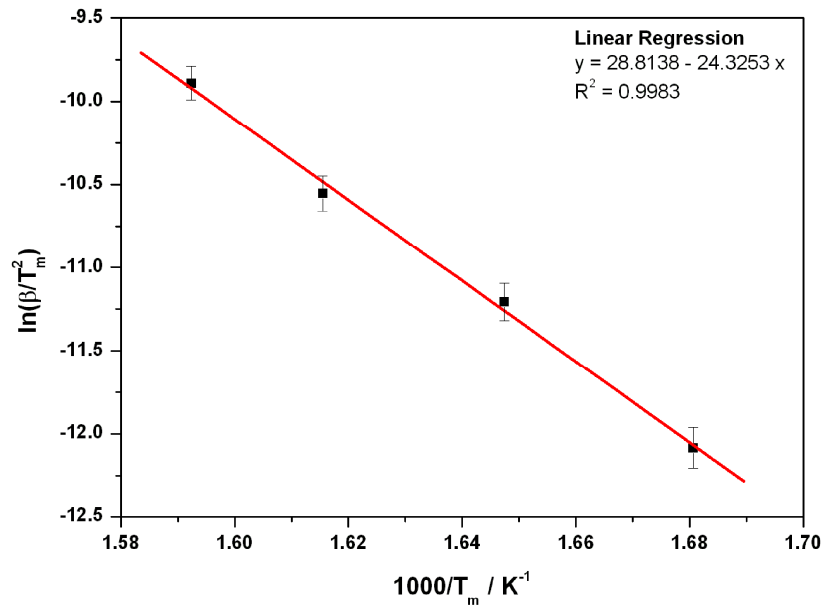


Figure 7-10: Kissinger plot for the LT thermal event for Sample 20 (nano).

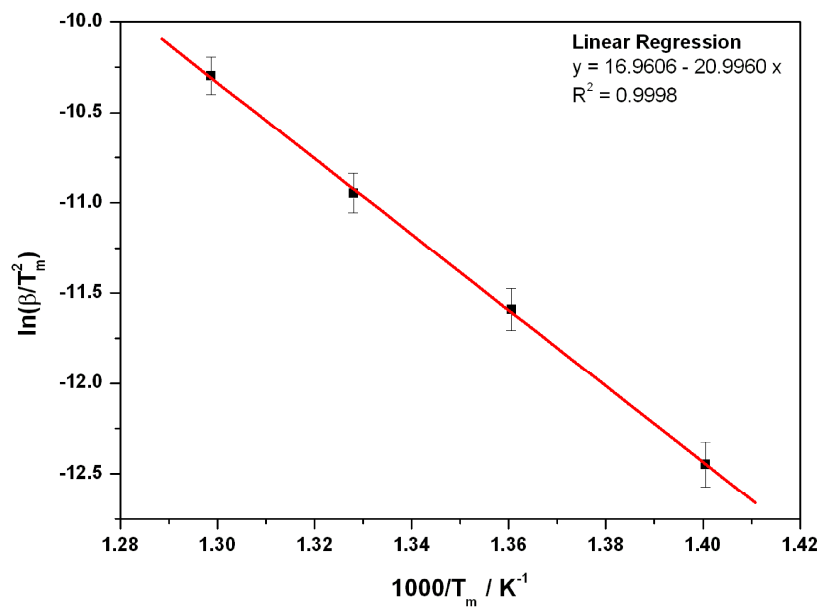


Figure 7-11: Kissinger plot for the HT thermal event for Sample 20 (nano).

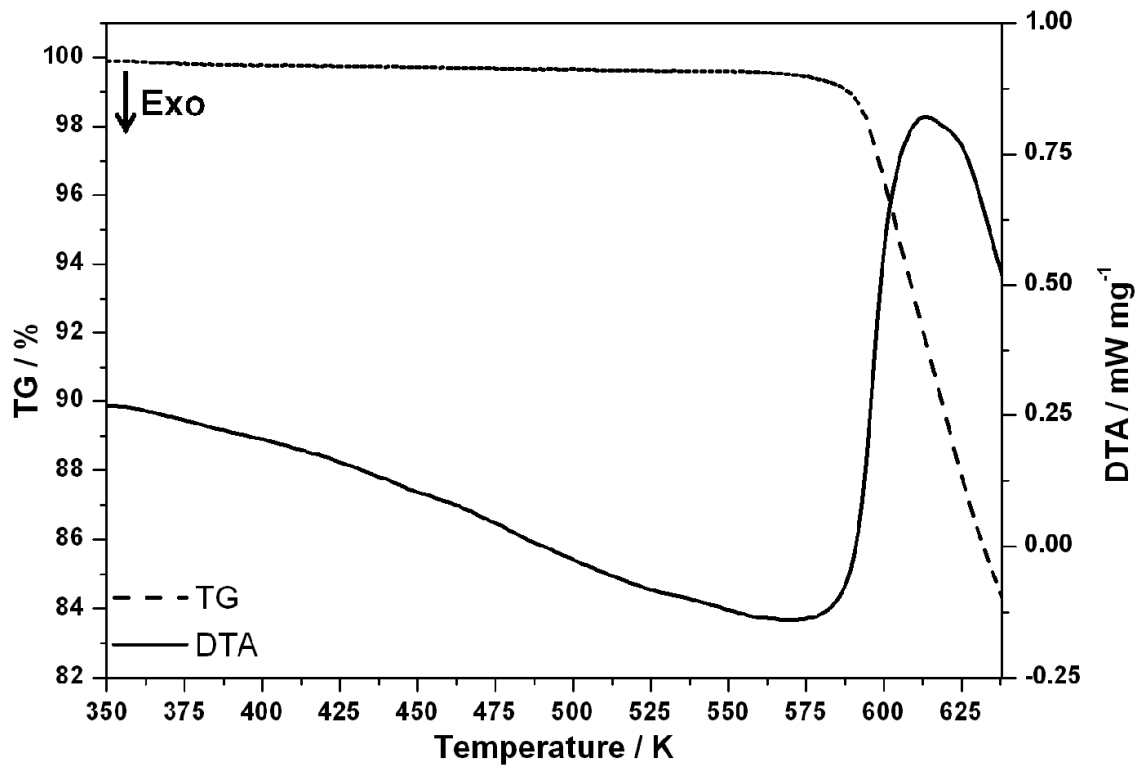


Figure 7-12: TG (dashed line) and DTA (full line) data obtained for Sample 6.

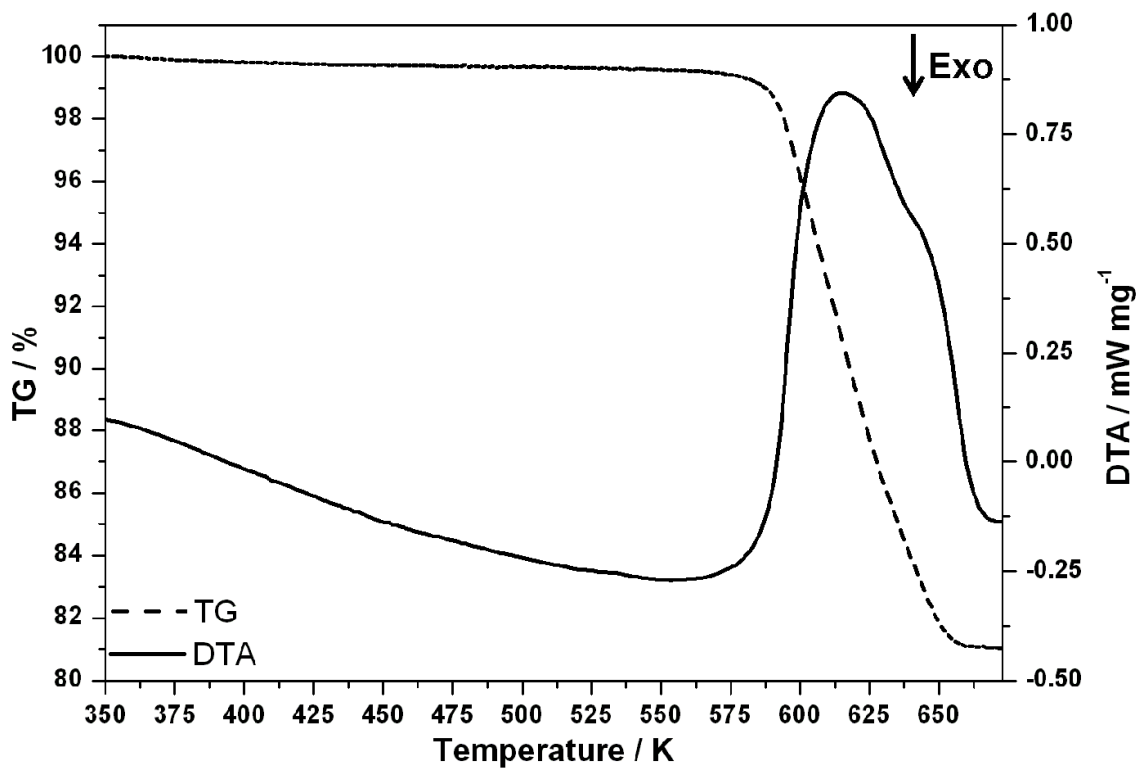


Figure 7-13: TG (dashed line) and DTA (full line) data obtained for Sample 7.

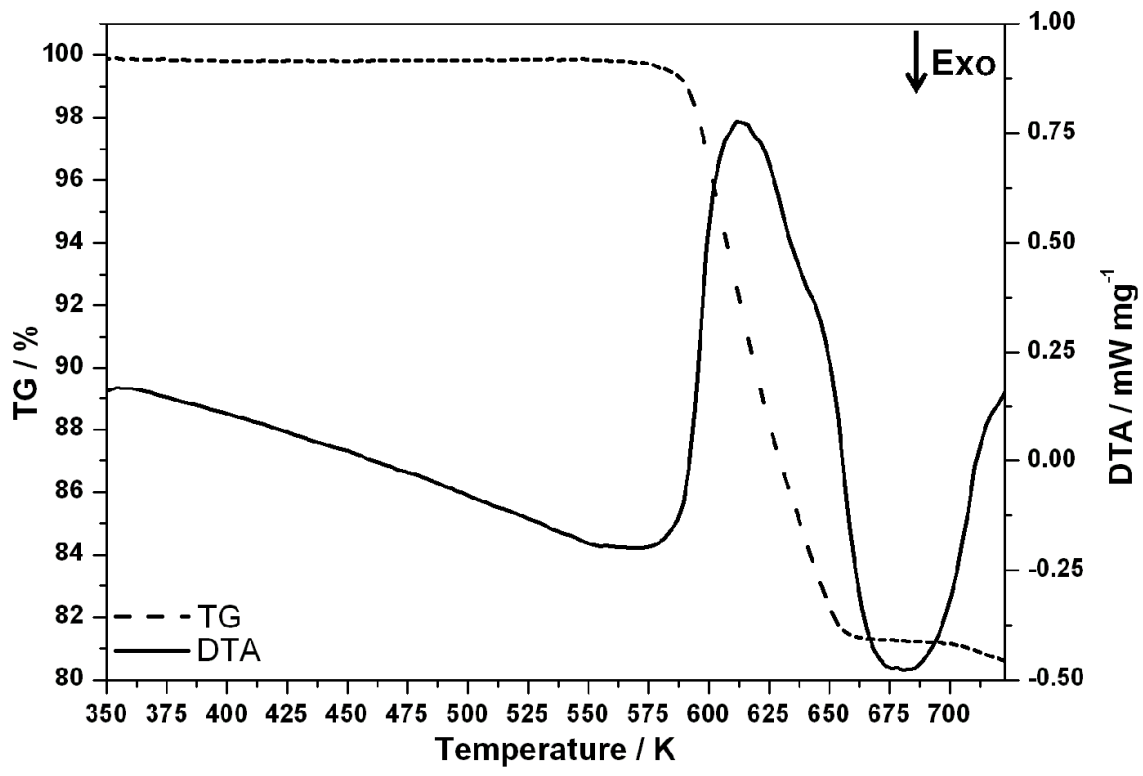


Figure 7-14: TG (dashed line) and DTA (full line) data obtained for Sample 8.

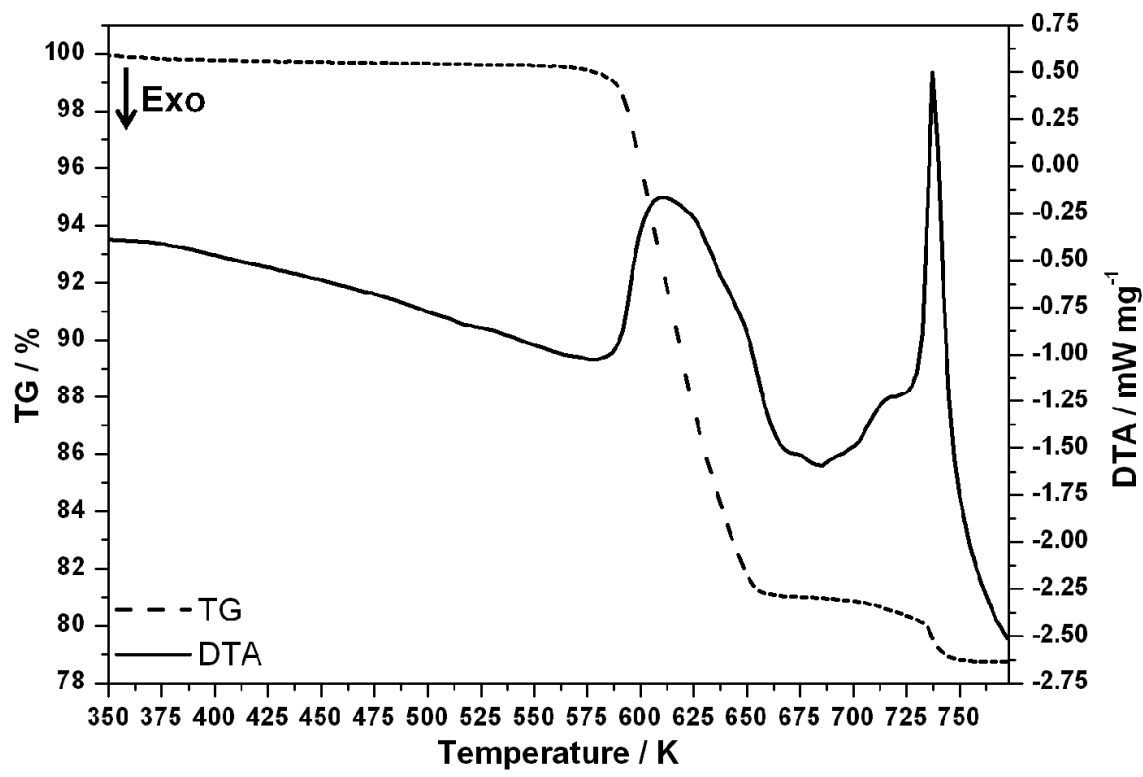


Figure 7-15: TG (dashed line) and DTA (full line) data obtained for Sample 9.

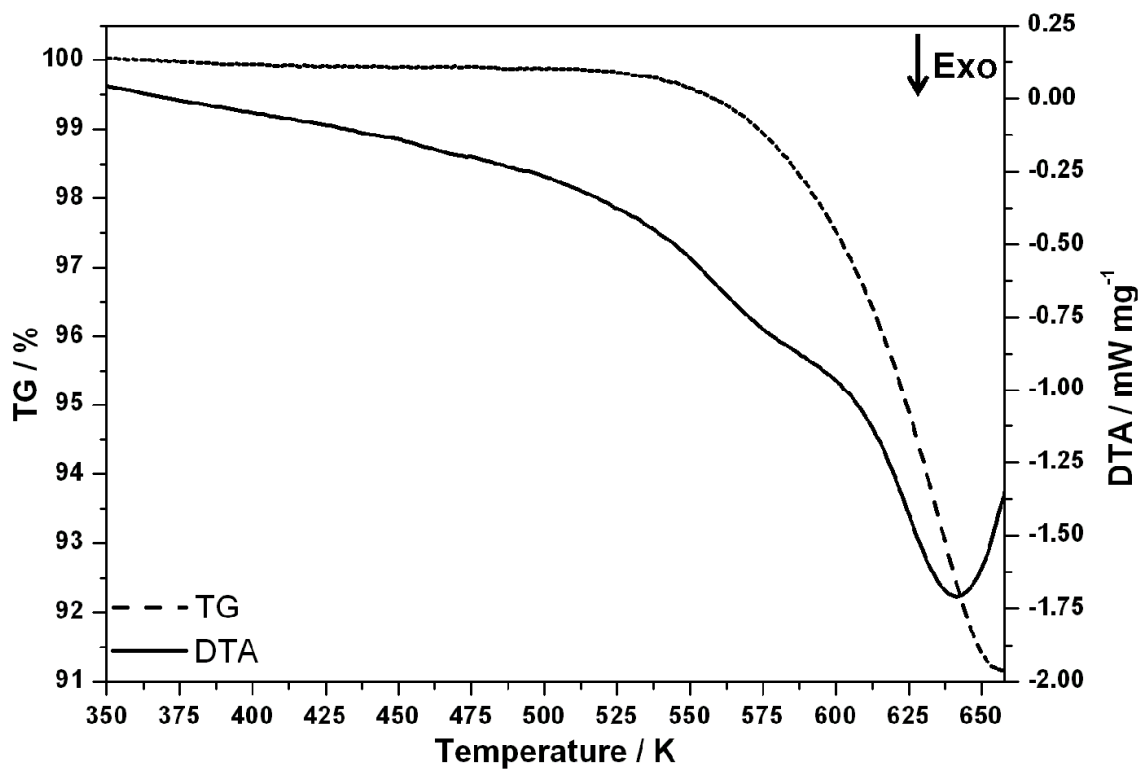


Figure 7-16: TG (dashed line) and DTA (full line) data obtained for Sample 12.

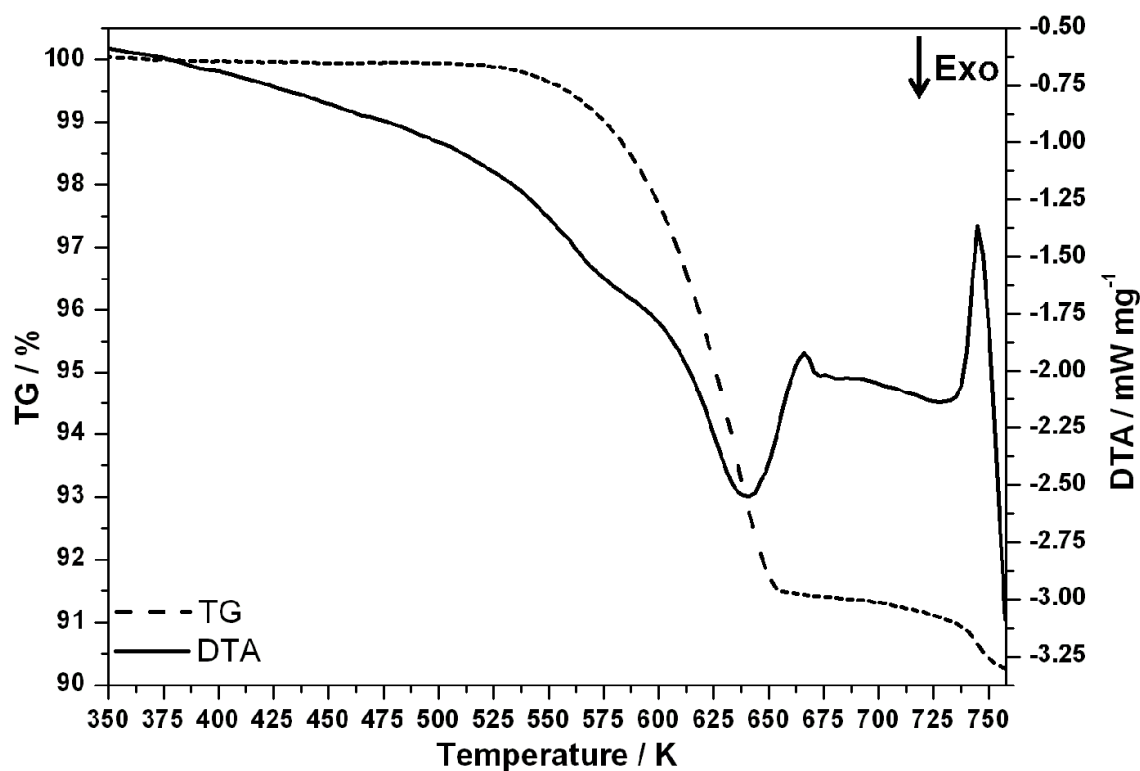


Figure 7-17: TG (dashed line) and DTA (full line) obtained for Sample 13.

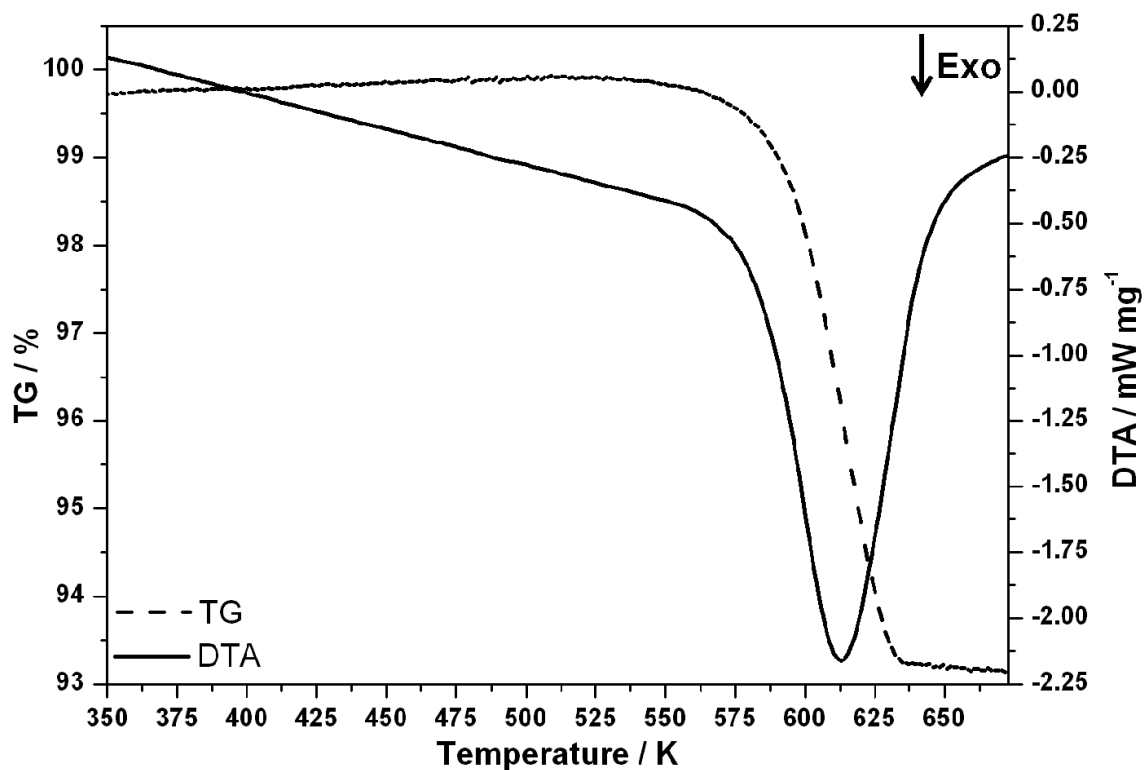


Figure 7-18: TG (dashed line) and DTA (full line) data obtained for Sample 16.

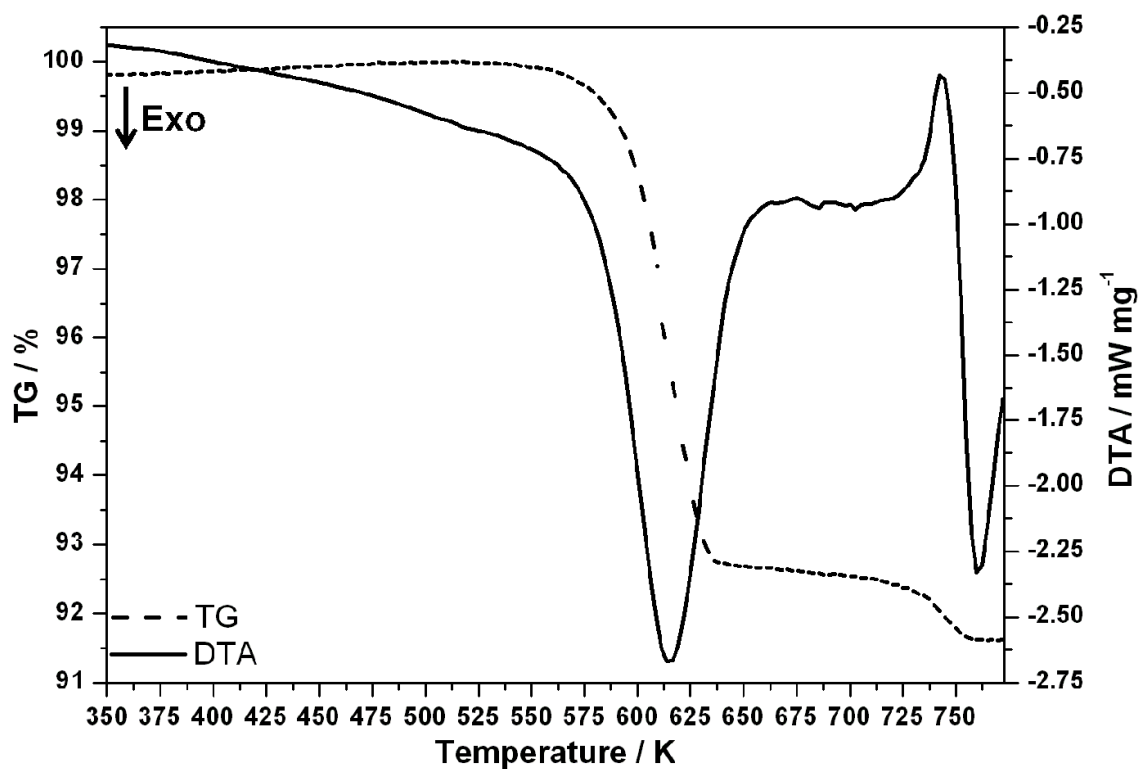


Figure 7-19: TG (dashed line) and DTA (full line) data obtained for Sample 17.

## 7.2 Appendix B: Tables and Figures for Chapter 4

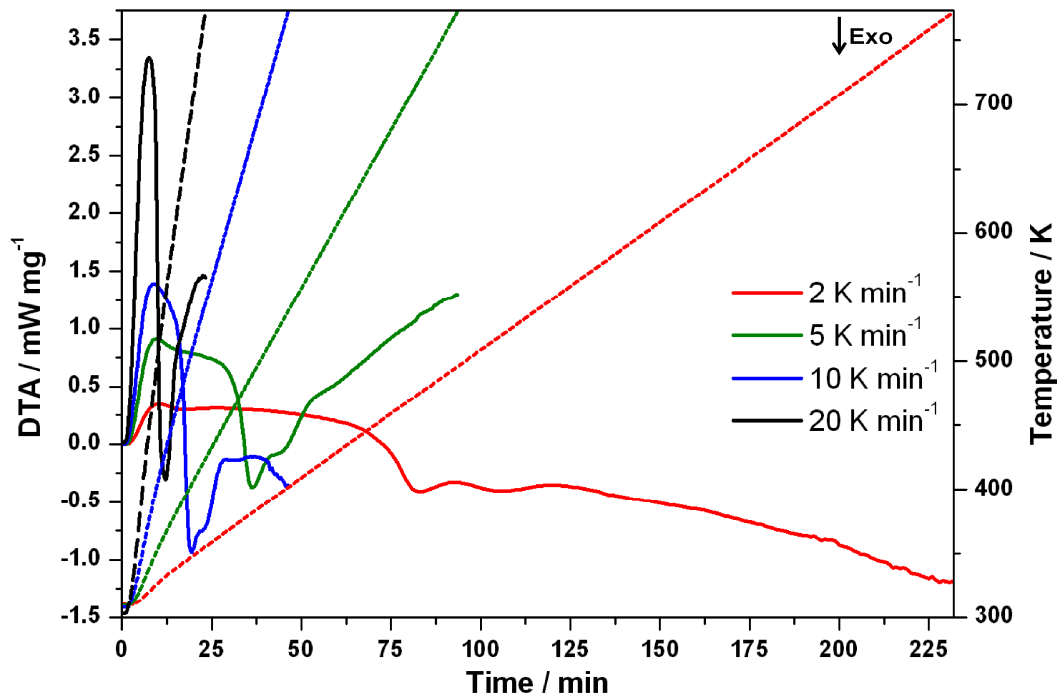


Figure 7-20: DTA profiles used to obtain Kissinger plots for Sample 6 (nano). Dashed and full lines indicate temperature and DTA profiles respectively.

Table 7-2: Selected data from the PND Rietveld refinement for Sample 13 (458 K).

Empirical Formula	Mg(OD) <sub>2</sub>	LiD	MgO	Li <sub>2</sub> O
<b>Crystal System</b>	Trigonal	Cubic	Cubic	Cubic
<b>Space Group</b>	<i>P-3m1</i>	<i>Fm-3m</i>	<i>Fm-3m</i>	<i>Fm-3m</i>
<b>Lattice Parameters</b>				
<i>a</i> / Å	3.1462(1)	4.0941(1)	4.236(2)	4.6305(6)
<i>c</i> / Å	4.7888(2)			
<i>V</i> / Å <sup>3</sup>	41.054(3)	68.629(5)	76.04(8)	99.29(4)
<i>Z</i>	1	4	4	4
<b>Unit Cell Formula</b>				
<b>Weight / M<sub>w</sub></b>	60.331	35.820	161.216	119.524
<b>Density / g cm<sup>-3</sup></b>	2.440	0.867	3.521	1.999
<b>Wt. %</b>	59.3(5)	19.9(4)	15.7(4)	5.1(4)
<b>Temperature / K</b>			458	
<b>No. of Variables</b>			77	
<b>No. of Observations</b>			5965	
<b>Rwp %</b>			2.89	
<b>Rp %</b>			5.56	
<b>χ<sup>2</sup></b>			1.38	

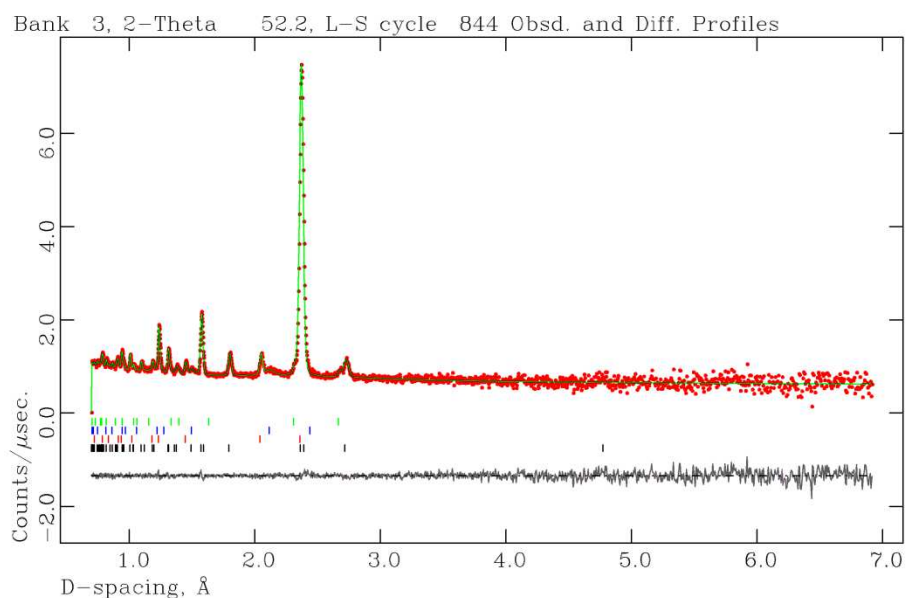


Figure 7-21: Observed, calculated and difference (OCD) plot from the PND Rietveld refinement for Sample 13 (458 K) from PND data, Bank 3 (low angle, 20° 40-67). The green, blue, red and black tick marks indicate reflections from Li<sub>2</sub>O, MgO, LiD and LiOD respectively.

Table 7-3: Selected data from the PND Rietveld refinement for Sample 14 (468 K).

Empirical Formula	Mg(OD) <sub>2</sub>	LiD	MgO	Li <sub>2</sub> O	LiOD
<b>Crystal System</b>	Trigonal	Cubic	Cubic	Cubic	Tetragonal
<b>Space Group</b>	<i>P-3m1</i>	<i>Fm-3m</i>	<i>Fm-3m</i>	<i>Fm-3m</i>	<i>P4/nmm</i>
<b>Lattice Parameters</b>					
<i>a</i> / Å	3.1463(1)	4.0965(1)	4.2359(7)	4.6295(3)	3.5599(7)
<i>c</i> / Å	4.7914(2)				4.374(4)
<i>V</i> / Å <sup>3</sup>	41.076(3)	68.743(5)	76.01(4)	99.22(2)	55.42(5)
<i>Z</i>	1	4	4	4	2
<b>Unit Cell Formula</b>					
<b>Weight / M<sub>w</sub></b>	60.331	35.820	161.216	119.524	49.908
<b>Density / g cm<sup>-3</sup></b>	2.439	0.865	3.522	2.000	1.495
<b>Wt. %</b>	46.8(7)	16.5(4)	25.8(6)	8.8(4)	2.1(2)
<b>Temperature / K</b>			468		
<b>No. of Variables</b>			87		
<b>No. of Observations</b>			5799		
<b>Rwp %</b>			2.61		
<b>Rp %</b>			4.71		
<b>χ<sup>2</sup></b>			1.12		

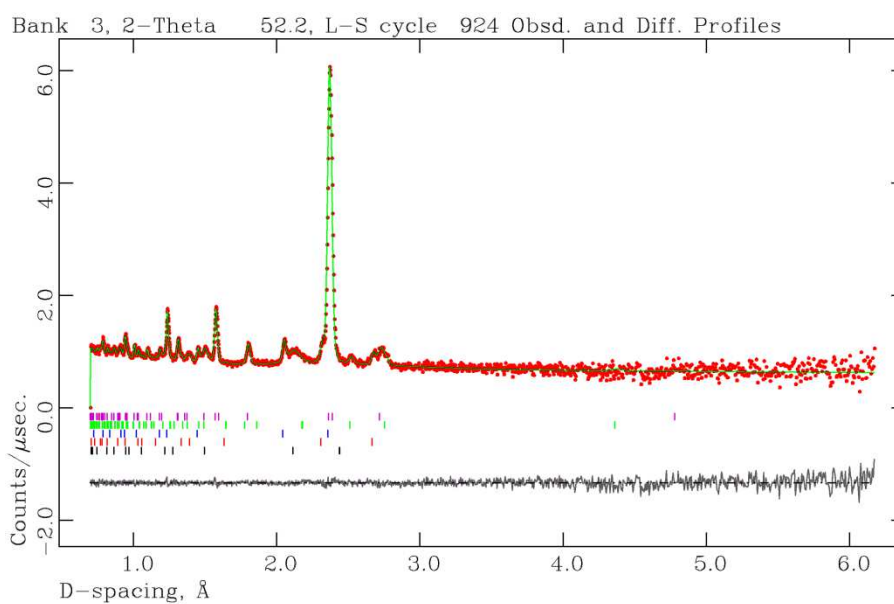


Figure 7-22: Observed, calculated and difference (OCD) plot from the PND Rietveld refinement for Sample 14 (468 K) from PND data, Bank 3 (low angle, 2θ° 40-67). The purple, green, blue, red and black tick marks indicate reflections from Mg(OD)<sub>2</sub>, LiOD, LiD, Li<sub>2</sub>O and MgO respectively.

Table 7-4: Selected data from the PND Rietveld refinement for Sample 15 (478 K).

Empirical Formula	Mg(OD) <sub>2</sub>	LiD	MgO	Li <sub>2</sub> O	LiOD
<b>Crystal System</b>	Trigonal	Cubic	Cubic	Cubic	Tetragonal
<b>Space Group</b>	<i>P</i> -3 <i>m</i> 1	<i>Fm</i> -3 <i>m</i>	<i>Fm</i> -3 <i>m</i>	<i>Fm</i> -3 <i>m</i>	<i>P</i> 4/ <i>nmm</i>
<b>Lattice Parameters</b>					
<i>a</i> / Å	3.1461(1)	4.0984(1)	4.2366(5)	4.6301(3)	3.5606(3)
<i>c</i> / Å	4.7945(3)				4.361(2)
<i>V</i> / Å <sup>3</sup>	41.097(4)	68.842(5)	76.04(3)	99.26(2)	55.30(2)
<i>Z</i>	1	4	4	4	2
<b>Unit Cell Formula</b>					
<b>Weight / M<sub>w</sub></b>	60.331	35.820	161.216	119.524	49.908
<b>Density / g cm<sup>-3</sup></b>	2.438	0.864	3.521	2.000	1.499
<b>Wt. %</b>	35.6(8)	15.1(4)	34.2(8)	10.4(4)	4.8(3)
<b>Temperature / K</b>			478		
<b>No. of Variables</b>			86		
<b>No. of Observations</b>			5813		
<b>Rwp %</b>			2.56		
<b>Rp %</b>			4.68		
<b>χ<sup>2</sup></b>			1.02		

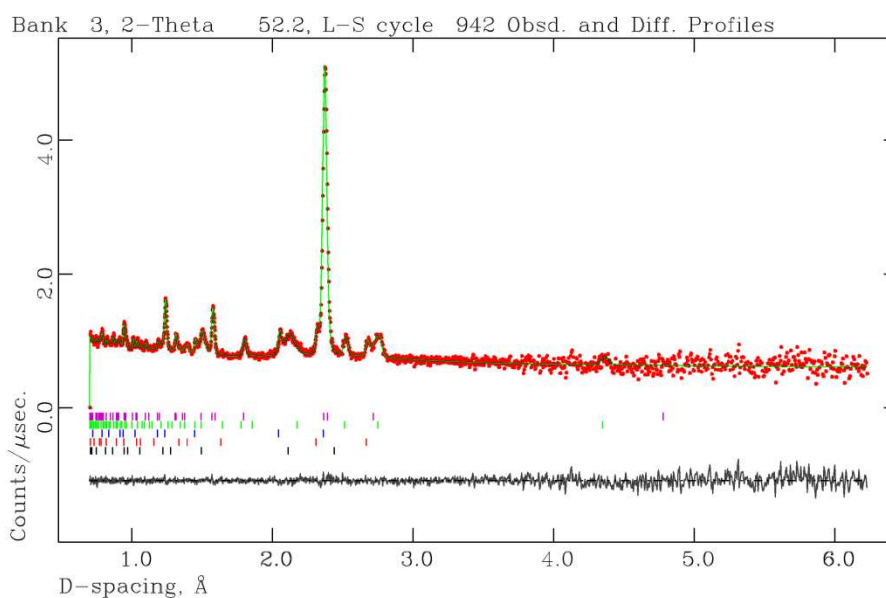


Figure 7-23: Observed, calculated and difference (OCD) plot from the PND Rietveld refinement for Sample 15 (478 K), Bank 3 (low angle, 20° 40-67). The purple, green, blue, red and black tick marks indicate reflections from Mg(OD)<sub>2</sub>, LiOD, LiD, Li<sub>2</sub>O and MgO respectively.

Table 7-5: Selected data from the PND Rietveld refinement for Sample 16 (488 K).

Empirical Formula	Mg(OD) <sub>2</sub>	LiD	MgO	Li <sub>2</sub> O	LiOD
<b>Crystal System</b>	Trigonal	Cubic	Cubic	Cubic	Tetragonal
<b>Space Group</b>	<i>P-3m1</i>	<i>Fm-3m</i>	<i>Fm-3m</i>	<i>Fm-3m</i>	<i>P4/nmm</i>
<b>Lattice Parameters</b>					
<i>a</i> / Å	3.1458(1)	4.1007(1)	4.2352(4)	4.6311(2)	3.5614(2)
<i>c</i> / Å	4.7973(5)				4.361(1)
<i>V</i> / Å <sup>3</sup>	41.113(6)	68.955(6)	75.97(1)	99.32(1)	55.32(1)
<i>Z</i>	1	4	4	4	2
<b>Unit Cell Formula</b>					
<b>Weight / M<sub>w</sub></b>	60.331	35.820	161.216	119.524	49.908
<b>Density / g cm<sup>-3</sup></b>	2.437	0.863	3.524	1.998	1.498
<b>Wt. %</b>	21.4(5)	13.5(4)	44.1(6)	12.3(5)	8.7(4)
<b>Temperature / K</b>			488		
<b>No. of Variables</b>			86		
<b>No. of Observations</b>			5882		
<b>Rwp %</b>			2.57		
<b>Rp %</b>			5.46		
<b>χ<sup>2</sup></b>			0.99		

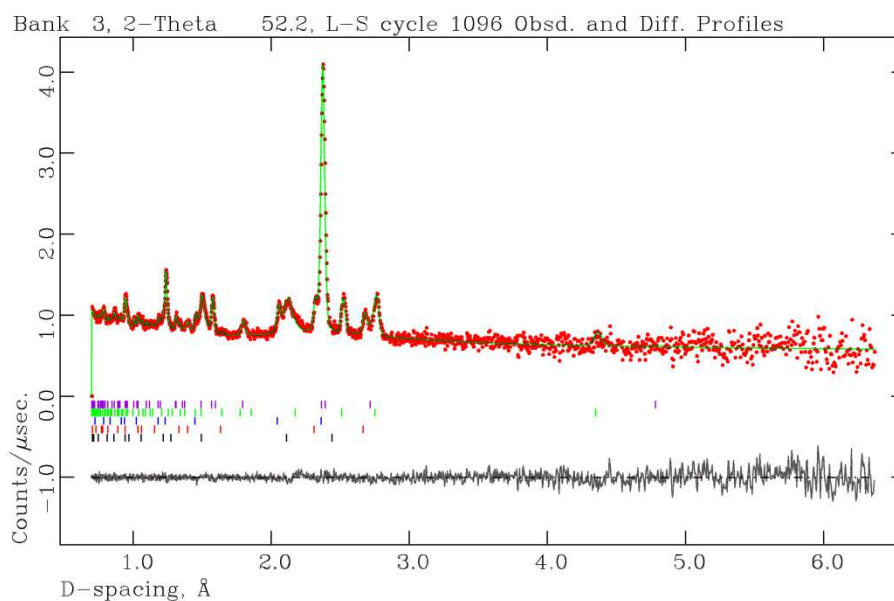


Figure 7-24: Observed, calculated and difference (OCD) plot from the PND Rietveld refinement for Sample 16 (488 K) from PND data, Bank 3 (low angle, 20° 40-67). The purple, green, blue, red and black tick marks indicate reflections from Mg(OD)<sub>2</sub>, LiOD, LiD, Li<sub>2</sub>O and MgO respectively.

Table 7-6: Selected data from the PND Rietveld refinement for Sample 17 (498 K).

Empirical Formula	Mg(OD) <sub>2</sub>	LiD	MgO	Li <sub>2</sub> O	LiOD
<b>Crystal System</b>	Trigonal	Cubic	Cubic	Cubic	Tetragonal
<b>Space Group</b>	<i>P-3m1</i>	<i>Fm-3m</i>	<i>Fm-3m</i>	<i>Fm-3m</i>	<i>P4/nmm</i>
<b>Lattice Parameters</b>					
<i>a</i> / Å	3.1445(3)	4.1025(1)	4.2349(3)	4.6314(2)	3.5618(2)
<i>c</i> / Å	4.794(1)				4.3617(9)
<i>V</i> / Å <sup>3</sup>	41.05(1)	69.045(7)	75.95(2)	99.35(2)	55.33(1)
<i>Z</i>	1	4	4	4	2
<b>Unit Cell Formula</b>					
Weight / M <sub>w</sub>	60.331	35.820	161.216	119.524	49.908
Density / g cm <sup>-3</sup>	2.441	0.861	3.525	1.998	1.498
Wt. %	9.8(4)	12.6(4)	52.7(8)	13.4(5)	11.5(5)
<b>Temperature / K</b>			498		
<b>No. of Variables</b>			74		
<b>No. of Observations</b>			5980		
<b>Rwp %</b>			2.70		
<b>Rp %</b>			6.46		
<b>χ<sup>2</sup></b>			1.04		

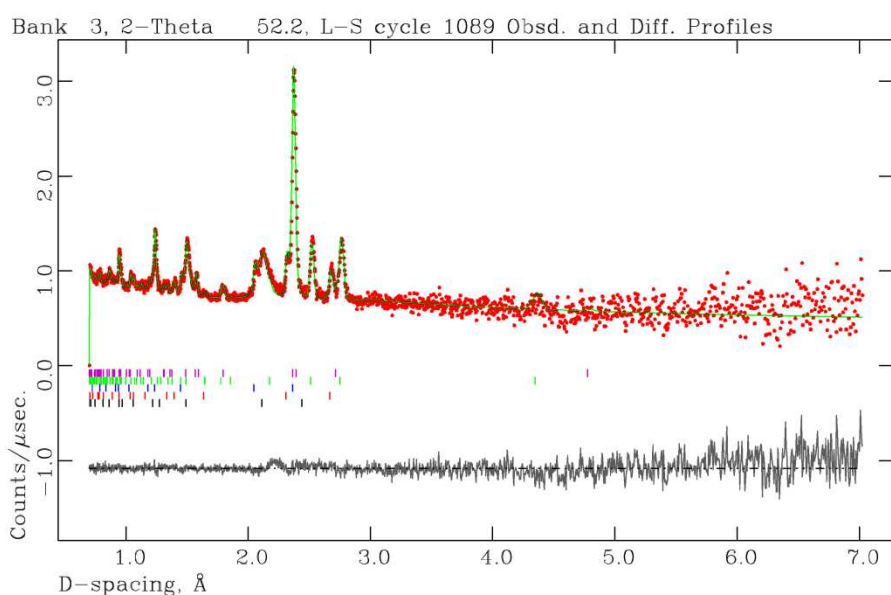


Figure 7-25: Observed, calculated and difference (OCD) plot from the PND Rietveld refinement for Sample 17 (498 K) from PND data, Bank 3 (low angle, 20° 40-67). The purple, green, blue, red and black tick marks indicate reflections from Mg(OD)<sub>2</sub>, LiOD, LiD, Li<sub>2</sub>O and MgO respectively.

Table 7-7: Selected data from the PND Rietveld refinement for Sample 18 (508 K).

Empirical Formula	LiD	MgO	Li <sub>2</sub> O	LiOD
<b>Crystal System</b>	Cubic	Cubic	Cubic	Tetragonal
<b>Space Group</b>	<i>Fm-3m</i>	<i>Fm-3m</i>	<i>Fm-3m</i>	<i>P4/nmm</i>
<b>Lattice Parameters</b>				
<i>a</i> / Å	4.1050(2)	4.2346(3)	4.6328(2)	3.5635(2)
<i>c</i> / Å				4.3649(8)
<i>V</i> / Å <sup>3</sup>	69.174(8)	75.94(2)	99.43(1)	55.43(1)
<i>Z</i>	4	4	4	2
<b>Unit Cell Formula</b>				
Weight / M <sub>w</sub>	35.820	161.216	119.524	49.908
Density / g cm <sup>-3</sup>	0.860	3.525	1.996	1.495
Wt. %	11.8(4)	59.9(9)	15.9(7)	12.4(6)
<b>Temperature / K</b>			508	
<b>No. of Variables</b>			79	
<b>No. of Observations</b>			5883	
<b>Rwp %</b>			2.66	
<b>Rp %</b>			5.08	
<b>χ<sup>2</sup></b>			1.08	

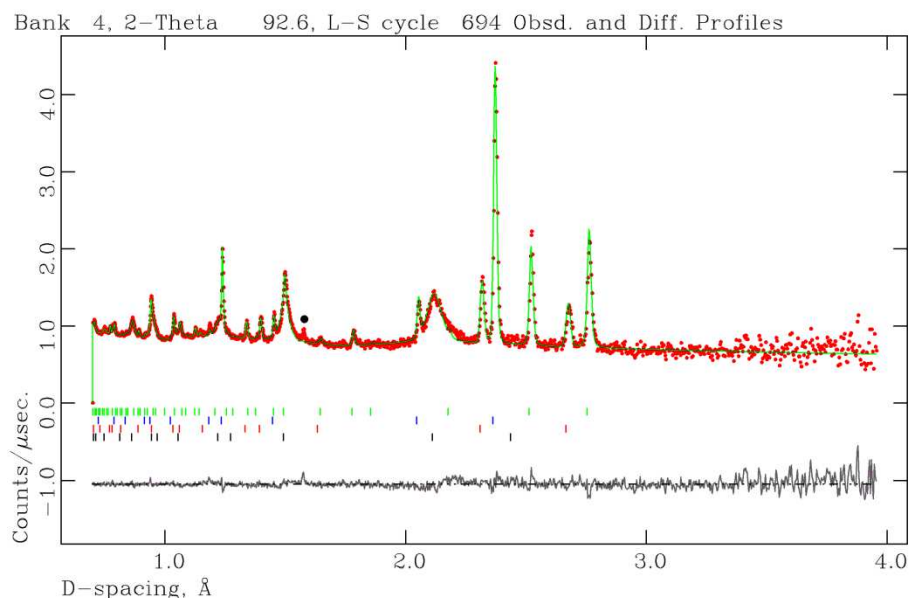


Figure 7-26: Observed, calculated and difference (OCD) plot from the PND Rietveld refinement for Sample 18 (508 K) from PND data, Bank 4 (90 degrees, 20° 75-113). The green, blue, red and black tick marks indicate reflections from LiOD, LiD, Li<sub>2</sub>O and MgO respectively. The black circle indicates the presence of Mg(OD)<sub>2</sub>.

Table 7-8: Selected data from the PND Rietveld refinement for Sample 19 (518 K).

Empirical Formula	LiD	MgO	Li <sub>2</sub> O	LiOD
<b>Crystal System</b>	Cubic	Cubic	Cubic	Tetragonal
<b>Space Group</b>	<i>Fm-3m</i>	<i>Fm-3m</i>	<i>Fm-3m</i>	<i>P4/nmm</i>
<b>Lattice Parameters</b>				
<i>a</i> / Å	4.1073(2)	4.2344(3)	4.6338(2)	3.5649(2)
<i>c</i> / Å				4.3652(8)
<i>V</i> / Å <sup>3</sup>	69.29(1)	75.92(2)	99.50(1)	55.47(1)
<i>Z</i>	4	4	4	2
<b>Unit Cell Formula</b>				
Weight / M <sub>w</sub>	35.820	161.216	119.524	49.908
Density / g cm <sup>-3</sup>	0.858	3.526	1.995	1.494
Wt. %	9.8(2)	58.8(4)	18.2(3)	13.2(3)
<b>Temperature / K</b>			518	
<b>No. of Variables</b>			74	
<b>No. of Observations</b>			5934	
<b>Rwp %</b>			2.64	
<b>Rp %</b>			5.37	
<b>χ<sup>2</sup></b>			1.02	

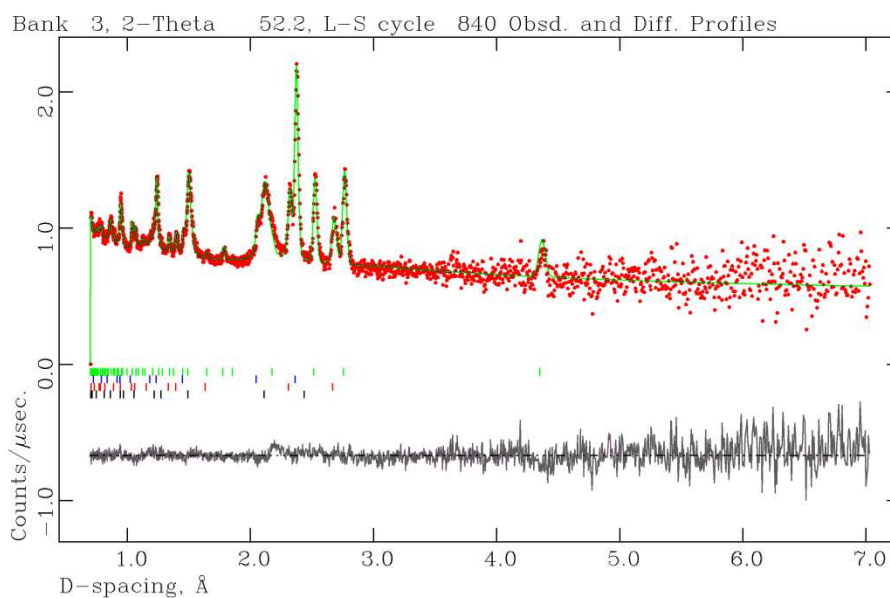


Figure 7-27: Observed, calculated and difference (OCD) plot from the PND Rietveld refinement for Sample 19 (518 K) from PND data, Bank 3 (low angle, 20° 40-67). The green, blue, red and black tick marks indicate reflections from LiOD, LiD, Li<sub>2</sub>O and MgO respectively.

Table 7-9: Selected data from the PND Rietveld refinement for Sample 21 (528 K).

Empirical Formula	LiD	MgO	Li <sub>2</sub> O	LiOD
<b>Crystal System</b>	Cubic	Cubic	Cubic	Tetragonal
<b>Space Group</b>	<i>Fm-3m</i>	<i>Fm-3m</i>	<i>Fm-3m</i>	<i>P4/nmm</i>
<b>Lattice Parameters</b>				
<i>a</i> / Å	4.1092(2)	4.2329(3)	4.6346(2)	3.5656(2)
<i>c</i> / Å				4.3674(8)
<i>V</i> / Å <sup>3</sup>	69.39(1)	75.84(1)	99.55(1)	55.52(1)
<i>Z</i>	4	4	4	2
<b>Unit Cell Formula</b>				
Weight / M <sub>w</sub>	35.820	161.216	119.524	49.908
Density / g cm <sup>-3</sup>	0.857	3.530	1.994	1.493
Wt. %	8.9(3)	59.8(6)	20.9(6)	10.4(4)
<b>Temperature / K</b>			528	
<b>No. of Variables</b>			62	
<b>No. of Observations</b>			5696	
<b>Rwp %</b>			2.70	
<b>Rp %</b>			4.47	
<b>χ<sup>2</sup></b>			1.07	

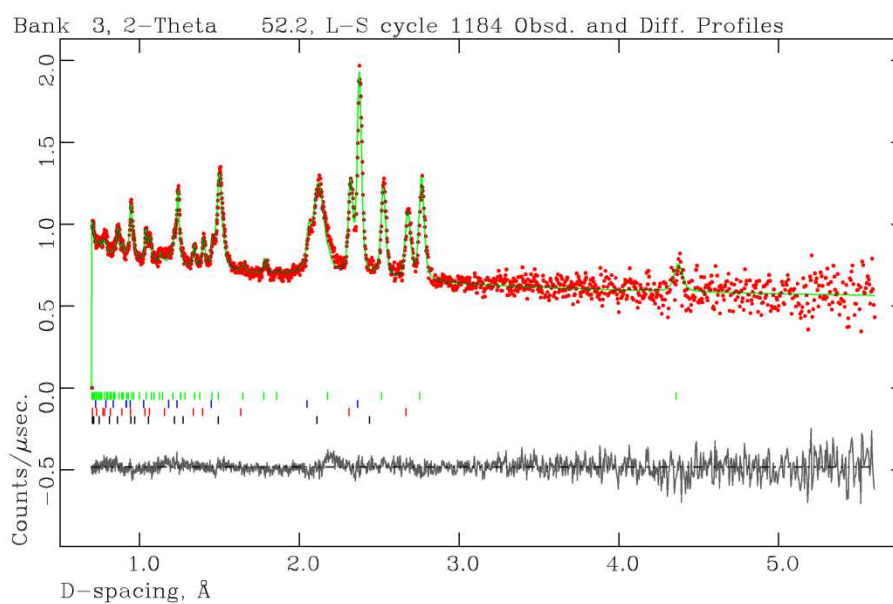


Figure 7-28: Observed, calculated and difference (OCD) plot from the PND Rietveld refinement for Sample 21 (528 K) from PND data, Bank 3 (low angle, 2θ° 40-67). The green, blue, red and black tick marks indicate reflections from LiOD, LiD, Li<sub>2</sub>O and MgO respectively.

Table 7-10: Selected data from the PND Rietveld refinement for Sample 22 (538 K).

Empirical Formula	LiD	MgO	Li <sub>2</sub> O	LiOD
<b>Crystal System</b>	Cubic	Cubic	Cubic	Tetragonal
<b>Space Group</b>	<i>Fm-3m</i>	<i>Fm-3m</i>	<i>Fm-3m</i>	<i>P4/nmm</i>
<b>Lattice Parameters</b>				
<i>a</i> / Å	4.1116(2)	4.2328(3)	4.6360(2)	3.5670(3)
<i>c</i> / Å				4.369(1)
<i>V</i> / Å <sup>3</sup>	69.51(1)	75.84(1)	99.64(1)	55.59(1)
<i>Z</i>	4	4	4	2
<b>Unit Cell Formula</b>				
Weight / M <sub>w</sub>	35.820	161.216	119.524	49.908
Density / g cm <sup>-3</sup>	0.856	3.530	1.992	1.491
Wt. %	8.2(3)	60.6(7)	22.3(7)	8.9(4)
<b>Temperature / K</b>			538	
<b>No. of Variables</b>			65	
<b>No. of Observations</b>			5815	
<b>Rwp %</b>			2.67	
<b>Rp %</b>			4.83	
<b>χ<sup>2</sup></b>			1.06	

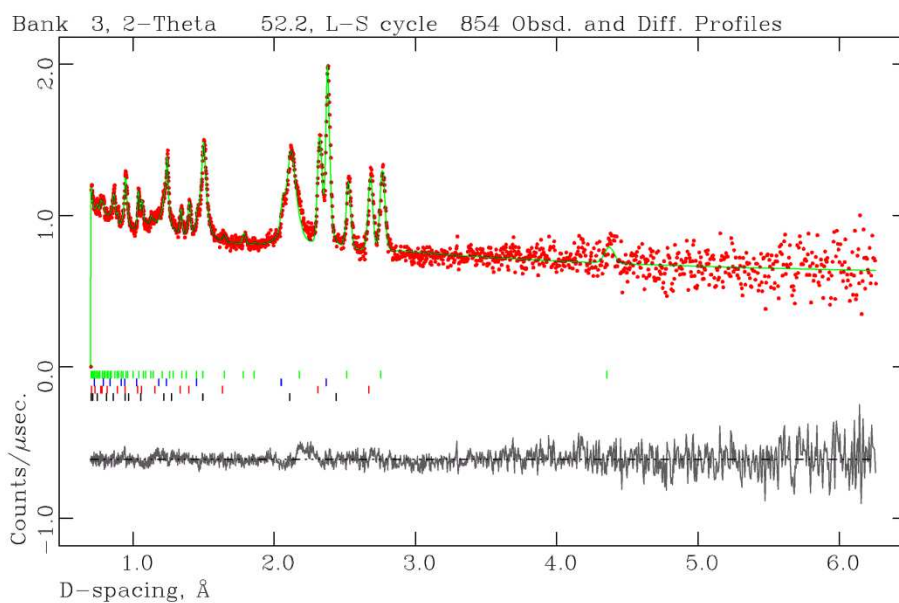


Figure 7-29: Observed, calculated and difference (OCD) plot from the PND Rietveld refinement for Sample 22 (538 K) from PND data, Bank 3 (low angle, 2θ 40-67). The green, blue, red and black tick marks indicate reflections from LiOD, LiD, Li<sub>2</sub>O and MgO respectively.

Table 7-11: Selected data from the PND Rietveld refinement for Sample 23 (548 K).

Empirical Formula	LiD	MgO	Li <sub>2</sub> O	LiOD
<b>Crystal System</b>	Cubic	Cubic	Cubic	Tetragonal
<b>Space Group</b>	<i>Fm-3m</i>	<i>Fm-3m</i>	<i>Fm-3m</i>	<i>P4/nmm</i>
<b>Lattice Parameters</b>				
<i>a</i> / Å	4.1134(2)	4.2321(3)	4.6366(2)	3.5676(3)
<i>c</i> / Å				4.369(1)
<i>V</i> / Å <sup>3</sup>	69.87(1)	76.14(1)	100.03(1)	55.60(2)
<i>Z</i>	4	4	4	2
<b>Unit Cell Formula</b>				
Weight / M <sub>w</sub>	35.820	161.216	119.524	49.908
Density / g cm <sup>-3</sup>	0.855	3.532	1.991	1.490
Wt. %	6.6(4)	60.3(6)	26.1(5)	7.0(3)
<b>Temperature / K</b>			548	
<b>No. of Variables</b>			63	
<b>No. of Observations</b>			5728	
<b>Rwp %</b>			2.70	
<b>Rp %</b>			4.68	
<b>χ<sup>2</sup></b>			1.01	

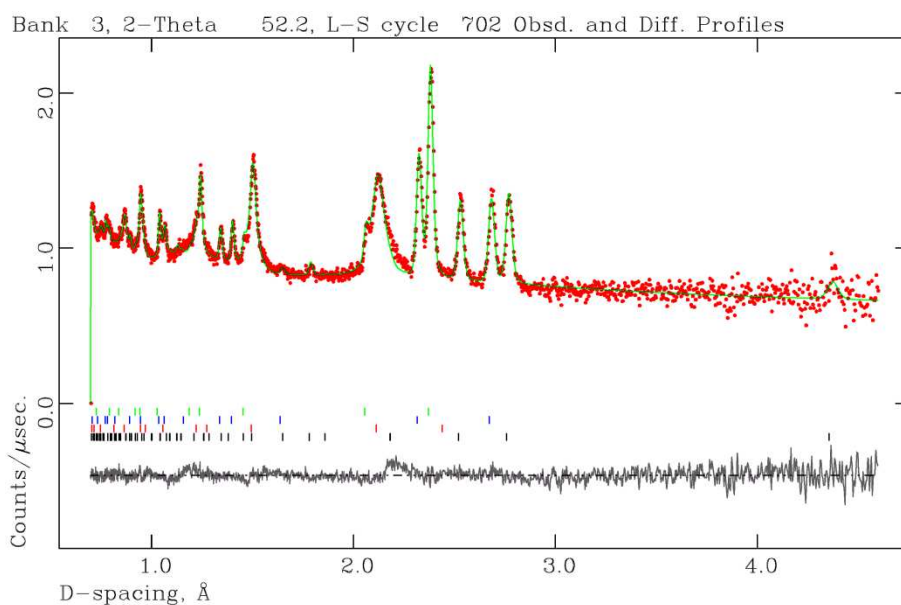


Figure 7-30: Observed, calculated and difference (OCD) plot from the PND Rietveld refinement for Sample 23 (548 K) from PND data, Bank 3 (low angle, 2θ° 40-67). The green, blue, red and black tick marks indicate reflections from LiD, Li<sub>2</sub>O, MgO and LiOD respectively.

### 7.3 Appendix C: Figures for Chapter 5

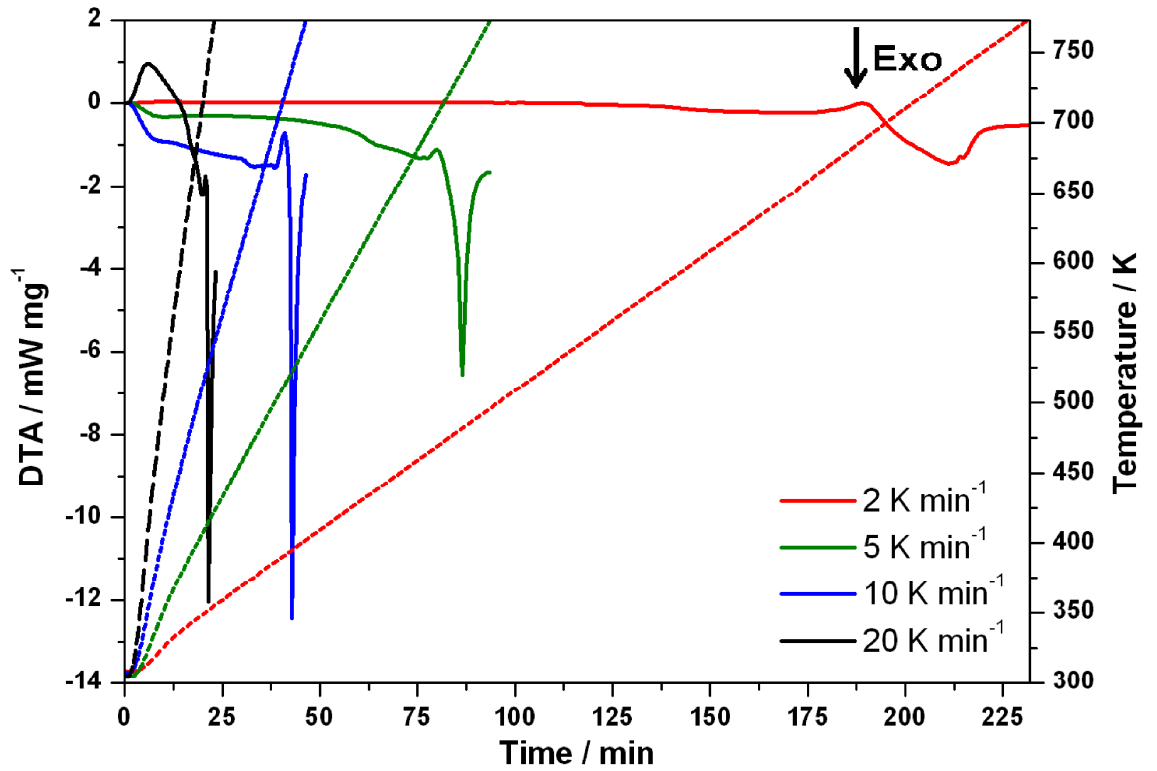


Figure 7-31: DTA profiles used to obtain Kissinger plots for Sample 20 (bulk LiOH – MgH<sub>2</sub> system). Dashed and full lines indicate temperature and DTA profiles respectively.

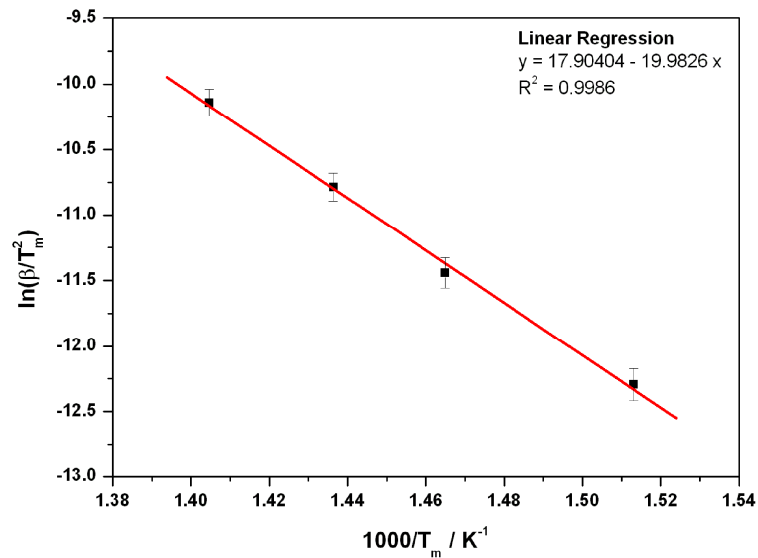


Figure 7-32: Kissinger plot for the LT thermal event for Sample 20 (bulk LiOH – MgH<sub>2</sub> system).

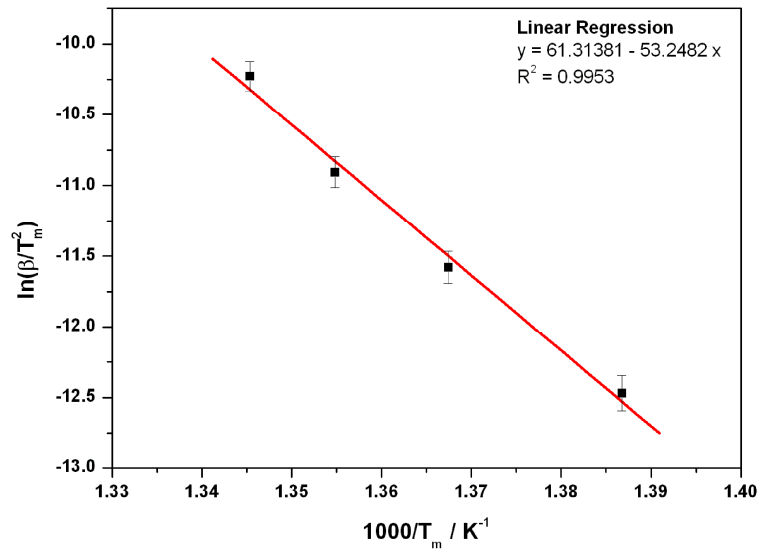


Figure 7-33: Kissinger plot for the HT thermal event for Sample 20 (bulk LiOH – MgH<sub>2</sub> system).

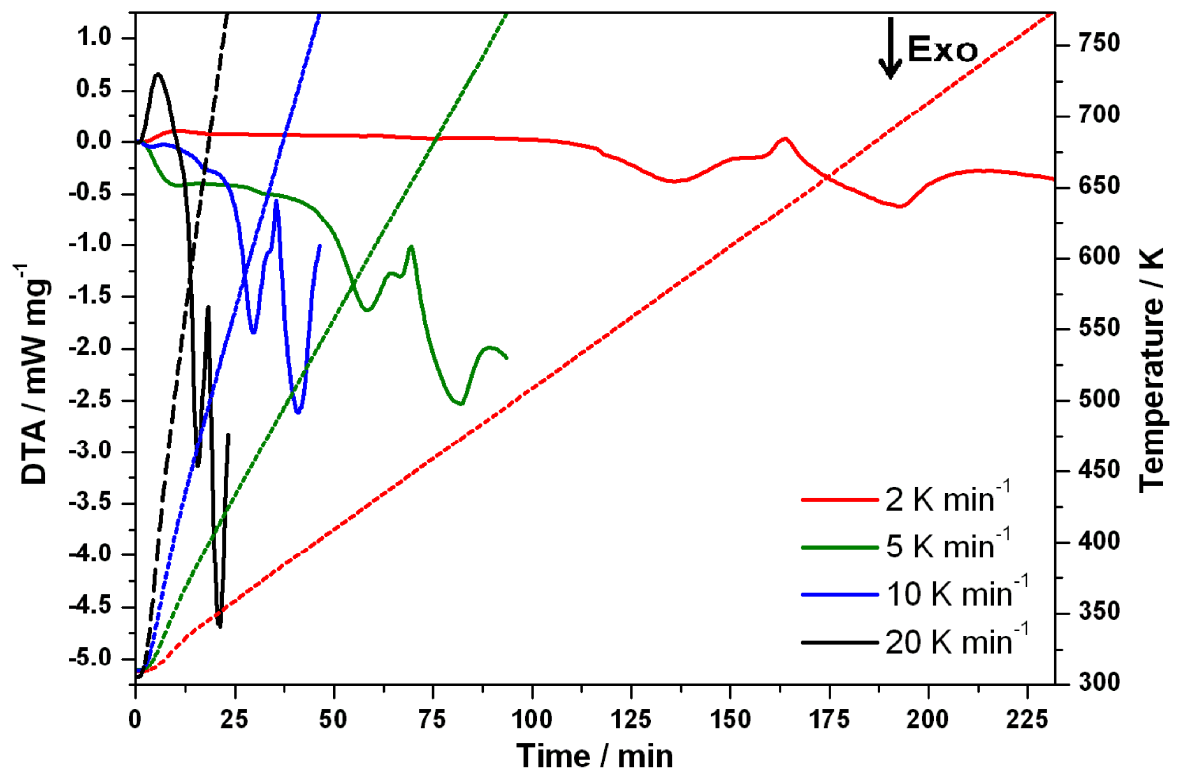


Figure 7-34: DTA profiles used to obtain Kissinger plots for Sample 21 (milled LiOH – MgH<sub>2</sub> system). Dashed and full lines indicate temperature and DTA profiles respectively.

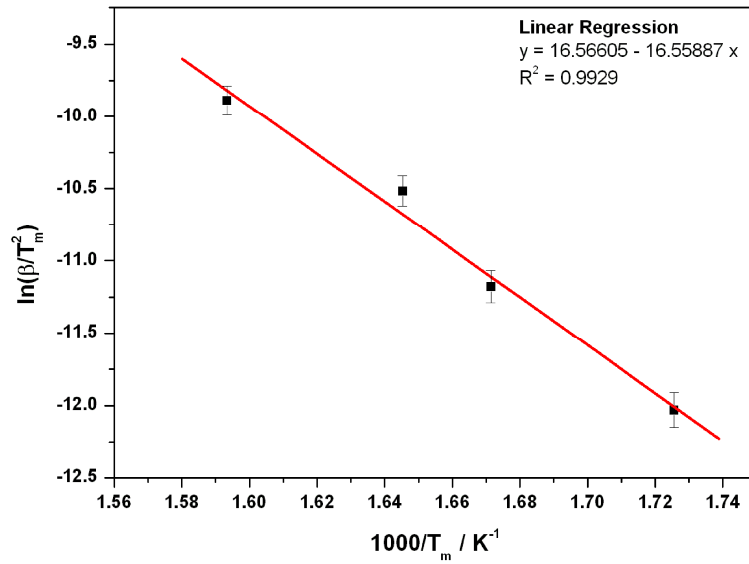


Figure 7-35: Kissinger plot for the LT thermal event for Sample 21 (milled LiOH – MgH<sub>2</sub> system).

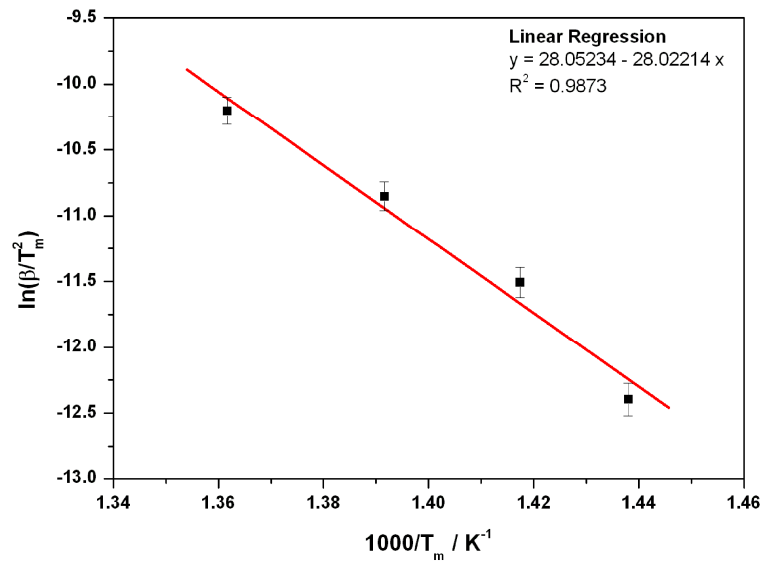


Figure 7-36: Kissinger plot for the HT thermal event for Sample 21 (milled LiOH – MgH<sub>2</sub> system).

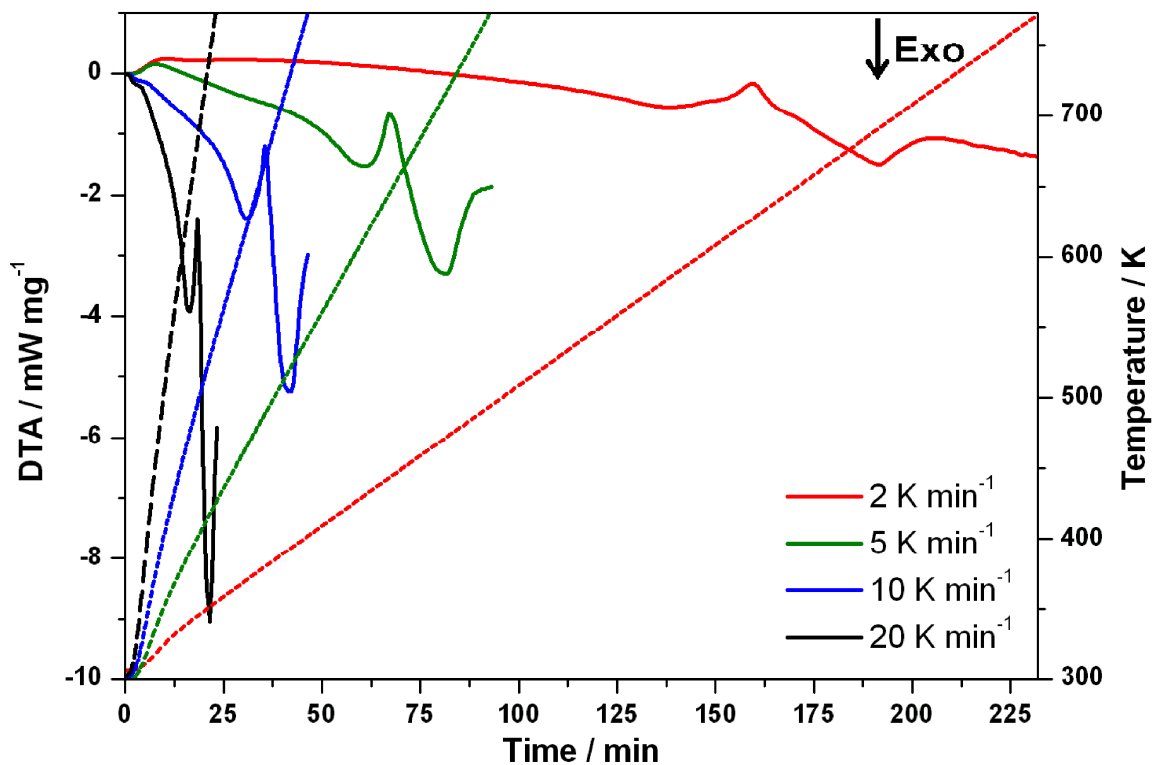


Figure 7-37: DTA profiles used to obtain Kissinger plots for Sample 22 (nano LiOH – MgH<sub>2</sub> system). Dashed and full lines indicate temperature and DTA profiles respectively.

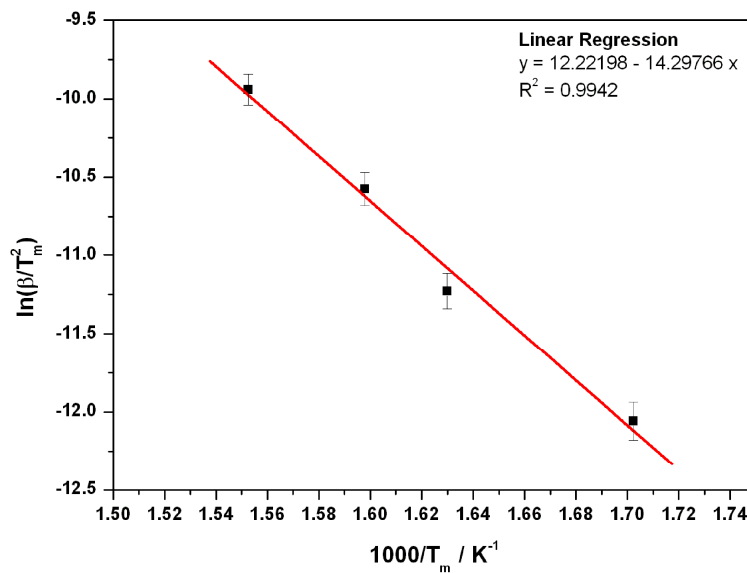


Figure 7-38: Kissinger plot for the LT thermal event for Sample 22 (nano LiOH – MgH<sub>2</sub> system).

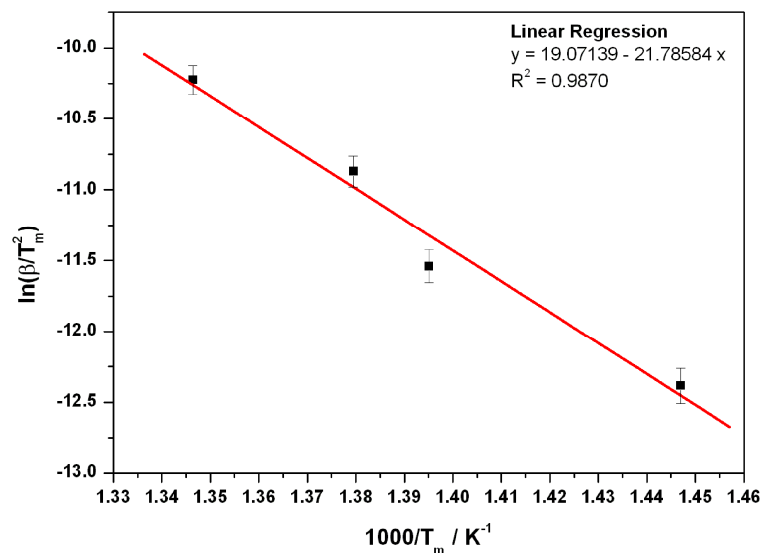


Figure 7-39: Kissinger plot for the HT thermal event for Sample 22 (nano LiOH – MgH<sub>2</sub> system).

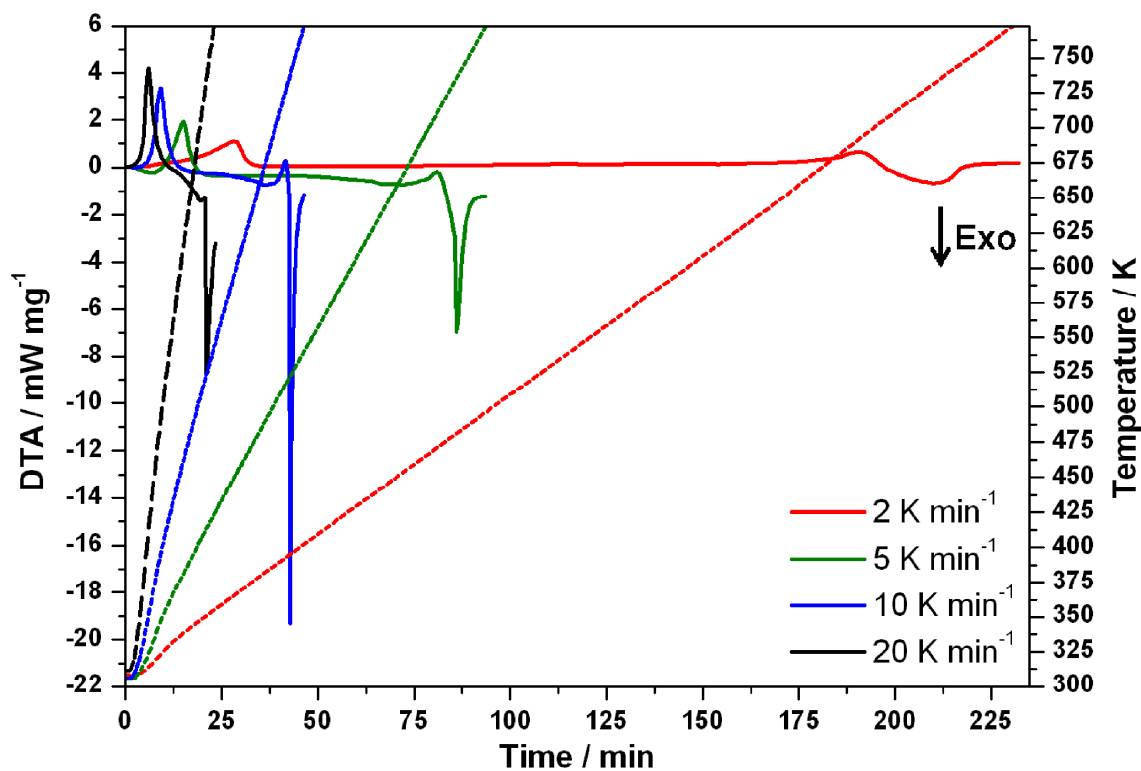


Figure 7-40: DTA profiles used to obtain Kissinger plots for Sample 40 (bulk LiOH·H<sub>2</sub>O – MgH<sub>2</sub> system). Dashed and full lines indicate temperature and DTA profiles respectively.

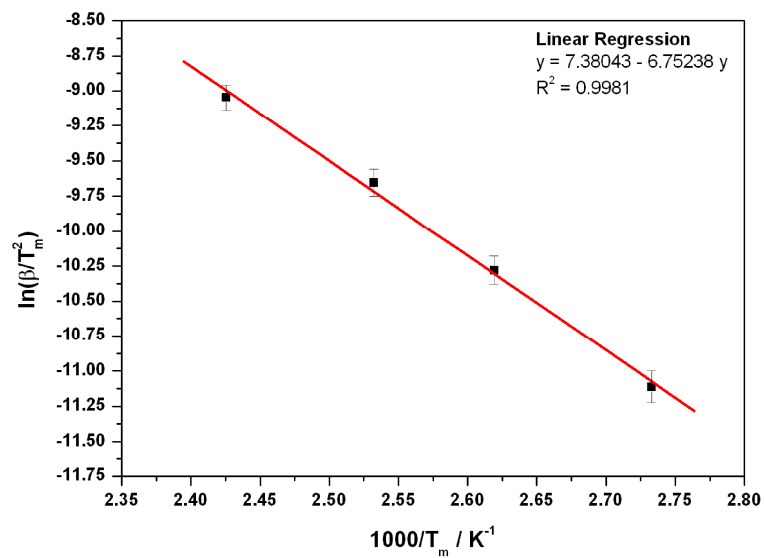


Figure 7-41: Kissinger plot for the thermal event 1 for Sample 40 (bulk  $\text{LiOH}\cdot\text{H}_2\text{O} - \text{MgH}_2$  system).

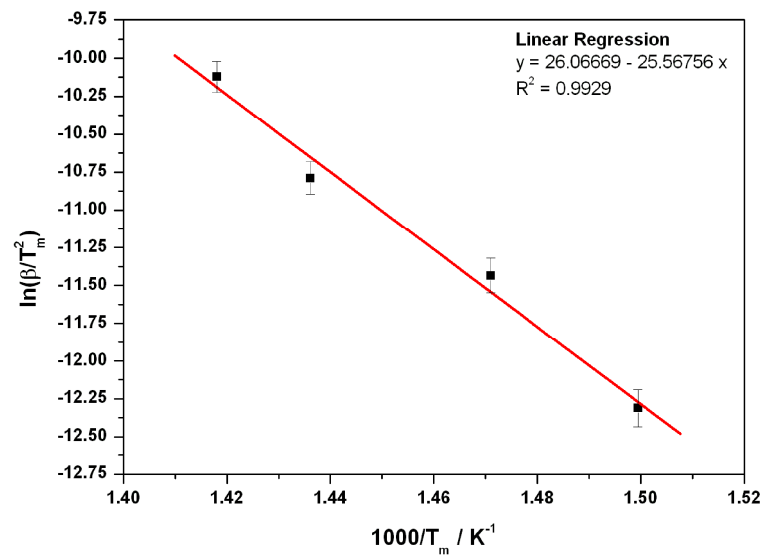


Figure 7-42: Kissinger plot for the thermal event 2 for Sample 40 (bulk  $\text{LiOH}\cdot\text{H}_2\text{O} - \text{MgH}_2$  system).

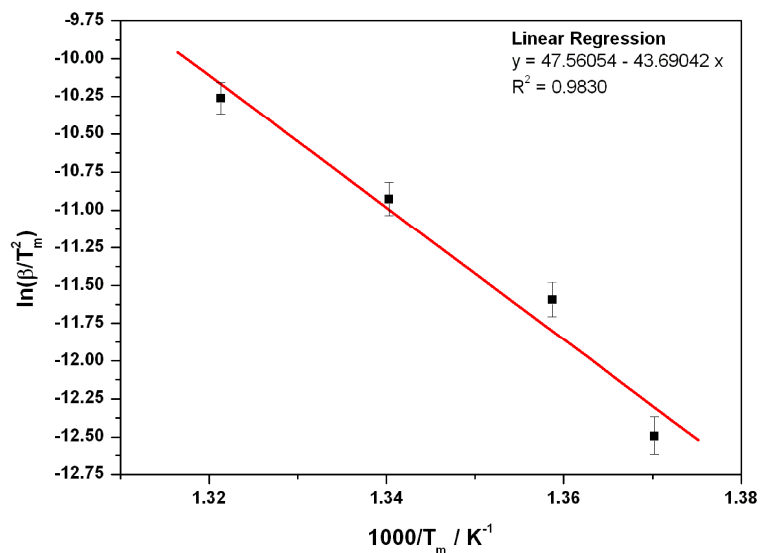


Figure 7-43: Kissinger plot for the thermal event 3 for Sample 40 (bulk  $\text{LiOH}\cdot\text{H}_2\text{O} - \text{MgH}_2$  system).

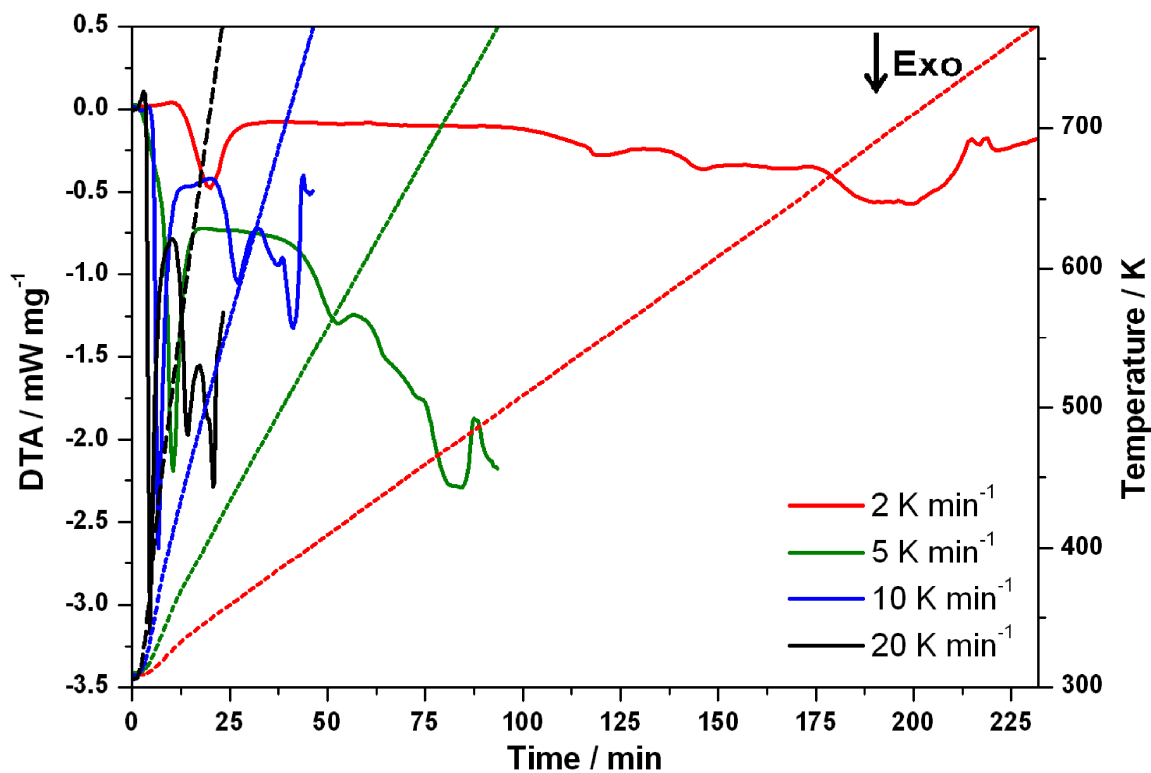


Figure 7-44: DTA profiles used to obtain Kissinger plots for Sample 41 (milled  $\text{LiOH}\cdot\text{H}_2\text{O} - \text{MgH}_2$  system). Dashed and full lines indicate temperature and DTA profiles respectively.

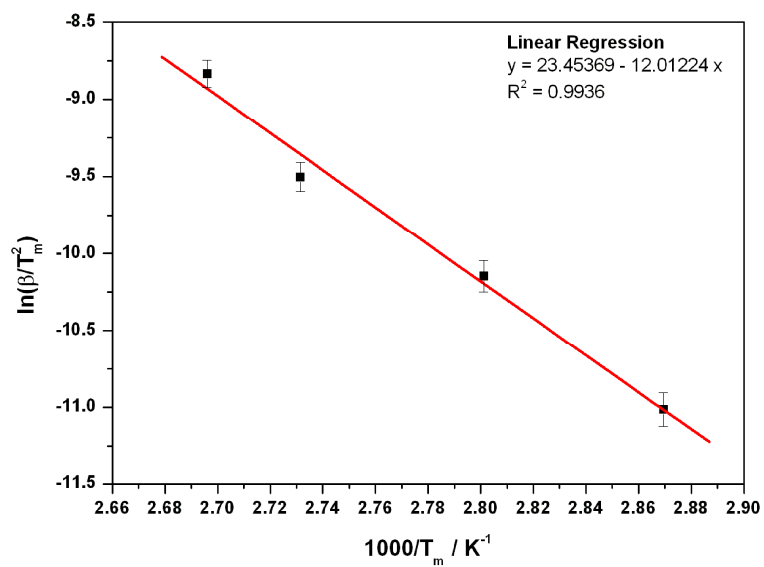


Figure 7-45: Kissinger plot for the thermal event 1 for Sample 41 (milled LiOH·H<sub>2</sub>O – MgH<sub>2</sub> system).

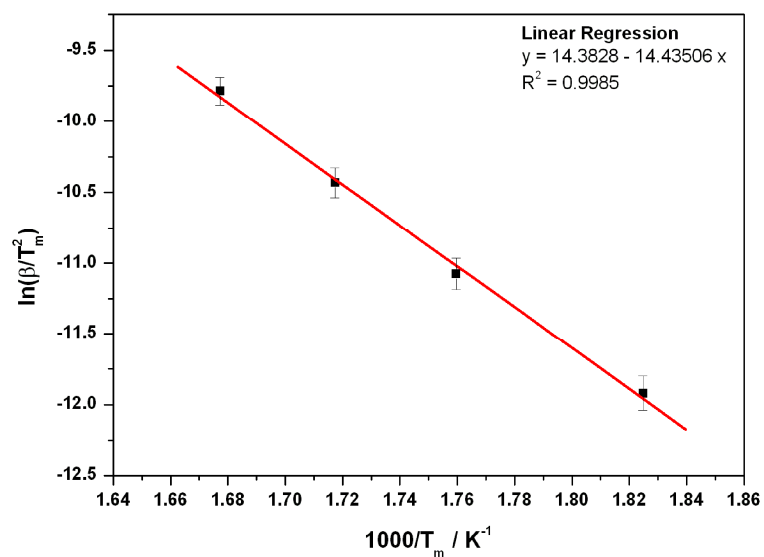


Figure 7-46: Kissinger plot for the thermal event 2 for Sample 41 (milled LiOH·H<sub>2</sub>O – MgH<sub>2</sub> system).

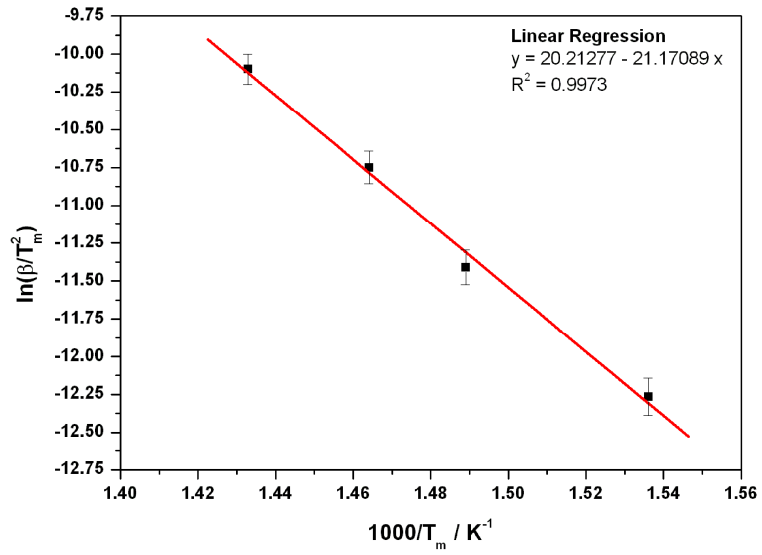


Figure 7-47: Kissinger plot for the thermal event 3 for Sample 41 (milled LiOH·H<sub>2</sub>O – MgH<sub>2</sub> system).

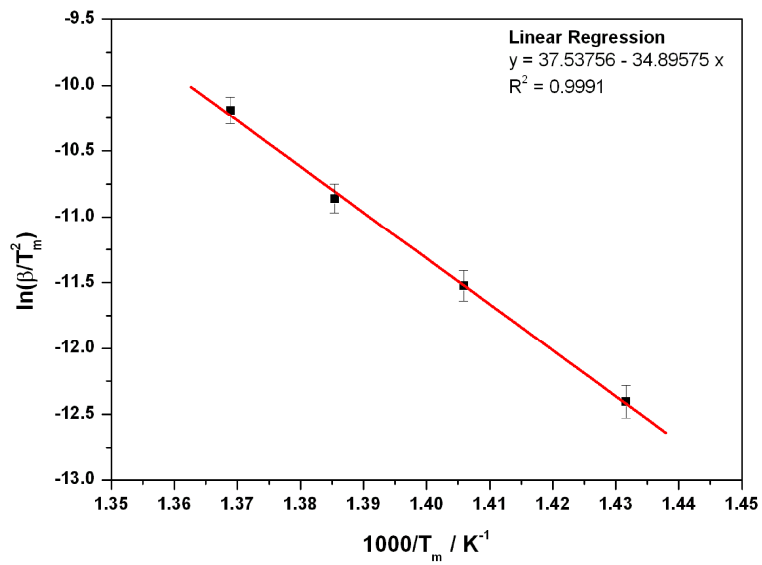


Figure 7-48: Kissinger plot for the thermal event 4 for Sample 41 (milled LiOH·H<sub>2</sub>O – MgH<sub>2</sub> system).

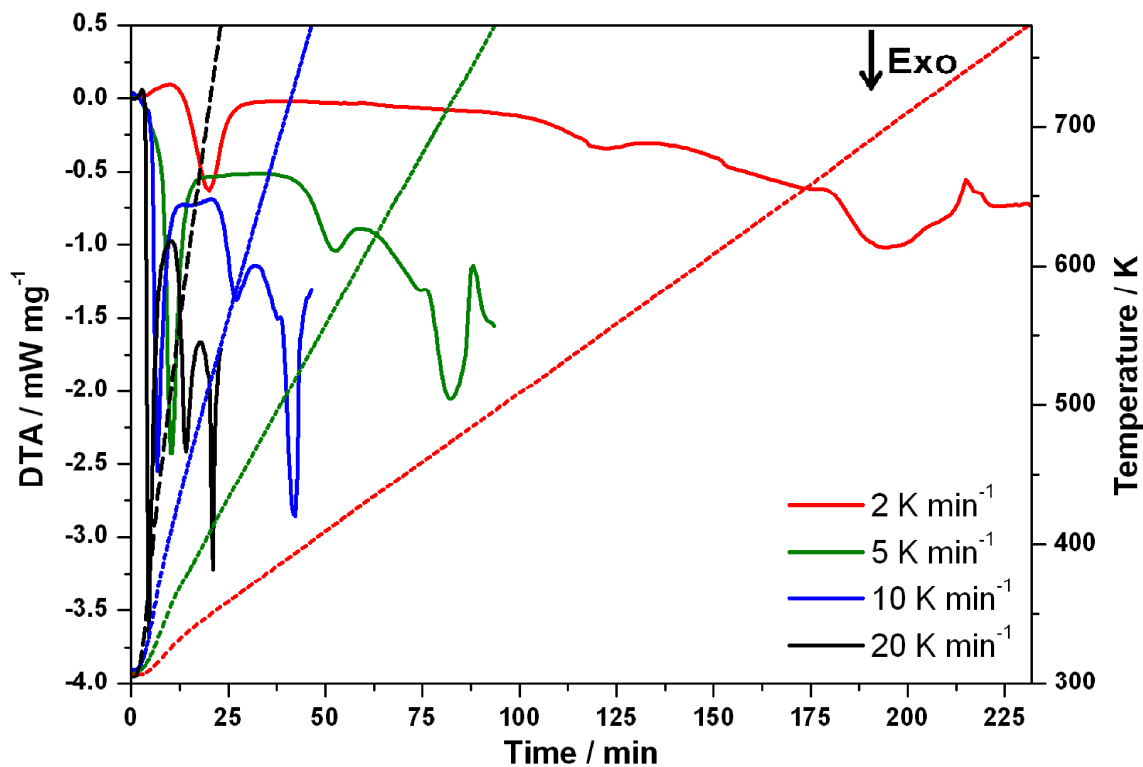


Figure 7-49: DTA profiles used to obtain Kissinger plots for Sample 42 (nano LiOH·H<sub>2</sub>O – MgH<sub>2</sub> system). Dashed and full lines indicate temperature and DTA profiles respectively.

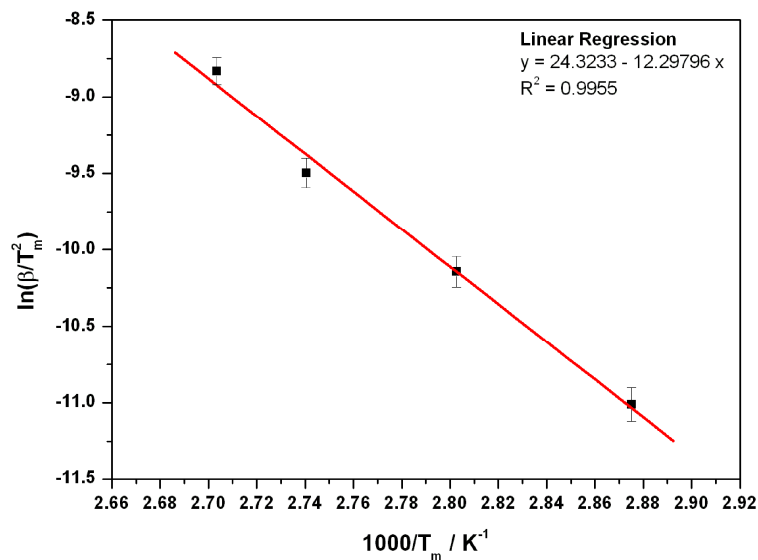


Figure 7-50: Kissinger plot for the thermal event 1 for Sample 42 (nano LiOH·H<sub>2</sub>O – MgH<sub>2</sub> system).

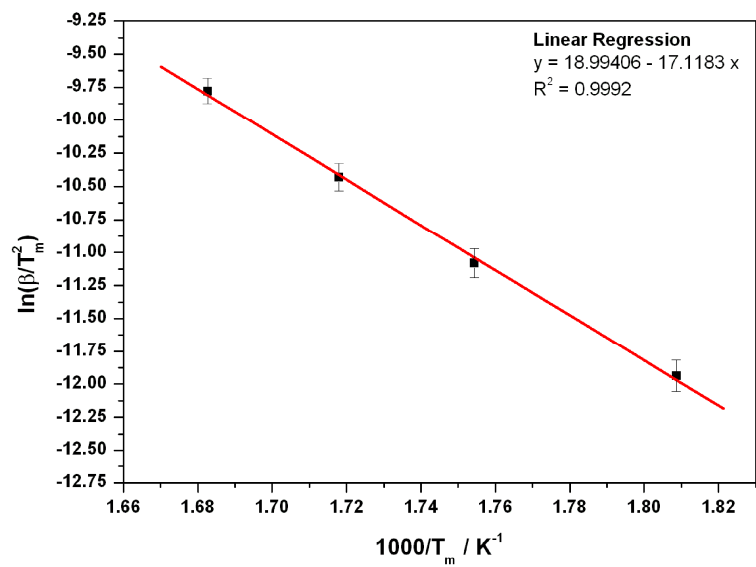


Figure 7-51: Kissinger plot for the thermal event 2 for Sample 42 (nano LiOH·H<sub>2</sub>O – MgH<sub>2</sub> system).

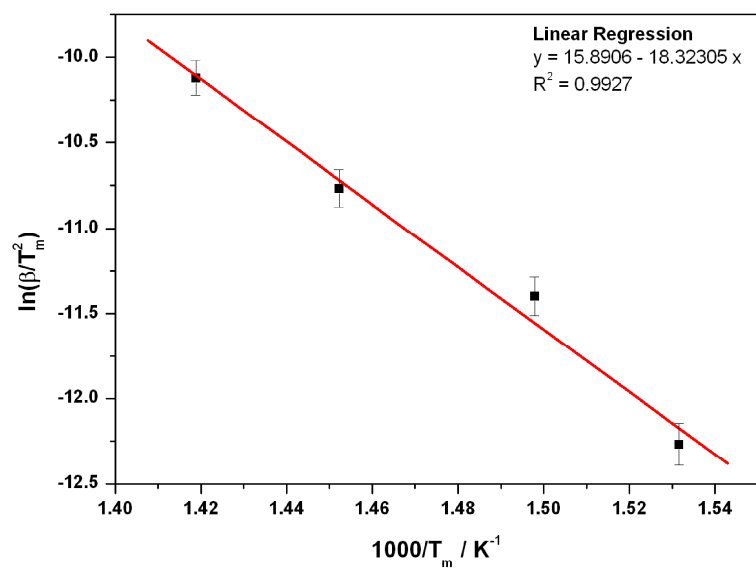


Figure 7-52: Kissinger plot for the thermal event 3 for Sample 42 (nano LiOH·H<sub>2</sub>O – MgH<sub>2</sub> system).

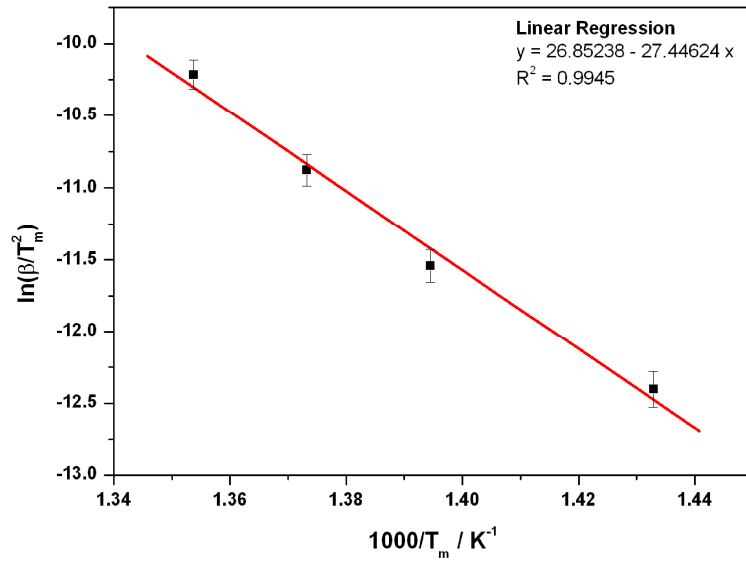


Figure 7-53: Kissinger plot for the thermal event 4 for Sample 42 (nano LiOH·H<sub>2</sub>O – MgH<sub>2</sub> system).

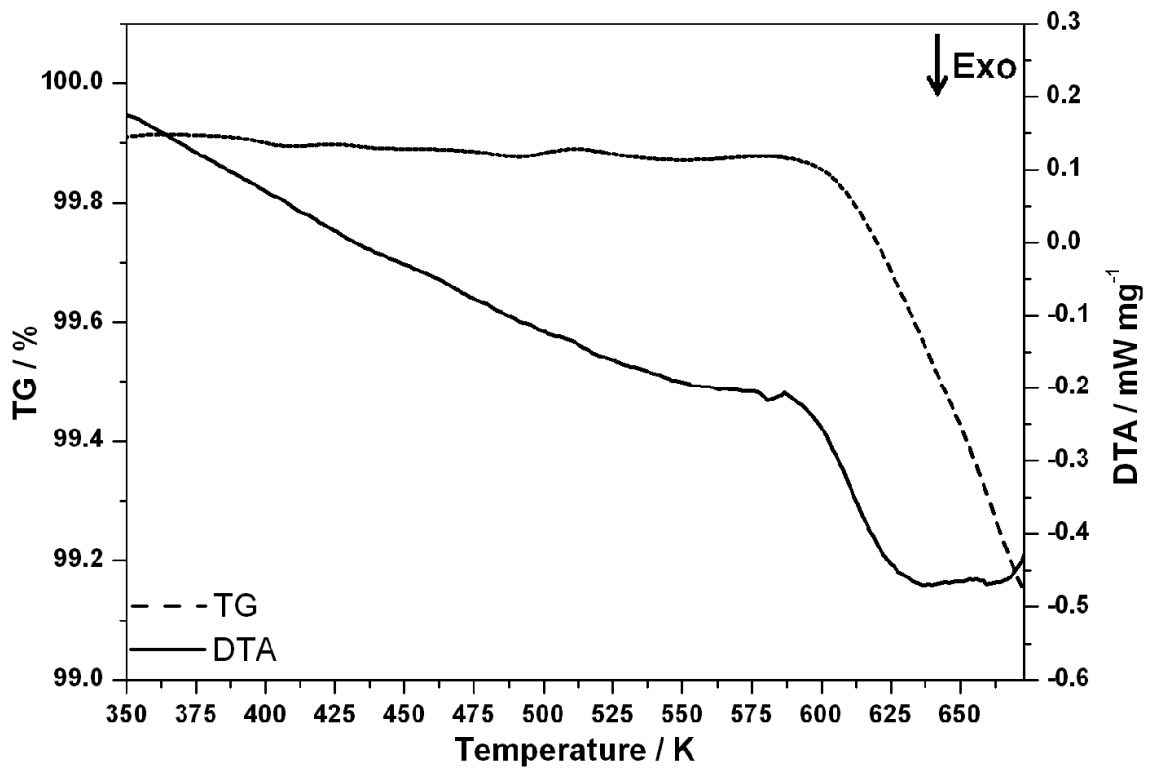


Figure 7-54: TG (dashed line) and DTA (full line) data obtained for Sample 8.

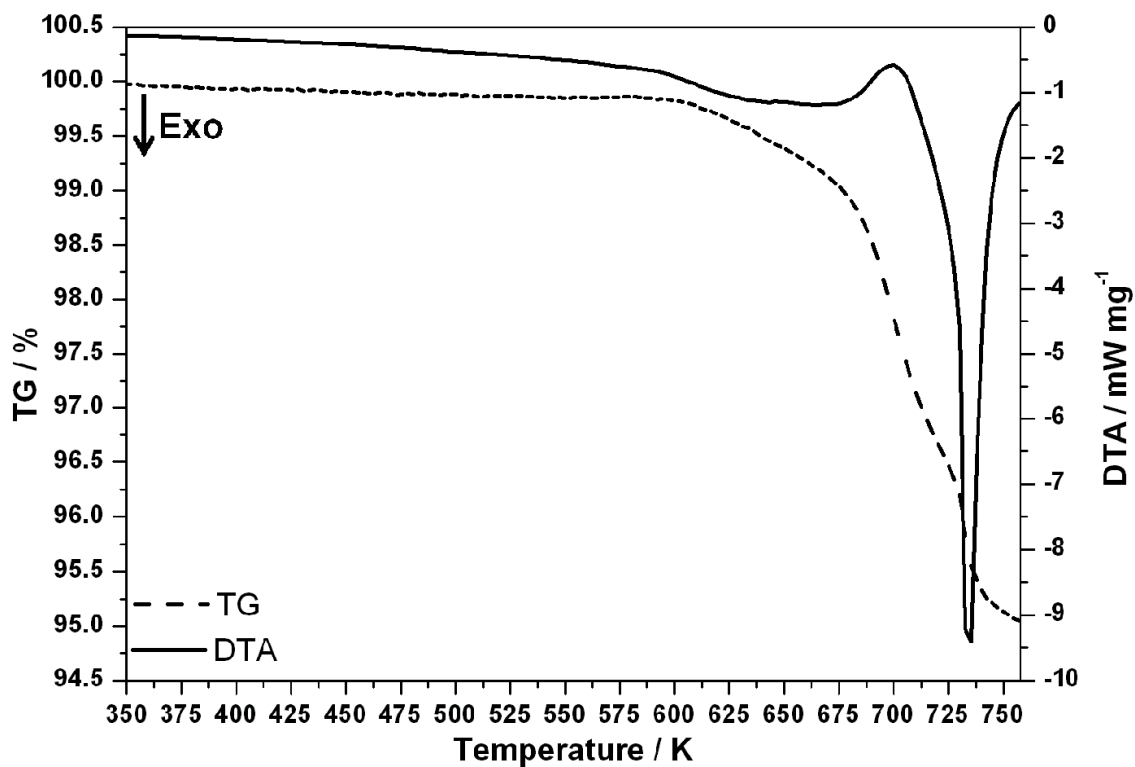


Figure 7-55: TG (dashed line) and DTA (full line) data obtained for Sample 9.

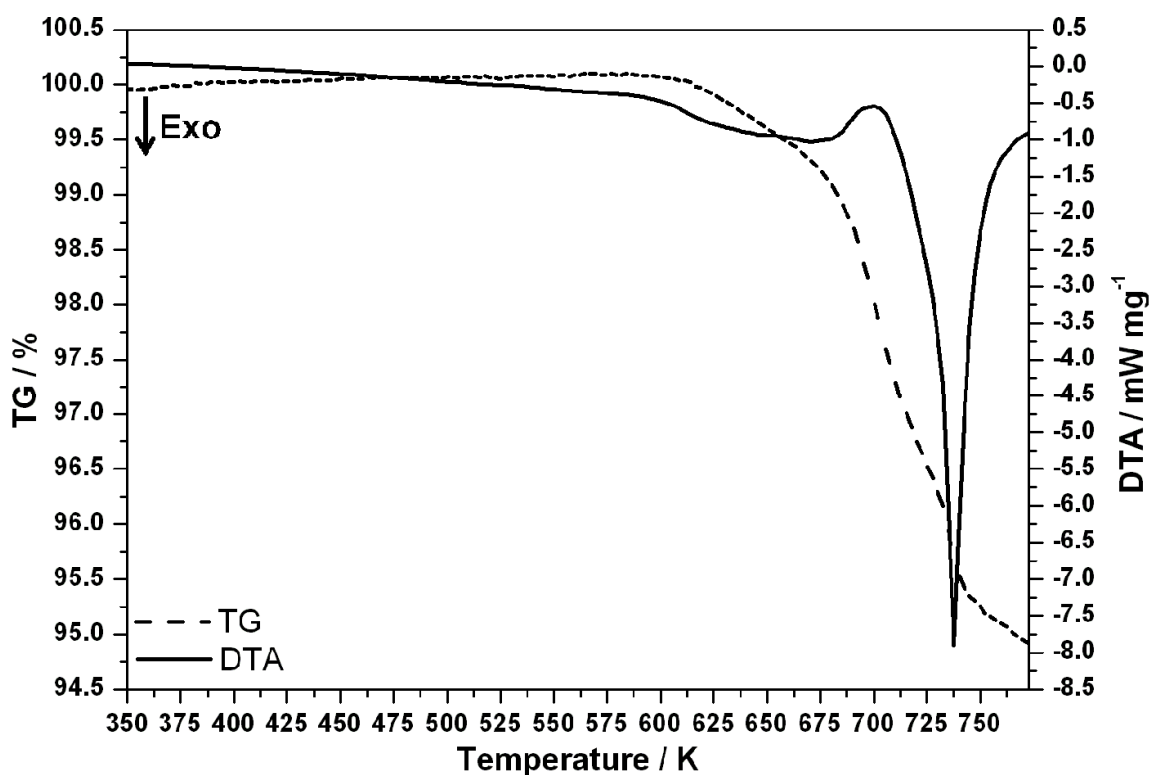


Figure 7-56: TG (dashed line) and DTA (full line) data obtained for Sample 10.

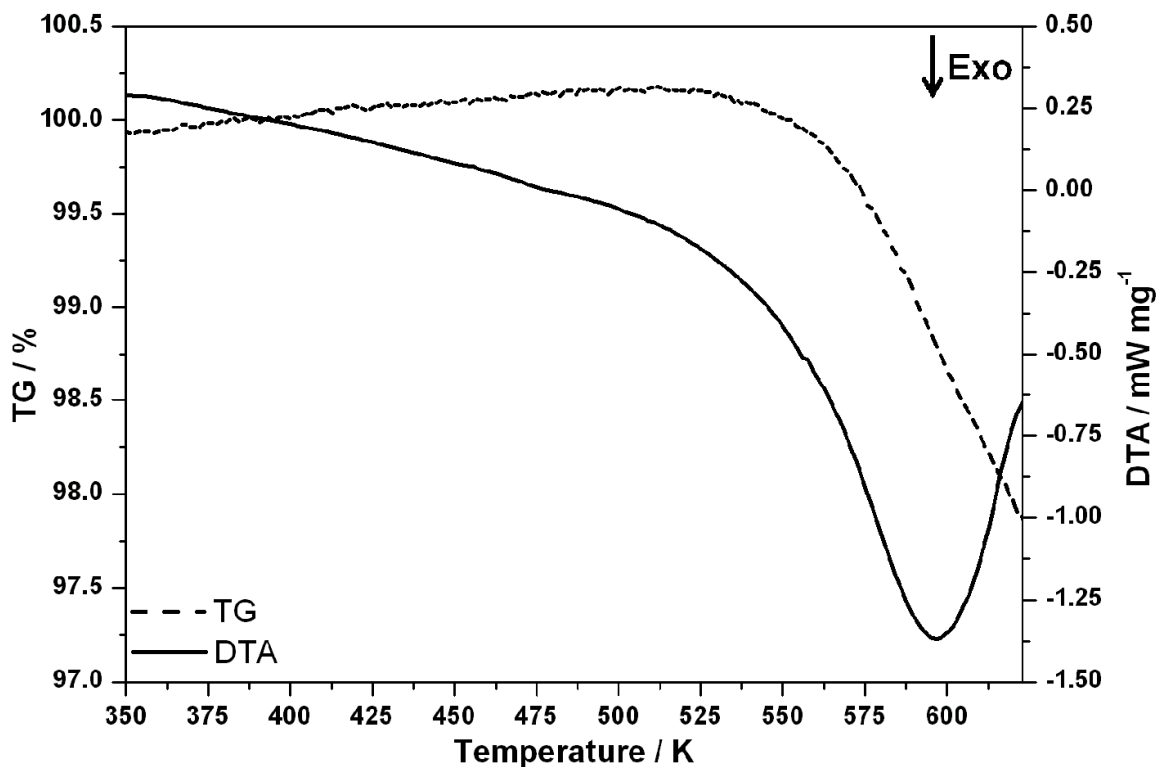


Figure 7-57: TG (dashed line) and DTA (full line) data obtained for Sample 13.

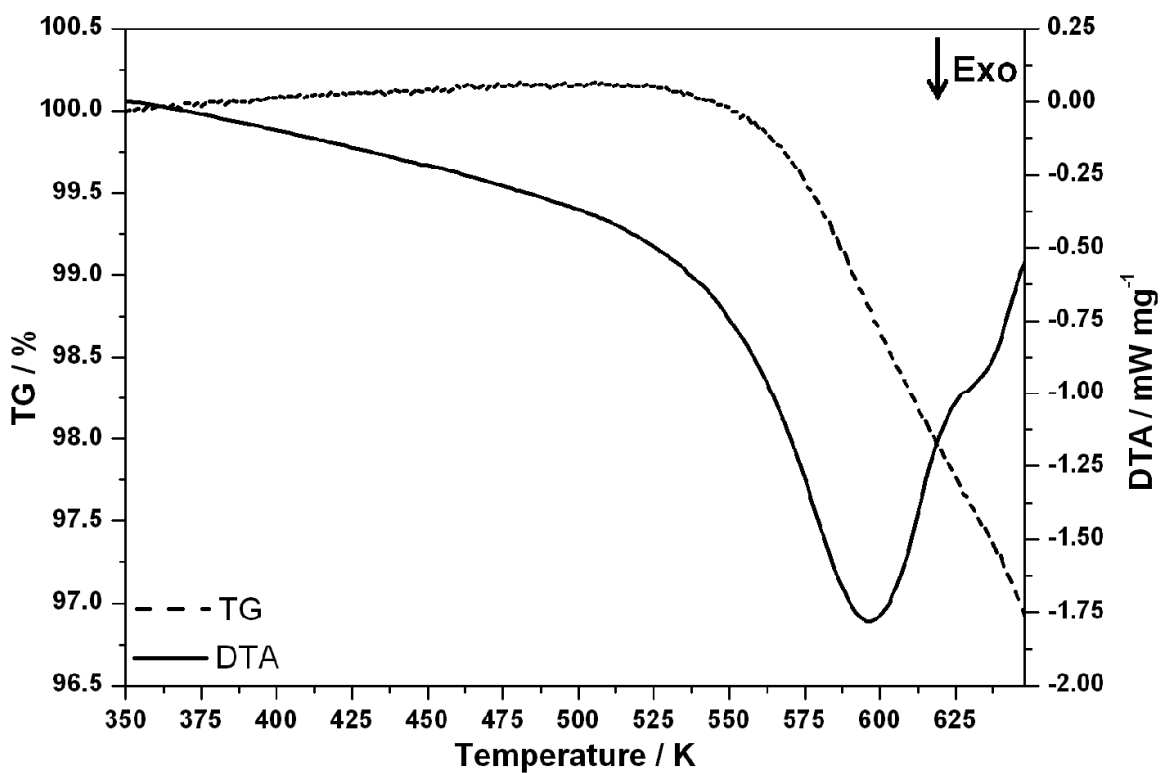


Figure 7-58: TG (dashed line) and DTA (full line) data obtained for Sample 14.

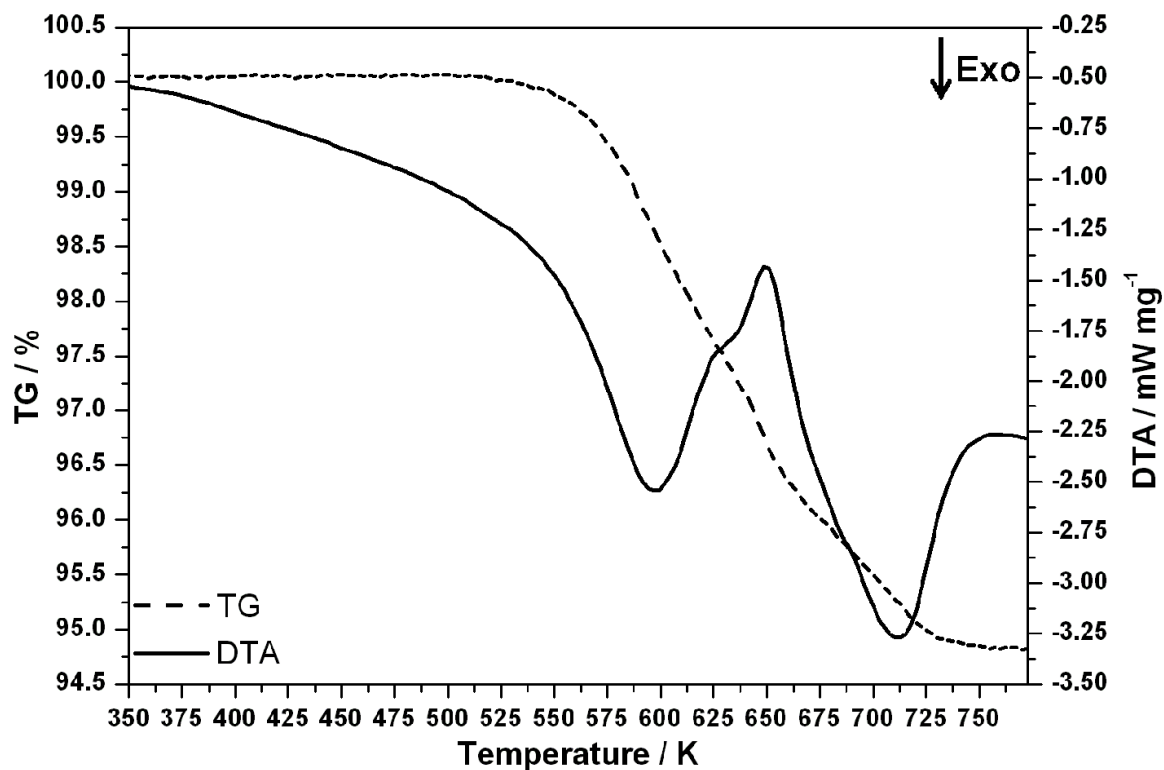


Figure 7-59: TG (dashed line) and DTA (full line) data obtained for Sample 15.

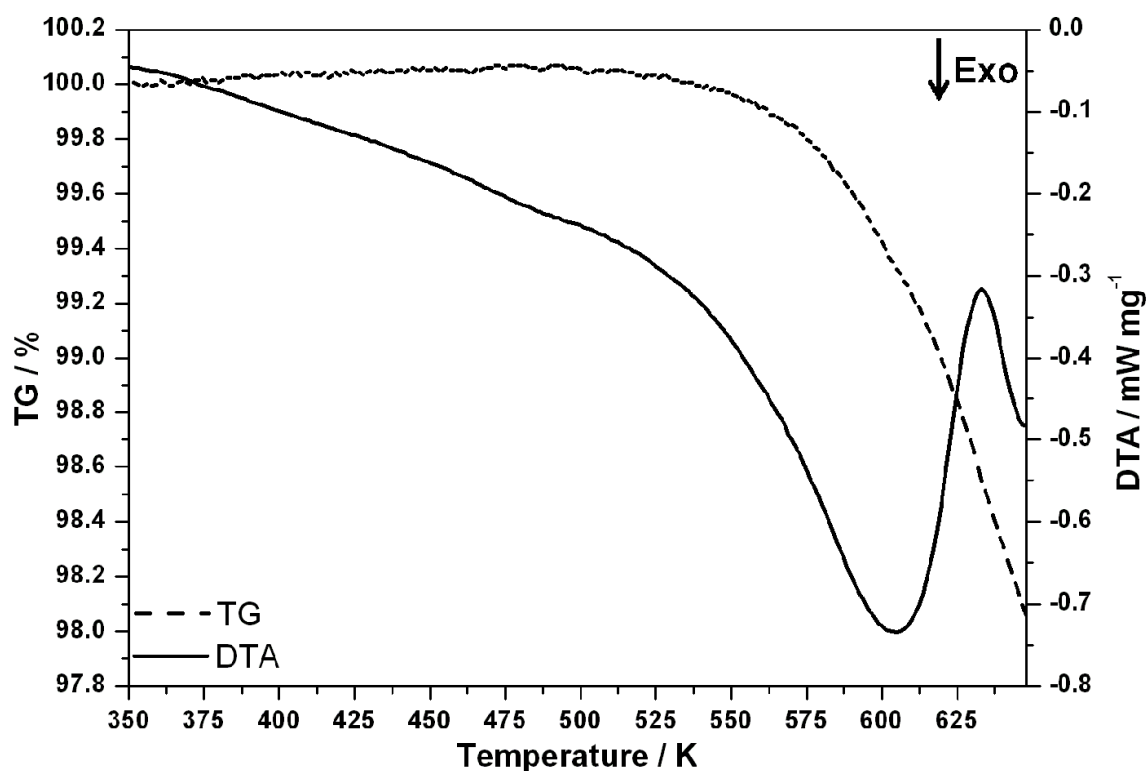


Figure 7-60: TG (dashed line) and DTA (full line) data obtained for Sample 18.

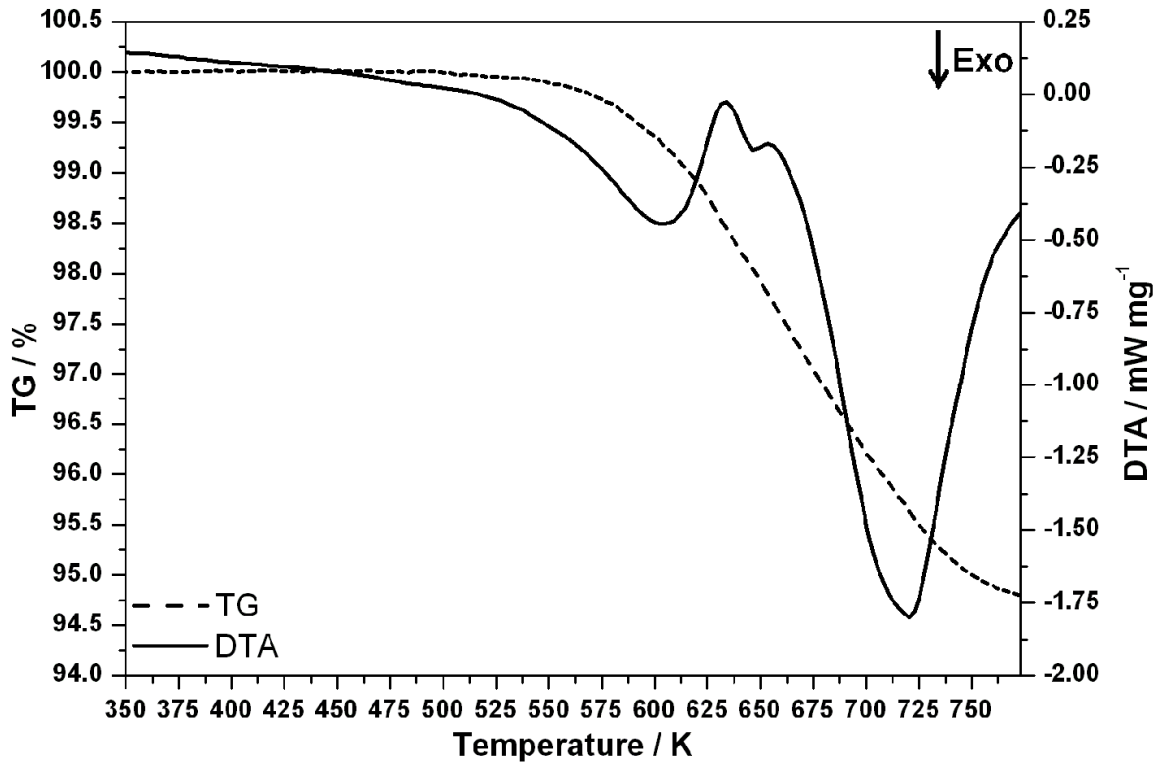


Figure 7-61: TG (dashed line) and DTA (full line) data obtained for Sample 19.

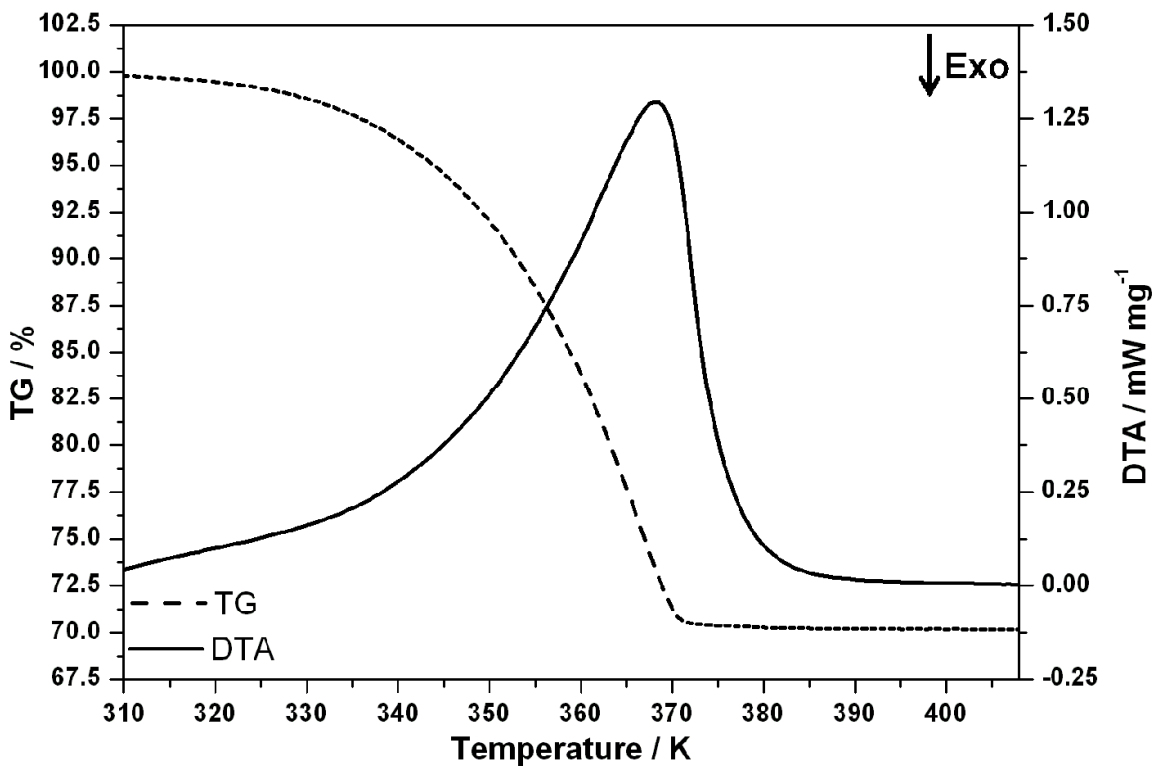


Figure 7-62: TG (dashed line) and DTA (full line) data obtained for Sample 25.

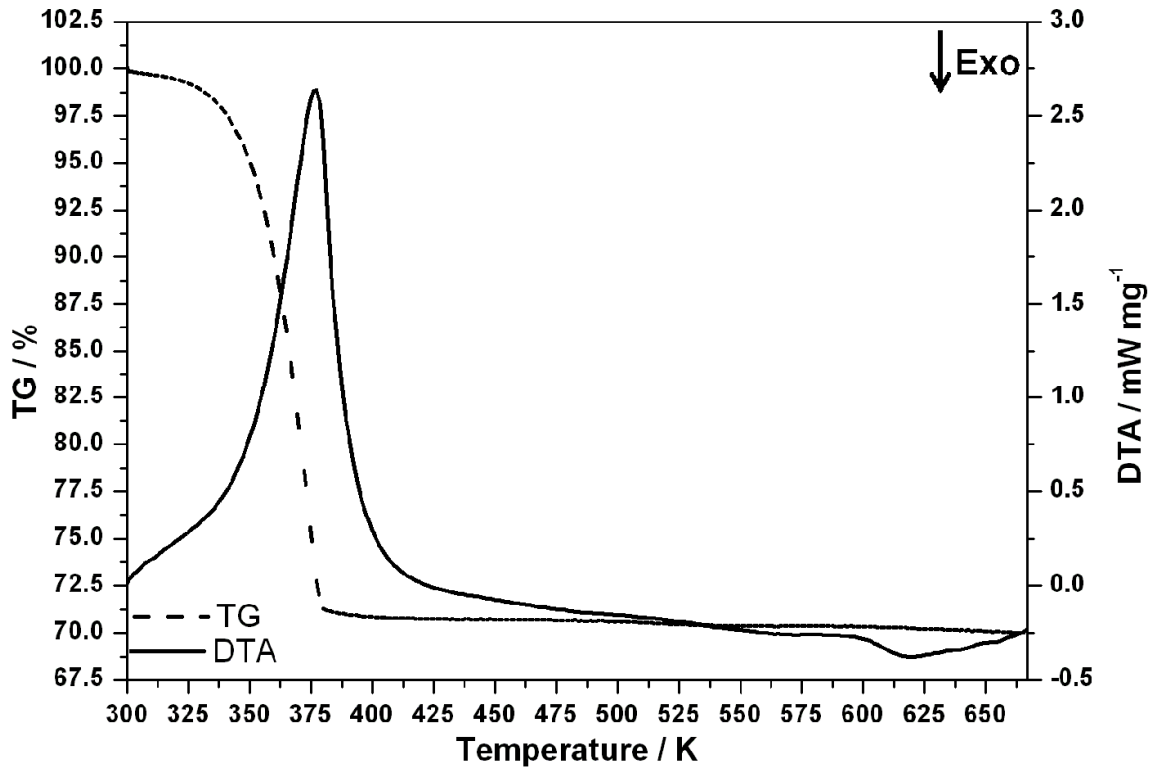


Figure 7-63: TG (dashed line) and DTA (full line) data obtained for Sample 26.

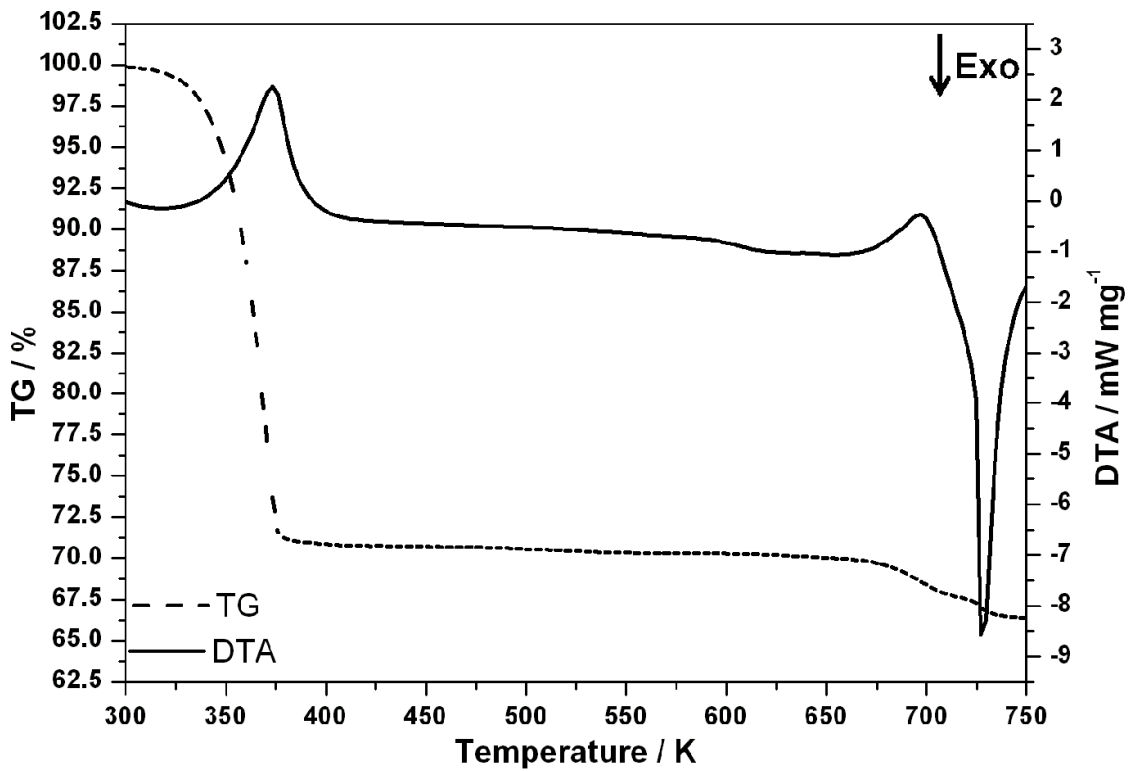


Figure 7-64: TG (dashed line) and DTA (full line) data obtained for Sample 27.

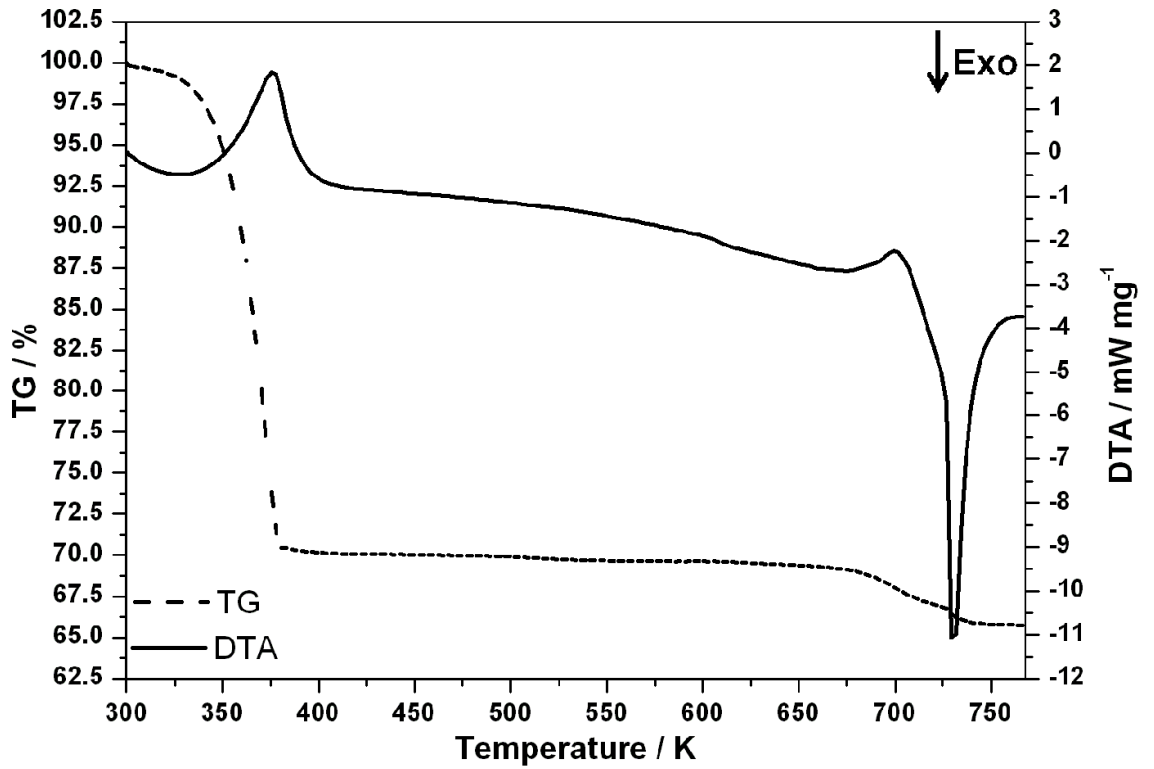


Figure 7-65: TG (dashed line) and DTA (full line) data obtained for Sample 28.

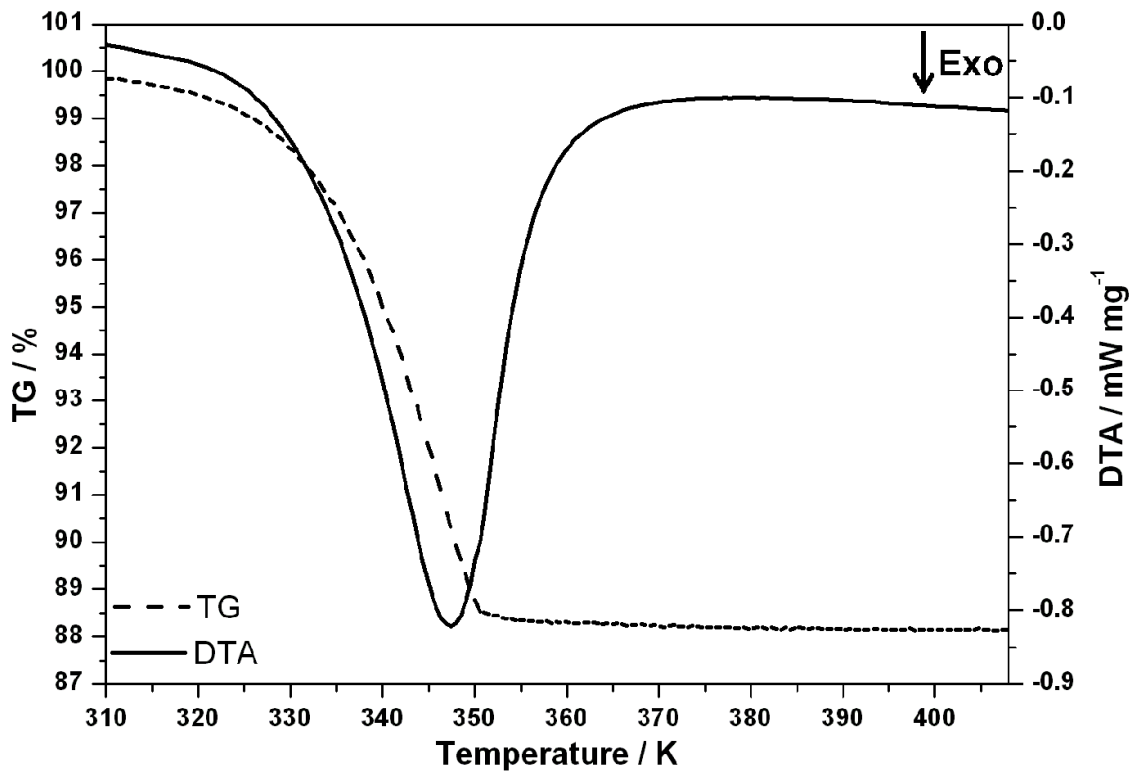


Figure 7-66: TG (dashed line) and DTA (full line) data obtained for Sample 31.

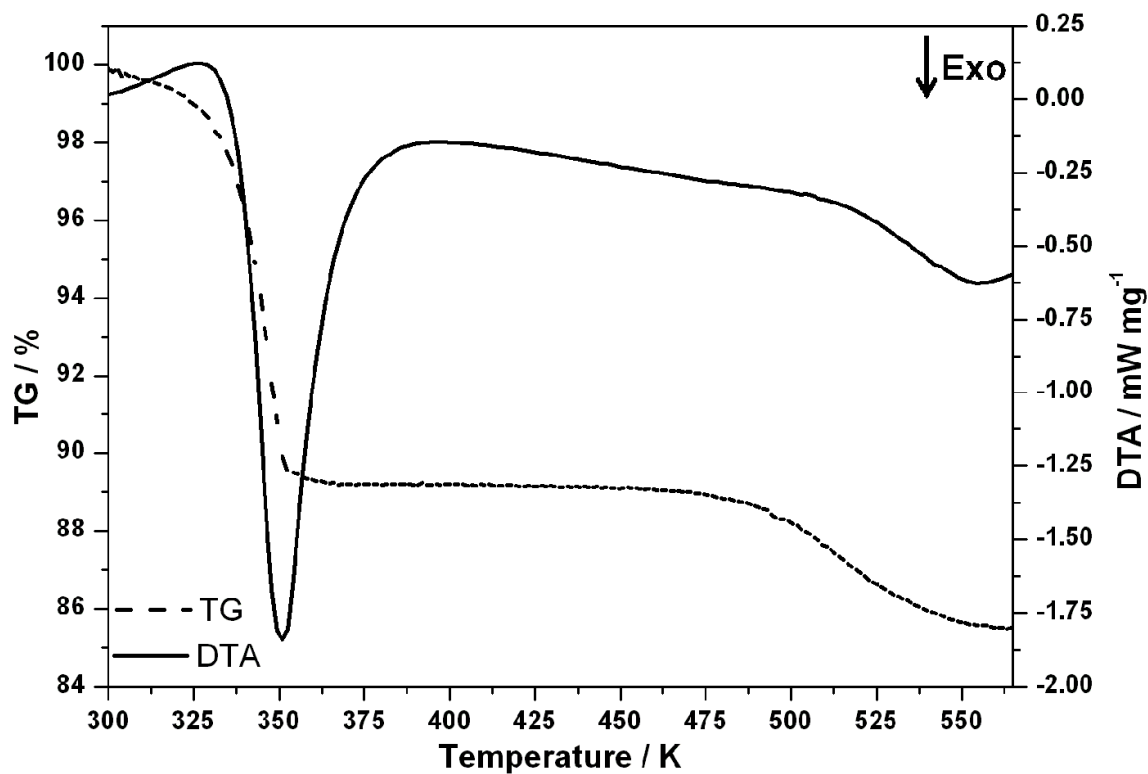


Figure 7-67: TG (dashed line) and DTA (full line) data obtained for Sample 32.

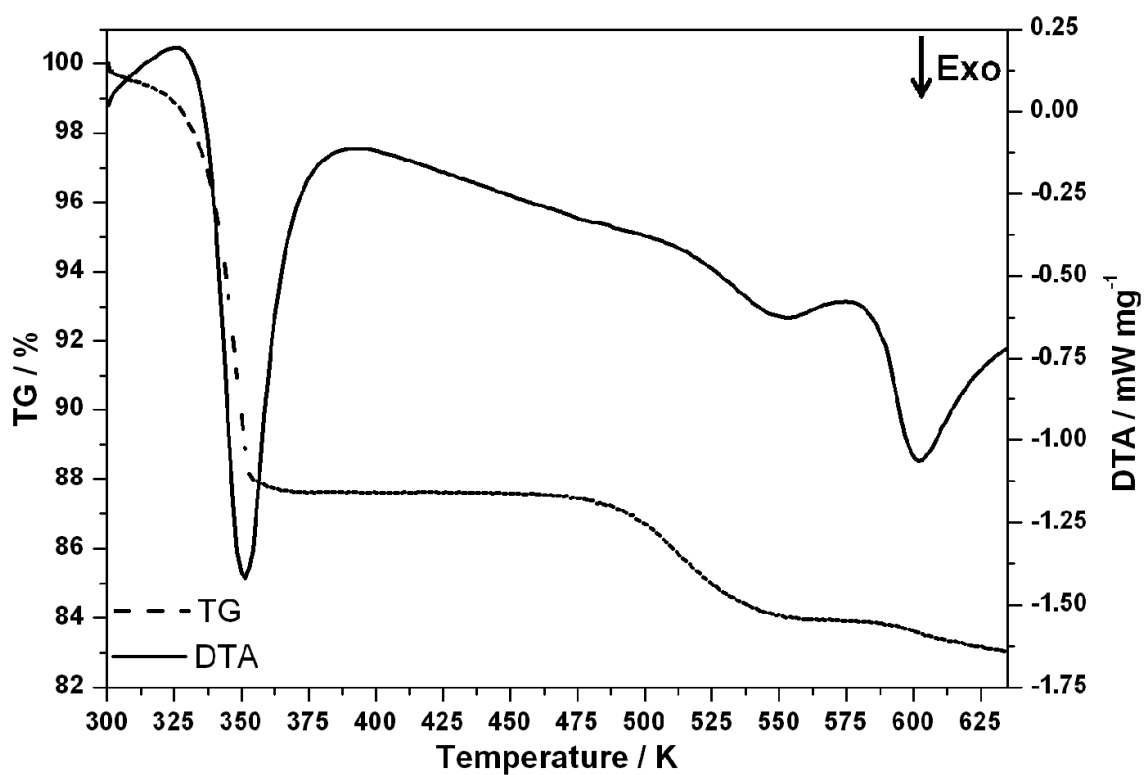


Figure 7-68: TG (dashed line) and DTA (full line) data obtained for Sample 33.

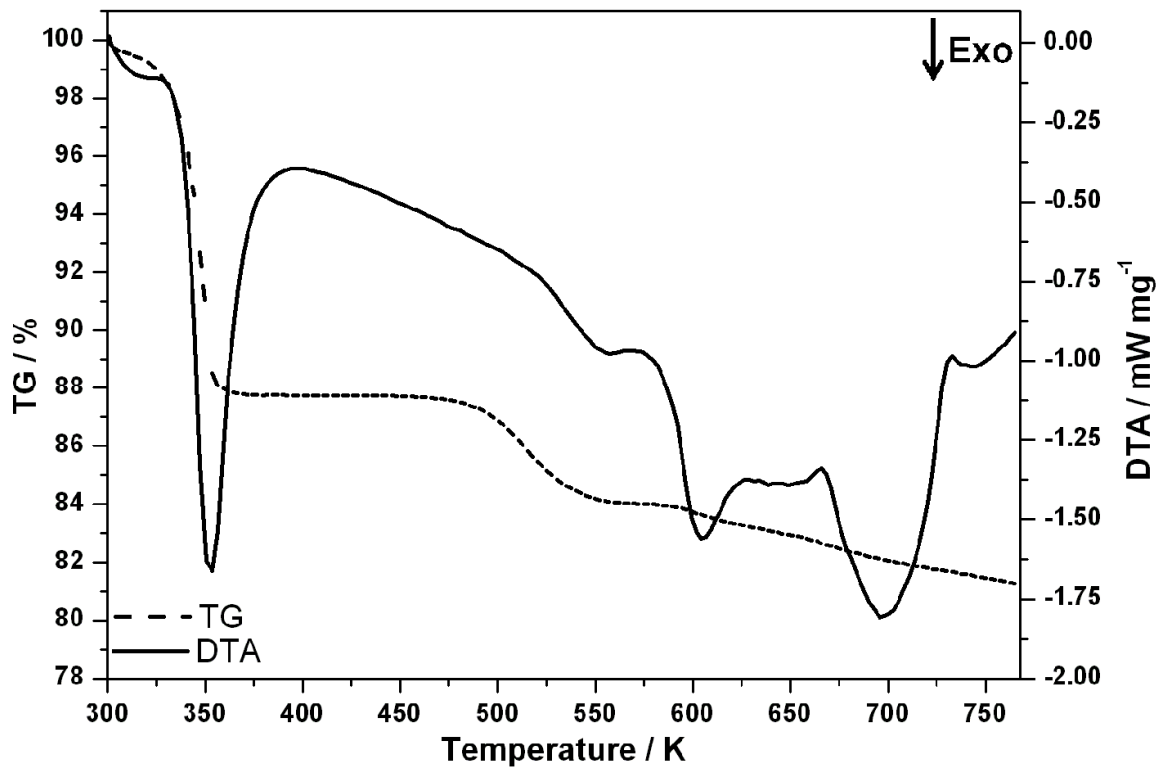


Figure 7-69: TG (dashed line) and DTA (full line) data obtained for Sample 34.

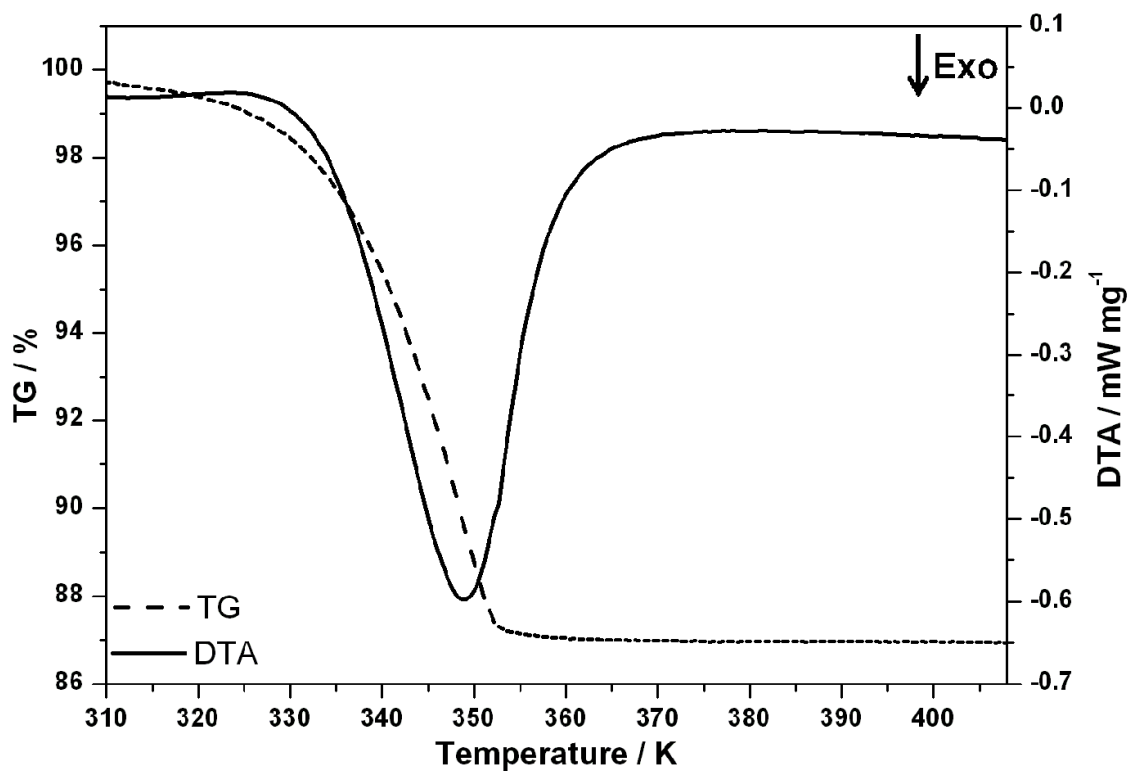


Figure 7-70: TG (dashed line) and DTA (full line) data obtained for Sample 37.

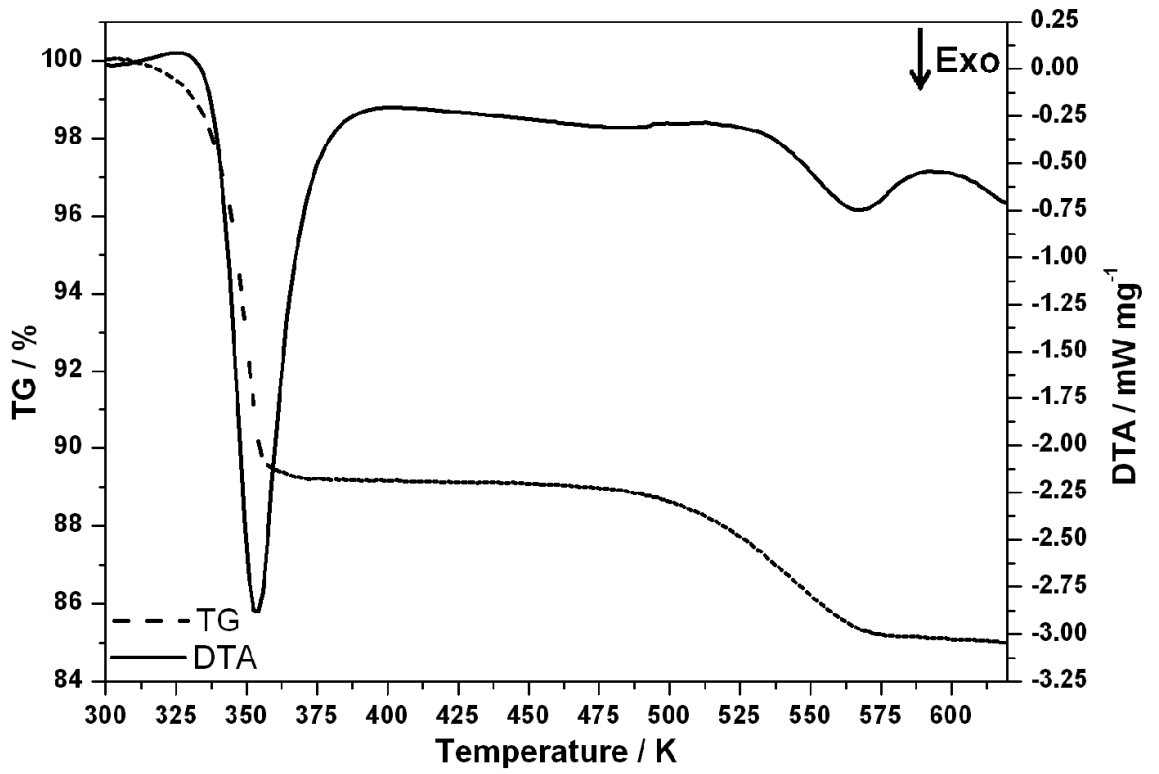


Figure 7-71: TG (dashed line) and DTA (full line) data obtained for Sample 38.

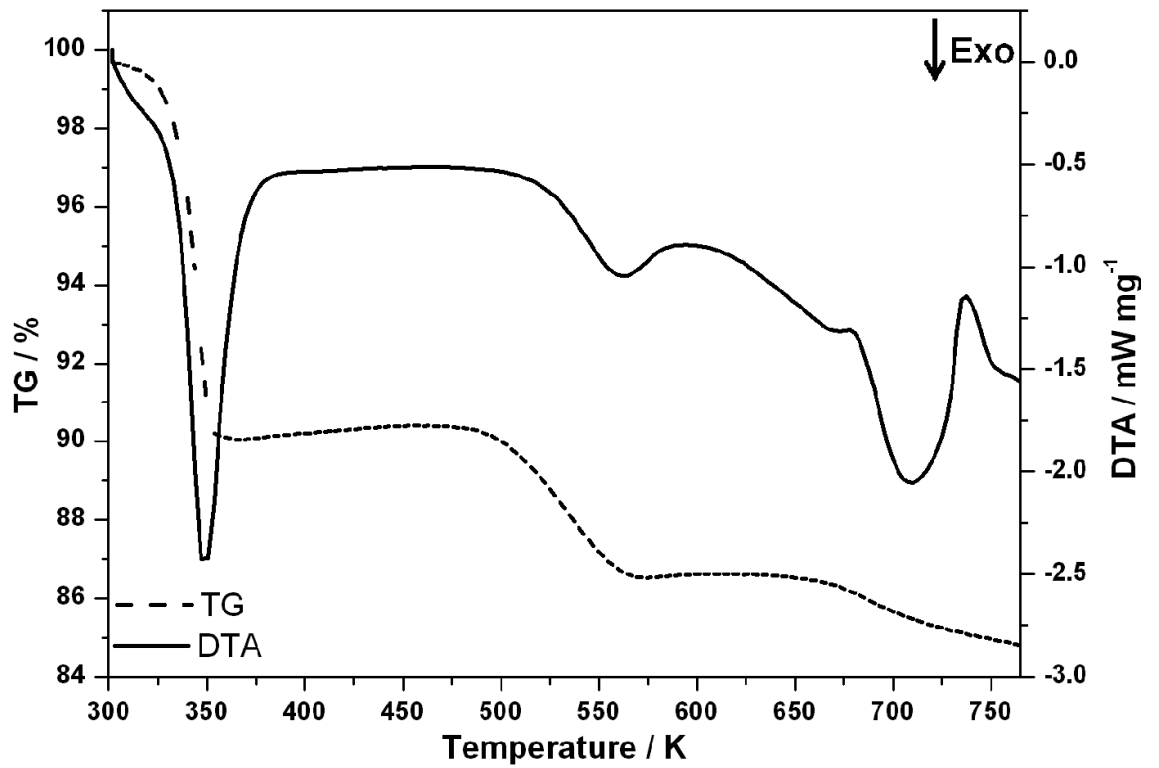


Figure 7-72: TG (dashed line) and DTA (full line) data obtained for Sample 39.